Chem Soc Rev

ROYAL SOCIETY OF CHEMISTRY

REVIEW ARTICLE

View Article Online
View Journal | View Issue

Cite this: *Chem. Soc. Rev.*, 2023, **52**, 3778

Probing the binding and activation of small molecules by gas-phase transition metal clusters *via* IR spectroscopy†‡

André Fielicke [ab]

Isolated transition metal clusters have been established as useful models for extended metal surfaces or deposited metal particles, to improve the understanding of their surface chemistry and of catalytic reactions. For this objective, an important milestone has been the development of experimental methods for the size-specific structural characterization of clusters and cluster complexes in the gas phase. This review focusses on the characterization of molecular ligands, their binding and activation by small transition metal clusters, using cluster-size specific infrared action spectroscopy. A comprehensive overview and a critical discussion of the experimental data available to date is provided, reaching from the initial results obtained using line-tuneable CO_2 lasers to present-day studies applying infrared free electron lasers as well as other intense and broadly tuneable IR laser sources.

Received 9th January 2023

DOI: 10.1039/d2cs00104g

rsc.li/chem-soc-rev

[a] *Fritz-Haber-Institut der Max-Planck-Gesellschaft, 14195 Berlin, Germany. E-mail: fielicke@fhi-berlin.mpg.de*
[b] *Institut für Optik und Atomare Physik, Technische Universität Berlin, 10623 Berlin, Germany*

† This work is dedicated to the many scientists, engineers, technicians that envision, construct, and operate large-scale experimental infrastructures and support the scientific projects of the users of such facilities.

‡ Electronic supplementary information (ESI) available: Table of experimental vibrational frequencies of gold cluster complexes with O_2. See DOI: https://doi.org/10.1039/d2cs00104g

André Fielicke

André Fielicke studied chemistry and obtained his doctoral degree at Humboldt-Universität zu Berlin (Germany). In 2001 he joined the group of Gerard Meijer at the FOM Institute for Plasmaphysics in Nieuwegein, the Netherlands, where he learned about the fascinating capabilities of infrared free electron lasers for gas-phase spectroscopy. Ever since the vibrational spectroscopy of clusters using FELs has been a central topic of his research. Today he leads a research group within the Department of Molecular Physics at the Fritz-Haber Institute in Berlin, Germany.

1 Introduction

1.1 Coordinately unsaturated metal clusters

"Cluster chemistry may provide valuable insights to chemisorption and catalysis on surfaces" the American coordination (and surface) chemist Earl L. Muetterties – rather cautiously – wrote in the subheading of his 1977 article in Science entitled Molecular Metal Clusters.[1] With this statement he refers to the, at that time, newly introduced concept of the cluster-surface analogy that sees clusters as 'little pieces of metal with chemisorbed species on the periphery'. While this picture, with some limitations, is indeed appropriate, used up to date and one of the main motivations for this review, the clusters Muetterties and his contemporaries had been studying are rather different to what we may have in mind today for cluster models of a reactive metal surface. From initially studying polyhedral borane anions, like the famous icosahedral $B_{12}H_{12}^{2-}$, Muetterties later developed a strong interest in the relation between transition metal (TM) cluster chemistry and the surface science of metals. He concluded that the, at his time, 'virtually unknown area of coordinately unsaturated metal clusters'[2] may bear suitable synthetic models for a reactive metal surface. In the late 1970s, the time may have been ripe for such type of models as the analogy between cluster compounds and ligand covered surfaces had been raised also by others,[3] realizing full well that there remain also significant differences, *e.g.*, in the metal's coordination or in the electronic structure that is discrete for a cluster containing only a few atoms as opposed to the continuous band structure of an extended metal.

In order to prove the suitability – and also the limits – of such a cluster/surface analogy the central questions that emerge are: how does the geometrical and electronic structure of a coordinately unsaturated or completely bare metal cluster affect its reactivity? What are the elementary binding mechanisms for the ligands and the structural properties of the cluster complexes formed? When does the metal binding lead to an activation of bonds, eventually even to bond-breaking within the ligand and to further reactions in the cluster complex? How does this all depend on the coordination of the active metal centers and the size of the cluster? How does the charge a metal cluster may be carrying affect the reaction behavior?

A prerequisite for answering these questions is information on the electronic and geometric structure of the clusters themselves and of their complexes. With a few exceptions (*e.g.*, Zintl type ions), ligand-free metal clusters can only be studied under very special conditions: isolated in vacuum, embedded in (inert) cryogenic matrices, or deposited on surfaces in an ultrahigh-vacuum environment. However, cluster densities are usually rather low (see below), which hinders the use of standard analytical techniques. The density problem may be, to some extent, overcome by accumulating clusters over prolonged times (minutes to hours). Handling the samples at cryogenic temperatures can extend the time-window available for characterization. A more severe problem remains for embedded or deposited species, as their identity may be easily obscured, due to disintegration or other reactions occurring already during sample preparation, and interactions between the clusters or with the substrate or matrix. In addition, metal clusters and their complexes are often directly grown in a matrix or on a surface from their constituents. This typically leads to a distribution of different species defeating unambiguous, and direct, size or composition specific assignments. Nevertheless, despite these difficulties, matrix isolation spectroscopy has made significant contributions to the understanding of small metal clusters and their complexes.[4] On the other side, clusters deposited on surfaces can be studied in real space by imaging techniques like scanning probe microscopy[5] or aberration corrected electron microscopy.[6] The latter clearly reproduces – on a graphite substrate – the tetrahedral structure of Au_{20}, which had been identified before by using gas-phase spectroscopy.[7]

1.2 Experimental characterization in the gas phase

Bare metal clusters are difficult to access with the methods of preparative synthetic chemistry. Such systems are usually not stable in condensed phase. However, in the gas phase completely ligand-free clusters can be prepared by sputtering or aggregation from atomic vapors.[8] For many transition metals, thermal evaporation, due to their high melting and boiling temperatures as well as their reactivity towards many refractory materials at elevated temperatures, raises significant technical difficulties. Accordingly, the introduction of the laser vaporization technique[9] in 1981 was a breakthrough for the facile production of uncovered, bare metal clusters – composed out of essentially any metal, in wide size-ranges, and even in different charge states. Following a similar principle, electric discharges have also been used for sputtering or vaporization.[10] Together, these comparably simple and universal ways for cluster production enabled intensive studies of the transition metal clusters' chemistry in the gas phase.[8b,11]

Though, the great flexibility in the cluster production comes at a very high price:

- The statistical aggregation process generally leads to a broad distribution of differently sized clusters.
- The high instability towards condensation requires handling of the clusters in molecular beams or – for charged clusters – using ion beam (or trap) techniques.
- This typically sets limits on the experimental observation time frame to a few 100 microseconds in a molecular beam. Longer characterization times (ms–s) can be realized by storing charged clusters in ion traps.
- Finally, the total number of clusters that can be produced in a single experiment and achievable densities are rather limited as illustrated by the space charge limit of ion traps of about 10^6 to 10^7 ions cm^{-3}.

These densities still correspond to a nearly perfect vacuum, such that one can neglect cluster–cluster interactions. Also, collisions with background gases can be controlled *via* the experimental conditions. Therefore, the clusters can be studied practically isolated in vacuum, in a well-defined environment, and there are no ill-characterized interactions with a support or a solvent.

Specifically for the characterization of metal clusters and their complexes *in the gas phase* and thus in an isolated environment a variety of experimental techniques have been employed. Those are reaching, *e.g.*, from an analysis of mass spectral intensity patterns to decipher composition and relative stabilities,[12] over studies in flow or collision cells that result in information on reactivities and (collision) cross sections,[8b,11,13] electron diffraction,[14] measurements of magnetic and electric moments in Stern-Gerlach type beam deflection experiments,[15] towards a wide range of spectroscopic techniques.

Historically, due to the availability of suitable lasers, the spectroscopy of metal clusters has been mostly performed in the visible and ultraviolet spectral region, thus typically inducing electronic excitations and/or ionization.[16] Because of the dense electronic structure of transition metals, these spectra are congested and (with few exceptions) not well resolved, meaning they usually lack vibrational and rotational resolution. More recently, a few examples for vibrationally resolved optical excitation spectra of small gas-phase gold clusters and their complexes have been reported.[17] However, a quantitatively correct assignment of a transition metal cluster's electronic spectrum is still far from trivial even with the advanced quantum chemical methods available today. Exceptions are clusters of the 'simple' metals like the alkali metals that can be reasonably described using a one electron-shell model, the 'jellium' model, which naturally also explains the evolution of their size-dependent stabilities, *i.e.*, the appearance of 'magic numbers'.[12,16a,18]

For anionic metal clusters, photoelectron spectroscopy has been – and still is – extensively applied, as one can obtain selectivity for size and composition by a preceding mass spectrometric separation step for the negatively charged clusters.

Being an optical spectroscopy, anion photoelectron spectroscopy (APES) primarily probes the electronic structure and can deliver insights into orbital interactions and electron transfers that lead to the formation of chemical bonds between metal and ligands.[19] The spectra are often rather complex and contain information on the anionic as well as the neutral cluster species and, in some cases, vibrational substructures can be resolved for the neutral states formed upon detachment. Vibrational progressions are governed by the Franck–Condon overlap and, therefore, indicate changes in metal–ligand interaction upon ionization. An example is the observation of progressions with $\sim$1350 cm^{-1} for $Au_n(O_2)^-$ (n = 2, 4, 6), revealing that the detachment involves the π^* orbital of O_2 and drives a transition from superoxide (O_2^-) to only weakly activated O_2 in the neutral complex.[20]

Using bright X-ray sources like synchrotrons or X-ray free electron lasers, core level photoelectron and X-ray absorption spectroscopy of gas-phase metal clusters also became possible.[21] Similar to ESCA (electron spectroscopy for chemical analysis)[22] and its derivatives, element-specific information on the local coordination environment can be obtained that is, however, in practice often limited due to comparably small chemical shifts and, therefore, an inherent finite energy resolution. Further, studies of the X-ray magnetic circular dichroism have shown to give a sensitive measure for the magnetic properties of metal clusters[23] and thereby complement the traditional Stern-Gerlach type experiments.

Without any doubt, all these achievements contribute to the todays understanding of (transition) metal clusters. A central question thereby – already from early on – was to draw connections between intrinsic cluster properties and their reaction behavior. However, such analyses were mostly focused on electronic properties as expressed by, *e.g.*, ionization or excitation energies, HOMO–LUMO gap, or similar quantities.[24] Initially, structural arguments typically played roles in the discussion of saturation compositions, *i.e.*, cases where the surface of a metal cluster is fully covered with ligands. Special counting schemes were suggested to relate the coordination of a cluster's surface atom with the number of ligands it can bind, and from this approach geometrical models for the metal clusters had been developed. More details about this chemical probe method[25] and related present-day insights are discussed later for TM clusters saturated with N_2.

Unambiguous information on the structures of a wider range of bare metal clusters only became available with the advent of modern density functional theory methods coupled with efficient search schemes for geometric configurations, in particular, global structure optimization methods.[26] The comparison of predicted properties of the identified structures with experimental observables has proven to be an effective approach not only for figuring out the actual cluster structures, but, at the same time, the suitability of the theoretical approach can be tested.[27] Assignment of experimental data based on quantum-chemical predictions is nowadays a widely used and very successful approach and, of course, not limited to the field of cluster science. Noteworthy, comparing complex multidimensional data, like spectra or diffraction patterns, has the potential to result in a more definite structural assignment then comparing quantities that are represented by a single number only, like ionization energies or collision cross sections. With a combination of different experimental techniques, *i.e.*, effectively increasing the dimensionality of the observable, even isomer selective spectroscopy of metal clusters can be performed, by discriminating isomers *via* their different reactivities, isomer specific spectroscopic properties (using hole burning spectroscopy), or an isomer selective detection scheme, for instance *via* near-threshold ionization.[28]

With these possibilities to characterize isolated transition metal clusters in the gas phase, they become important models in the study of the chemical behaviour of extended metal surfaces and for metal nanoparticles relevant in heterogeneous catalysis. More specific information on the chemistry of metal clusters have been obtained, *e.g.*, from the investigation of their reaction kinetics, equilibrium compositions, by collision induced fragmentation of cluster complexes, or by studying the (thermal) desorption of ligands from the clusters. Such aspects will not be further discussed here, as in the last years a number of reviews,[29] books,[30] and thematic journal issues[31] have been devoted – entirely or in part – to the topic of gas-phase chemistry of metal clusters and their potential as model systems for catalysis. For instance, a comprehensive review of gas-phase reactivity studies of metal clusters, relevant mechanistic aspects and theories, the reactivity of monolayer-protected metal clusters and metal cluster catalysis has been given by Luo, Castleman, Jr., and Khanna in 2016.[11d]

In this review, the focus will be set on the characterization of the metal–ligand interaction in such complexes of transition metal clusters *via* vibrational spectroscopy, or more specifically *via* infrared spectroscopy. Vibrational spectroscopy directly probes force constants and thereby primarily local properties of the metal–ligand binding, like the binding configuration, type and strength of the bonds formed between ligand and metal atom(s), as well as impacts on the internal bonding of the ligand, as, for instance, bond activation or consecutive reactions within the complex. Infrared spectroscopy is a well-established technique for probing ligand–metal interactions, *e.g.*, in the fields of (inorganic) coordination chemistry, in surface science, and to characterize heterogeneous catalysts.[32] While the bonds that are probed are localized at the ligand and the actual binding site of the cluster, they still sense the entire system and, thus – to some extent – reflect the total electronic and geometric structure of the complex. An example is the charge state and cluster-size specific C–O activation in TM carbonyls – reflecting the d-electron density involved in the π-backdonation – that can be probed *via* the C–O stretching frequency, ν(C–O) (see Section 3.1.2).

1.3 Size-dependent properties of clusters

Small metal clusters, M_n, in the size regime containing a few to hundreds of atoms, 'where each atom counts', often show peculiar size-dependent chemical and physical properties.[33] Generally one may distinguish between (i) ensemble effects

leading to smooth changes of a property P that can be described by scaling laws in the typical form of $P(n) = P_\infty + \alpha \cdot n^k$ (in case of $k = -1/3$, P scales with the inverse cluster radius like the ionization energy of a metallic sphere;[33b] P_∞ may be seen as the bulk value of P) and (ii) more discontinuous changes caused by the emergence of special electronic or geometrical structures for certain cluster sizes. This variability also arises in the capabilities to bind and activate small molecules and makes metal clusters interesting objects not only in their own right, as oddities at the nano-scale between atom and bulk, but naturally also for applications where one strives for a specific, tailor-made reaction behavior. Furthermore, as clusters are precisely defined, well-characterizable systems of limited size, they are perfectly suited to provide quantitative reference data, *e.g.*, to help the understanding of more extended, complex systems like deposited metal nanoparticles relevant in catalysis, or to test the suitability of theoretical approaches.[29c,f,34]

As an example, the discovery of Haruta and co-workers in the late 1980s that gold nano-particles deposited on oxidic supports can act as an effective as well as selective low temperature oxidation catalyst,[35] has triggered a vast amount of experimental studies on gold clusters in the gas phase, but also of gold particles in the form of colloids, ligand-stabilized, or deposited on a substrate.[30b–d,36] By today, gold clusters are probably among the best experimentally characterized cluster systems. Gold clusters have been well studied with respect to their electronic and geometric structures,[37] isomerism and fluxionality,[28d,38] thermodynamic stabilities,[39] radiative and optical properties,[17,40] as well as chemical reactivity and reaction thermochemistry.[24e,41] Even a number of cases have been demonstrated, where small gold clusters act as gas-phase catalyst, *e.g.*, in the oxidation of CO by O_2.[42] Rather central for such oxidations is the capability to bind and activate molecular oxygen for which a strong cluster-size dependent reactivity – anti-correlated with the electron binding energy[24e] – is seen for anionic Au clusters. A central hypothesis for understanding this behavior was the formation of superoxo (O_2^-) species that could be eventually clearly detected in $Au_n(O_2)^-$ (for even numbered n) complexes – and also for O_2 bound to certain cationic and neutral Au clusters – *via* the characteristic O–O stretch vibration at about 1100 cm^{-1}.[43] Further details are given in Section 3.1.4. Also co-adsorbates of the form $Au_2(O_2)(CO)_m^-$ have been characterized by their IR spectrum giving structural information about these possibly relevant intermediates in the CO oxidation catalyzed by Au_2^-.[44] Far-infrared spectroscopy even has provided detailed information on the internal geometrical structures of gold clusters.[7b,45]

This review is focused on the characterization of complexes of bare transition metal clusters with small molecules using IR action spectroscopy and related techniques. It does not discuss the wide area of ligand-stabilized clusters that are often produced in bulk-quantities by preparative methods. If macroscopic amounts of samples are available, characterization with more standard commercial and widespread analytical equipment becomes possible to get insight into structure and properties.[46] Instead, the focus is set on transient species that are produced and characterized *in vacuo*, often in a range of differently sized clusters, M_n. Particular attention is given to small clusters containing typically less than 30 atoms, for which size (and composition) specific experimental data has been obtained. Metal atom complexes, including clusters of several ligands/molecules around a single metal atom are not covered. However, if appropriate in the context, relevant references, in particular reviews, will be indicated. The majority of complexes discussed contain just a single ligand, which would correspond for a surface at the low coverage limit.

The review is structured as follows: after this introduction, where more general aspects of metal clusters and their chemistry have been discussed, the experimental techniques for obtaining mass-selective infrared spectra are introduced in the second section. Particular attention is given to infrared action spectroscopy using infrared free electron lasers, which have emerged as superior light sources for action spectroscopy in terms of intensity and wavelength tunability, covering practically the complete chemically relevant infrared region, from about 50 cm^{-1} to 4000 cm^{-1}. The following section discusses the data for the various cluster complexes in order of increasing complexity of the ligands, *i.e.*, molecular size. Most information exists for the smallest ligands, in particular for complexes with H_2, CO, N_2, and O_2 that are discussed more extensively. The activation of such small molecules plays a crucial role as an initial elementary step in a large number of industrially relevant chemical processes like the Haber-Bosch process, Fischer–Tropsch synthesis, or oxidations involving O_2.[47]

The discussion of the single ligands in Section 3 starts with general remarks about their binding mechanism, reactivity, and summarizes the vibrational properties of the ligands as a free molecule, in atomic complexes and/or adsorbed on metal surfaces, which is followed by the data available for the respective metal cluster complexes. If relevant, further aspects are discussed like insights obtained from the vibrational spectra into different binding geometries, molecular *vs.* dissociative binding, cluster size effects, studies of saturated complexes or other ligand-specific topics. While it cannot be the aim to discuss all the relevant studies and their results here at length, the tables preceding each chapter pursue completeness, covering the literature from the mid-1980s until end of 2022 (Table 2 – diatomics; Table 7 – triatomics; Table 8 – 4-atomic and larger ligands). Complexes containing different, co-adsorbed, ligands and examples, where the IR absorption is found to induce thermal reactions (except the simple case of dissociation into the initial reactants), are discussed subsequently. The closing outlook sketches some of the actual, potential, and/or desirable further developments that will enhance the understanding for the fascinating gas-phase chemistry of transition metal clusters.

2 IR action spectroscopy using FELs and other tunable IR sources

2.1 Characterization of gas-phase clusters *via* action spectroscopies

Metal clusters in the gas phase provide a perfect laboratory for systematically studying the influence of particle-size (n),

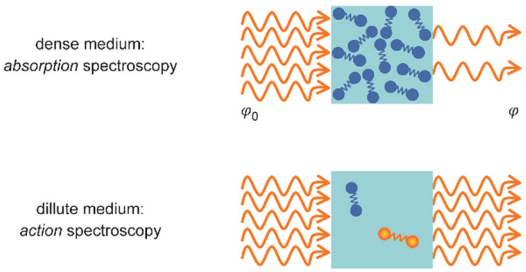

Fig. 1 Measurement of optical spectra *via* analyzing either the decrease in photon fluence φ due to light absorption by a dense sample (top) or a resulting modification within the medium (bottom).

complex composition and coverage (m), or charging (q) on the chemical interaction between ligand and cluster in the complex $M_nL_m^q$. However, the combination of very low densities and the presence of a cluster size-distribution demands specialized techniques for their spectroscopic characterization.[48] The size-distribution is, most commonly, analyzed using mass spectrometry. The required sensitivity in the spectroscopy, together with cluster-size selectivity, then again is obtained by detecting the absorption process using a mass spectrometric signal.

Whereas in 'classical' absorption spectroscopies the attenuation of light by a sample is analyzed as function of the light's frequency, alternative measures for the interaction between sample and light can be changes within the sample itself (Fig. 1). Upon absorption of a photon, its energy – and momentum – is deposited in the sample and can induce secondary processes (Fig. 2) that are then quantitatively analyzed. Accordingly, such methods are therefore usually termed 'consequence' or 'action' spectroscopies.§ On a molecular scale, these actions can be categorized as (i) changes of charge state, *i.e.*, ionization or electron detachment, (ii) changes of particle mass indicating fragmentation or other reaction (even growth) processes, or, more generally, (iii) changes of the molecules' quantum state. Possible observables are, for instance, depletion of the initially absorbing species, appearance of reaction products, and emission of electrons or photons (fluorescence). Furthermore, the excited species may exchange energy *via* gas-phase collisions, which can lead to de-excitation, or, depending on the collisional energy, facilitate collision induced dissociation.[49] Finally, in particular at low internal energies, even subtle changes in quantum state may result in completely altered reactivities, such that the (enhanced) formation of an addition product can serve to detect the photon absorption process.[50]

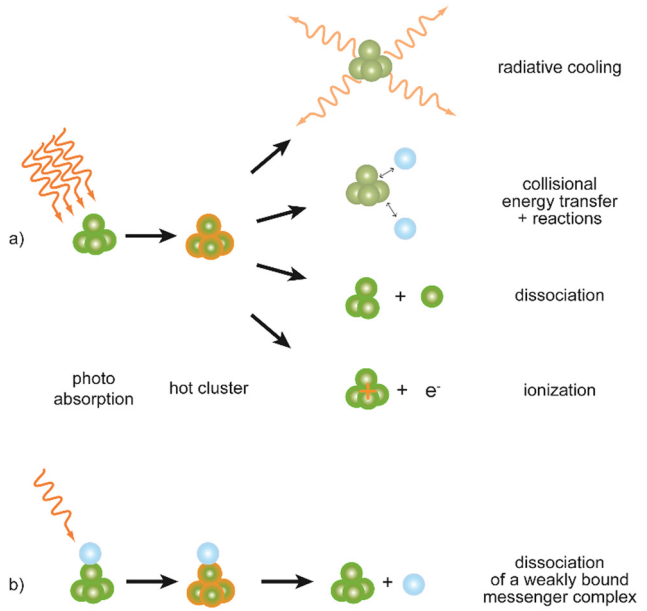

Fig. 2 Possible processes following absorption of (multiple) IR photons by a cluster complex. (a) Depending on its internal energy upon excitation, a cluster may undergo different relaxation processes: radiative cooling usually is slow in comparison to dissociation and ionization (photodetachment in case of anions). The impact of collisions strongly depends on the experimental regime (pressure and observation time) but can be neglected in molecular-beam experiments. (b) Using weakly bound messenger complexes – often with atoms of the noble gases – the internal energy required to observe an action, here the dissociation, can be significantly lowered. These actions may be used to detect photoabsorption of charged as well as neutral species, however, the latter always requires an (additional) ionization step to be analyzed by mass spectrometry.

Parent or product species can be ionic or neutral. However, in the case of neutral species, an additional ionization step, typically UV photoionization, needs to be included to allow for mass spectrometric detection.[51] Using the (crude) assumption of a constant ionization efficiency for a given neutral species at a fixed photon energy for ionization, the intensity of the detected cations is – below saturation – directly proportional to the intensity of the corresponding initially neutral cluster. However, such assumption may only be valid well above the ionization threshold, as the ionization efficiency actually depends on the state – or internal energy – of the cluster. This dependence of the ionization efficiency on the internal energy near the threshold can be used to detect IR absorption by neutral clusters before their ionization.[52]

In an absorption process, the number of photons removed out of a laser beam and the number of cluster complexes undergoing an 'action' are, obviously, directly related and may be, in case of one-photon absorption, assumed to be equal. However, as the total number of cluster complexes in the gas phase is many orders of magnitude lower than the number of photons, it is much more straight-forward to analyze the resulting comparably large relative changes in the abundance of the complex upon absorption and not the change in photon fluence.

§ Probably what one could call the first infrared action spectrum of a molecular substance had been recorded already in 1927/8 by Marianus Czerny.[379] The method he termed 'photography in the infrared' goes even back to Sir John Herschel – son of Friedrich Wilhelm Herschel, discoverer of the infrared radiation – who used a related approach 1840 for thermal imaging of the solar spectrum.[380] The name of the method, 'evaporography', hints at its basic principles: In Czerny's experiments the radiation from a Nernst globar was spectrally dispersed over a glass plate covered by a thin film of a substance (camphor or naphthalene) that sublimes quickly already at ambient temperature and is in equilibrium with its saturated vapor. At the location of the film where the IR radiation hits the frequency of a vibrational transition it is absorbed and accelerates sublimation, finally leading to a well-recognizable contrast between absorbing and non-absorbing areas. This process is particularly remarkable, as it intrinsically compensates for background signal stemming from black-body radiation.

For photodissociation, the change in ion abundance I as a function of IR frequency ν – or generally the depopulation of an initial state upon optical pumping – is described by an expression similar to the Beer–Lambert law

$$\frac{I(\nu)}{I_0} = \mathrm{e}^{-\sigma(\nu)\varphi(\nu)} \quad (1)$$

and can be very sensitively determined, unlike the practically constant (or very weak change in) photon fluence $\varphi(\nu)$ (in photons per unit area, *i.e.*, the time integrated photon flux). The one photon absorption cross sections $\sigma(\nu)$ for allowed infrared transitions are typically on the order of 10^{-21}–10^{-18} cm^2. Pulsed infrared lasers can reach – in pulses of about 10 μs duration – energies of up to 100 mJ (*i.e.* 5×10^{18} photons at 1000 cm^{-1}) or more which, when focused and carefully overlapped with the clusters in space, may induce changes in I/I_0 on the order of 10% or more. This change in ion abundance can be easily measured, on the other end, the change in photon fluence will be only on the order of 10^{-12} or lower. As a side note, computationally predicted IR intensities are often expressed as absolute integrated infrared intensities A in units of km mol^{-1} ($A = \sigma \cdot N_A/\lambda$, with λ the wavelength and N_A the Avogadro constant). The use of this unit appears particularly convenient as the numerical values of typical IR intensities are then on the order of a few ten to few hundreds km mol^{-1}. Theoretical approaches for calculating infrared spectra of isolated molecules or clusters have been discussed elsewhere and may also account for anharmonicities or non-rigidity, *i.e.*, fluxional behavior.[53] Within this review, comparisons are frequently made to calculated predictions usually on the level of density functional theory (DFT).

2.2 Infrared multiple photon absorption and the messenger technique

Using IR radiation, the 'action' (Fig. 2a) will be dissociation of a cluster complex, although, in particular for strongly bound clusters, also photoionization[52a,54] (for neutral species) or photodetachment[55] (for anions) may become energetically feasible. Noteworthy, these processes, including most dissociation reactions, typically require much higher internal energies of a cluster complex than can be reached by the absorption of *a single* IR photon. The mid-infrared region considered here ranges from about 2.5 to 40 μm (4000–250 cm^{-1}) which relates to photon energies of 0.5 to 0.03 eV (1 eV = 96.485 kJ mol^{-1} = 8065.54 cm^{-1}). For comparison, M–L binding energies of iron cluster monocarbonyls, Fe_n^+–CO,[56] are measured to be 1.4–2.8 eV depending on cluster-size, and for Au_n^-–O_2 (even sized Au clusters) they are 0.4–1 eV.[41b] This illustrates that at the typical stretching frequencies of a carbonyl (CO) ligand at around 2000 cm^{-1} or a superoxo (O_2^-) ligand at 1100 cm^{-1} at least four or five IR photons need to be absorbed by a single initially cold complex to overcome the M–L binding and to be able to observe dissociation of these complexes.

Sequential absorption of multiple IR photons by a single complex may be accomplished at sufficiently high photon fluences,[57] *i.e.*, in an infrared laser beam. After absorption of a photon, anharmonic coupling between the initially excited vibrational mode and the background modes of the cluster complex can lead to rapid intramolecular vibrational energy redistribution (IVR). The speed of this process strongly depends on the coupling strength between the initially driven oscillator and the background modes acting as heat bath, as well as on the density of states, the latter rapidly increasing with size of the system and with its internal energy. Measurements on extended surfaces find a vibrational lifetime of 2–3 ps for the internal stretch of CO chemisorbed on metals, while for CO physisorbed on non-metallic NaCl this process is much slower and happens only within milliseconds.[58] These examples illustrate extreme cases for adsorbed molecules. More typical values for IVR times within larger molecules range from several ten picoseconds to nanoseconds.[59]

Usually, as cross-anharmonicities tend to be small, the vibrational resonance will undergo – with increasing internal energy – only small shifts. However, this may be compensated by the fast IVR processes, resulting in a lifetime broadening of the absorption transition.[60] At even higher internal energies the wealth of multi-mode resonances (combination modes) leads to a quasi-continuum of states. Therefore, a complex can repeatedly cycle between resonant absorption and energy redistribution towards the heat-bath of low-frequency modes. As a result, if the excitation laser is not too narrowband and the irradiation is of sufficient duration, a single molecule or cluster is capable of sequentially absorbing tens or even hundreds of IR photons in a vibrational resonance, reaching internal energies of up to several ten eV.[61] The probably most extreme case is reached in IR resonance enhanced multiple photon ionization (IR-REMPI) spectroscopy where the thermionic ionization of sufficiently stable clusters is used to detect their vibrational spectra.[54a]

The majority of spectral information discussed in this review has been obtained using direct infrared multiple photon dissociation (IR-MPD). Its variant, the messenger technique[62] (Fig. 2b) – for metal clusters often using physisorbed Ar atoms as messenger tag – is applied in the investigation of cold complexes, where the presence of a weakly van-der-Waals-bound tag may also stabilize meta-stable configurations within the entrance channel at low temperature. Thereby, further reaction towards thermodynamically more favorable products may be suppressed, allowing for the characterization of otherwise inaccessible species.[63] Furthermore, a messenger complex can dissociate after absorption of only a single or very few photons, thus it dramatically increases the sensitivity for weak absorption bands, or at low IR frequencies.[63b,64] Compared to IR-MPD, the messenger technique gives the possibility to more effectively avoid band broadening by saturation effects at high IR laser fluence and to reduce the anharmonic band shifts, such that spectra obtained using a messenger tag are usually much better resolved compared to those measured by IR-MPD.[65] However, the binding of any messenger species to a cluster has an effect on its structure, affects the vibrational spectrum, and may even over-stabilize certain isomers, such that the isomer distribution in the complex does not necessarily map the distribution for the non-tagged cluster.[28c,66] It is usually found that such effects

scale with the polarizability of the messenger and they are often negligible for He complexes.[67]

The binding strength between noble gas atoms and metals can vary strongly with the type and size of system, metal, electronic state and charge, *etc.* For instance, for complexes with atomic transition metal cations, the bond dissociation energies range approximately from a few ten meV for He, to 0.15–0.5 eV for Ar, and nearly 1 eV for Xe.[68] For the other extreme, somehow closer to a neutral metal cluster, the adsorption of noble gas atoms on an extended, overall neutral metal surface, the binding energies scale typically in a similar manner: from only a few meV for He to about 0.3 eV for Xe, but also depend on the adsorption site and coverage.[69] In neutral metal rare-gas complexes the attractive component of the binding is usually determined by comparably weak dispersion interaction, while in ionic complexes charge induced dipole interactions result in a significantly stronger binding. Also, (partly) covalent interactions are found, in particular for the heavier noble gases Ar, Kr, and Xe.[70] In case of binding of multiple ligands to a cluster, the M–L binding energy often strongly drops after 'saturation' of the cluster – caused by steric or electronic effects – such that additional (molecular) ligands may also act like messengers.[71] As a side note, embedding neutral and charged molecules or clusters in superfluid He droplets (at about 0.4 K) is by now a well-established technique for their spectroscopy – including in the IR – in a nearly non-disturbing environment at low temperature.[72] The fast dissipation of energy from the molecule into the superfluid He surrounding minimizes hot-bands and band shifts due to (cross-) anharmonicities.

2.3 Experimental realizations

A sketch of the experimental set-up as used by the author and collaborators for obtaining IR spectra of metal cluster complexes is depicted in Fig. 3 (see ref. 73 for details). It resembles other arrangements used for depletion spectroscopy in molecular beams.[74] In contrast to experiments involving guided ion beams or ion traps, see below, it becomes possible to prepare and characterize neutral as well as charged (usually singly charged cations or anions) species under very similar conditions. The set-up allows for the production and characterization of clusters typically in a size range starting with the atom, to clusters containing up to 20–50 atoms, and their complexes with molecules added to the source formed at temperatures between about 80 and 400 K. However, most experiments are performed close to room temperature (≈300 K).

Clusters are formed by laser ablation of a solid metal target by a pulsed Nd:YAG laser (532 nm, 1–20 mJ per pulse, ≈5 ns pulse duration) and injection of a short pulse of He gas into the source channel. The amount of complex formation and the (average) number of ligands sticking to a cluster is controlled *via* the pressure and opening time of a second – again pulsed – reaction gas inlet valve. Typical total pressures in the source during cluster formation and their reactions can be estimated, by comparison to the optimal pressures measured for similar cluster sources,[75] to be a few 10 mbar, consisting mostly of He carrier gas. This relates to a He stagnation pressure of typically 5–10 bar upstream the pulsed valve.

Complex formation is stopped at the end of the reaction and thermalization channel by expansion into vacuum resulting in total reaction times on the order of ≈100–200 μs. To obtain spectra, the IR laser beam is counter-propagated to the cluster beam and loosely focused through an aperture that defines the overlap between the beams. Then, the experiment is run at twice the repetition rate of the IR laser (5 or 10 Hz) to allow for alternate on/off measurements of the mass spectrometric intensities as a function of IR frequency (Fig. 4). From the ratio of these intensities, relative IR intensities are calculated following eqn (1). Neutral cluster complexes can be detected after UV photoionization, usually by an ArF excimer (6.4 eV) or an F_2

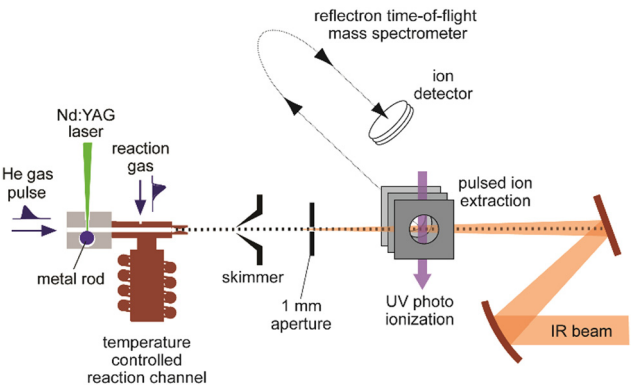

Fig. 3 Experimental set-up for IR action spectroscopy of metal cluster complexes in a molecular beam. Clusters are produced by laser vaporization and aggregation in the presence of a short pulse of He. Reactions with gas, injected *via* a second pulsed valve, occur under thermalized conditions in a copper channel that can be temperature controlled by a flow of liquid N_2 and an electrical heater in the 80–400 K range. After expansion into vacuum, the clusters pass through a skimmer and an aperture before being detected in a reflectron time-of-flight (ToF) mass spectrometer. Depletion spectra are determined from analyzing mass-specific intensity changes induced by irradiation with IR light.

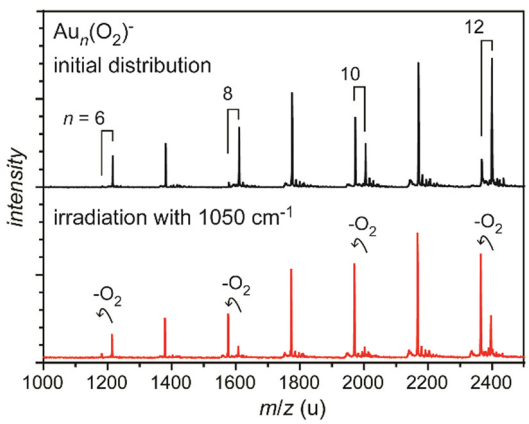

Fig. 4 Mass spectra of O_2 complexes of anionic gold clusters. Upper trace: initial mass distribution, only even-sized clusters form stable complexes with a single O_2 molecule in abundance. Lower trace: upon IR irradiation at 1050 cm^{-1} (≈50 mJ per pulse), the complexes get depleted, while the intensities of the corresponding pure gold clusters increase. The amount of depletion varies for the different sizes, as the absorption bands are slightly shifted relative to each other, see Fig. 29.

(7.9 eV) laser. Overall, typically several 100 to 1000 single mass spectra are averaged per frequency step to compensate for the inherent instabilities of the laser vaporization source.

Principally, such approach allows for a characterization of all species in the beam that can undergo dissociation, as it misses a mass selection step before the interaction with the IR laser light. Consequently, for a given charge state a large number of differently sized complexes can be investigated simultaneously. However, the mass spectral intensities may be affected by ingrowth due to fragmentation of larger complexes, *e.g.*, through fragmentation cascades or other processes leading to mass coincidences between parents and fragmentation products. Therefore, potential fragmentation pathways need to be carefully considered. The effect of fragmentation cascades can be reduced at very low reactant partial pressure, such that – at maximum – only a single ligand binds per cluster. As a consequence, mass spectral intensities of complexes formed under such conditions are typically very low.

In more evolved tandem-mass spectrometric experiments (MS^2 or MS^n), ionic complexes of a specific mass/charge ratio can be selected out of a broader size distribution, interrogated, *e.g.*, by interaction with IR radiation, and finally the product distribution is re-analyzed by mass spectrometry.[77] Due to the initial mass selection, the difficulties with fragmentation cascades are removed and often the fragmentation products can be analyzed background-free. This can significantly improve the quality of the generated IR spectra compared to depletion spectra. These instruments may be equipped with a cryogenic ion trap allowing for an efficient cooling of the ions, and thus, for the formation of complexes with very weakly bound – hence only mildly disturbing – messengers like He, Ne or H_2.[76,78] Fig. 5 shows an example of such an arrangement based on a quadrupole mass selector and a reflectron ToF mass spectrometer.[76] An alternative approach employs Fourier transform ion cyclotron resonance (FT-ICR) mass spectrometers to both store and mass analyze ions.[79] The FT-ICR cell itself may be cooled to reduce the effects of blackbody infrared radiation on the stored complexes,[77l] but thermalization *via* collisions is – due to the low pressure inside an FT-ICR cell – ineffective (Fig. 9). Initial cooling and complex formation, therefore, may be realized in a preceding gas-filled ion trap.[77i]

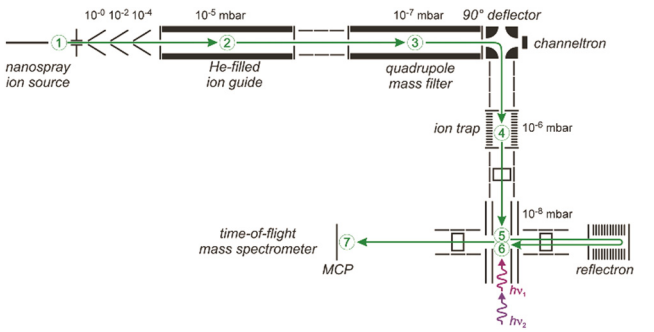

Fig. 5 Schematic of a 6 K ring-electrode ion-trap triple mass spectrometer. Ions are generated, guided and mass-selected in the first branch (1–3) of the spectrometer. The second branch houses the cryogenic trap (4) where the ions are accumulated, cooled by collisions with He and where messenger complexes can be formed. In the last branch (5–7) the product distribution is analyzed in a time-of-flight mass spectrometer. The ions exiting the trap can be irradiated with IR light in the extraction region of the time-of-flight mass spectrometer (5) and, a second time using a different laser, when they pass through this region again (6) returning from the reflectron and flying towards the micro channel plate (MCP) ion detector (7). This arrangement can be used for isomer selective spectroscopy *via* (IR) hole burning. Reproduced from ref. 76 with permission of the publisher (Taylor & Francis Ltd, https://www.tandfonline.com).

Finally, mass selected ions can be embedded in superfluid He droplets by guiding a beam of He droplets through an ion cloud held in an ion trap.[80] In this way the heavy droplets can pick up and flush out the ions from the trap, while – under evaporation of He atoms – nearly instantaneously thermalizing them to the droplet temperature. Such a procedure can be expected to lead to a distribution of ionic isomers in the droplets that closely resembles the one present in the trap.

2.4 IR-MPD spectroscopy of metal cluster complexes using CO_2 lasers

The IR-MPD spectrum of $Fe_8(CH_3OH)$ has been the first reported for a metal cluster complex that was produced by laser ablation and interrogated in a molecular beam.[81] In these experiments, a line tunable pulsed CO_2 laser, providing about 50–100 mJ per pulse, was used to obtain the depletion spectrum between 930 and 1085 cm^{-1}. This spectrum is discontinuous and contains gaps – the largest between 986 and 1040 cm^{-1} – due to the output characteristics of the CO_2 laser that only emits at specific ro-vibrational line-transitions. These gaps in the emittance of the CO_2 laser can be partially filled, and the tuning range extended to lower frequency, by using different CO_2 isotopologues. Still, the entire tuning range of a CO_2 laser is rather limited to around 10 μm (880–1090 cm^{-1}).

A comparison of the IR-MPD spectra of two different hydrogenated iron clusters measured using the entire emission range of a CO_2 ($^{12}CO_2$ + $^{13}CO_2$) laser, as well as with an IR-FEL over a significantly larger wavenumber range is shown in Fig. 6. The CO_2 laser spectrum exhibits for Fe_9H_{10} – and for the other sizes and compositions studied – features in the 880–1090 cm^{-1} range that have been, in conjunction with DFT calculations for the model cluster $Fe_{13}H_{14}$, assigned to vibrations of bridging and face-capping H-species.[82] Additional spectroscopic data in the same spectral range has been obtained for deuterated Fe clusters of analogous compositions. Due to the increased reduced mass for Fe–D vibrations compared to Fe–H and the related isotope shift of about $1/\sqrt{2}$, the spectra of the deuterated complexes can be used as an indication for the spectra of the hydrogenated species in the 1250–1540 cm^{-1} range.[82] Thus, the spectroscopy of isotopologues is an additional approach to extend the accessible spectral range, similar to changing the CO_2 isotopologues in the lasing medium. However, when studying isotopologues one needs to be aware of isotope effects in the complex formation, which may also affect the respective product distributions. Further details about metal-hydrogen complexes and an assignment of the spectrum of $Fe_6H_4^+$ can be found in Section 3.1.1.

2.5 The rise of IR-FELs in molecular and cluster spectroscopy

For the characterization of many transition metal complexes, the spectral range accessible by CO_2 lasers is clearly insufficient.

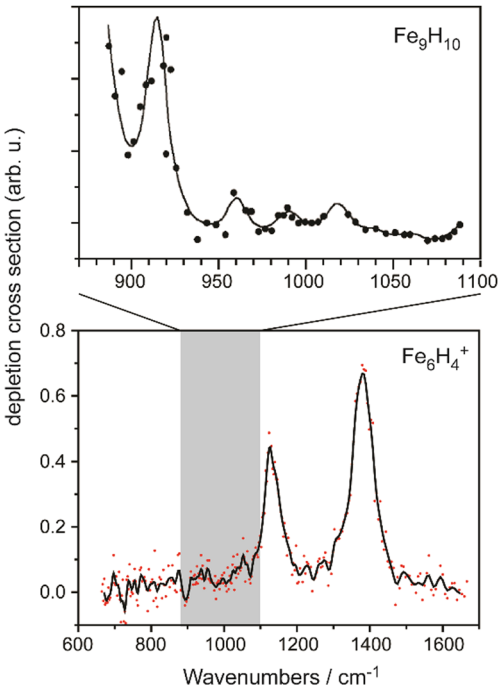

Fig. 6 IR-MPD spectra of hydrogenated iron clusters. Top: spectrum of neutral Fe_9H_{10} measured with a CO_2 laser over the entire emission range reachable using $^{12}CO_2$ and $^{13}CO_2$. Adapted from ref. 82, with the permission of AIP Publishing. Bottom: spectrum of $Fe_6H_4^+$ measured using FELIX in the region of metal-hydride vibrations. Data from ref. 83. The gray area marks the wavenumber range accessible by CO_2 lasers.

Either it does not cover enough features to draw stringent conclusions about the metal–ligand interaction, or simply that the relevant vibrational fundamentals (or possibly detectable overtones and combination modes) do not fall in that region around 10 μm. Thus, an intense and widely tunable light source, which is not dependent on discrete molecular transitions nor limited to the spectral transmission range of a dense lasing medium, was highly desirable.

The free electron laser[84] (FEL), as invented by John M. J. Madey, provides such a 'transparent' lasing medium and has hence been demonstrated to be capable of producing light from millimeter-waves to hard X-rays.[85] Compared to other lasers, even a single FEL may be capable of emitting light over an extremely wide frequency range. For example, the mid-IR FEL at the Fritz-Haber institute (Berlin, Germany) can be tuned in total from about 3 to 60 μm, which results in a factor of 20 in wavelength tunability.[86] The lasing medium of a free electron laser consists of relativistic electrons that are 'free' as they are not bound to atoms or molecules, but travelling through a vacuum. More precisely, FELs rely on the coherent emission of synchrotron radiation by accelerated relativistic electrons. At the same time, the electron beam acts as the light amplifying medium, essentially by stimulated transfer of energy from the electrons' motion towards the radiation field.

Although the first IR-FEL has been demonstrated in the mid-1970s,[87] it took until the mid-1990s for FELs to find their applications in gas-phase molecular spectroscopy. Early uses of these intense high-power IR sources were, apart from envisioned military purposes,[88] focused on, *e.g.*, material processing, surgery, as well as nonlinear and/or time-resolved spectroscopy in the condensed phase.[89] Gas-phase studies were initially concentrated on IR-MPD with one goal being isotope selectivity to use the process for isotope separation or enrichment.[90] Another topic was the study of IR matrix-assisted laser desorption (MALDI).[91]

The first mass-selective study of isolated molecules using an IR-FEL was reported in 1996. By measuring the IR spectrum of *p*-aminobenzoic acid (PABA) using an IR/VUV two color ionization scheme, a sensitivity increase of about eight orders of magnitude – compared to the direct absorption by a 10 cm cell filled with 1.4 Torr of PABA – was demonstrated.[92] This was quickly followed by recording the IR-REMPI spectrum of C_{60} between 6 and 20 μm in an effusive molecular beam.[93] Upon heating *via* absorption of many IR photons this cluster undergoes, due to its high stability, delayed thermal ionization rather than fragmentation. The detection of the resulting C_{60}^+ cations provides a sensitive and selective means for probing the IR absorption spectrum. It was realized that this method for obtaining vibrational spectra can be applied also to other strongly bound clusters and, subsequently, the IR spectra of other fullerenes and clusters of metal carbides, oxides, and nitrides have been determined.[54a]

Today about a dozen FELs operate in the mid-IR range worldwide.[94] Table 1 lists IR-FELs that have been more dedicated to gas-phase spectroscopic studies. Owing to the significant costs of installation and operation, but also the size and complexity of an FEL, they are often run as central institutional facilities (of universities or research institutes). Many also grant significant parts of the available beam time to the projects of external users.

Starting around the year 2000, several experiments, particularly dedicated to IR spectroscopy in molecular beams or on trapped molecular ions, have been (permanently) installed at the FEL facilities CLIO (France), FELIX (The Netherlands), and FEL-TUS (Japan), including the aforementioned cluster set-up[95] which was followed, *e.g.*, by a Paul-type quadrupole ion trap/ToF-MS experiment[96] where mostly ions of astrophysical interest have been studied,[97] and FT-ICR mass spectrometers.[77f,h,98] Using an FEL, the first IR-MPD spectra of transition metal cluster complexes have been measured in 2001 using FELIX.[99] These studies focused on silver cluster-ammonia complexes and extended former CO_2 laser studies that where more limited in the frequency range, see Section 3.3.1.[100]

An overview about some more recent cluster studies using short-wavelength FELs – a complementary field of research that is rapidly emerging since the first XUV FEL started its operation 2005 in Hamburg (Germany) – has been given by Bostedt and co-authors.[101] Also the combination of a VUV-FEL with IR lasers allowing for the spectroscopy of neutral molecules or clusters and complementing earlier studies[52a,92] where an IR-FEL had been combined with a fixed frequency VUV-laser has been highlighted recently.[52b]

2.6 Working principle of an IR-FEL

The principles, designs aspects, and specifications of (IR) free electron lasers have been described in detail before,[85,89a,102,103,104a,107,108] including in the context of their

Table 1 IR-FELs used in gas-phase molecular spectroscopy

Institution (location)	FEL	Operational since	Spectral range (μm)	Macropulse repetition rate (Hz)	Macropulse energy (mJ)	Ref.
University Paris-Saclay (Orsay, France)	CLIO[b]	1991	3–90	25	<100	102
FELIX Laboratory, Radboud University	FELIX[c]					
(Nijmegen, The Netherlands)	FEL1	1991	30–150	<10	<100	103
	FEL2	1992	3–45	<10	<200	103*a*
	FELICE[d]	2009	5–100	<10	<5000	104*a*,*b*
	FLARE[e]	2011	100–1500		<100	105
Tokyo University of Science (Tokyo, Japan)	FEL-TUS[f]	2000	5–14	1–5	<65	106
Fritz-Haber Institute of the Max-Planck	FHI-FEL					107
Society (Berlin, Germany)	mid-IR/far-IR	2012	3–60/(5–165)[a]	5–20	<100	86
National Synchrotron Radiation Laboratory	FELiChEM					
(Hefei, PR China)	mid-IR/far-IR	2019	2.5–50/40–200	1–10	<200	108

[a] Projected specifications are given in parentheses. [b] Centre Laser Infrarouge D'Orsay. [c] Free Electron Laser for Infrared eXperiments. [d] Free Electron Laser for IntraCavity Experiments. [e] Free Electron Laser for Advanced spectroscopy and High Resolution Experiments. [f] Formerly FEL-SUT, from 'Science University of Tokyo'.

use in molecular spectroscopy.[48c,54a,109] The following discussion of these aspects is therefore limited to the very basics. It shall be noted that these principles are generally valid for FELs throughout the full electromagnetic spectrum. However, there are significant differences in the accelerator technologies used for obtaining electron beams of rather different energy and, maybe even more important, in the amplification mechanism that occurs, for long-wavelength FELs usually in an oscillator-configuration using a closed resonator, while at short wavelength, where highly reflective mirrors are not available, different principles are used.[85c,89b] Essentially, in this case, the multi-pass oscillator arrangement is replaced by a single pass amplification in a much longer undulator. This, together with larger accelerators for reaching higher electron kinetic energies, makes short-wavelength FELs generally significantly larger and more costly than mid-IR FELs.

A simplified sketch of an IR-FEL is depicted in Fig. 7. It consists of an electron accelerator – in all cases listed in Table 1 these are linear normal-conducting radiofrequency accelerators (LINACs) – and an undulator which is a periodic magnet structure that is located within a cavity formed out of two (metal) mirrors. In hole-coupled resonators, a small hole with a diameter of a few mm in one of the cavity mirrors allows for out-coupling of a fraction of the radiation from the oscillator. All this is usually located within a radiation-safe and during operation inaccessible vault, as running of the FEL goes along with – unwanted but difficult to avoid – ionizing radiation. FEL facilities also incorporate systems for the characterization (power and spectrum) and manipulation (*e.g.*, for changing the polarization or attenuation), as well as for the transport of the IR beam to the place of an experiment outside the vault.

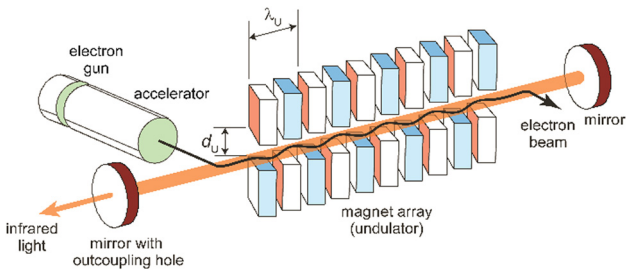

Fig. 7 Scheme of an infrared free electron laser. Undulator period (λ_U) and undulator gap (d_U) are indicated.

In an FEL, a beam of electrons – each carrying a rest mass of m_e and a charge of $-e$ – is accelerated to relativistic kinetic energies, in case of IR-FELs typically to E_{kin} = 10–50 MeV. This corresponds to a relativistic (Lorentz) factor

$$\gamma = 1 \Big/ \sqrt{1-(v/c)^2}$$

of 20.6 to 98.8 (approximately 2 times the value of E_{kin} in units of MeV) or to roughly 99.9 to 99.99% of the speed of light, c, in vacuum. The electrons are injected into a periodic magnetic field produced by the undulator, where the electron beam gets periodically deflected and, hence, spontaneously emits synchrotron radiation that peaks in forward direction as a narrow cone. The relativistic electrons traveling along the axis of the FEL resonator sense the undulator as an oncoming electromagnetic wave of period λ_U, shrunk due to the Lorentz contraction by $1/\gamma_\parallel$, where $\gamma_\parallel$ is determined by the velocity component of the electrons in forward direction, $v_\parallel$. Therefore, in the moving frame of the electrons, they form Hertz oscillators emitting light with a wavelength λ.

$$\lambda = \frac{\lambda_U}{\gamma_\parallel} \tag{2}$$

In the resting laboratory frame this wave is seen contracted by a (longitudinal) relativistic Doppler shift.

$$\lambda_{obs} = \frac{\sqrt{1-(v_\parallel/c)}}{\sqrt{1+(v_\parallel/c)}}\lambda \approx \frac{1}{2\gamma_\parallel}\lambda \tag{3}$$

As the electrons are not moving on a straight path through the oscillator, but wiggle through the undulator field, the velocity in forward direction gets reduced depending on the amplitude of the deflection. This results in $\gamma_\parallel$ being lower compared to the total γ depending on the strength of the magnetic field B – expressed by the dimensionless parameter K – on the FEL axis.

$$\gamma_\parallel = \frac{\gamma}{\sqrt{1+K^2}} \quad \text{with} \quad K = \frac{e\lambda_U}{2\pi m_e c}B \tag{4}$$

Putting together eqn (2)–(4) one obtains the undulator equation that forms also the resonance condition for an FEL.

$$\lambda_{obs} \approx \frac{\lambda_U}{2\gamma^2}(1 + K^2) \quad (5)$$

With K being on the order of 1, typical undulator periods measuring a few centimeters and a γ of 100 ($E_{kin} \approx 50$ MeV), such a device emits infrared radiation of few μm wavelength.

Wavelength tuning can be achieved by changing either the undulator period (λ_U), the undulator parameter (K) by changing the undulator gap (d_U), or γ *via* the kinetic energy of the electron beam. In practice, changing of the undulator gap is done more easily and allows – at a given beam energy – to vary the wavelength by a factor of 2–3. To access other wavelength ranges the kinetic energy is adjusted, but changes of the electron beam parameters usually require extensive adjustments of the accelerators and electron beam optics.

The electron beam has, determined by the type of accelerator used, a unique time structure that is also imprinted in the temporal structure of the emitted light (Fig. 8). In the case of LINACs, it consists of a train of few ps long electron bunches spaced by typically 1 ns, each containing a charge of about 0.2–1 nC, leading to peak currents within an electron bunch of 10–100 A. To limit the power consumption, as well as the thermal load in normal-conducting accelerators, the pulse train is restricted to a length of 5–10 μs and repeats at several Hz.

The electron bunches emit, as described before, spontaneous and incoherent radiation in the oscillator. Amplification is reached by an interaction of the electromagnetic wave that is building up in the oscillator and the electrons wiggling along the undulator axis. Electrons moving in-phase with the light wave get decelerated due to the ponderomotive force acting between them, while out-of-phase moving electrons get accelerated. This results in a micro-bunching of the electrons within the pulse, with a modulation period equal to the IR wavelength. The packages moving in-phase with the wave now radiate coherently and, thereby, amplify the initial radiation. 'Spent' electron pulses leave the oscillator, get dumped and the oscillator is repeatedly refilled with 'fresh' electrons from the accelerator until the macropulse stops. The resulting light pulses have a – *via* the detuning of the cavity mirrors adjustable – near-transform limited bandwidth of 0.3–10% (fwhm) of the central wavelength and, accordingly, a pulse length of a few 100 fs to several ps. Several thousand of these micropulses – typically spaced by 1 ns and, thus, mirroring the time structure of the electron bunches – form a macropulse of light of 5–10 μs duration that can contain energies of up to 100–200 mJ.

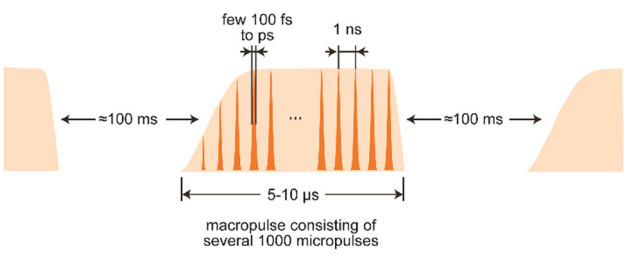

Fig. 8 Typical pulse train structure of the infrared light emitted by an IR-FEL.

In these aforementioned conventional hole-coupled FELs typically only a few percent of the IR radiation is coupled out and used in experiments. However, inside the cavity much higher fluences are present. This is used in FELICE, the Free Electron Laser for IntraCavity Experiments, which is part of the FELIX facility and designed to perform experiments on optically thin media inside the FEL cavity.[104] In addition, if experiments are not performed at the highest available fluence of FELICE, *i.e.*, in the region of the optical focus inside the cavity, but at a wider beam waist, the much larger overlapping volume with the molecular beam (or an ion cloud) significantly enhances the sensitivity. This allows for, in particular, the study of IR multiple photon excitation of species with extremely low absorption cross sections, like metal clusters. Also, normally very weak signals stemming from overtones and combination bands can adopt appreciable intensities in such experiments.[55]

2.7 Other IR laser sources

Table-top systems for the generation of intense and tunable infrared radiation are, aside from molecular lasers, usually based on nonlinear frequency conversion of pulsed ns lasers either in an optical parametric oscillator (OPO), *via* difference frequency mixing (DFM), or by combining both methods in a consecutive way, see below. At first glance, the time averaged output characteristics of current commercially available IR-OPO systems can be similar to that of IR-FELs used in molecular spectroscopy, see Fig. 9. Even peak power, pulse energy, and overall repetition rate may be comparable, but the main difference lies in the details of the pulse structure. While the macropulse of an FEL extends over several microseconds and facilitates cycling of a single cluster or molecule over very many absorption/IVR steps within one macropulse, a pulse of an IR-OPO system that is only a few ns long limits passing through such cycles.

Depending on the OPO medium – typically potassium titanyl phosphate (KTP) or (periodically poled) lithium niobate – these lasers can be broadly tuned approximately in the 2.1–4.7 μm (2100–4800 cm^{-1}) range and pulse energies exceeding 10 mJ at pulse durations of 5–10 ns can be generated.[112] Longer wavelengths are reachable – albeit with about an order of magnitude lower power – *via* difference frequency mixing (DFM), *e.g.*, in $AgGaSe_2$.[112a] Therefore, these table-top IR lasers are clearly outperformed by FELs at longer wavelength, typically above 4.5 μm (below 2200 cm^{-1}). In combination with messenger tagging, however, also IR spectra of metal cluster complexes have been measured up to about 8 μm (1200 cm^{-1}) with IR-OPO systems, *e.g.*, for discriminating nitride formation from molecular N_2 absorption on a Ta_4^+ cluster.[113] In general, these systems have a bandwidth on the order of 0.1–1 cm^{-1}. DFM/OPA systems as developed, *e.g.*, by Gerhards for the spectroscopy of isolated molecules and metal cluster complexes,[114] show a performance that is overall similar to the aforementioned OPOs.

A comparison of different table-top IR-OPOs with rather different time–structure for their suitability for IR-MPD spectroscopy of mass selected molecular ions at around 3 μm in a 3D quadrupole ion trap has been reported recently.[112b] The comparison includes two pulsed ns lasers running at 10 Hz and 20 kHz, a pulsed ps laser at a repetition rate of 80 MHz, as well as a cw OPO. The pulsed lasers

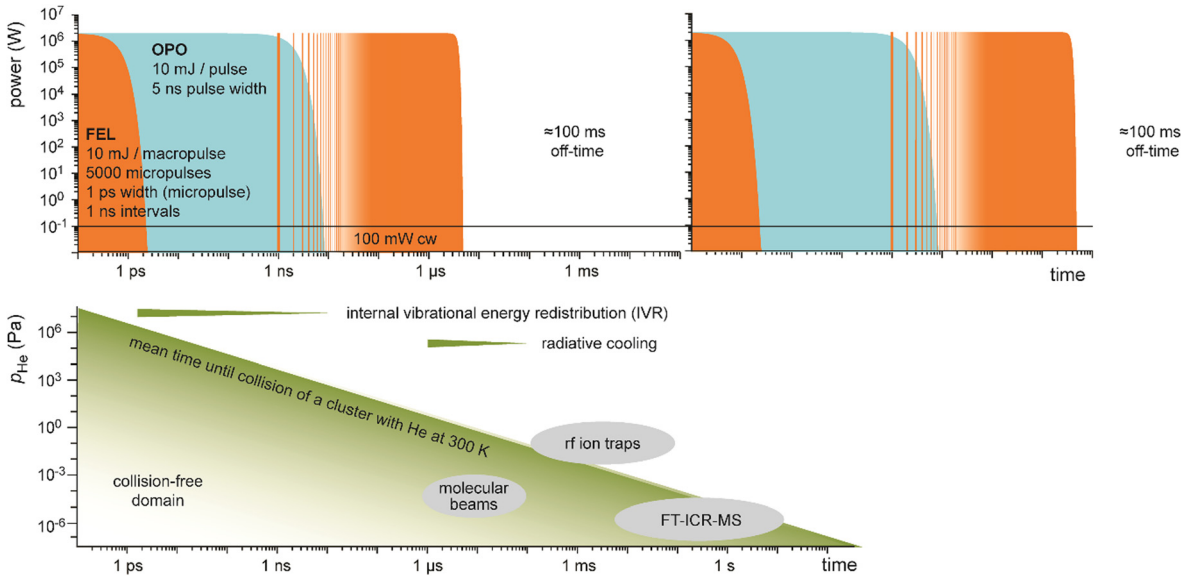

Fig. 9 Time structure of IR lasers used for infrared multiple photon dissociation plotted over 12 time decades to cover the laser pulses as well as the duty-time intervals (first pulse maxima are at t = 0). For illustration purposes, ns OPO (blue) and IR-FEL (orange) are assumed to have the same (macro)pulse energy of 10 mJ repeating at a rate of 10 Hz. This results in a time-averaged power of 100 mW (horizontal black line). Their peak power is comparable, although the lasers have very different temporal structures. Bottom: Typical time-scales of energy dissipation processes relevant in IR-MPD together with time and pressure scales of different experimental environments used in IR-MPD spectrosopy. Collisional rates between a cluster and He atoms are estimated using the hard-sphere model for Au_8^+ at 300 K, with the experimental collision cross section taken from ref. 110. Radiative cooling rates for metal clusters have been reported in ref. 111.

had similar average power (150–600 mW), while that of the cw laser was significantly higher (5.4 W). Under the conditions in a gas-filled radiofrequency ion trap, collisional deactivation becomes a relevant parameter counteracting the IR pumping (Fig. 9). Therefore, IR-MPD yields are dependent not only on the absorption cross sections of the ions, dissociation energy, average IR power, and irradiation time, but also on background pressure, IR peak-power, and duty cycle. This is different from the (nearly) collision-free environment in a molecular beam or in an FT-ICR cell, where collisional cooling is of less importance, and only becomes relevant – along with radiative processes – at long storage times.

A more extended overview of experimental methods to produce tunable IR radiation for the spectroscopy of transient gas-phase species has been given by Bernath.[115] However, other IR lasers like the molecular CO or far-IR lasers, as well as lead-salt, F-center, or quantum-cascade lasers are less frequently applied in studies of metal cluster complexes, mostly due to their low (peak) powers and limited tunability. This holds also for frequency conversion *via* mixing with microwave radiation or by harmonics generation, *i.e.*, for shifting the output of a CO_2 laser into the region around 5 µm (2000 cm^{-1}). Exceptions are some high-resolution studies of complexes formed in superfluid He droplets.[72b,116]

3 Probing ligand binding and chemistry on metal clusters

3.1 Diatomic ligands

3.1.1 H_2. Binding mechanism. Molecular hydrogen, H_2, in its $(\sigma)^2(\sigma^*)^0$ ground state configuration can be considered the most simple neutral molecule. Binding to transition metals can either be *via* physisorption, chemisorption of the intact H_2 molecule, or by splitting the H–H bond and the H atoms forming strong M–H σ bonds. Chemical binding of molecular hydrogen to metal centers has been only discovered relatively recent in coordination complexes.[170] Also on extended metal surfaces, molecular chemisorption is comparably rare and mostly observed at low temperatures, *i.e.*, <20 K, or on open surfaces with low coordination metal sites.[171]

The binding of H_2 to M can be described *via* donation from the fully occupied $\sigma(H_2)$ orbital into an empty metal d orbital, thus forming a 3-center 2-electron bond. A significant additional stabilization is given through a back-bonding by donation out of symmetrically fitting occupied metal orbitals into the empty $\sigma^*(H_2)$ orbital. That way the H_2 molecule is bound side-on to the metal. Thus, the H_2-complexes can be seen as prototypes for σ-complex formation.[172] The binding mechanism suggests that the strength of the M–(H_2) interaction and the weakening of the H–H bond are strongly correlated, which will also be seen in the frequencies of the corresponding stretch vibrations.

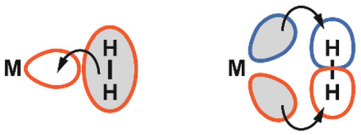

Both contributions to the M–(H_2) bonding link H–H bond activation and formation of M–(H_2) bond(s) and allow for a gradual transition from weakly bound molecular complexes

Table 2 Summary of experimental studies on the vibrational spectroscopy of gas-phase metal cluster complexes with diatomic molecules

Molecule	Metal	System	Cluster sizes (n)	Coverage (m)	Method[a]
H_2	Sc	$Sc_nO[H_2]_m^+$, $Sc_nO_2[H_2]_m^+$	3–20	Saturated	IR-MPD[83]
	V	$V_n[H_2]_m^+$	4–20	Saturated	IR-MPD[83,117]
		$V_n[H_2]_mCO^+$	5–9	Saturated	IR-MPD[117]
	Fe	$Fe_n[H_2]_m$; $Fe_n[D_2]_m$	9–20	Saturated	IR-MPD, CO_2[82]
		$Fe_n[H_2]_m^+$	4–15	Saturated	IR-MPD[83]
	Ru	$Ru_8[H_2][N_2]_4^+$	8	1	IR-PD[118]
	Co	$Co_n[H_2]_m^+$	4–20	Saturated	IR-MPD[83]
		$Co_n[H_2]_mCO^+$	4–20	0–6, saturated	IR-MPD[b 119]
	Ni	$Ni_n[H_2]_m^+$	4–15	Saturated	IR-MPD[83]
		$Ni_n[H_2]_m^+$	4–6	1	IR-MPD[120]
	Pt	$Pt_n[H_2]_m^+$	2–7	Saturated	IR-MPD[121]
	Cu	$Cu_n[H_2]_m^+$; $Cu_n[D_2]_m^+$	4–7	1	IR-MPD[122]
	Al/V	$Al_nV[H_2]_m^+$	10–12, 13, 15	1	IR-MPD[123]
		$Al_nV_2[H_2]_m^+$	2, 3, 6, 8–12	1	IR-MPD[124]
	Al/Nb	$Al_nNb[H_2]_m^+$	2–9	Saturated	IR-MPD[125]
	Al/Rh	$Al_nRh[H_2]_m^+$	1–12	1	IR-MPD[126]
		$Al_nRh_2[H_2]_m^+$	2–13	1, 2	IR-MPD[127]
CO	Ti	$Ti_n[CO]_m^+$	1, 2	Saturated	IR-PD[128]
	Cr	$Cr_n[CO]_m^+$	2	7–9	IR-PD[129]
	W	$W_n[CO]_m$	5–14	1	IR-MPD[130]
	Re	$Re_n[CO]_m^+$	4–14	1, 2	IR-MPD[130]
	Fe	$Fe_n[CO]_m^+$	18–30	1	IR-MPD[130]
		$Fe_n[CO]_m^+$	1–3	Saturated	IR-PD[131]
		$Fe_n[CO]_m^-$	2	4–9	IR-PD[132]
		$Fe_n[CO]_m^-$	1–5	Saturated	IR-MPD[133]
	Ru	$Ru_n[CO]_m^{+/-}$	4–19	1	IR-MPD[130]
	Co	$Co_n[CO]_m^{+/0/-}$	3–37	1	IR-MPD[134]
		$Co_n[CO]_m^+$	2–4	Saturated	IR-PD[135]
	Rh	$Rh_n[CO]_m^{+/0/-}$	3–34	1	IR-MPD[73a,134,136]
		$Rh_n[CO]_m^+$	1–6	Saturated	IR-MPD[137]
	Ir	$Ir_n[CO]_m$	3–21	1	IR-MPD[138]
	Ni	$Ni_n[CO]_m^{+/0/-}$	4–23	1	IR-MPD[134,139]
		$Ni_n[CO]_m^+$	2–4	Saturated	IR-PD[140]
		$Ni_n[CO]_m^-$	1–3	1, saturated	APES[141]
	Pd	$Pd_2[CO]_m^+$	2	5–8	IR-PD[142]
		$Pd_n[CO]_m^{+/0/-}$	3–12	1	IR-MPD[139]
		$Pd_n[CO]_m^-$	2, 3	2	APES[141a]
	Pt	$Pt_n[CO]_m^{+/0/-}$	3–25	1	IR-MPD[139]
		$Pt_n[CO]_m^+$	3–14	1	IR-MPD[143]
		$Pt_n[CO]_m^-$	1–4	Saturated	APES[141]
	Cu	$Cu_n[CO]_m^+$	2–4	Saturated	IR-PD[144]
		$Cu_nC[CO]_m^-$	4–10	3–7	IR-MPD[145]
		$Cu_2O_2[CO]_m^+$	2	3–7	IR-PD[146]
	Au	$Au_2[CO]_m^-$	2	0–3	APES[147]
		$Au_n[CO]_m^-$	3–14	1, saturated	IR-MPD[148]
		$Au_n[CO]_m^+$	4–8	1	IR-MPD[149]
		$Au_n[CO]_m^+$	4–14	1	IR-MPD[150]
		$Au_n[CO]_m^+$	3–10	Saturated	IR-MPD[151]
		$Au_2O_2[CO]_m^-$	2	2–6	IR-PD[44]
	Pt/Mo	$Pt_nMo[CO]_m^+$	2–13	1	IR-MPD[143]
	Au/Pd	$Au_nPd[CO]_m^+$	3–13	1	IR-MPD[150]
N_2	Nb	$Nb_n[N_2]_m^-$	2–8, 10, 11	1	APES[152]
	Ta	$Ta_4[N_2]_m^+$	4	1–5	IR-PD[113]
	W	$W_n[N_2]_m^-$	6–8	1	APES[152,153]
	Fe	$Fe_n[N_2]_m^+$	8–20	1, 2	IR-PD[71b]
		$Fe_n[N_2]_m^+$	13, 17, 18	Saturated	IR-PD[71b]
	Ru	$Ru_n[N_2]_m$	5–16	1, 2	IR-MPD[154]
	Ni	$Ni_n[N_2]_m^+$	5–20	1, 2, saturated	IR-PD[155]
		$Ni_n[N_2]_m^+$	9, 13	1-saturated	IR-PD[156]
	Co	$Co_n[N_2]_m^+$	8–17	1	IR-PD[77i]
	Rh	$Rh_n[N_2]_m^+$	6–15	1, saturated	IR-PD[157]
NO	Rh	$Rh_n[NO]_m^+$	6–16	1	IR-MPD[158]
		$Rh_n[NO]_m^+$	6, 7	2, 3	IR-MPD[159]
	Ir	$Ir_n[NO]_m^+$	3–6	1	IR-MPD[158b,160]
	Pt	$Pt_n[NO]_m$	4–18	1	IR-MPD[161]
	Au	$Au_n[NO]_m^+$	4–20	1	IR-MPD[149]
		$Au_n[NO]_m^-$	4	1, 2	IR-MPD[162]

Table 2 (*continued*)

Molecule	Metal	System	Cluster sizes (n)	Coverage (m)	Method[a]
	Rh/Ta	$Rh_nTa[NO]_m^+$	2–8	1	IR-MPD[158b,163]
	Rh/Ir	$Rh_nIr[NO]_m^+$	3–7	1	IR-MPD[164]
O_2	Cu	$Cu_n[O_2]_m^-$	6, 7	1	APES[165]
	Ag	$Ag_n[O_2]_m^-$	2, 8	1	APES[166]
	Au	$Au_n[O_2]_m$	4, 7, 9, 11, 21	1–3	IR-MPD[43b]
		$Au_n[O_2]_m^+$	2–8, 10, 12, 21, 22	1–4	IR-MPD[43c,167]
		$Au_n[O_2]_m^-$	2, 4, 6	1	APES[20,166b,168]
		$Au_n[O_2]_m^-$	4, 6, 8, 10, 12, 14, 18, 20	1	IR-MPD[43a]
		$Au_2[O_2][C_2H_4]_{0,1,2}^+$	2	1	IR-MPD[169]

[a] IR-MPD – infrared multiple photon dissociation using IR-FELs; IR-MPD, CO_2 – IR-MPD using line-tunable CO_2 laser; IR-PD – infrared photo dissociation employing OPO/OPA or DFM/OPA lasers as IR sources; APES – anion photoelectron spectroscopy. [b] Only ν(CO) range.

with short H–H bonds to σ-bound M hydrides where the H–H unit is completely broken. The 'true' H_2 complexes with H–H distances ≤1 Å are often termed after Kubas, stretched dihydrogen complexes are those in the range of 1.0–1.3 Å, and compressed dihydrides fall in the range 1.3–1.6 Å. Overall they are usually called non-classical hydrides.[173] For comparison, the H–H atomic distance in free H_2 is 0.741 Å.[174]

Complexes with single metal atoms. Dihydrogen and dihydride complexes of metal atoms have been intensively studied by cryogenic matrix isolation IR spectroscopy.[175] For example, $Pd(H_2)$ synthesized by reaction of Pd atoms with H_2 in an Ar matrix has been a key system for the detection of chemically bound H_2 by single metal atoms, see Table 3.[176] For weakly bound (non-covalent) $M–H_2(D_2)$ complexes with metal cations, gas-phase IR-PD spectra have been obtained with rotational resolution.[177]

Metal cluster reactivity. Reactions of H_2 with neutral and charged clusters have been intensively studied already in the late 1980s and 90s both under single collision conditions, *e.g.*, for cluster ions trapped in FT-ICR mass spectrometers, or under multiple collision conditions in higher pressure regions of cluster sources. This work has been summarized before, *e.g.*, by Knickelbein[11b] and by Luo, Castleman, Jr., and Khanna.[11d] For late transition metal clusters, M_n, often a strong size dependence in reactivity is found, with reaction rate constants changing dramatically just by addition of another M atom. In many cases the reactivity correlates with experimental observables of the valence electron structure. For iron clusters, for instance, a high ionization energy – as measure of a strong stabilization of the HOMO – is connected with low reactivity. This has been explained by an electron transfer model, where the donation of electrons from the cluster's HOMO into the $\sigma^*(H_2)$ is the rate determining step.[24a] While this corresponds to the backdonation part of the M–(H_2) interaction, a more recent explanation (anti)correlates reactivity with the HOMO–LUMO promotion energy,[24c] which involves relative energies of filled and empty metal orbitals that are both essential in the molecular hydrogen chemisorption and activation as described above. Also for TM doped Al clusters the shape and occupation of frontier orbitals and their interactions with the $\sigma^*(H_2)$ orbital have been identified as significant parameters in the activation of H_2 and the formation of stable complexes with molecular H_2 *vs.* dihydride-formation.[123,127a]

Vibrational modes and frequencies. For dihydrogen side-on bound to a single metal atom, there are three vibrational normal modes: the H–H stretch and the M–(H_2) symmetrical and antisymmetrical stretch vibrations. In larger entities there exist additional bending and torsional modes. The three stretching modes are, due to the binding mechanism, highly coupled, and this essentially leads to a significant IR intensity for ν(H–H).

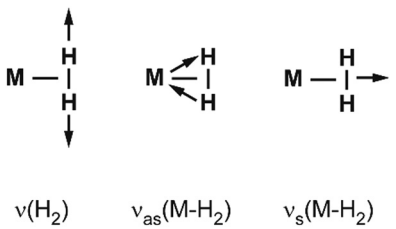

Examples for experimentally observed vibrational frequencies of different dihydrogen species, including the free H_2 molecule, simple metal complexes, surface adsorbates, and H_2 bound to metal clusters are given in Table 3. Typically, the stretch frequencies of chemisorbed H_2 are found in the ranges 2200–3500 cm^{-1} for ν(H–H), 1200–1600 cm^{-1} for ν_{as}(M–H_2), and 650–950 cm^{-1} for ν_s(M–H_2). The broad ranges reflect the

Table 3 Experimentally observed vibrational frequencies for selected dihydrogen species (in cm^{-1})

System	ν(H–H)	ν_{as} (M–H_2)	ν_s (M–H_2)	δ (M–H_2)	Ref.
H_2, free molecule	4161.166 32(18)				178
$W(CO)_3(P^iPr_3)_2(H_2)$	2695	1567	953	465	179
$Pd(H_2)$	2971.4	1507.5	950.0		176
Ni(510)–H_2 surface	3210	1185	670	230	180
$Ni_4(H_2)^+$	~3480[a]		680		120
$Ni_4H_4(H_2)_4^+$	~3420[a]		710		83
$Ni_5H_6(H_2)_5^+$	~3450, ~3560[ab]		650, 760[b]		83
$Al_{12}Rh_2(H_2)^+$		1580	820		127a
$Al_{13}Rh_2(H_2)^+$		1590	830		127a

[a] Calculated from the experimental value of the D_2 complex. [b] Two different types of coordination sites.

wide variability in the H–H bond activation and metal binding strength in these systems. The M–H_2 deformation modes, δ(M–H_2), are found below 500 cm^{-1}. Not unexpectedly, usually a clear anti-correlation between ν(H–H) and ν(M–H_2) is seen, *e.g.*, in complexes with less activated H_2 and high ν(H–H) the bonding to M is weak and, correspondingly, ν(M–H_2) are found at lower values within the given ranges. The observation of a band in the range for ν(H–H) is a very characteristic experimental sign for molecular hydrogen adsorption, as for metal/hydrogen systems no other vibrational fundamentals are expected above $\sim$2200 cm^{-1}.

For M cluster hydrides containing dissociated H_2, M–H vibrational frequencies are for two-fold bridging H typically $\nu_s(\mu_2\text{-H}) \approx 1400$ cm^{-1} and $\nu_{as}(\mu_2\text{-H}) \approx 1200$ cm^{-1}; for three-fold face-capping H $\nu_s(\mu_3\text{-H}) \approx 1200$ cm^{-1} and $\nu_{as}(\mu_3\text{-H}) \approx 800$ cm^{-1} (Table 4). The M–H stretch vibrations of the dihydrides of single transition metal atoms are, in most cases, found in the 1500–2100 cm^{-1} range,[175] *i.e.*, well above the ranges of the vibrational fundamentals of higher coordinated H and still below ν(H–H) of chemisorbed H_2.

Molecular and dissociative adsorption. Molecular precursors in the formation of stable hydrogen complexes of transition metal clusters have been proposed before based on the detection of inverse temperature dependencies of the overall reaction rate at low temperature.[182] Using IR-MPD spectroscopy, such molecular cluster complex has been detected for $H_2(D_2)$ bound to Ni_4^+ clusters (Fig. 10).[120] The $Ni_4D_2^+$ complex shows a band at 2460 cm^{-1} that is assigned to ν(D–D). Another prominent band is observed for ν_s(Ni–H_2) at 680 cm^{-1}. These are related to side-on bound H_2 on a single Ni atom of (quasi-) tetrahedral Ni_4^+. While the spectrum of $Ni_4H_2^+$ contains additional features in the 800–1200 cm^{-1} range that are attributed to a second isomer containing dissociated H_2, the bands assigned to molecular H_2 are missing for the $Ni_5H_2^+$ and $Ni_6H_2^+$ complexes.[120] Comparison to IR spectra calculated *via* DFT methods assigns bands in the 800–1400 cm^{-1} range to stretches of bridging (μ_2) or trigonal face-capping (μ_3) hydrides. The ν_{as}(Ni–H_2) band of chemisorbed H_2 on Ni_4^+ falls in that range and is therefore, alone, not sufficient to prove a molecular adsorption. The second, lower abundant isomer of $Ni_4H_2^+$ contains H-atoms bridging two neighbored edges of the Ni tetrahedron. $Ni_5H_2^+$ and $Ni_6H_2^+$ are found to contain μ_2- and μ_3-bound hydride, respectively.[120]

The structural differences in these complexes go along with a change in reactivity. The rate constants for complex formation

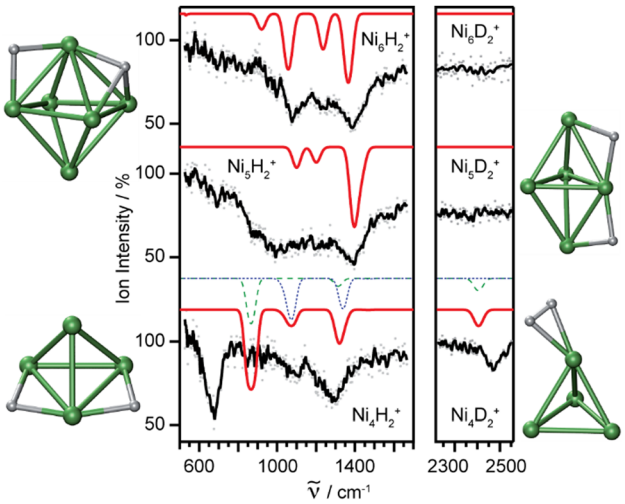

Fig. 10 IR-MPD spectra of $H_2(D_2)$ bound to small nickel cluster cations Ni_n^+ (n = 4–6). Due to experimental constraints, ν(H–H) was not accessible directly and only ν(D–D) could be determined. The experimental depletion spectra are compared to simulated spectra (red traces) from DFT (BP86/TZVP) calculations for the shown low energy structures. The simulated spectrum of $Ni_4H_2^+$ is a linear combination with a ratio of 4 : 1 of the spectra of the molecular adsorbate (dashed line) and the one with atomic H (dotted line) respectively. Reproduced from ref. 120 with permission from the PCCP Owner Societies.

with H_2 as determined by a pseudo-first-order model scale as 1 : 65 : 85 for Ni_4^+, Ni_5^+, and Ni_6^+, respectively, *i.e.*, Ni_4^+ reacts nearly two orders of magnitude slower.[120] This difference in reactivity can be understood assuming a precursor mediated dissociative adsorption as depicted in Fig. 11A. Initially, a molecular precursor complex (either physisorbed or chemisorbed) is formed that can easily (barrier-free) fall apart again into the bare cluster and H_2. For H–H dissociation, the system has to overcome an activation barrier with a height depending

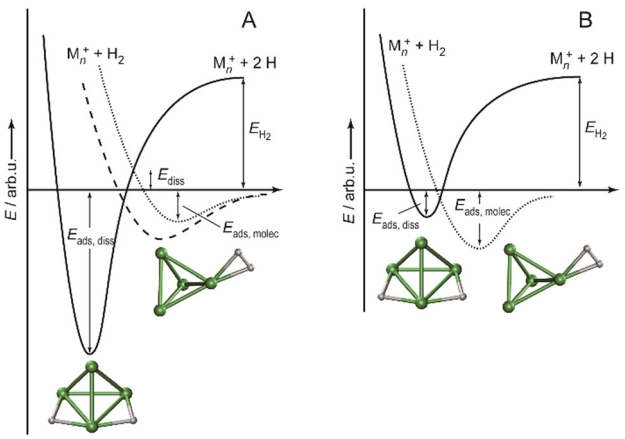

Fig. 11 Schematic potential energy diagrams plotting total energy (E) of complexes between dihydrogen and a metal cluster as function of a simplified one-dimensional reaction coordinate. (A) Shows the more classical case of dihydride formation as non-activated (dashed line) or activated (dotted line) process after molecular precursor formation. (B) Illustrates the situation in case molecular adsorption is energetically favored as for $Ni_4H_2^+$. Adapted from ref. 181 with permission of the author.

Table 4 Experimental frequency ranges for IR active collective M–H vibrations of saturated 3d TM cluster hydrides (in cm^{-1})[a]

Metal	ν_s(M–μ_2H)	ν_{as}(M–μ_2H)	ν_s(M–μ_3H)	ν_{as}(M–μ_3H)
Sc[b]	1100–1110	[c]	[c]	[c]
V	1420–1430	[c]	1270–1280	810
Fe	1350–1400	1130–1220		
Co	1385–1400	1030–1110	1150–1230	[c]
Ni			1210–1270	[c]

[a] Data from ref. 83 and 181. [b] Clusters contain in addition a single O atom. [c] No clearly resolved bands in the experimental spectra.

on the depth of the molecular interaction potential and the crossing position with the dissociative adsorption potential. In the case of a high barrier, the complex misses the possibility for stabilization by forming the dihydride, which is usually thermodynamically more favored. Overall a low reactivity is observed. In $Ni_4H_2^+$, however, the situation appears slightly different, as for this cluster the molecular complex is predicted to be more stable than the dihydride isomer (Fig. 11B). Nevertheless, as the molecular complex has no possibility for further stabilization but can rapidly decompose again without barrier, the observed reaction rate for Ni_4^+ is much lower than for $Ni_5H_2^+$ and $Ni_6H_2^+$.[120,181]

For the molecular complex, a comparison of the experimental band positions to calculated harmonic frequencies indicates systematic deviations due to a significant overestimation of the Ni–H_2 binding in the DFT calculations (PB86/TZVP), *i.e.*, ν(D–D) values are predicted much too low, while ν_s(Ni–H_2) are too high as is the case for the H_2-saturated Ni clusters discussed further below.[83,120] The challenges in accurately predicting the properties of elongated H_2 complexes have been discussed already by Kubas.[170a] The potential for the H–H stretch has been found in several cases to be extremely flat with variations in d(H–H) by $\approx$0.1 Å leading to energy changes of only a few kJ mol^{-1}.[183] Therefore, it comes not as a big surprise that DFT calculations have difficulties in locating the correct minimum within such a shallow potential. Instead, the full (nuclear) Schrödinger equation needs to be solved to accurately describe the motion of the light H atoms.[170a,183]

For small cationic copper clusters Cu_n^+ (n = 4–7) H_2 (or D_2) adsorption has been investigated by experimental IR-MPD spectroscopy and computational searches for potential reaction products using a minima hopping search procedure (DFT:PBE and PBE0). Based on a comparison of experimental and predicted IR spectra in the 350–1700 cm^{-1} range, it is concluded that multiple isomers are present for all sizes. For n = 5 it is found that the products are dominated by hydrides, while for the other sizes molecular adsorbates prevail.[122]

Saturated TM cluster hydrides. Neutral iron clusters Fe_n (n = 9–20) covered with hydrogen until saturation have been investigated already by Knickelbein using a line-tunable, pulsed CO_2 laser (Fig. 6).[82] Stoichiometries of the Fe_nH_m cluster complexes are close to n/m = 1. From the observation of band patterns in the 885–1090 cm^{-1} range that were sensitive to cluster size and change when H is replaced by D, it had been concluded that indeed ligand related modes where observed and a comparison with model calculations revealed dissociative complex formation.

In the case of saturated hydrides of vanadium cluster cations V_n^+ (n = 5–9), a close correlation between the number of triangular facets of the metal clusters and the number of H atoms in the complex is found.[117] The structures of bare V_n^+ had been determined before from their far-IR spectra.[184] Indeed, from the IR-MPD spectra of the saturated hydrides and comparison to spectra from DFT calculations (BP86/TZVP) it becomes apparent that most H ligands are μ_3-bound. Probably due to space constraints, a minor number of μ_2-bridges is also present in some of these hydrides. In $V_6H_8^+$ all facets of the octahedral V_6-core are covered by μ_3-H, and it shows, due to the high symmetry, a particularly simple IR spectrum (Fig. 12). O_h-$V_6H_8^+$ has three (triply degenerate) IR active modes, all of t_{1u} symmetry, a collective ν_a(V–μ_3H) experimentally seen at 1275 cm^{-1}, a collective ν_{as}(V–μ_3H) at 810 cm^{-1} and, below the range measured (350–2200 cm^{-1}), metal cluster modes that are essentially V–V stretches.

In a comparative study of several 3d transition metals (Sc, V, Fe, Co, Ni), the IR-MPD spectra of hydrogen saturated cluster cations containing up to $\sim$20 metal atoms have been determined in the 500–1600 cm^{-1} range.[83] For Sc, due to its high oxophilicity, only clusters of the type Sc_nO^+ could be investigated. Typical stoichiometries of these complexes are for Fe and Co $m/n \approx 1$, for Sc and V about $m/n \approx$ 1.3–1.5, and for Ni it reaches up to $m/n \approx 3$.

Smaller 3d metal cluster hydrides (n = 4–6) have pronounced band patterns in their IR-MPD spectra that allow for detailed structural assignments by comparison with results from DFT (BP86/TZVP) calculations (Fig. 12). For larger clusters, mostly broader, unresolved features are seen. Most bands are found in the 800–1400 cm^{-1} range, indicative of bridging (μ_2) or trigonal face-capping (μ_3) hydrides. Fe cluster hydrides are found to contain exclusively μ_2-H. Sc, Co, and V clusters bind H depending on their size either as μ_2-H or μ_3-H or a mixture of both.[83]

For Ni, however, prominent bands are found between 600 and 800 cm^{-1} that are for almost all cluster sizes even the most intense signals in the depletion spectra. These bands are assigned to ν_s(Ni–H_2) and their observation goes along with the detection of a band corresponding to ν(D–D) in the deuterated complexes. The H–H stretch was expected to be experimentally not accessible due to limitations of the IR source. The chemisorbed H_2 ligands are attached to every Ni atom in the clusters in addition to μ_3-H covering the facets. $Ni_5H_{16}^+$, *e.g.*, contains 6 μ_3-H and 5 σ-bound H_2 ligands. The molecular ligands bind in two nonequivalent sites, either in equatorial positions or to the top and bottom of the Ni_5^+ trigonal bipyramid. This leads to a splitting of the ν(H–H) and ν_s(M–H_2) bands (Fig. 12 and Table 3). In $Ni_4H_{12}^+$ and $Ni_6H_{18}^+$ the μ_3-H, as well as σ-(H_2) binding sites, are all equivalent and the observation of broad ν(H–H) and ν_s(M–H_2) bands has been attributed to the presence of additional isomers or to a broadening due to a low barrier for rotation of the σ-(H_2) ligands.[83] The IR-MPD spectra measured for the larger H saturated clusters can, in most cases, be explained with the same H binding motifs as for the small clusters, for which DFT calculations have been performed to facilitate structural assignments.[83] An overview on the assigned M–H modes is given Table 4.

For cationic platinum clusters saturated with hydrogen ($Pt_2H_{10}^+$, $Pt_3H_{12}^+$, $Pt_4H_{12}^+$, and $Pt_5H_{16}^+$) IR-MPD spectra have been reported in the 550–2050 cm^{-1} range.[121] Experiments were performed with isotopically enriched ^{194}Pt to facilitate determination of the exact compositions. Basin-hopping Monte Carlo simulations were used to search for low-energy isomers at the DFT (BP86/def2-SVP) level. These were further optimized at the TPSS/def2-TZVP level and the IR spectra calculated to compare with the experimental data. The structures assigned

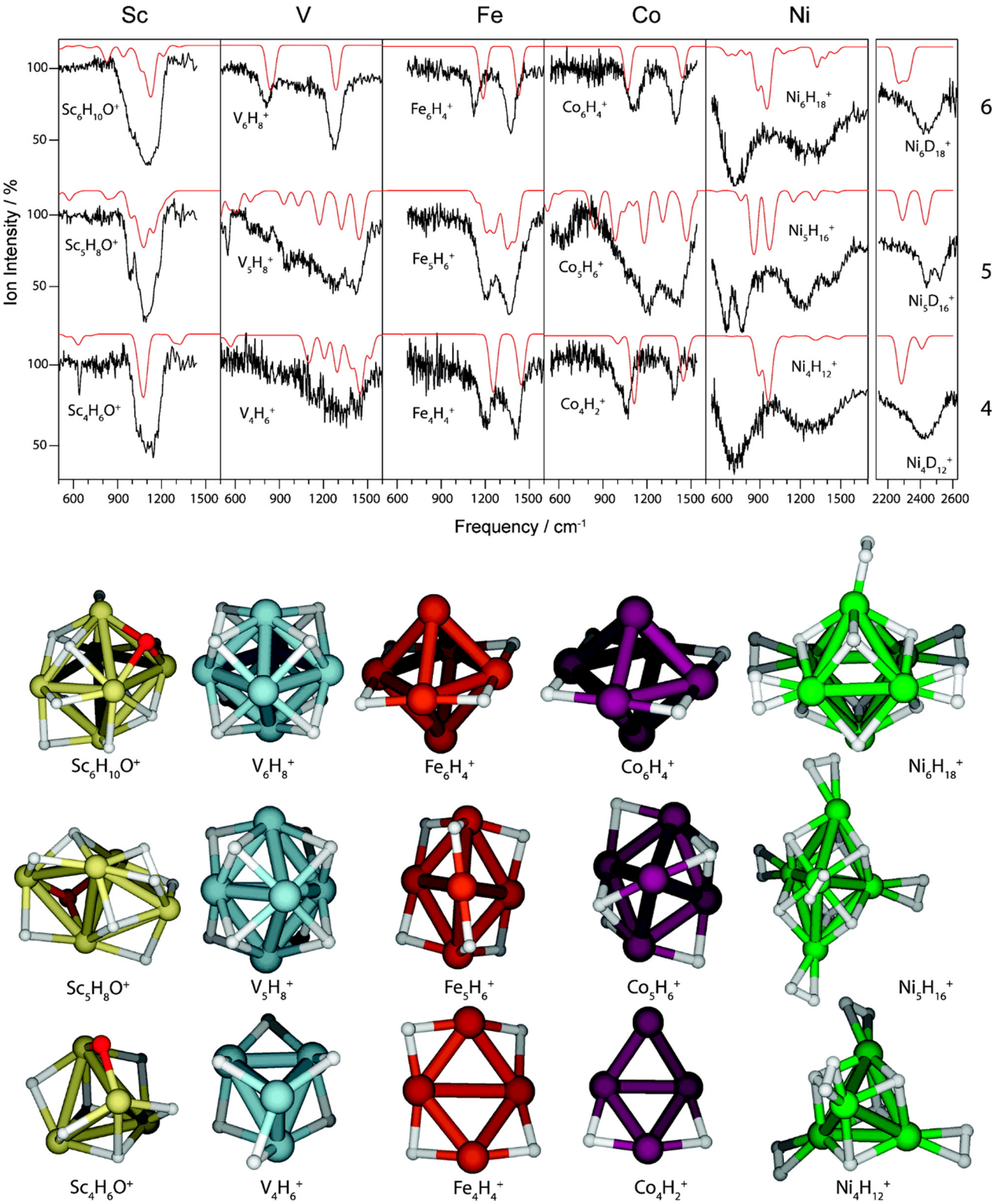

Fig. 12 Experimental IR-MPD spectra of H saturated 3d transition metal cluster cations compared to simulated depletion spectra for the structures shown below. DFT calculations (BP86/TZVP). Reprinted with permission from ref. 83. Copyright 2008 American Chemical Society.

contain μ_2-H and σ-(H_2) ligands, for $Pt_4H_{12}^+$, and $Pt_5H_{16}^+$, in addition to terminal (μ_1) H. The ν(Pt–μ_1H) and ν(H–H) fundamentals were predicted in the 2000–2250 cm^{-1} and 2500–3200 cm^{-1} ranges, respectively, thus above the experimental range. The ν(H–H) and ν(Pt–μ_2H) stretching modes are highly coupled, making detailed assignments of the observed

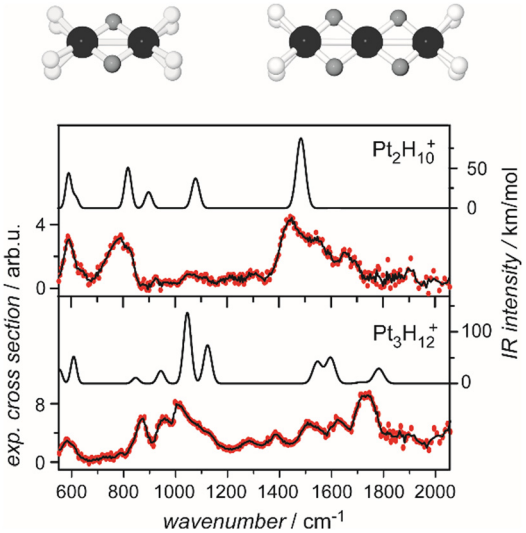

Fig. 13 Structures of H-saturated cationic platinum clusters (top) determined by comparison of IR-MPD spectra with calculated IR spectra of low energy isomers. Adapted with permission from ref. 121. Copyright 2013 American Chemical Society.

bands difficult.[121] Experimental IR-MPD spectra and calculated IR spectra for the lowest energy isomers of the structurally similar $Pt_2H_{10}^+$ and $Pt_3H_{12}^+$ are compared in Fig. 13.

TM doped Al clusters. Hydrogen binding to gas-phase aluminum clusters has been studied mainly under the aspect of reversible hydrogen storage and addition of transition metal atoms to Al clusters is known to significantly enhance the reactivity towards molecular hydrogen.[185] Neutral Al_n clusters are largely unreactive towards H_2 with the exceptions of n = 6–8.[186] For cationic clusters, Al_n^+ (n = 10–12, 14–27), activation barriers between 1.3 and 2.2 eV are found, with the barriers increasing with size and showing a pronounced odd/even oscillation with n, the even n (open shell) clusters having the lower barriers.[187] From the photoelectron spectra of anionic $Al_nD_2^-$ species it has been concluded that, depending on cluster size, physisorbed molecular D_2, chemisorbed D_2, or hydrides may be present, however, no clear vibrational progressions have been observed.[188] The matrix IR spectra of alanes $(AlH_3)_n$ (n = 1–4) in solid H_2 reveal stretching frequencies of (terminal) Al–μ_1H in a comparably narrow range of 1884–1942 cm^{-1}, while those of bridging H depend strongly on the Al–H–Al angle and can be found in a rather wide range from 1268 cm^{-1} (Al_2H_6, b_{2u}) to 1871 cm^{-1} (Al_4H_{12}, b_1,b_2).[189]

IR-MPD spectra of TM doped aluminum clusters reacted with H_2 have given information on both, the activation mechanism of H_2 by the doped Al cluster as well as the final H binding sites. The first spectrum reported was on $Al_{10}VH_2^+$ (Fig. 14).[123] In the measured range of 800–2100 cm^{-1} three bands have been observed, at about 1200 cm^{-1}, 1350 cm^{-1}, and 1900 cm^{-1}. The latter is at a typical value for ν(Al–μ_1H), indicating dissociation of the H_2 molecule. Comparison to calculated spectra (DFT: PBE/def2-TZVP) led to assignments of the lower frequency bands to ν_s and ν_{as} of a μ_2-H bridge between the V dopant atom and an Al atom. The spectra reported for $Al_{11}VH_4^+$, $Al_{12}VH_2^+$, $Al_{13}VH_2^+$, and $Al_{15}VH_2^+$ all show similar features, though much less pronounced: a ν(Al–μ_1H) band at about 1900 cm^{-1} and bands between 1100 cm^{-1} and 1500 cm^{-1}, typical for bridging H.[123] When two V atoms are introduced into Al clusters[124] formation of a V–H–V bridge is found for most of the investigated H complexes, $Al_nV_2H_2^+$ (n = 2–12, no spectra reported for n = 4, 5, 7). The characteristic ν_s band at ≈1500 cm^{-1} is close to the value measured for μ_2-H on pure V clusters, see Table 4. For n = 3, 6, 8, 10 again a sharp band at 1900 cm^{-1} is seen that is related to ν(Al–μ_1H). For other sizes, Al–H–V bridges are also predicted to be present in the assigned structures (DFT: PBE/def2TZVP).[124]

For Al clusters doped with single Rh atoms, Al_nRh^+, the IR-MPD spectra revealed molecular H_2 adsorption on the smallest clusters (n = 2, 3) *via* the detection of ν_s(Rh–H_2) and ν_{as}(Rh–H_2) at 650 cm^{-1} and 1230 cm^{-1}, respectively, in the case of $Al_3RhH_2^+$.[126] For Al_2Rh^+, only the complex with two H_2 units has been characterized for which two bands at 790 and 910 cm^{-1} are observed that are assigned, by comparison to the calculated spectrum (DFT: PBE/def2TZVP) for the lowest energy isomer, to the in-phase and out-of-phase symmetric stretching modes of two Rh–H_2 bonds predicted at 904 and 1099 cm^{-1}. An additional feature around 1900–2000 cm^{-1} suggests the presence of more than one isomer in the experiment. The H complexes of the larger clusters (n = 4–10) all show a clear band in the 1860–1890 cm^{-1} range- that is assigned to ν(Al–μ_1H).[126] The Al_nRh^+ clusters with n = 1–3, and 7 are found to be the most reactive with H_2, and the abundances of the hydrogenated clusters correlate well with the calculated binding energies of molecular H_2. It is, therefore, concluded

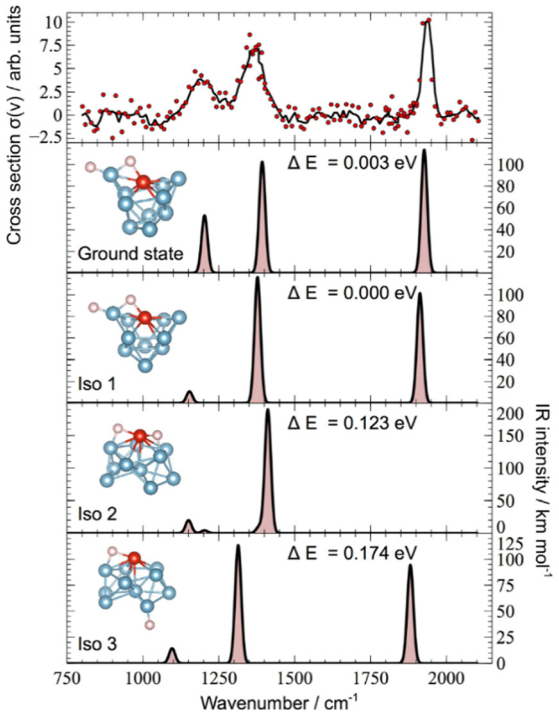

Fig. 14 Experimental IR-MPD spectra *vs.* calculated IR spectra for energetically low-lying isomers of $Al_{10}VH_2^+$. The metal cluster framework of the assigned structure ('Ground state') is very similar to the ground state structure of the bare $Al_{10}V_2^+$ cluster. Reprinted from ref. 123 with permission of John Wiley and Sons.

that the initial molecular adsorption of H_2 is the determining step for hydrogen interaction with the Al_nRh^+ clusters.[126] A similar relation is found for Al clusters doped with two Rh atoms, n = 1–9.[127b]

Larger $Al_nRh_2^+$ clusters (n = 10–13) show a pronounced size-dependence in the formation of complexes with H_2.[127a] Their IR-MPD spectra are compared to predicted IR spectra for the lowest energy isomers in Fig. 15. While for n = 10, 11 H–H dissociation and spillover to Al is indicated through the detection of ν(Al–μ_1H) at approximately 1900 cm^{-1}, the features in the spectra for n = 12, 13 can be assigned to ν_s(Rh–H_2) and ν_{as}(Rh–H_2) of molecular H_2 complexes with the H_2 bound to a single Rh atom. DFT calculations reveal for n = 11–13 formation of strongly bound Kubas complexes, which for n = 12, 13 are even thermodynamically favored such that no H–H splitting occurs.[127a]

For most of the $TM_{1,2}Al_n^+$ clusters studied, the ability to activate and bind H_2 appears to be limited to only 1 or 2 H_2 units per cluster. This can be understood, based on the vibrational spectra for the complexes discussed above, by the presence of TM bound hydride species in the complexes, *i.e.*, terminal TM–H or TM–H–Al bridges. Their persistence indicates an incomplete spillover of H towards the Al atoms – after activation and bond dissociation occurring at the TM center(s) – thereby effectively blocking the activation site for further H_2 molecules.

However, Nb doping of Al clusters leads to a different behavior, and up to 6 H_2 units are found to bind to an Al_nNb^+ (n = 1–12) cluster.[125] For the exemplary case of $NbAl_8H_8^+$ a particularly simple IR-MPD spectrum has been recorded, displaying only a single, comparably narrow, band at about 1900 cm^{-1} that can be readily assigned to ν(Al–μ_1H). DFT calculations reveal for the structure of the complex an unusual 8-fold coordinated central Nb atom surrounded by Al–H units. This complex, with 20 valence electrons in total, fulfills the 18 electron rule for the central Nb, while two more electrons are delocalized over a slightly distorted hexagonal Al_6H_6 ring surrounding it.

Further systems. For the ground state of neutral Au_2H, vibrational modes at 2050(100) cm^{-1} and 148(4) cm^{-1} are determined from vibrational progressions in the photoelectron spectra of its anion Au_2H^- and assigned to ν(Au_2–H) and ν(Au–Au), respectively.[191] While the anion is found to be linear, the neutral adopts a bent structure with $\angle$(Au–Au–H) = 131°.[191b]

In Ne matrix two isomers of V_2H_2 have been identified, which can be interconverted by irradiation. Linear HVVH has two IR active modes (π_u and σ_u^+) at 343.4 cm^{-1} and 1570.7 cm^{-1} and the lower energy twofold H-bridged $V_2(\mu_2\text{-H})_2$ isomer has modes at 565.4 cm^{-1} (a_1), 917.2 cm^{-1} (b_2), 1405.3 cm^{-1} (a_1), 1425.1 cm^{-1} (b_2).[192]

3.1.2 CO. Binding mechanism. The binding of CO to TM centers has been intensively studied theoretically,[193] though certain details, such as the interplay of covalent interactions, orbital polarizations, and bond strengths, are still under discussion.[194] The TM–CO bond is usually described in terms of the Blyholder model[195] as σ-donation/π-acceptor interaction involving the frontier orbitals of CO: the HOMO, a σ_s* orbital that is largely localized at the C atom, thus often designated as the C-lone pair, and the LUMO, a π* orbital (Fig. 16). Interaction of the filled σ_s* orbital with an empty, symmetrically fitting, metal-centered orbital leads to formation of an M–CO σ bond. To fulfill neutrality this e-transfer towards M goes along with the interaction of a filled d-type orbital on M with the π* orbital of CO, *i.e.*, π backdonation. The latter has (for ''classical'' carbonyls) two important consequences: (i) the strengthening of the M–CO interaction through formation of an additional π bond and (ii) the weakening of the C–O bond due to the (partial) occupation of an orbital with pronounced C–O anti-bonding character. This binding mechanism naturally describes many experimental observations related to CO as ligand or adsorbate on TMs.[196] Most important is the sensitivity of the C–O bond strength to the degree of π backdonation that can be experimentally evaluated by determining the shift of ν(C–O) in the chemically bound system, relative to the free CO

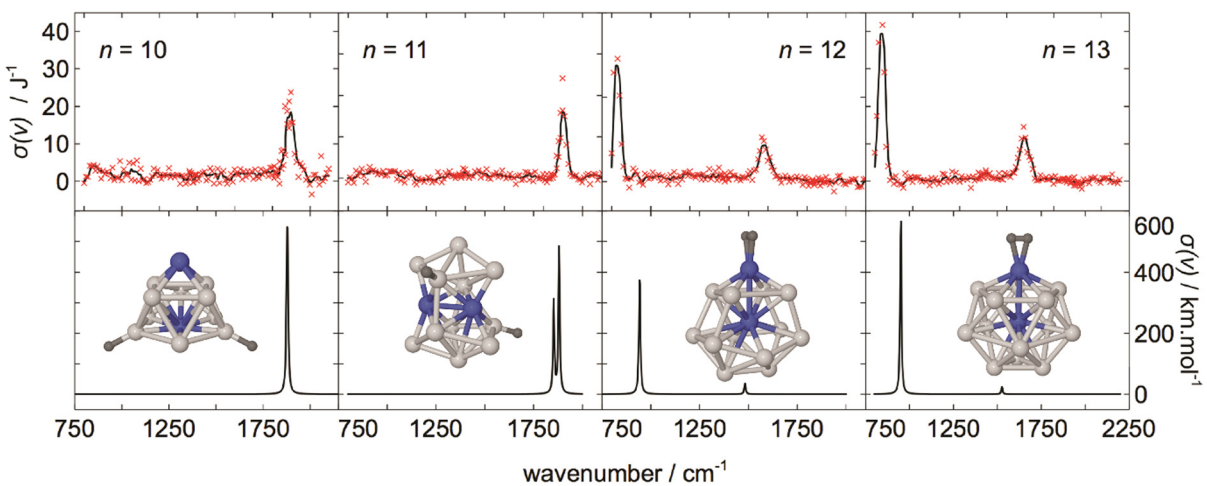

Fig. 15 Comparison of experimental IR-MPD and simulated IR spectra for energetically low-lying isomers of $Al_nRh_2H_2^+$ (n = 10–13). The color scheme for the structures is as follows: Ru – blue, Al – lightgrey, H – darkgrey. Adapted with permission from ref. 190. Copyright 2018 American Chemical Society.

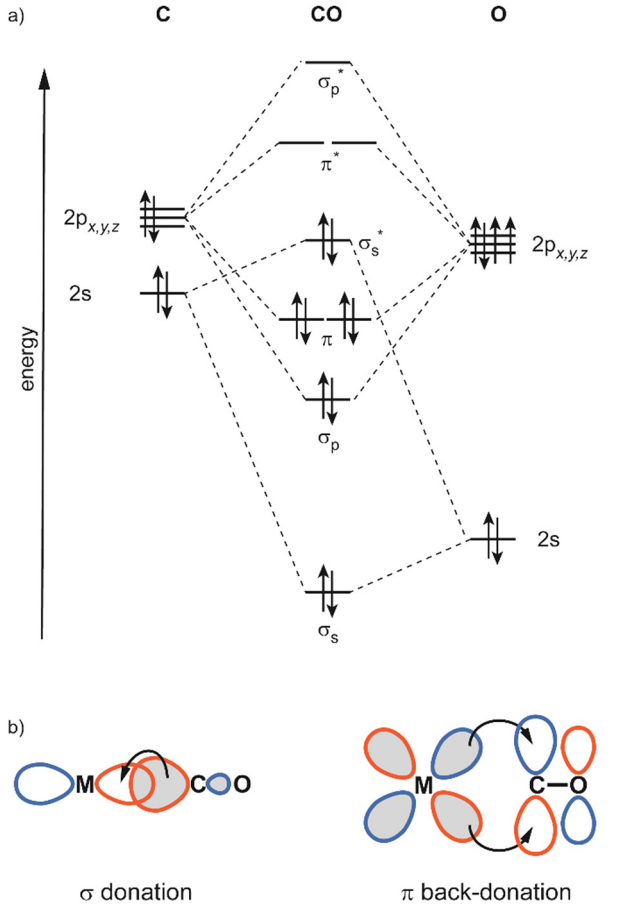

Fig. 16 (a) Molecular orbital diagram for the ground state of CO; (b) bonding contributions in linear TM–CO complexes.

molecule. Further, as will be shown more in detail below, the C–O bond strength becomes sensitive to the (partial) charge at the metal center. Finally, backdonation from multiple M atoms can weaken the C–O bond even more, giving a simple method to evaluate the CO binding geometry.

The localization of the σ_s* HOMO leads to metal binding through the C atom. CO binding atop (terminal) to a single M atom (μ_1) forms linear M–CO units, a consequence of the π system in M–CO. Other common coordination geometries are symmetrically bridging CO ligands between two M atoms (μ_2) or CO capping a face of 3 M atoms (μ_3).

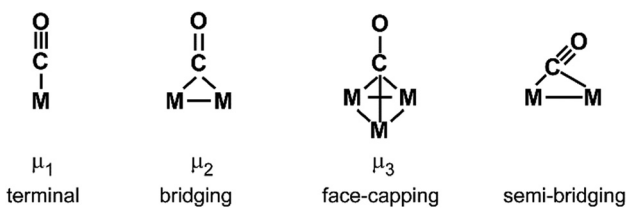

Unsymmetrically (semi-)bridging CO ligands with one short and one long M–C distance are less common and can be classified into two types: (i) one having an M–C–O angle significantly deviating from linearity due to additional π back-bonding into the CO's π* orbital from the more distant metal atom *via* interaction with an M–M antibonding orbital. Those can be seen as intermediates between terminal and symmetrical-bridging CO ligands. However, a linear semi-bridging CO (ii) indicates, according to Hall,[197] π back-bonding from a filled π orbital along the M–M entity, *i.e.*, it stabilizes the M–M bonding orbital, while the bent semi-bridging carbonyl stabilizes an M–M antibonding orbital.

Complexes with single metal atoms. Vibrational data of unsaturated transition metal carbonyls, neutrals and as cationic or anionic species, has been reviewed by Zhou, Andrews and Bauschlicher, Jr.,[193c] though this work is concentrating on studies in low temperature matrices. Results from gas-phase IR spectroscopy on mononuclear ionic carbonyls are summarized in ref. 198. More recent studies from M. F. Zhou and co-authors include carbonyls of the lanthanides, actinides, and of main group 2 elements (Ca, Sr, Ba) that behave like transition metals by involving their d orbitals in the bonding.[199]

Metal cluster reactivities. The reactivity of CO with transition metal clusters and the relation to the CO binding energy has been summarized before.[200] Overall, there is only little size-dependence.[201] Few-atom sized clusters are comparably unreactive, and for larger clusters reactivity increases smoothly with size. This observation is explained by a combination of geometrical effects and a better initial stabilization of the (entrance channel) complex through a longer life-time with increasing density of vibrational states.[202] A lowered reactivity of small anionic Rh clusters in comparison to the cations has been related to Pauli repulsion between the electron cloud extending outside the surface of the metal cluster and preventing reactive collisions with the CO.[202] More pronounced size-effects have been observed for cluster systems that are well-known to show stabilizations due to electronic shell closings, like the coinage metal clusters.[203] For instance, for neutral Au_n (n = 9–68) the reactivity is found to be particularly high for n = 16, 18, 32. Assuming CO as 2e-donor ligand, the corresponding CO complexes contain 18, 20, and 34 valence electrons, respectively. These numbers agree to electronic shell closings within the spherical jellium model and may be related to an increased stability of the complexes, *i.e.*, a higher CO binding energy.[203c] Notably, such variations are not found for Au_n^+ (n = 1–65) studied in an FT-ICR mass spectrometer.[41a] Inconsistencies between the predictions from shell closing arguments and the observed reactivity and stability patterns of copper clusters have been pointed out before.[203b] Instead, it had been concluded that the symmetry of the cluster's HOMO is the relevant factor. Thus, a HOMO with π symmetry would allow for stronger back-bonding and thereby increase the stability of the complex.[203b]

Effects of heteroatom doping of TM clusters on the CO reactivity have been investigated more recently for Pt and Au clusters.[143,150,190,204] For instance, doping Au_n with one or two Ag atoms lowers the reaction probability, but, due to the similar electronic configuration of Au and Ag, the reactivity pattern is not changing.[204a] More pronounced changes are observed for Au clusters doped by metals with open d-shells like V or Pd.[150,204c] For the latter system, detailed RRKM simulations

allowed the experimental rate constants to be related to the CO binding energies (E_b), and good agreement to the values from DFT calculations is obtained.[150] For Pt clusters no significant change in the dissociation rates of the CO complexes is found upon doping with Sn or Ag, while the rates increase, *i.e.*, E_b decrease, upon Nb or Mo doping.[204b] This is understood by a different charge transfer from the dopant to the Pt atoms in these cases. While through replacement of Pt in the cluster by Nb and Mo the electron density is enhanced at the reacting Pt atom, it stays rather constant for Sn and Ag. Based on an analysis of the calculated density of states, it is argued that more positively charged Pt leads to a stronger stabilization of the CO σ_s* orbital with concomitant better acceptor properties of the cationic Pt, thereby leading to a higher E_b.[143,190,204b]

Vibrational modes and frequencies. Most important to characterize CO ligands or adsorbates on TM has been the C–O stretching vibration as it gives direct information on the activation of the internal C–O bond. In classical carbonyls, where M → CO π backdonation governs the interaction, ν(C–O) is found below that of free CO at 2143 cm^{-1} ($\tilde{\nu}_e - 2\tilde{x}_e\tilde{\nu}_e$). The lowering of ν(C–O) can be related to the ability of the metal to donate electrons to the CO's π* orbital that depends on the orbital overlap, its ionization energy, and the effective (partial) charge at the binding site. In addition to the effect of these electronic factors on ν(C–O), it can also give indications about the coordination geometry of the CO ligands.[32a,205] While terminal (μ_1) CO ligands have ν(C–O) typically well above 1900 cm^{-1}, interaction of the CO with multiple M atoms leads to an incremental lowering of ν(C–O) by about 100–200 cm^{-1} per additional M atom the CO is bound to. This is illustrated in Fig. 17 for complexes of cationic, neutral, and anionic rhodium clusters with a single CO ligand, $Rh_nCO^{+/0/-}$.[73a,136] For most complexes, a band at higher frequencies is observed that corresponds to $\nu(\mu_1$-CO) with its exact position depending on cluster size and charge state. Bands at lower frequencies are seen for some of the complexes, *e.g.*, in the case of the cations for Rh_3CO^+ at 1903 cm^{-1} and for Rh_4CO^+ at 1788 cm^{-1} that are assigned to μ_2 and μ_3 structures, respectively. With Rh_5CO^+ showing the band at 2054 cm^{-1}, this corresponds to shifts of 151 cm^{-1} from μ_1 to μ_2 and of 115 cm^{-1} from μ_2 to μ_3. The observation of two bands in the ν(CO) range for a number of $Rh_nCO^{+/0/-}$ complexes indicates the presence of isomers with CO binding in μ_1 as well as μ_2 coordination.[73a]

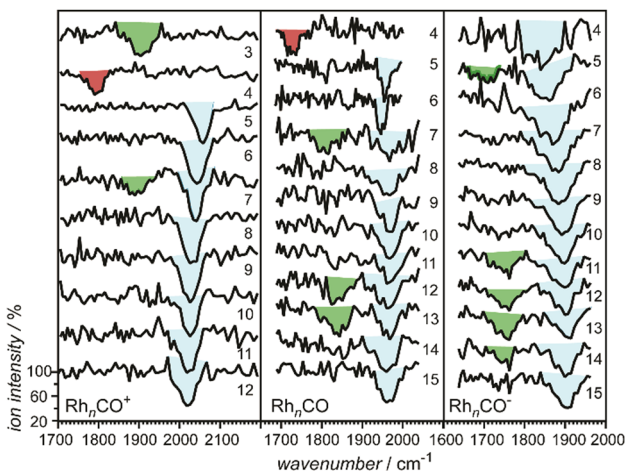

Fig. 17 IR spectra of $Rh_nCO^{+/0/-}$ in the range of the CO stretch vibration. For most clusters atop (μ_1, blue shading) binding is observed, only for the smallest clusters, Rh_3CO^+ and $Rh_4CO^{+/0}$, exclusive μ_2-bridging (green shading) or μ_3-capping (red shading) is found, respectively. For several clusters isomers with μ_1-atop and μ_2-bridging CO ligands are present. Adapted from ref. 200. Copyright (2009), with permission from Elsevier.

Values of ν(C–O) higher than that of free CO have been observed only for few metal carbonyls. These carbonyls termed "non-classical" are typically cationic metal centers, often containing coinage metal atoms. For instance, ν(C–O) for $CuCO^+$, $AgCO^+$, and $AuCO^+$ measured in Ne matrices are 2234.4 cm^{-1}, 2233.1 cm^{-1}, and 2236.8 cm^{-1}, respectively.[206] Central to the understanding of such carbonyls is the role of the CO σ_s* orbital. Notably, questions about the anti-bonding character of the σ_s* orbital have been raised more recently, as it is found to have no node between C and O.[194a] Instead it is thought to be weakly C–O bonding. A detailed analysis of the bonding in these species has been given lately.[194d]

Spectroscopic investigations of ν(M–CO), located typically in the 300–600 cm^{-1} range, are comparably rare, although it would give a more direct measure of the strength of interaction between metal and CO. The difficulty lies in the low IR intensity of such modes, therefore, often other spectroscopic techniques are used for the characterization. A larger amount of data for ν(M–CO) exists for surface species investigated by electron energy loss spectroscopy.[196] Some stable metal cluster carbonyls have been characterized in early Raman and far-IR studies.[207] APES of $Pt_3(CO)_6^-$ has resolved a low energy vibrational progression at 425 ± 30 cm^{-1} that is assigned to a collective ν(Pt–CO) mode.[141] More recently, ν(M–CO) was determined in matrix-IR studies of Fe_2CO and Co_2CO at 483.2 cm^{-1} and 488.7 cm^{-1}, respectively, and the bending modes, δ(M–CO), at 371.6 cm^{-1} and 357.9 cm^{-1}.[208] In both studies, the authors emphasize the challenges of the measurements as the intensities of these modes are about 2 orders of magnitudes lower than for ν(CO) measured for the same samples. Far-IR bands of Pd_nCO (n = 2–4), grown in Ne and Ar matrices, have been assigned to M–CO bending and stretching modes of CO bound in either μ_1, μ_2, or μ_3 configuration, depending on the cluster size.[209] Using synchrotron radiation, far-IR spectra between 50 and 650 cm^{-1} have been obtained for bulk $Ru_3(CO)_{12}$, $H_4Ru_4(CO)_{12}$, and bimetallic $Ru_3(\mu\text{-}AuPPh_3)(\mu\text{-}Cl)(CO)_{10}$ dispersed in polyethylene matrices gave access to ν(M–CO), related bending modes, and the metal core vibrations.[210]

Intensity of ν(CO). An important additional aspect for the investigation of metal carbonyls using vibrational spectroscopies is the usually high IR intensity of ν(CO) that facilitates experimental characterizations. The enhancement of the IR intensity of ν(CO) for CO adsorbed to low coordinated metal surface sites can be explained by an antenna effect.[211] For metal clusters, this effect leads to a steady increase of the ν(CO) IR intensity with cluster size. This is illustrated for Au_nCO^+ in Fig. 18 where the calculated IR intensities[41a] are compared to

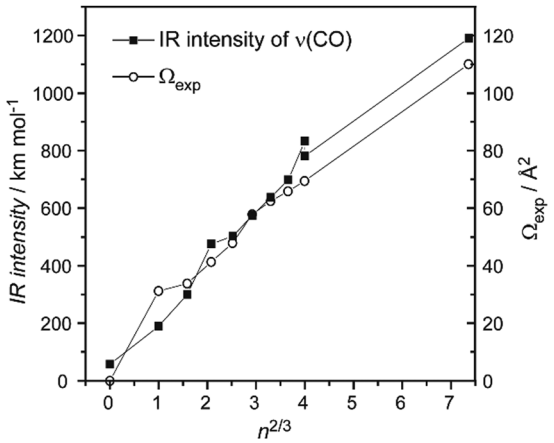

Fig. 18 Intensity of the C–O stretching vibration calculated for Au_nCO^+ (n = 1–8, 20) compared to the experimental cross section of bare Au_n^+ as function of $n^{2/3}$, *i.e.*, an idealized cross section. The experimental cross sections are determined from the ion mobility in He.[110] IR intensities were calculated for the lowest energy isomers at the DFT-BP86 level. For n = 8 two values are given as two isoenergetic isomers were found.[41a] The IR intensity at n = 0 (metal cluster cross section of zero) refers to that of neutral CO.

the geometrical cross sections Ω of Au_n^+, as determined from the ion mobilities.[110] For this system both properties appear to be closely related, which can be understood by the following considerations. For CO bound to a discrete metal cluster, the transition dipole moment $\partial\mu/\partial Q$ of the ν(CO) mode is increased through charge separation over a distance that is essentially given by the dimensions of the metal cluster, thus significantly larger than the molecular dimensions of the local C–O oscillator. This is a consequence of the binding mechanism that couples e-transfer from the metal and C–O bond strength, and thereby also the change of charge distribution in the cluster-CO entity during the ν(CO) vibration. The effective charge separation distance l may be approximated by the sum of the cluster diameter plus the distance of the CO molecule from the cluster surface. If the charge transferred along the normal coordinate Q stays constant with cluster size one obtains a linear relation between the IR intensity scaling with $(\partial\mu/\partial Q)^2$ and l^2, the latter being proportional to a slightly enlarged cluster cross section that, in turn, can be approximated by Ω.

Molecular and dissociative adsorption. The reaction of CO with metals can lead to two different types of products, either to metal carbonyls containing molecular CO ligands, or to carbide and oxide species as a result of dissociative adsorption. The detection of a vibrational band in the 1400–2200 cm^{-1} range for an M_nCO complex is a strong indication for the presence of an intact CO unit in the complex, as the frequencies related to vibrations of M–C and M–O species as well as the metal cluster modes are well below that range.

Fig. 19 gives a compilation of available data from gas-phase IR-MPD studies.[63b,73a,117,130,134,136,138,139,143,148–151,200,213] In short, for the late transition metals CO binds intact, indicated by the presence of a ν(CO) band, while for the group 5 transition metals (V, Nb, Ta) such a band could not be detected,[117,213,214]

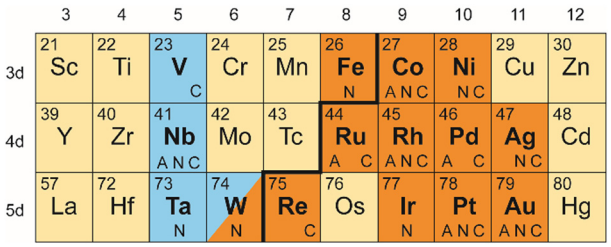

Fig. 19 Chemisorption behavior of CO on TM clusters as identified by the presence or absence of ν(CO) absorption bands in the cluster complex (complexes formed at ≈300 K). Orange shading denotes verification of molecular chemisorption through the presence of ν(CO) bands, while blue shading designates the absence of any ν(CO) bands indicating a dissociation of CO on the cluster surface. The bold line gives the borderline between molecular and dissociative adsorption on extended surfaces at ≈300 K as suggested by Brodén.[212] The lettering specifies if the experiments have been performed on anionic (A), neutral (N), or cationic (C) clusters. Adapted from ref. 200. Copyright (2009), with permission from Elsevier.

leading to the conclusion that CO dissociates on these clusters. $Nb_nCO^{-/0/+}$ (n = 3–8) has been studied more in detail by intracavity IR-MPD using FELICE and DFT calculations (BP86/def2-SVP). The IR spectra are dominated by strong bands around 600–700 cm^{-1} that are assigned to stretch vibrations of separated carbide and oxide units.[214] As far as data is available, these trends are independent of the clusters' charge state and only for tungsten a particular size-dependence is seen, marking for the 5d elements at W the transition between dissociative and molecular adsorption.[130] There are no studies of the vibrational spectra for single CO molecules bound to gas-phase clusters of the earlier TM (group 3 and 4) or of Cr, Mo, Mn, and Tc.

In the M_nCO complexes with intact CO ligands, the C–O bond gets gradually more activated when moving from metals at the end of the d-rows towards the earlier TM and one observes a decrease in ν(CO). Table 5 and Fig. 20 illustrate this behavior with the experimentally determined values of $\nu(\mu_1$-CO) in gas-phase neutral TM cluster complexes. For each of the 3d, 4d, and 5d metals, ν(CO) increases with further filling of the d-shell and within a row, the highest values are seen for the coinage metals. Within a group the C–O activation appears to follow the order 3d > 4d > 5d.

This chemistry of CO seen for the gas-phase TM clusters is very similar to that of extended surfaces. While clearly

Table 5 Average values for ν(CO) (in cm^{-1}) assigned to atop (μ_1) CO ligands in neutral M_nCO complexes containing up to 30 metal atoms. Adapted from ref. 200. Copyright (2009), with permission from Elsevier

Group\row	6	7	8	9	10	11
3d			Fe^{130} 1865	Co^{134} 1940	Ni^{139} 1994	
4d			$Ru^{a,130}$ ~1910	$Rh^{73a,134,136}$ 1960	$Pd^{a,139}$ ~2000	$Ag^{b,200}$ 2090
5d		W^{130} 1927		Ir^{138} 1976	Pt^{139} 2020	$Au^{c,200}$ 2091

[a] Average of anionic and cationic clusters. [b] From $Ag_5(CO)_3$. [c] From complexes that contain 3–5 CO ligands and 3–11 Au atoms.

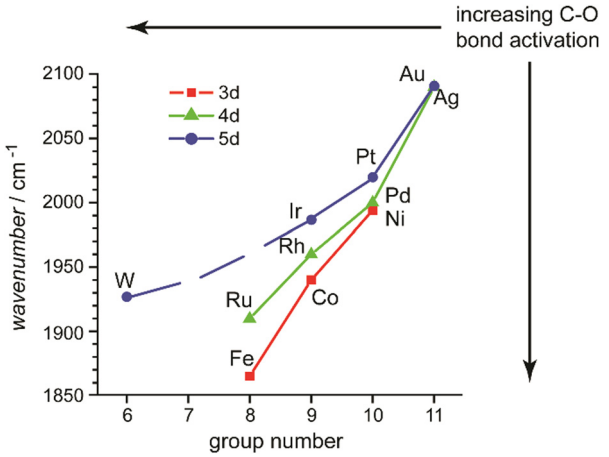

Fig. 20 Observed C–O stretching frequency *versus* group number for CO bound in atop positions on neutral transition metal clusters. Further details about the data are included in Table 5. Adapted from ref. 130, with the permission of AIP Publishing.

dependent on the particular surface structure, CO coverage and temperature, a borderline between the elements with dissociative *vs.* molecular CO adsorption on their extended surfaces[212] is often drawn, as shown in Fig. 19, and the tendency of the earlier transition metals for CO dissociation has been explained by the up-shift of the d-band center relative to the Fermi energy when going from the late to the early transition metals (from right to left in the periodic system of elements).[215] This leads to a gradual increase in the M–CO π backdonation and at the same time an over-stabilization of oxide and carbide *vs.* molecular CO for the early TM. Similar arguments hold also for the activation and dissociation of other molecules by transition metal surfaces, *e.g.*, N_2 and NO.

Binding geometries. CO binds, according to the assignments based on measured values of ν(CO), to most transition metal clusters in atop geometry. This is in agreement with the predictions for the preferred μ_1 adsorption sites at metal surfaces of low CO coverage.[215b,216] Only for Ni and Pd is binding in higher coordination hollow sites energetically preferred. For complexes of gas-phase transition metal clusters with a single CO molecule, $M_nCO^{+/0/-}$, the experimental observations are summarized in the following.

The IR-MPD spectra for CO complexes of the 3d transition metals Fe, Co, Ni indicate exclusively μ_1-binding.[130,134,139] Only for small anionic Ni clusters vibrational progressions in APES at 1800 ± 80 cm^{-1} (Ni_2CO^-) and 1750 ± 80 cm^{-1} (Ni_3CO^-) have been related to CO binding in higher (μ_2 or μ_3) coordination.[141] Also, for the noble metals Ag, Au, Pt, as well as Ir, CO is found to only bind in μ_1 configuration,[63b,138,139,143,148–151,200] though in a study on small Au clusters grown in cryogenic Ar matrix a band at 1852.9 cm^{-1} has been assigned to $Au_5(\mu_2\text{-CO})$.[217]

For the remaining 4d and 5d TM a wider range of CO binding geometries is observed. A band assigned to μ_1-CO is present for all investigated Ru clusters (anions: n = 4–15; cations: n = 4–20) and some clusters in the n = 9–16 size range show a minor signal corresponding to a μ_2 isomer.[130] Rh clusters bind CO in μ_1, μ_2, or μ_3 coordination depending on cluster size and charge state as discussed above.[73a,134,136] In particular for Rh the number of clusters binding CO in μ_2 coordination and the apparent abundance of these complexes is increasing with electron density on the metal, similar to that observed for Rh nanoparticles supported on zeolites.[218] CO binding in higher coordination is also seen for Pd with μ_1, μ_2, and μ_3 isomers appearing, *e.g.*, for all anionic and cationic complexes, $Pd_nCO^{-/+}$, in the n = 6–9 size range.[139] However, while for Rh μ_1-coordination is prevailing (Fig. 17), Pd favors CO binding in higher coordination. This agrees with data from matrix-IR spectroscopy, where for the Pd dimer isomers with μ_1 and μ_2 bound CO have been identified, while for trimer and tetramer CO binds in μ_3 coordination.[209] Comparing CO binding within the late 4d TM Ru, Rh, and Pd there is a tendency of CO binding in higher coordination towards the end of the row.

Within the late transition metals of group 9 (Co, Rh, Ir) and group 10 (Ni, Pd, Pt) the 4d metals stand out as only for Rh and Pd clusters CO is found to bind in μ_2 or μ_3-coordination.[139,200] For the group 10 metals this behavior has been ascribed, based on gradient-corrected DFT calculations for CO bound to cluster models of the Ni, Pd, and Pt (100) surfaces, to a relativistic effect stabilizing CO in μ_1-configuration.[219] In non-relativistic calculations the M–CO bond length is found to increase monotonically in the row Ni < Pd < Pt, related with a decrease in CO binding energy. If scalar-relativistic corrections are applied, the M–CO distance shortens for Pd and Pt, and the CO binding energy increases. Both effects are, however, nearly absent for bridge-bound CO leading to a stabilization of atop Pt–CO relative to bridge bound CO. In the case of Pd, bridge bound CO ligands remain the more stable species.[219] A similar mechanism can be expected for the group 9 metals.

For Ru cluster complexes a size dependent oscillation of ν(CO) is seen with odd numbered clusters having a clearly lower ν(CO) for both, μ_1- and μ_2-CO, compared to the complexes with even n.[130] The effect is more pronounced for the cations with differences ranging from 30 cm^{-1} to 100 cm^{-1} compared to the anions where it is only ≈15 cm^{-1}. Ru is the only metal for which such an effect is observed. It may be related to the special growth pattern of the Ru clusters that is, for small clusters (n = 8–12), based on a cubic motif.[221] The odd-sized clusters contain apex atoms capping a square plane. Such structural element is also found in Ru_{15}^- but not present for any even-sized Ru cluster or Ru_{13}^-.

ν(CO) as probe of electron density. Investigation of $\nu(\mu_1\text{-CO})$ for charged metal cluster carbonyls, $M_nCO^{+/-}$, reveals a distinct size dependence with the frequencies decreasing with growing cluster size for the cationic clusters and increasing for the anions. Their values appear to approximately converge for large sizes towards values seen for neutral clusters that themselves do not show much size-dependence of ν(CO). Fig. 21 shows this size and charge dependence for Rh clusters[134] and similar correlations have been reported for CO bound to clusters of Co, Ni, Pd, Pt, and Au.[73a,134,139,143,148,149]

The effect can be understood within a charge dilution model,[134] where it is assumed that the total charge of the

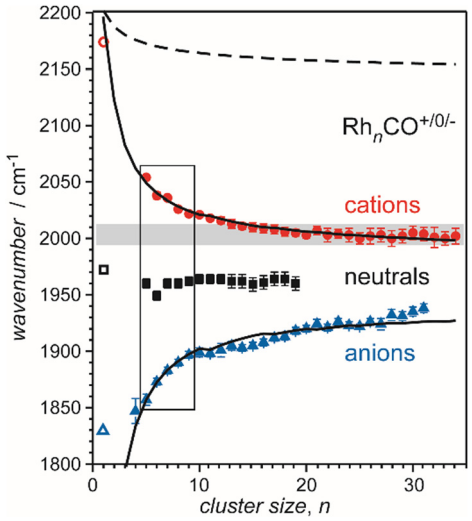

Fig. 21 Frequency of the ν(CO) vibration of μ_1-CO in Rh$_n$CO$^{+/0/-}$ as a function of cluster size and fits to the charge dilution model derived in ref. 134. The dashed line illustrates the pure electrostatic effect $\Delta\nu_{ES}$. The small box marks the data for n = 5–9, replotted in Fig. 22 as function of charge state. Data of the atomic species (open symbols) have been measured in a cryogenic Ne matrix.[220] Values reported for $\nu(\mu_1$-CO) on Rh surfaces are marked by a grey band. Adapted from ref. 200. Copyright (2009), with permission from Elsevier.

cluster $z{\cdot}e$ is equally distributed over n_S surface atoms of the cluster, *i.e.*, the cluster behaves like a metallic sphere.

Then, for a CO molecule binding to a surface atom of a charged metal cluster, it can be assumed that this charge dilution gets directly reflected in the occupancy P of the π^* orbital:

$$P(\pi^*) = P(\pi^*)_\infty - \gamma{\cdot}z/n_S$$

Here, z/n_S is the fraction of the charge number at the CO binding site and γ a proportionality factor expressing how much a variation in the charge influences the occupation. With increasing number of surface atoms the fractional charge per surface atom converges to zero, hence, within this charge dilution model, $P(\pi^*)_\infty$ corresponds to the value of the neutral clusters. In addition to the change in the orbital occupation, the charge residing at the metal cluster leads also to an electrostatic polarization effect, and both are influencing the C–O stretching force constant. Thereby, ν(CO) is shifted with respect to the value of the bulk limit ν_∞.

$$\nu(\mathrm{CO}) = \nu_\infty + \Delta\nu_{ES} + \gamma'{\cdot}z/n_S$$

The electrostatic effect $\Delta\nu_{ES}$, in comparison to the influence of the π back-bonding, causes only a minor change in ν(CO). Details on the derivation of this relation have been reported in ref. 134. Fits of the model to the experimental values of ν(CO) for Rh$_n$CO$^{+/-}$ are included in Fig. 21. This relation allows to quantitatively probe electronic properties like charge distribution, and effects of co-adsorbates or dopants in clusters *via* the experimental determination of ν(CO).

CO adsorption and measurement of ν(CO) is a technique widely used to characterize the oxidation state of surface adsorption sites, *e.g.*, atomic or nano-scale metal particles deposited on a support.[222,223] While gas-phase metal clusters lack the interaction with a support, they allow to determine ν(CO) as function of their precise size, CO coverage and charge state. In that sense, they are useful model systems for comparison to the deposited counterparts to develop a scale for local charging based on ν(CO). Such approach had been used before to estimate the oxidation state of mononuclear metal carbonyls MCO (M = Rh, Pd, Ir) prepared on alumina films by comparison to ν(CO) obtained for the cationic, neutral and anionic species in cryogenic matrices.[222] An example for gas-phase CO complexes is shown in Fig. 22 where the values for ν(CO) for CO bound to small Rh clusters are plotted as function of charge state and compared to ν(CO) for CO interacting with Rh clusters containing on average 5–6 metal atoms that are supported on highly ordered Al_2O_3.[222] Based on ν(CO), the charge on the supported clusters is estimated to +0.5 −+0.6*e*.[73a] Similar data for differently charged gas-phase complexes has been obtained for Au,[40] Co,[134] Ni,[139] Pd,[139] and Pt[139] clusters. In case of platinum model-catalysts for CO oxidation, the comparison facilitates the characterization of oxidation state and particle size of the metal, from single atoms to nanoclusters.[223b,224]

The same principle can also be used to study how electron density of a metal cluster is altered by co-adsorbates or dopants. In case of co-adsorption of hydrogen with CO on cationic cobalt clusters containing 4–20 Co atoms, ν(CO) is, in most cases, blue-shifted compared to the H-free system (Fig. 23). The shift increases close to linearly with the number of H in Co$_n$[H$_2$]$_m$CO$^+$.[119] This is interpreted as H_2 binding dissociatively and charge getting localized in Co–H bonds thus reducing the amount of electron density available for π back-bonding. Comparing the shifts of ν(CO) per co-adsorbed H-atom and the shifts in ν(CO) for the same-sized charged *vs.* the neutral clusters gives a gauge for the amount of charge localization. For Co clusters, a single H-atom has the same effect on the electron density of the metal cluster as 0.09–0.25 of a single positive charge.[119,200]

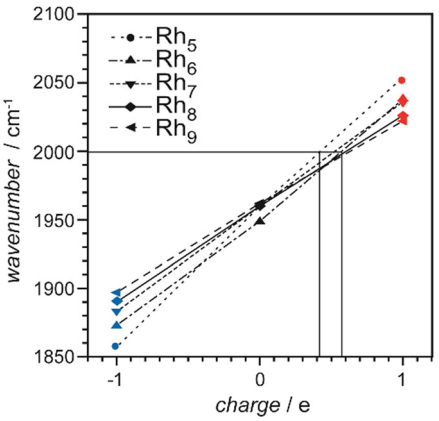

Fig. 22 Effect of charge on ν(CO) of μ_1-bound CO in small rhodium cluster–CO complexes containing 5–9 rhodium atoms. The horizontal line indicates the observed ν(CO) value of 2000 cm^{-1} for CO adsorbed on Rh clusters of similar size grown on highly ordered Al_2O_3.[222] Adapted with permission from ref. 73*a*. Copyright 2004 American Chemical Society.

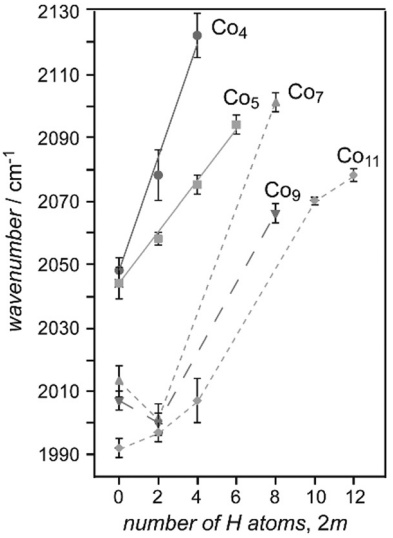

Fig. 23 Effect of co-adsorbed hydrogen on ν(CO) in cationic cobalt cluster carbonyls $Co_n[H_2]_mCO^+$. Adapted from ref. 200. Copyright (2009), with permission from Elsevier.

Exceptions are seen for n = 7–9, where binding of the first H_2 unit induces a small red-shift for ν(CO) indicating an increase of electron density. This could be a sign of molecular H_2 complexes, as in these the TM ← H_2 σ-donation outweighs the TM → H_2 backdonation.[193b]

Studying the infrared driven CO oxidation in co-adsorbates of O and CO on cationic platinum clusters $Pt_nO_mCO^+$ (n = 3–7, m = 0, 2, 4), also an effect of the oxide species on ν(CO) has been observed. Similar to hydride, the oxygen adatoms lead to a localization of electron density and reduce the extent of π backdonation to CO.[63b] For anionic $Au_2O_2(CO)_n^-$ complexes, the large blue shift of ν(CO) of about 200 cm^{-1} compared to $Au_2(CO)_2^-$ indicates the presence of a formally neutral Au_2 entity in the mixed complex, which is in line with the formation of a superoxo species (O_2^-).[44] Another example for using ν(CO) to gauge local charging has been CO bound to Mo doped Pt clusters, where the influence of Mo doping on the reactivity has been discussed above. Here, a combination of quantum chemical calculations, experimental studies of CO binding energies, and IR spectroscopy revealed that electron transfer between Mo and Pt atoms within the cluster depends on the cluster's size. A correlation between the cluster–CO bond strength and the dopant-induced electron transfer was found; sizes with a more positive charge on the platinum binding site have lower CO binding energies.[143]

Site dependence of CO binding in mixed metal clusters. For cationic gold clusters doped with a single Pd atom $PdAu_{n-1}^+$ (n = 4–14), shifts in ν(CO) compared to the values seen for pure Au_n^+ clusters have been interpreted as signature of CO binding to the Pd dopant.[150] While for most $PdAu_{n-1}(CO)^+$ the measured ν(CO) are 30–70 cm^{-1} below those for $Au_n(CO)^+$, for n = 4, 5, 11 both values are very similar. This leads to the conclusion, that only for these sizes CO is bound to an Au atom, and in the other cases it is Pd-bound. The assignments are supported by the structures of the putative global minima of $PdAu_{n-1}(CO)^+$ identified using the Birmingham Parallel Genetic Algorithm (BPGA)[225] combined with DFT. In all cases, CO is μ_1 bound to a single metal atom.

Saturated homoleptic cluster carbonyls. Studies of saturated cluster carbonyls by molecular or ion beam techniques allow for comparison to the properties of stable, in bulk quantities synthesizable, cluster carbonyls.[141a,226] The stoichiometries of such cluster carbonyls can be often well described by the Wade-Mingos rules, *i.e.*, electron counting rules relating the total number of valence electrons contributed from ligands and TM atoms to a specific structure of the metal cluster skeleton.[227] While initial experimental studies were limited to characterization by mass spectrometry, more recently also vibrational data on the gas-phase cluster carbonyls has been obtained. Thus, the structural models derived from the electron counting can be tested and further information on the binding modes of the ligands, or even full structural characterization, becomes accessible.

A first example for such gas-phase synthesis and characterization by IR-MPD spectroscopy in the ν(CO) range were anionic iron carbonyl clusters up to $Fe_5(CO)_{14}^-$, synthesized by ion-molecule reactions between $Fe(CO)_4^-$ and $Fe(CO)_5$.[133] For most of these carbonyls the spectra are dominated by bands assigned to μ_1-CO, however, *e.g.*, $Fe_2(CO)_8^-$ and $Fe_4(CO)_{13}^-$ show additional bands red-shifted by about 150 cm^{-1} that are related to μ_2-CO. For $Fe_2(CO)_8^-$, this assignment was confirmed by comparison to results of DFT calculations (B3LYP/LACVP+*) predicting a C_s structure with two symmetric μ_2-CO bridges.[133] It is noted in this study that extending the experiment to the range of M–CO vibrational bands should give valuable additional information. The often very low IR intensities of such modes in comparison to the intensities of ν(CO), however, make this a challenging task. IR-MPD spectra including the range of M–CO stretch and deformation modes (300–600 cm^{-1}) in addition to the ν(CO) range (1800–2200 cm^{-1}) have been measured for cationic saturated Rh cluster carbonyls containing 1–6 Rh atoms and their structures have been assigned by comparison with results of DFT calculations (B3LYP/TZVP).[137] For instance, $Rh_3(CO)_9^+$ has a paddle wheel structure with only μ_1-CO ligands, $Rh_4(CO)_{12}^+$ is tetrahedral, again exclusively μ_1-CO ligated. $Rh_6(CO)_{16}^+$ has an octahedral metal core capped by four μ_3-CO and each Rh atom binding two more μ_1-CO. This structure is nearly identical to that of the well-known neutral $Rh_6(CO)_{16}$. For other Rh carbonyls, the structures differ between neutral and cationic species. While neutral $Rh_2(CO)_8$ and $Rh_4(CO)_{12}$ contain two or three μ_2-CO, respectively, there are exclusively μ_1-CO ligands in the corresponding cations. For $Rh_4(CO)_{12}$, the transition upon ionization from a bridge-bonded structure to one containing only μ_1-ligands is attributed to a destabilization of the HOMO that is involved in the μ_2-CO binding.[137]

While these initial studies have been utilizing the IR free electron laser FELIX, dissociation spectroscopy of metal carbonyls in the range of ν(CO) has also been performed using IR-OPOs. More recently, several studies have extended the spectroscopy of charged gas-phase mononuclear TM carbonyls extensively performed, *e.g.*, by Duncan[198,228] towards binuclear or even larger (up to tetramer) clusters.[44,128,131,132,135,140,142,144,146,229] These measurements, however, are so far limited to the range of ν(CO).

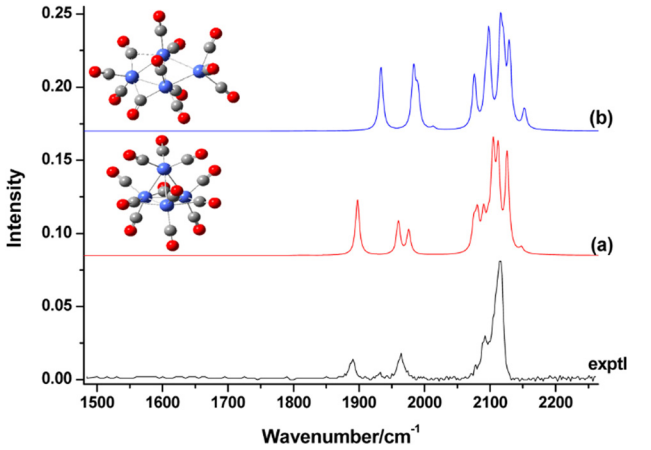

Fig. 24 Experimental and simulated vibrational spectra of $Co_4(CO)_{12}^+$ in the frequency range of ν(CO). The experimental spectrum (bottom line) was measured by monitoring the CO fragmentation channel leading to the formation of $Co_4(CO)_{11}^+$. The simulated spectra (a and b) were obtained from scaled harmonic vibrational frequencies and intensities for the two lowest energy structures calculated at the B3LYP/6-31+G(d) level. Reprinted with permission from ref. 135. Copyright 2014 American Chemical Society.

Fig. 24 shows exemplary the IR-PD spectrum of the cationic saturated cluster carbonyl $Co_4(CO)_{12}^+$.[135] It contains three μ_2-CO in a structure similar to neutral $Rh_4(CO)_{12}$, but is of lower symmetry. A rather unusual CO binding motif is seen in binuclear chromium carbonyls $Cr_2(CO)_n^+$ (n = 7–9).[129] These carbonyls can be structurally characterized as neutral 18e $Cr(CO)_6$ unit in which one CO ligand forms a linear bridge to a $Cr(CO)_{n-6}$ fragment. Within the $Cr(CO)_6$ unit, binding is described by the donation/back-bonding scheme as described before involving σ_s* and π* orbitals of CO, while O-binding to form the bridge involves donation from the CO's σ_p orbital to the lower coordinated Cr atom and π-backdonation into the perpendicular π* orbital of CO. Thereby, CO in the Cr–C–O–Cr bridge acts as 4e donor. The ν(CO) of the linearly bridging CO is found at 1740–1797 cm^{-1}, the stretches of the terminal ligands in $Cr_2(CO)_n^+$ (n = 7–9) are reported between 2044–2174 cm^{-1}.[129]

In addition to these homometallic carbonyl clusters, a number of cationic and anionic hetero-binuclear transition metal carbonyls have been studied containing a combination of late 3d transition metal (Fe, Co, Ni) atoms and a Zn, Cu, group 3 TM (Sc, Y, La), or U atom.[229,230] These complexes involve saturated CO coordinated building blocks which preclude multiple bonding between the metal centers, except for the very low coordinated species $MFe(CO)_3^-$ (M = Sc, Y, La, U). The latter contain a triple bond between the metal atoms, in case of the group 3 TM even an additional 5c–2e bond involving both metal and the carbon atoms.[230c,e]

3.1.3 N_2. Binding mechanism. The N_2 molecule is isoelectronic to CO, as ligand in metal complexes it often behaves similarly. For example, binding to TM centers can be described by the Blyholder model[195] as σ-donation/π-acceptor interaction, however, the donator and acceptor strengths are generally lower than for CO. As a result, TM-(N_2) binding is usually weaker compared to TM-CO and, *e.g.*, for metal surfaces it is known that (for the same surface) N_2 has a significantly lower heat of adsorption and activation energy for desorption compared to CO.[196] With increasing amount of electron transfer towards N_2 the triple bond (in the free molecule) is successively weakened as the anti-bonding π* orbital gets filled with up to four electrons. While towards isolated metal atoms the N_2 unit usually is bound end-on (μ_1), to multiple metal atoms it can bind in bridging geometries of various hapticity.[231]

Complexes with metal atoms. Himmel and Reiher reviewed in 2006 the literature on the interaction of N_2 with metal atoms and metal–atom dimers studied *via* gas-phase as well as matrix-isolation experiments.[231] More recent investigations include a comparison of N_2 and CO binding to Rh^+ in the gas phase[228c] and of N_2 reacted with Ir atoms in cryogenic matrices.[232]

Metal cluster reactivities. The field of N_2 binding and activation by gas-phase metal-containing species, including metal clusters, their hydrides, carbides, oxides, and nitrides, has been reviewed lately by He *et al.*[233] In many cases, the cluster-size dependent reactivity resembles that of H_2.[11b,30e] For example, neutral Nb clusters exhibit a strong anti-correlation of the reactivity with the clusters' ionization energy and DFT calculations for small cluster models like Nb_2N_2 lead to the conclusion that dissociation of the molecular ligand requires charge transfer by transit of an avoided crossing between neutral and ionic potentials. Using a charge transfer model, an inverse correlation is predicted between reactivity and an effective ionization energy which is in agreement with the experimental finding.[24d] More recently, a comparative experimental study of cationic, anionic, and neutral Co clusters has shown an exceptional low reactivity of N_2 towards Co_6^+. A quantum chemical analysis of the system reveals a particular stable open-shell superatomic structure of D_{3d} symmetry for Co_6^+ causing the low reactivity.[234] The often observed increase of reactivity at low temperature points to the initial formation of a weakly bound molecular complex. This forms the precursor to the activated irreversible dissociation into atomic N on the cluster surface, alternatively molecular N_2 can be released again from the molecular complex.[11b]

Vibrational modes and frequencies. In complexes with metals ν(N–N) is usually lower compared to the value observed for free N_2 at 2329.9 cm^{-1} ($\tilde{\nu}_e - 2\tilde{x}_e\tilde{\nu}_e$). Due to the variability in N–N bond order (between 3 and 1), ν(N–N) can be found in a wide frequency range, *i.e.*, for N_2 covered TM surfaces vibrational bands between *ca.* 1050 cm^{-1} and 2250 cm^{-1} are all ascribed to the internal stretch of molecularly chemisorbed N_2.[196] The N–N bond lengths in N_2 complexes and the corresponding ν(N–N) frequencies are anti-correlated and follow Badger's rule.[235] Simple examples for this variation of ν(N–N) with BO are free N_2 (N≡N) with 2330 cm^{-1}, E-diimide (HN=NH) 1529 cm^{-1},[236] and hydrazine (H_2N–NH_2) 1077 cm^{-1}.[237] Nitrido complexes typically have ν(M≡N) frequencies between 900 and 1100 cm^{-1}.[32d]

Anion photoelectron spectra of $Nb_nN_2^-$ (n = 2–8, 10, 11) and $W_nN_2^-$ (n = 6–8) show vibrational progressions of 0.15–0.30 eV (≈1200–2400 cm^{-1}) and 0.2 eV (≈1600 cm^{-1}), respectively, that are assigned to molecularly chemisorbed N_2.[152,153]

IR spectroscopy. Neutral Ru_n clusters (n = 5–16) complexed with one and two N_2 ligands have been investigated using FELIX in the 1300–2300 cm^{-1} range. Their IR-MPD spectra have been interpreted in terms of presence of σ-bonded N_2 that is oriented perpendicular to the cluster surface, *i.e.*, end-on (μ_1) bound.[154] Bands are found 120–220 cm^{-1} below ν(N–N) of free N_2 (Fig. 25), indicating some amount of N–N bond activation. Ru_8N_{2m} and Ru_9N_{2m} appear somehow special, as for Ru_9N_{2m} two ν(N–N) bands are observed, showing the presence of two differently activated dinitrogen species. One of these bands is the lowest ν(N–N) frequency observed in this study, while the maximum of ν(N–N) is observed for Ru_8N_{2m}.[154]

Complexes of cationic Fe, Co, Ni, and Rh clusters with N_2 have been studied by IR-PD in an FT-ICR mass spectrometer.[71b,77i,155–157] In these experiments, the complexes are formed and thermalized under multiple collision conditions in a hexapole ion trap held at 26 K. IR-PD is performed with an OPO/OPA system in a cryogenic (10 K) ICR cell to avoid heating of the cluster complexes due to black body radiation. Complexes with a single N_2 ligand show a similar behavior as seen for the complexes with a single CO. The IR spectra of most complexes contain a comparably narrow band that may be indicative of a single (or structurally very similar) N_2 binding site(s) for a given cluster size. Model calculations (DFT: PBE0/cc-pVTZ) for $Co_{10}N_2^+$, however, show that N_2 binds always in μ_1-geometry and that there is only little variation in ν(N–N) for rather different adsorption sites with shifts of less than 10 cm^{-1}.[77i] With increasing cluster size, ν(N–N) decreases proportional to $1/n_S$ (n_S being the number of surface atoms in the cluster), as observed for CO, see Fig. 26. The frequency change can be explained by the charge dilution model as described before for CO, confirming the similar binding mechanism involving a relevant amount of backdonation into the π* orbitals.

In particular for some larger clusters ($n \geq 10$), multiple bands have been detected in the range of ν(N–N). The shifts between these bands are on the order of up to 50 cm^{-1}, much smaller as between, *e.g.*, μ_1-CO and μ_2-CO. Thus it is concluded that the bands are all associated with μ_1-N_2, but that the ligands are bound to metal atoms of different metal coordination. Bands more shifted to the red have been related to N_2 bound to metal atoms of higher coordination, while more blue-shifted bands have been suggested to indicate N_2 adsorbed on top of low coordinated M atoms.[155,157] These different adsorption sites may be present in a single cluster structure or the reactive sites of different isomers. However, the N_2 reaction kinetics do not show multi-exponential behavior, which would indicate co-existence of multiple metal cluster isomers. On the other side, bi-exponential behavior has been detected, *e.g.*, for Rh_n^+ (n = 6–8, 11, 12) in reactions with NO or N_2O.[238] It is well conceivable that under the cryogenic conditions the N_2 complexes can be trapped in *meta*-stable adsorption geometries, leading to several observable IR bands for a single composition.

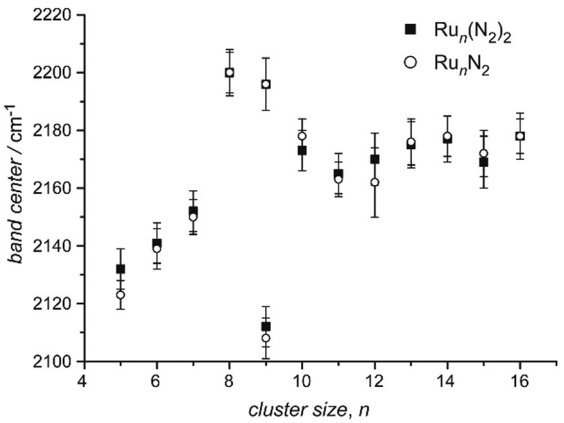

Fig. 25 Band positions of the ν(N–N) vibration in Ru_nN_2 (open circles) and $Ru_n(N_2)_2$ (black squares) complexes (n = 5–16). The error has two contributions: an uncertainty in the wavelength calibration of about 0.2% (~4 cm^{-1}) that applies equally to all values (thus not changing relative peak positions). The second contribution is an estimated part to account for deviations from a Gaussian line profile of the depletion bands. Reprinted with permission from ref. 154. Copyright 2013 American Chemical Society.

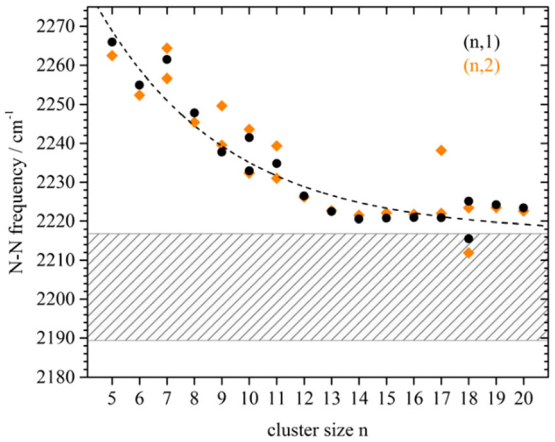

Fig. 26 ν(N–N) of $Ni_n(N_2)^+$ (black dots) and $Ni_n(N_2)_2^+$ (orange diamonds) as function of cluster size (n = 5–20). The dashed line is to guide the eye and corresponds to the charge dilution model for ν(CO), see Section 3.1.2. The shaded area indicates the range of ν(N–N) stretching frequencies on various Ni surfaces. Reprinted from ref. 155, with the permission of AIP Publishing.

Molecular and dissociative adsorption. IR-PD spectra of $Ta_4(N_2)_m^+$ (m = 1–5) formed at cryogenic temperatures (26 K)[113] contain for $n > 2$ broad bands in the 2200–2300 cm^{-1} range that have been tentatively assigned to ν(N–N) of end-on bound N_2 as well as bands in the range of 1443–1475 cm^{-1} that correspond to activated N_2 bound across an edge of the Ta_4 tetrahedron. For $Ta_4(N_2)_m^+$ (m = 1, 2), no bands are observed in the IR-PD spectra leading to the conclusion that in these complexes N_2 is fully dissociated. This behavior is supported by the measured association kinetics as well as DFT calculations revealing submerged activation barriers below the entrance channel that allow for spontaneous cleavage of the first and second N_2 ligand, while the dissociation of a third N_2 molecular is kinetically hindered.[113]

Saturated homoleptic N_2 complexes. The saturated adsorption of molecular N_2 to TM clusters has been used to elucidate metal cluster structures *via* the chemical probe method.[25] Hereby it is assumed that the number of N_2 molecules (or other ligands like CO, H_2O, or NH_3) binding to a metal atom of the cluster's surface

is reflecting its coordination geometry within the cluster. Thus, by counting the available N_2 binding sites for a given structural model and comparison to the experimentally observed saturation stoichiometries, structural information may be gained.

In more recent experiments the kinetics of the stepwise N_2 adsorption on cationic Fe, Co, Ni, Rh clusters at cryogenic temperatures – from the first N_2 ligand up to saturation – has been studied together with the IR spectra of the formed complexes and compared to predictions from DFT calculations. Thereby, information on cluster structure, N_2 coordination geometries, and adsorption induced rearrangements have been obtained.[77i,155–157,239]

Two examples for the evolution of the IR spectra in the ν(N–N) range for $Ni_n(N_2)_m^+$ species with increasing coverage, m, are shown in Fig. 27. $Ni_9(N_2)_m^+$ and $Ni_{13}(N_2)_m^+$ present a rather different behavior, which has been related to their different – 'rough' *vs.* 'smooth' – surface morphologies.[156] The ν(N–N) bands are found in the 2180–2255 cm^{-1} range, thus assigned to μ_1-N_2. In case of $Ni_9(N_2)_m^+$, with increasing coverage, m, a multitude of bands appear, indicative of non-equivalent N_2 binding sites. Further, the adsorption limit of m = 13 exceeds the number of metal atoms in the cluster revealing the presence of geminal N_2 ligands, *i.e.*, several N_2 molecules binding to a single Ni atom. This interpretation is supported by the reaction kinetics, showing individual pseudo-first-order rates for each N_2 addition step and a drop of the rate for the addition of the 9th N_2 ligand, which is supposed to bind in a geminal position.

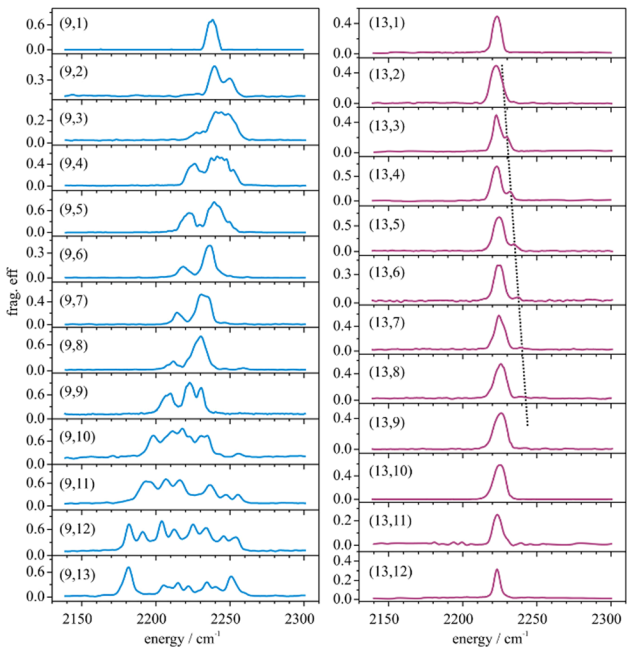

Fig. 27 IR-PD spectra of $Ni_9(N_2)_m^+$ (left) and $Ni_{13}(N_2)_m^+$ (right) at 26 K. Note the variation in the observed band positions and splittings with further adsorption for $Ni_9(N_2)_m^+$ in contrast to the single dominant band for all $Ni_{13}(N_2)_m^+$. The black dotted line highlights a minor peak that has been tentatively assigned to combination bands with N_2 wagging modes. Reprinted with permission from ref. 156. Copyright 2017 American Chemical Society.

The high adsorption capability of the Ni_9^+ cluster with its non-equivalent adsorption sites is suggested to be indicative of a cluster with 'rough' surface. In contrast, the IR spectrum of $Ni_{13}(N_2)_m^+$ hardly changes with coverage, m. Each complex, in essence, shows a single band that is not shifting with m. The rate constants for the complex formation also do not vary with composition. Finally, the saturation limit of m = 12 strongly suggests the presence of an icosahedral structure with its 12 equivalent surface atoms forming a 'smooth' surface.[156]

Further systems. In the cationic boron complexes $B(NN)_3^+$ and $B_2(NN)_{3,4}^+$, the binding between N_2 and B shows much similarity to the binding in transition metal carbonyl complexes.[240] The ν(N–N) bands are found in the 1888–2240 cm^{-1} range, well below ν(N–N) of free N_2. Structures of the complexes are assigned by comparison to results of DFT (B3LYP/aug-cc-pVTZ) calculations. Using an energy decomposition analysis of natural orbitals it is shown that orbital interactions account for 67–78% of the binding energy with the strongest contribution being NN → B σ donation followed by B → NN π backdonation out of occupied p (π) orbitals.

3.1.4 O_2. Binding mechanism. The chemistry of the oxygen molecule in the $^3\Sigma_g^-$ ground state is largely determined by its half-filled, doubly-occupied π* orbitals. Successive one-electron reduction leads to superoxide O_2^- and peroxide O_2^{2-}, while oxidation to O_2^+ requires (in the gas phase) 12.07 eV[241] which can only be achieved with extreme oxidants. Formation of oxide ions O^{2-} *via* dissociation of the O–O bond requires in total transfer of 4 electrons. The molecular orbital scheme of O_2 is shown in Fig. 28. The σ_p and π orbitals are fully occupied, while there is one electron in each of the degenerate π* orbitals leading to a formal bond order (BO) of 2. Increasing the occupation of π* leads to a reduction of BO to 1.5 in superoxide,

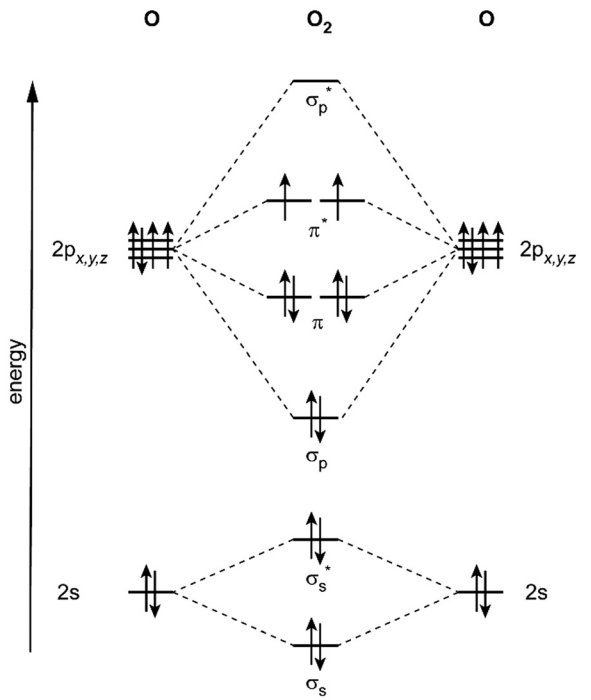

Fig. 28 Molecular orbital diagram for the $^3\Sigma_g^-$ ground state of O_2.

Table 6 Properties of different oxidation states of O_2

	O_2^+	O_2	O_2^-	O_2^{2-}
Name	Dioxygenyl	Dioxygen	Superoxide	Peroxide
Configuration	$\sigma_p^2\pi^4\pi^{*1}$	$\sigma_p^2\pi^4\pi^{*2}$	$\sigma_p^2\pi^4\pi^{*3}$	$\sigma_p^2\pi^4\pi^{*4}$
Formal bond order	2.5	2.0	1.5	1.0
ν(O–O) (cm^{-1})	1872[a,245]	1556.2[a,245]	1072[a,245]	762[b]
r(O–O) (Å)	1.117[245a]	1.208[245a]	1.34[246]	1.50[c]

[a] $\tilde{\nu}_e - 2\tilde{x}_e\tilde{\nu}_e$. [b] Solid K_2O_2, Raman spectrum, ref. 247. [c] Solid Na_2O_2, ref. 248.

O_2^-, and 1 in peroxide, O_2^{2-}. This change goes along with a reduction of the O–O stretching frequency and an increasing bond length, r(O–O). The values given in Table 6 are for the isolated, gas-phase species or from ionic solids, *i.e.*, when there is no (or negligible) covalent interaction between the dioxygen species and other atoms. However, due to hybridization between the dioxygen π* orbitals and d-orbitals on the metal, the M–(O_2) bond can be significantly covalent. Binding modes to a single metal atom can be end-on (η^1) or side-on (η^2), as well as bridging between multiple metal atoms (Fig. 31, right). The η^2 structures are in most cases identified as peroxo complexes, although the exact amount of electron transfer from the metal into the anti-bonding π*(O_2) strongly depends on the system and the O–O bond order takes on a continuous range of values covering both peroxo and superoxo species.[242]

Complexes with metal atoms. Data for complexes of transition metal atoms with O_2 have been extensively reviewed by Gong, Zhou, and Andrews[243] and more lately by Hübner and Himmel.[4b]

Oxide clusters. The aforementioned reviews[4b,243] include data on oxides of single metal atoms, metal dimers, and small multinuclear clusters. The vibrational spectroscopy of gas-phase metal oxide clusters, structural and related reactivity aspects have been further summarized by Asmis, Sauer, and Schwarz.[48e,244]

Metal cluster reactivities. Mass spectrometric reactivity studies of metal clusters with oxygen have been extensively discussed in the review by Luo, Castleman, Jr., and Khanna.[11d] The reaction of O_2 with metal clusters can lead to dramatic changes in the observed cluster-size distributions. For instance, in case of $O_2 + Al_n^-$, under multiple collision conditions, the reactive Al clusters get stepwise oxidized under elimination of neutral Al_2O and degrade until a comparably unreactive, *i.e.*, stable cluster-size is reached. After such oxygen-etching, the distribution is dominated by the least reactive clusters Al_{13}^-, Al_{23}^- and Al_{37}^-, which have electron counts agreeing to shell closings within the jellium model.[11d] Rate constants for the $O_2 + Al_n^-$ reaction show an effect of cluster spin on the reaction and a strong anti-correlation of the rate to the electron binding energies of the Al_n^- odd-n clusters.[249] A more recent study emphasizes the determining effect of the electron binding energies on the activation energies and, therefore, interprets the barrier to arise from charge transfer to the π* orbital of O_2.[250]

In studies of transition metal clusters under single-collision conditions, however, only a smooth change of the reactivity with size is observed with the noteworthy exception of the coinage metal clusters. For neutral niobium clusters, the reaction rates are near the gas-kinetic collision rate, indicating a facile, irreversible adsorption not depending on details of cluster geometrical or electronic structure.[11b,24d] For anionic V, Cr, Co, Ni (and Al) clusters the activation energy for the reaction with O_2 is found to correlate with the electron binding energy. This correlation can be further extrapolated to the bulk properties suggesting a common oxidation mechanism based on electron transfer from the metal towards O_2.[251]

The literature about coinage metal (Cu, Ag, Au) clusters reacting with O_2 (and other molecules) has been evaluated several times more recently.[11d,29d–f,252] Anionic coinage clusters exhibit a pronounced odd/even oscillation of the reaction rate that is anti-correlated with the electron binding energies of the clusters. The even-numbered coinage cluster anions M_{2n}^- are open-shell due to the $d^{10}s^1$ atomic configurations and typically show lower electron binding energies than their neighboring sizes. The unreactive Au_{16}^- is exceptional with its high detachment energy that is due to the stable cage-structure and the degenerate t_2^6 HOMO of the closed-shell Au_{16}^{2-},[37b,253] leading to a triplet ground state for the neutral Au_{16} cage. Due to this strong anti-correlation of reactivity and electron binding energy, it had been concluded early on that spin pairing as well as transfer of a comparably weakly bound electron from the metal cluster to O_2 and formation of a superoxide species might be determining for the binding.[254] Similar relations between electronic structure and reactivity are found for Cu_n^+ (ref. 255), Ag_n^+ (ref. 256), and Cu_n (ref. 254*b* and 257) clusters. The other neutral species as well as Au_n^+ (except for n = 10, ref. 254*a*) are reported unreactive.

Vibrational modes and frequencies. Most diagnostic for dioxygen complexes is ν(O–O) as its value is strongly correlated with the O–O bond order. Calculated Mayer BO in (partly) covalent complexes can take intermediate values compared to the ionic systems listed in Table 6.[242] ν(O–O) values are generally found in the 650–1900 cm^{-1} range and they not only depend on the oxidation state but are also sensitive to the coordination geometry. Details are given in the right part of Fig. 31. There is significant overlap with the frequency range of oxo species, the products of O_2 dissociation. ν(M=O) are usually found in the 800–1050 cm^{-1} range. The stretch vibrations of bridging oxo groups M–O–M are typically between 400 and 900 cm^{-1}.[48c,243]

Low frequency modes related to O_2 ligands have been measured for $Au_2(O_2)_2^+$ at 245 cm^{-1} and 325 cm^{-1} and are assigned to Au–O_2 bending modes of only very weakly activated O_2 with a reported experimental ν(O–O) of 1472 cm^{-1}.[169]

Vibrationally resolved APES. Anion photoelectron spectra of $Cu_6O_2^-$ and $Cu_7O_2^-$ formed by oxidation of the copper clusters with O_2 show vibrational progressions of 150 meV (≈1200 cm^{-1}) and have been assigned to ν(O–O) of adsorbed O_2^-.[165] For $Ag_2O_2^-$ and $Ag_8O_2^-$, progressions of 170 meV (≈1400 cm^{-1}) are seen, respectively, indicative of a molecular adsorbate.[166a] $Au_nO_2^-$ (n = 2, 4, 6) formed by reaction of metal clusters with molecular O_2 yield progressions of about 150–180 meV.[20a,166b,168] Use of atomic O in the production of $Ag_2O_2^-$ and $Au_2O_2^-$ leads to different spectra without vibrational substructure which is attributed to the formation of oxides.[166b] Uncertainties of these APES data

were reported to be 10–20 meV. Vibrational progressions in APES are mostly providing information on the neutral species formed in the electron detachment process with the exception of hot-bands due to the presence of vibrationally excited anions. Therefore, unambiguous assignments are usually only obtained by comparison to calculated data and spectrum modelling, *e.g.*, through Franck–Condon simulation.

O_2 activation by anionic gold clusters. IR-MPD spectroscopy on the species formed in the gas-phase reaction of Au_n^- with O_2 clearly identifies superoxide units in all $Au_{2k}O_2^-$ (k = 2–7, 9, 10) complexes.[43a] In the 700–1400 cm^{-1} range studied, the IR signature of these complexes is a single, comparably narrow peak, centered between 1053 cm^{-1} and 1081 cm^{-1}, depending on cluster size. The only exception is $Au_8O_2^-$ that exhibits a broader signal with its detailed shape varying depending on cluster source and reaction conditions (Fig. 29 and Table S1, ESI‡). This broad signal appears to be composed out of three poorly resolved bands of changing relative intensities and has been related to (i) the well-known co-existence of two isomers for Au_8^-[28d] and (ii) that one of these isomers can bind O_2 in either end-on, η^1 coordination or $\mu_2(\eta^1{:}\eta^1)$ bridging coordination. For the smaller clusters ($k \leq 5$), the measurements have been complemented by DFT calculations (TPSSh/def2-TZVP). Results are shown in Fig. 30. It is concluded that the higher frequency ν(O–O) in the 1060–1075 cm^{-1} range relates to η^1-O_2^-, while the bands at slightly lower frequency ($\sim$1050 cm^{-1}) indicate $\mu_2(\eta^1{:}\eta^1)$-O_2^-.[43a] APES studies on these complexes in conjunction with DFT calculations (PBE0/CRENBL) led, for most sizes, to very similar structural assignments.[258]

O_2 activation by neutral and cationic gold clusters. Although neutral and cationic gold clusters have been considered to be unreactive towards O_2, with the exception of Au_{10}^+,[254a] more recently the formation of such complexes was seen at low temperature (−100 °C).[43b,c] Under these conditions, binding of multiple O_2 molecules is frequently observed, in contrast to the anionic species that only bind a single O_2 unit per cluster.

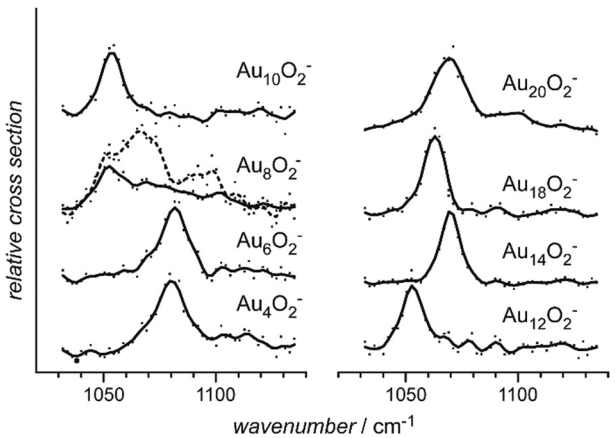

Fig. 29 IR-MPD spectra of even sized, anionic gold cluster-dioxygen complexes, $Au_{2n}O_2^-$. For $Au_8O_2^-$ two traces are shown, one continuous the other dashed and are intended to emphasize the different features observed in the spectra under different source conditions, see text. Reprinted from ref. 43*a* with permission of John Wiley and Sons.

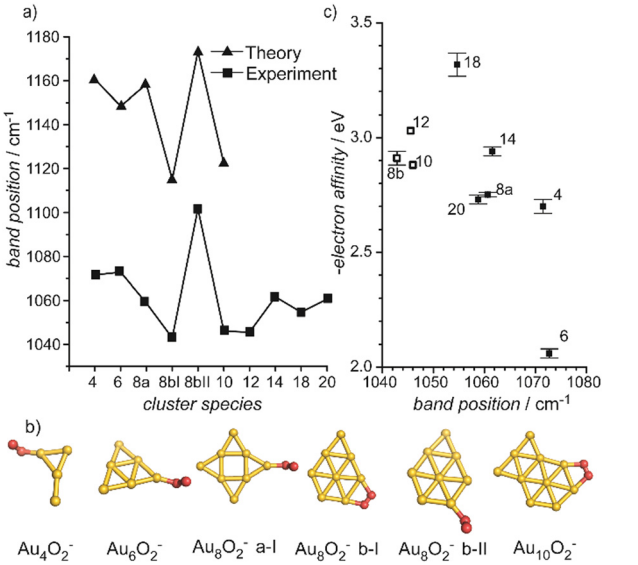

Fig. 30 (a) Comparison of predicted and experimentally observed O–O stretching frequencies in $Au_nO_2^-$. (b) Structures corresponding to the putative global minima and two additional isomers for $Au_8O_2^-$. (c) Correlation between electron affinities of the gold clusters and the experimentally determined ν(O–O) values. The labels indicate which cluster (and isomer) the data refer to. Open squares are $\mu_2(\eta^1{:}\eta^1)$ type binding, closed η^1. Adapted from ref. 43*a* with permission of John Wiley and Sons.

$Au_2(O_2)_{1,2}^+$ has also been reported in a co-adsorption study of O_2 and C_2H_4 onto Au_2^+ at room temperature.[169] For these complexes, ν(O–O) values somewhat below that of free O_2 are found that are slightly decreasing with increasing ligand coverage.

The IR-MPD spectroscopic results for the neutral and cationic complexes are summarized, together with the data for the anionic complexes, in Fig. 31 and Table S1 (ESI‡). The majority of the observed bands fall into the 1450–1550 cm^{-1} range and are assigned to physisorbed or very weakly activated O_2. For complexes of odd-sized neutral clusters, Au_n with n = 7, 9, 11, 21, and even-sized cationic clusters, Au_n^+ with n = 10, 12, 22, all having an odd number of electrons, presence of superoxo ligands has been demonstrated based on the detection of ν(O–O) in the 1050–1070 cm^{-1} range.[43b,c] A special situation is found for the cationic gold tetramer covered with 2–4 O_2 ligands, for which a band appears half-way between ν(O–O) of free O_2 and O_2^- at about 1260 cm^{-1}. Interestingly, a band at the same position can be observed for $Au_4O_2Ar_3^+$, thus it is assigned to a fractionally activated O_2 ligand. It has been concluded that its formation is enabled through solvation of the cationic cluster by the additional, not-activated O_2 ligands or the Ar atoms,[43c] similar to what is seen in reactivity studies of $H_2/N_2/CH_4$ and O_2 with Au_n^+.[182b,260] Overall, these assignments are well in line with the results of accompanying DFT calculations (TPSSh/def2-TZVP). In none of these calculations (partial) electron transfer from O_2 to the gold cluster, *i.e.*, a reaction towards dioxygenyl, is found. This may be understood as the ionization energies of the neutral gold clusters, although amongst the highest of all metals, are with $\leq$9.5 eV[261] still significantly lower than the IE of O_2 (12.07 eV[241]).

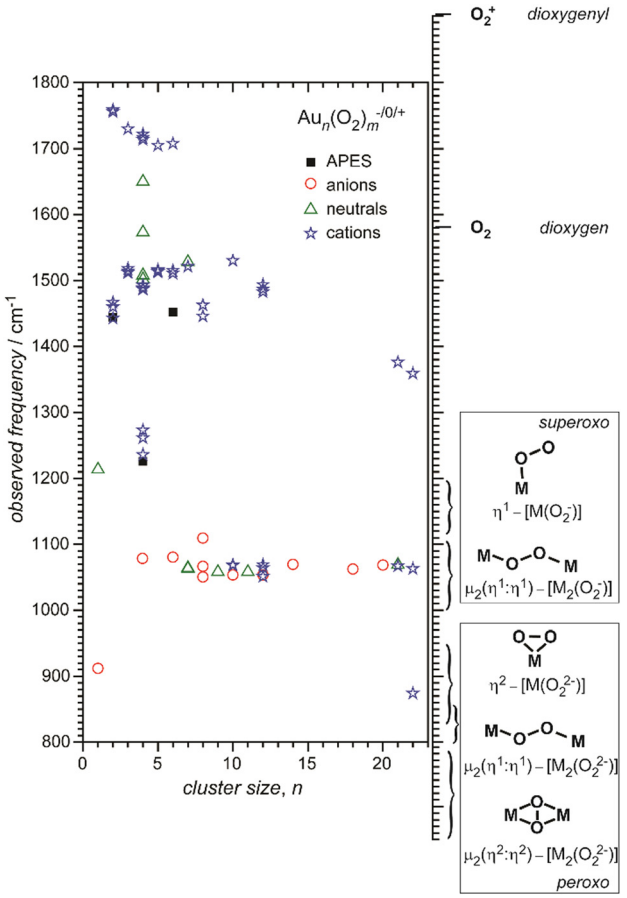

Fig. 31 Left: Experimentally observed vibrational frequencies in complexes of molecular O_2 with gold clusters. Right: Typical frequency ranges of ν(O–O) in different types of dioxygen species (ranges according to Fig. 1 in ref. 259). For the actual assignments done by comparison to results of DFT calculations, see text. Numerical values are given in Table S1 (ESI‡).

Therefore, bands observed blue-shifted from ν(O–O) of free O_2 have been assigned as due to combination bands of ν(O–O) and ν(M–O_2).[43c]

Energetic considerations for the Au–O_2 electron transfer. For the reactivity of the gold cluster anions, the correlation with electron affinity has been substantiated using an electrostatic model and it has been concluded that the electron transfer state will be stable if the electron binding energy of Au_n^- is less than 2.5 eV.[24e] This compares well with the observations for smaller Au_n^- ($n \leq 6$). APES on $Au_nO_2^-$ ($n \leq 7$) reveals that, while the even-sized anionic clusters chemisorb O_2, in the odd-n complexes it is only physisorbed.[20b] For the neutral complexes it is concluded from the results of DFT calculations, that O_2 binding can be followed by a structural change of the gold clusters giving additional stabilization, thus the ability to activate O_2 is connected to the structural flexibility of the gold cluster.[262] The metal cluster cores of Au_nO_2 (n = 7, 9) are then similar to those of the bare cations.[43b] In the cationic complexes, $Au_nO_2^+$, charge separation into O_2^- and a formally doubly charged gold cluster is expected to be energetically rather unfavorable and such reactivity is only observed for Au_{10}^+ and Au_{22}^+. In the di-cation, these clusters reach a closed shell within the spherical jellium model of 8 *vs.* 20 electrons.[43c] In case of adsorption of multiple ligands on cationic clusters, O_2 activation can be facilitated by a stabilization effect through solvation. The stabilization increases with charging and can, thereby, for Au_4^+, Au_{12}^+, and Au_{21}^+, compensate for the energy required to (formally) remove an electron from the metal cluster and transfer it to the O_2 moiety.[43c] DFT calculations (CAM-B3LYP/def2-QZVP) on Au_4^+ covered with 1–4 O_2 moieties can explain the experimentally observed bands, though the suggested structures are not the lowest in energy.[263] For the anionic complexes, $Au_{2k}O_2^-$ (k = 1–7), the O_2 desorption energies have been experimentally determined to be 0.90 ± 0.10 eV for k = 1 and around 0.5 eV for the larger cluster complexes.[41b]

Other metals. For metals other than the coinage metals, dioxo ligands are usually only observed when the metal is already highly oxidized as in $V_3O_8^+$, for which η^2-peroxo and η^2-superoxo isomers have been identified.[66a] Recent examples include $Rh_7O_m^+$ (m = 12, 14), where bands at 1020, 1050, and 1200 cm^{-1} have been assigned to $\mu_2(\eta^1{:}\eta^1)$-O_2^-,[264] and small platinum oxide clusters tagged with Ar, where a band between 1190 and 1220 cm^{-1} is assigned to η^2-O_2^-.[265]

Complexes of the palladium dimer with dioxygen have been characterized in cryogenic Ar matrix.[266] A ν(O–O) value of 875.6 cm^{-1} is assigned to the μ_2-($\eta^1{:}\eta^1$) $Pd_2(O_2)$ complex, while for the mixed oxygen/noble gas atom complexes, $Pd_2(O_2)_2Ng_2$ (Ng = Ar, Xe) with the same O_2 coordination, ν(O–O) has values between 937.8 cm^{-1} and 947.8 cm^{-1} depending on the Ng complexation.

3.1.5 NO. Binding mechanism. The NO molecule shows similarities with CO as well as O_2. The anti-bonding π^* orbital of NO is occupied with a single electron, and the nitrosyl cation NO^+ is isoelectronic with CO. Formally, the NO^+ ligand can interact with a TM center as a two electron donor according to the σ-donation/π-back-bonding mechanism.[267] NO usually coordinates to the metal *via* the N atom forming, as a μ_1-carbonyl analogue, a (nearly) linear M–N–O unit. There exist also stable bridging (μ_2) and face-capping (μ_3) binding geometries similar to the CO ligand. A bent M–N–O unit signifies only weak π-back-bonding and the ligand is then often described as NO^-.

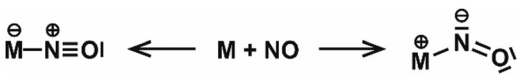

In addition, in TM complexes formed with multiple NO ligands, these radicals can undergo dimerization, forming an O═N–N═O entity that can be bound to the metal in various configurations.[268]

Vibrational modes and frequencies. For NO bound to transition metals, ν(NO) is usually lowered compared to the value of the free molecule of 1876 cm^{-1} ($\tilde{\nu}_e - 2\tilde{x}_e\tilde{\nu}_e$). Similar to the case of metal carbonyls, ν(NO) is used as indication for the coordination geometry with the following approximate ranges: atop (μ_1) 1680–1860 cm^{-1}, bridging (μ_2) 1480–1700 cm^{-1}, face capping (μ_3) 1150–1580 cm^{-1}.[269] However, for surface species structural assignments based solely on ν(NO) have shown to be in certain cases unreliable.[269,270]

Complexes with metal atoms. The data on unsaturated TM nitrosyls, mainly obtained *via* cryogenic matrix isolation IR spectroscopy, has been reviewed by Andrews and Citra in 2002.[271] More recently, cationic NO complexes of a number of late transition (Fe, Co, Rh, Ir) and coinage (Cu, Ag, Au) metal atoms have been studied in the gas phase by IR-PD.[268,272]

Metal cluster reactivities. There have been some rather detailed studies of the reactions of metal clusters with NO as for the other nitrogen oxides like N_2O, see below. The overall observations are similar to the reactions of transition metal clusters with O_2, the high exothermicity of oxide formation may lead to dissociative adsorption, and, in particular at higher coverage, subsequent boil-off of nitrogen, *e.g.*, in the form of N_2 or N_2O is found. Bakker and Mafuné recently have published a perspective on NO reduction by metal clusters.[273] Particularly well studied are reactions of Rh clusters.[273] For cations and anions the reactivity increases relatively smoothly with cluster size and is close to the predictions using the surface charge capture (SCC) model of Kummerlöwe and Beyer.[274] NO dissociation with formation of even oxides is followed by sequential addition of further NO molecules. Oxide formation continues until a cluster size specific critical composition is reached, after that NO molecules adsorb nondissociatively.[238a,275] For $Rh_n(NO)_m^+$ (n = 4–8) complexes formed under thermalizing conditions, temperature programmed desorption finds at elevated temperature loss of intact NO units for n = 4, 5, while for the larger clusters N_2 loss is observed.[276]

For silver cluster cations up to n = 10, there is a pronounced oscillation of the reaction rates for NO complex formation closely mimicking the reactivity pattern with O_2 with the odd-sized, *i.e.*, closed-shell, clusters being much less reactive. The sequential addition of NO proceeds to products of the type $Ag_nO(NO_2)_m^+$ and $Ag_n(NO_2)_m^+$ under release of N_2O.[277] A similar size-dependent reactivity is observed also for anionic Cu clusters.[278]

Molecular and dissociative adsorption. Cationic rhodium cluster complexes with a single NO molecule formed in a flow reactor at room temperature did not show any bands in the IR-MPD spectra obtained in the range of ν(NO).[161] This could indicate either a direct dissociation of the NO on the cluster surface or that such process is induced by the IR heating. Either way, the products would be strongly bound oxide and nitride species that will not fragment in the IR-MPD experiments. However, as described before, co-adsorption of an inert, weakly bound ligand like an Ar atom at low temperature can stabilize molecular entrance channel complexes, act as messenger for the IR excitation of non-dissociable species, but may also change the energetic order of isomers.[63a,66,265] Such Ar tagging method has been used to study the products of the reaction of Rh_n^+ (n = 6–16), Rh_nTa^+ (n = 2–8), and Ir_n^+ (n = 3–6) with NO at low temperature (173–263 K).[158a,b,159,160,163] In contrast to the room temperature studies one finds, except for the Ta doped clusters, bands that are related to molecularly bound NO.

For Rh_nNOAr^+ (n = 6–16), bands between 1810 cm^{-1} and 1825 cm^{-1} are assigned to $\nu(\mu_1\text{-NO})$ of linearly bound NO.[158a] In case of n = 7, 12–14, an additional band at about 1600 cm^{-1} signifies the presence of another isomer containing μ_2-NO. Interestingly, presence of μ_1- and μ_2-bound CO had been concluded before also for Rh_7CO^+, while other sizes in the n = 5–34 range show exclusively μ_1-CO.[73a] The IR spectra of Rh_nNOAr^+ show in the low frequency range several more bands than predicted for cluster complexes containing molecular NO and it is concluded, based on a comparison with the results of DFT calculations, that there must be a minor fraction of clusters with dissociatively bound NO present. The relative amount of molecular *vs.* dissociatively bound NO has been estimated by assuming that the experimental IR-MPD intensities scale linearly with the calculated IR intensities. For n = 6–10, fractions of between a few percent and up to 21% are assigned to isomers containing dissociatively bound NO, depending on the cluster size n.[158a] For Rh_6NO^+, structural isomers and different spin states have been screened by DFT calculations, finding a large number of low energy isomers, containing both molecularly and dissociatively adsorbed NO.[158c] This structural flexibility may be linked to the rich chemistry observed for Rh_6^+ including a distinctly bi-exponential kinetics for the addition of the first NO molecule.[238a,b] For complexes with multiple NO ligands, like $Rh_{6,7}(NO)_{1-3}Ar^+$, NO occupies different adsorption sites and, in part, undergoes dissociation depending on the coverage.[159] Replacement of a Rh atom in the cluster by Ta changes the chemistry completely.[163]

All complexes of the formal composition $Rh_nTaNOAr^+$ (n = 2–8) exhibit an intense feature in the 950–1000 cm^{-1} range (Fig. 32). This band is assigned to ν(Ta–O) and bands between 450 and 800 cm^{-1} to vibrations of nitride species with the N atoms bound in bridging or hollow sites. No bands corresponding to molecular NO ligands are observed. The experimental spectra are compared to predictions from DFT calculations and, *e.g.*, for Rh_5TaNO^+, the calculated spectrum of the ground state isomer agrees very well with the experimental spectrum obtained for $Rh_5TaNOAr^+$. The observation of complete dissociation of NO on Rh_nTa^+ is in line with the prediction of a significantly lowered barrier for the dissociation on the Ta doped species compared to the bare Rh cluster.[163] While Rh_nTa^+ clusters are examples of the extreme case of only dissociative NO adsorption and on pure Rh_n^+ only a minor amount of dissociation has been found, Ir, the heavier homologue of Rh, appears to be an intermediate case.[158b] The spectrum of Ir_6NOAr^+, for instance, contains a band at 1805 cm^{-1} (later a value of 1817 cm^{-1} was reported[160]) readily assigned to $\nu(\mu_1\text{-NO})$ and several more features in the 500–1000 cm^{-1} range that are indicative of dissociative NO adsorption. The latter amounts to a fraction of about 50% as determined from the relative band intensities and the attainable maximal depletion by exciting $\nu(\mu_1\text{-NO})$.

Comparing the calculated binding energies for O atoms to Rh_6^+, Ir_6^+, and Rh_5Ta^+, a significant increase of its value is found (−3.55 eV, −4.74 eV, −5.89 eV), causing the change in the reaction behavior. In contrast, the binding energies for the N atoms are hardly changing (−6.94 eV, −7.13 eV, −7.01 eV) for the different metal clusters.[158b] Smaller iridium clusters, Ir_n^+ (n = 3–5), show a similar behavior with clearly assignable features characteristic for molecular and dissociative adsorption of NO in comparable fractions.[160] The values of $\nu(\mu_1\text{-NO})$ monotonically decrease

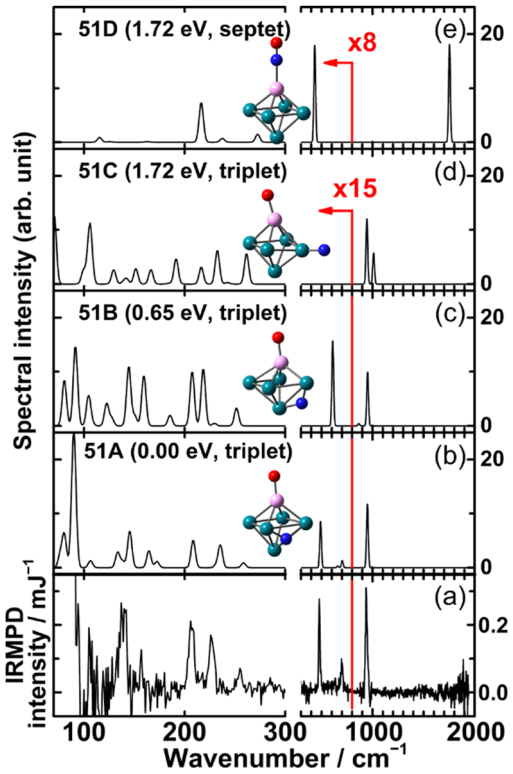

Fig. 32 (a) IR-MPD spectrum for $Rh_5TaNOAr^+$ and (b–e) DFT calculated vibrational spectra of stable isomers of Rh_5TaNO^+. At frequencies below 800 cm^{-1}, the experimental and calculated spectra are multiplied by the indicated factors to enhance visibility of the relatively weak bands at lower wavenumbers. For each structure (Rh dark-cyan, Ta pink, N blue, and O red), the relative formation energy and spin multiplicity are shown in parentheses. Reprinted with permission from ref. 163. Copyright 2019 American Chemical Society.

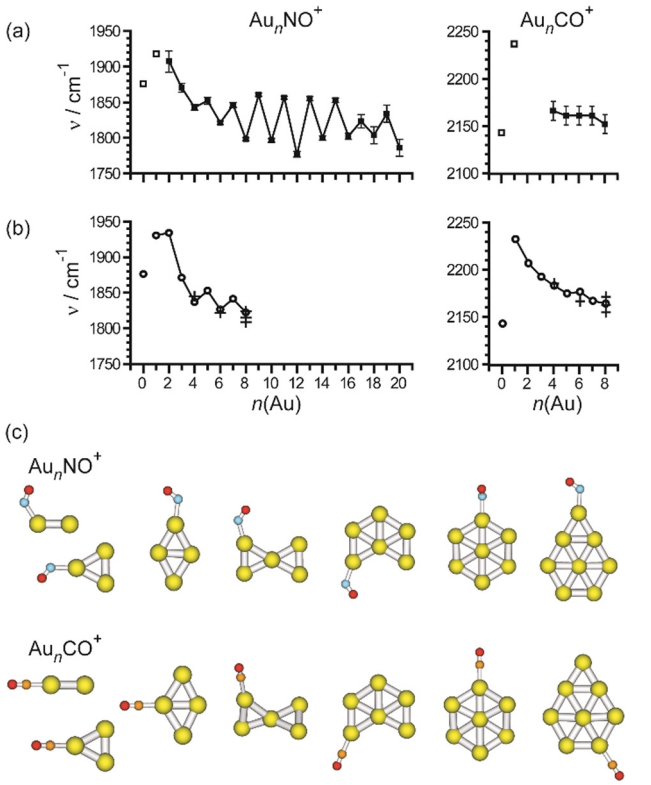

Fig. 33 Vibrational frequencies and structures of Au_nNO^+ and Au_nCO^+. (a) Experimentally determined frequencies for ν(NO) and ν(CO). Empty squares indicate the values for the free ligands and atomic gold complexes measured in noble gas matrices.[206b,279] (b) Calculated frequencies for ν(NO) and ν(CO) (DFT: B3LYP/TZVP). The frequencies of the lowest energy structures are shown as circles. Crosses mark the frequencies of low-lying structures with the ligand bound in alternative atop positions. The calculated structures of the lowest energy complex are depicted in (c). Reproduced from ref. 149 with permission from the PCCP Owner Societies.

with the size of the cationic clusters from 1863 cm^{-1} for n = 3 to 1817 cm^{-1} for n = 6 which is explained by an increased π-backdonation in the larger clusters. This is in line with the charge dilution model discussed before for carbonyl complexes, see Section 3.1.2.

For comparison, neutral Pt_nNO (n = 4–18) complexes formed at room temperature exhibit IR-MPD bands in the 1775–1792 cm^{-1} range, indicative of μ_1-NO, and there appears no clear size dependent pattern for ν(NO). The only exception is $Pt_{10}NO$ with a slightly more red-shifted ν(NO) of 1760 cm^{-1}. By excitation of ν(NO), all species can be depleted by 85–100% which gives upper limits for the abundance of dissociatively bound NO in these complexes of 0–15%.[161]

For NO bound to cationic Au_n^+ (n = 2–20) clusters, a size-dependent oscillation in ν(NO) is seen, with the open-shell, even-sized clusters having ν(NO) at around 1800 cm^{-1}, while the closed-shell, odd-sized-clusters have such a band about 50 cm^{-1} higher, see Fig. 33.[149] Complexes of the cationic gold clusters with CO do not show a similar size-dependent oscillation of ν(CO). This behavior is readily understood from an analysis of the binding situation based on DFT calculations. In case of the NO complexes, one π* orbital forms the HOMO (or SOMO), whereas for the CO complexes both the HOMO and the LUMO are metal centered orbitals. For the CO ligands, the π* orbitals are significantly higher in energy and barely interact with filled metal centered orbitals of the gold cluster. For the NO complexes, the HOMO is singly occupied for odd-sized Au_nNO^+ and doubly occupied for the even sizes, *i.e.*, NO acts as an electron acceptor. As a consequence, the formal N–O bond order is oscillating between 2.5 and 2. This oscillation in the bond strength is observed in the vibrational spectra.[149] Au_2NO^+ forms an exception, with the NO formally acting as electron donor. The HOMO of Au_2NO^+ is mainly Au centered and the vacated π* orbitals of NO form LUMO and LUMO+1 of the complex. Thereby for this sized cluster the binding situation is more similar to the CO complexes. The formal N–O bond order in Au_2NO^+ is 3, explaining the significantly higher ν(NO). For the negatively charged Au_4NO^-, ν(NO) is measured at 1485 cm^{-1}.[162] The structure is assigned, by comparison to the results of DFT calculations, to NO μ_1-bound to a *y*-shaped Au_4 cluster. The strong red-shift of ν(NO) into the range typical for μ_3-NO is the result of a significant larger amount of back-donation in the anion compared to the cation. For the complex of Au_4^- with two non-dissociatively bound NO molecules, the calculated most stable isomers contain an ONNO unit.

Table 7 Summary of experimental studies on the vibrational spectroscopy of gas-phase metal cluster complexes with triatomic molecules

Molecule	Metal	System	Cluster sizes (n)	Coverage (m)	Method[a]
H_2O	V	$V_n[H_2O]_m^+$	3–18	1–3	IR-MPD[280]
	Fe	$Fe_n[H_2O]_m^+$	6–15	1	IR-MPD[281]
	Co	$Co_n[H_2O]_m^+$	6–20	1	IR-MPD[282]
	Pt	$Pt_n[H_2O]_m^+$	3	1–4	IR-PD[283]
CO_2	Co	$Co_n[CO_2]_m^-$	3–17	1	IR-MPD[284]
	Pt	$Pt_n[CO_2]_m^-$	4–7	1	IR-MPD[285]
	Cu	$Cu_nC_{1,2}[CO_2]_m^-$	3–10	1	IR-MPD[145,286]
	Cu	$Cu_n[CO_2]_m^+$	4–25	1,2	IR-MPD[287]
OCS	Au	$Au_n[OCS]_m^+$	3–10	1	IR-MPD[288]
N_2O	Co	$Co_n[N_2O]_m^+$	1–5	1	IR-MPD[289]
	Rh	$Rh_n[N_2O]_m^+$	4–8	1	IR-MPD[73b,290]
		$Rh_nO_{0,1}[N_2O]_m^+$	5	1	IR-MPD[291]
	Pt	$Pt_n[N_2O]_m^+$	1–8	1	IR-MPD[292]
	Au	$Au_n[N_2O]_m^+$	3–7	1	IR-MPD[289]
NO_2	Au	$Au_n[NO_2]_m^-$	4	1	IR-MPD[162]
HCN	Mg	$Mg_n[HCN]_m$	2–6	1	HeIRSS[293]
	Cu	$Cu_n[HCN]_m$	1–3	1	HeIRSS[294]
	Zn	$Zn_n[HCN]_m$	1–4	1	HeIRSS[295]

[a] IR-MPD – infrared multiple photon dissociation using IR-FELs; IR-PD – infrared photo dissociation employing OPO/OPA or DFM/OPA lasers as IR sources; HeIRSS – Infrared laser Stark spectroscopy in superfluid He droplets.

The experimental IR-MPD spectrum of $Au_4(NO)_2^-$ is unfortunately rather poor, but it seems not to be in conflict with the theoretically predicted structure.[162]

3.2 Triatomic ligands

3.2.1 H_2O. Binding mechanism. Single water molecules bind to TM atoms usually *via* the O 2p lone pairs forming a dative bond. Upon interaction of H_2O with the metal, O–H bonds can be broken homolytically or heterolytically leading to hydroxy or oxo and hydrido species. Multiple H_2O molecules binding to metal centers have a strong tendency to cluster and to form H-bonded water networks.

Vibrational modes and frequencies. The free water molecule has three internal vibrational modes, the symmetrical and antisymmetrical O–H stretches, ν_s and ν_{as} at 3657 cm^{-1} and 3756 cm^{-1}, as well as the bending (scissoring) mode δ_s at 1595 cm^{-1}.[296] The latter is very indicative for the presence of an intact water molecule in a complex and can be used to distinguish between molecular and dissociative water adsorption. For hydroxy species, the M–O–H bending mode is typically found below 1200 cm^{-1}, vibrations related to oxo groups even lower.[32d] When chemically bound, six additional "external" vibrational modes exist stemming from the frustrated rotations and translations. The assignments of these modes appear not always fully straightforward. Bands for water adsorbed on surfaces and in complexes have been assigned in the approximate ranges of 650–900 cm^{-1} to the H_2O rocking mode, ρ_r, 450–650 cm^{-1} to the wagging mode, ρ_w, and 310–490 cm^{-1} to the M–OH_2 stretch, ν(M–O).[32d,297]

Complexes with metal atoms. The hydration of metal cations, structures, water activation within such complexes leading to release of H_2, and other reactions have been reviewed by Beyer.[298] In 2005, the application of IR-PD in the study of gas phase metal ion complexes including H_2O, CO_2, NH_3, and other molecules as ligands has been summarized by Duncan.[299] Due to the relevance, *e.g.*, for solvation processes or the electrochemical water splitting, the study of hydrated metal cations is a relative active field of research. Examples of more recent studies include hydrated Zn(II) cations $Zn(H_2O)_n^{2+}$ (n = 6–12),[300] hydrated and Ar tagged Zn(I) cations $Zn(H_2O)_n^+$ (n = 1–4),[301] larger $Zn(H_2O)_n^+$ (n = 2–35) complexes,[77l] the evolution of solvation shells in $[Au(H_2O)_nAr_x]^+$ (n = 1–8; x = 1, 2),[302] hydrated Cu(II) complexes $Cu(H_2O)_n^{2+}$ (n = 6–12),[303] or an analysis of the role of the noble gas tag with regard to vibrational frequency perturbations in $Co(H_2O)Ng^+$ (Ng = He, Ne, Ar) complexes.[67] The experimental investigations are often limited to the stretching modes of free and hydrogen bonded O–H, *i.e.*, the range of ~3000–3800 cm^{-1}.

Metal cluster reactivities. Adsorption of water on, *e.g.*, Fe, Co, and Ni clusters has been studied aiming for cluster structure elucidation, similar to the titration of surface sites using N_2 or H_2.[25,304] Mass spectra of neutral TM clusters reacted with water suggest non-dissociative attachment and it is concluded that the observed product distribution is thermodynamically controlled. However, for Fe clusters, a strong correlation between the average number of water molecules binding to a metal cluster of given size, n, and the reactivity towards H_2, that is assumed to be kinetically controlled, is found.[304a] Using a similar experimental set-up, a more recent study of the reaction of V_n^+ with water under thermalized conditions finds extensive oxide formation through dissociative adsorption of water molecules for n = 3–30 that is explained by a high V–O binding energy for $n \geq 3$.[305] On the other hand, extrema in the rate constants of the neutral V clusters for n = 10, 13, 16 have been related to superatomic orbital structure.[306]

Molecular and dissociative adsorption. Complexes of cationic vanadium clusters with water, $V_n(H_2O)_m^+$ (n = 3–18, m = 1–3), formed under thermalized conditions in a fast-flow reactor, have been characterized by IR-MPD in the range of the water bending mode, δ_s.[280] Consistent with the reactivity studies mentioned above, the mass spectra contain a significant amount of oxide and dioxide species, probably formed through water reduction under release of H_2. However, all water complexes (except for n = 5 that was of too low abundance to analyze) exhibit a band near 1600 cm^{-1} (Fig. 34), readily assigned to δ_s, proving the presence of a molecular water ligand. By excitation of this band, depletion by 20–60% is observed which sets a lower limit for the fraction of species containing an intact water molecule. For small cluster cations, δ_s is blue-shifted compared to free water. This can be explained by charge transfer between the metal cluster cation and the water molecule leading to an expansion of the H–O–H bond angle which finally results in a small blue shift in the bending mode.[307] Complexes containing multiple water molecules have their resonances only slightly red-shifted compared to those with a single ligand indicating independent absorption of the ligands without hydrogen bonding.[280]

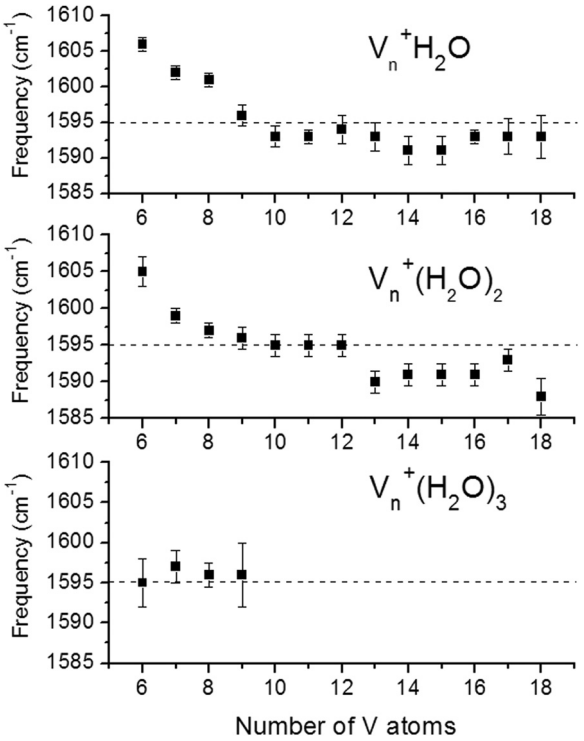

Fig. 34 Size dependence of the water bending mode in $V_n(H_2O)_m^+$ (n = 3–18, m = 1–3) compared to δ_s of the free water molecule at 1595 cm^{-1} (dashed line). Reprinted from ref. 280. Copyright (2004), with permission from Elsevier.

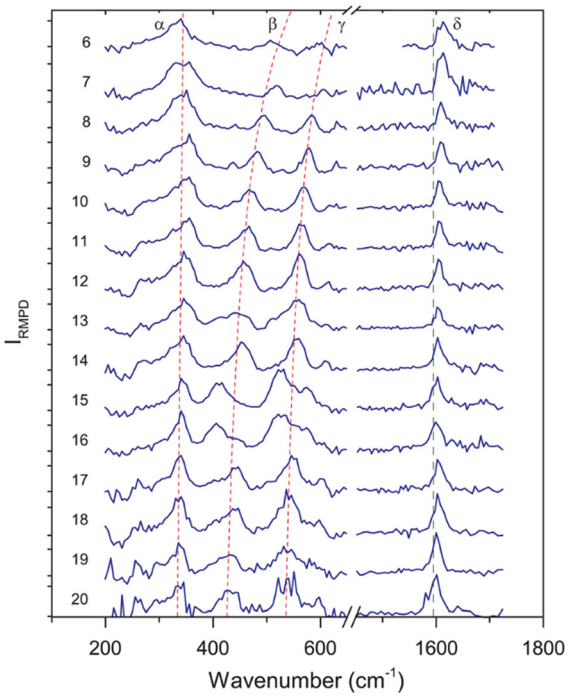

Fig. 35 IR-MPD spectra of $Co_nH_2O^+$ (n = 6–20) complexes in the 200–1700 cm^{-1} spectral range. The size dependence of three low-frequency bands is indicated by the red dashed lines; the frequency of the free water bending mode around 1600 cm^{-1} is indicated by the green dashed line. Reprinted with permission from ref. 282. Copyright 2015 American Chemical Society.

Cationic cobalt clusters complexed with single water ligands have been studied by IR-MPD in the 200–1700 cm^{-1} range, see Fig. 35.[282] Similar to the V clusters, for all $Co_nH_2O^+$ (n = 6–20), an intense band (δ) close to the position of the free H_2O bending mode is found that shifts nearly linear in frequency from 1614 cm^{-1} for the smallest size, n = 6, to 1590 cm^{-1} for n = 23. For all sizes, at least three more bands between 300 and 600 cm^{-1} are detected. The lowest frequency band, α, at about 340 cm^{-1} shows a very small red-shift with increasing size of only a few cm^{-1}, while the shifts for bands β and γ are much more pronounced from about 600 cm^{-1} to 540 cm^{-1} and 520 cm^{-1} to 410 cm^{-1}, respectively. The position (and intensity) of the water bending mode is well reproduced by DFT (OPBE/TZVP) calculations of model structures for n = 6, 9, 13 but the agreement is less good for the lower-frequency features.[282] Comparing the experimental band positions with the general ranges of the external water ligand modes given above, bands α, β, γ are tentatively assigned to M–OH_2 stretch, the rocking mode, ρ_r, and the wagging mode, ρ_w, respectively. Very similar features are observed in the IR-MPD spectra of $Fe_nH_2O^+$ (n = 6–15), however, the intensity of the low-frequency modes α, β, γ varies strongly with size, which is taken as indication for the presence of, in part, dissociated water ligands.[281]

Water binding to cationic platinum trimer clusters has been characterized by IR-PD in the 3000–3800 cm^{-1} range and compared to results of DFT calculations. All complexes, $Pt_3[H_2O]_mAr^+$ (m = 1–3) and $Pt_3[H_2O]_4^+$, exhibit two intense bands at about 3600 and 3700 cm^{-1} corresponding to O–H stretches, ν_s and ν_{as}. The band positions point to non-dissociative binding of all water molecules to Pt atoms *via* the O atom sides.[283]

3.2.2 CO_2. Binding mechanism. CO_2 in the ground-state is a rather unreactive non-polar molecule. It can (weakly) physisorb on metal centers, *e.g.*, by charge–quadrupole interaction in an end-on η^1-O arrangement (Fig. 36). The chemical binding and activation of CO_2 by metal centers usually is connected with its reduction. The HOMO of CO_2 is a fully occupied $1\pi_g$ orbital. One electron reduction leads to a partial filling of the LUMO, that corresponds to the $2\pi_u$ orbital in the linear structure of neutral

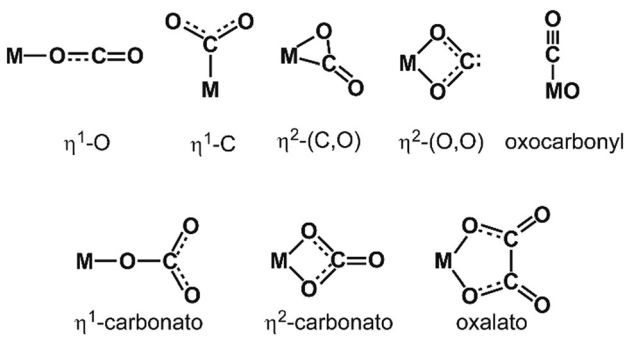

Fig. 36 Coordination types in metal-CO_2 complexes. The species depicted in the lower line require reaction of at least two CO_2 ligands with the metal. Adapted from ref. 308.

CO_2 and, as consequence, symmetry breaking and formation of a bent O=C=O$^-$ entity bound to the metal. The isolated CO_2^- anion is metastable and has a negative adiabatic electron affinity of about −0.6 eV.[309] It can be stabilized, *e.g.*, by C-binding to a metal center forming a metalloformate M–CO_2^- or undergo further reactions like dissociation into O and CO, or C–C coupling, for instance forming oxalate $^-O_2C–CO_2^-$. The coordination and surface chemistry of CO_2 has been reviewed extensively before[310] and Weber summarized the gas-phase ion chemistry of CO_2 with respect to its activation.[308,309]

Vibrational modes and frequencies. The change of molecular symmetry and orbitals upon binding of CO_2 to metal centers is well reflected by its internal vibrational modes. Infrared active in the unperturbed linear molecule are the antisymmetric stretch ν_{as} at 2349 cm^{-1} and the degenerate bend δ at 667 cm^{-1}. The symmetric stretch ν_s at 1333 cm^{-1} is only Raman active and its Fermi resonance with the overtone of the bend, 2δ, leads to a splitting into two modes at 1285 cm^{-1} and 1388 cm^{-1} in the Raman spectrum of gaseous CO_2.[296] Although only metastable, the anion CO_2^- can be stabilized by solvation, *e.g.*, in cryogenic noble gas matrices, and its IR spectrum has been determined in Ne. Due to the bent configuration, all three vibrational modes become IR active. The antisymmetric stretch ν_{as} of CO_2^- is strongly red-shifted compared to free CO_2 at 1658.3 cm^{-1}. The symmetric stretch ν_s is found at 1253.8 cm^{-1} and the bend δ at 714.2 cm^{-1}.[311] Fig. 37 gives an overview on the vibrational features of other relevant species and a comparison with the values for gas-phase CO_2, CO, and CO_2^-. Only little experimental data is available below 900 cm^{-1}, therefore for most species values, *e.g.*, for the CO_2 bending mode δ, are missing.

Complexes with metal atoms. The coordination chemistry of CO_2 in atomic complexes is rich of different structural elements, see Fig. 36. It reaches from weakly activated (or only physisorbed) η^1-O ligands that are the prevailing ligand type in cationic complexes with low CO_2 coordination, over metalloformates (η^1-C), different carbonato species to oxalate ligands.[308,309] For pure metal atoms or clusters, the formation of carbonato or oxalato ligands needs reaction of at least two CO_2 units with a metal center. Activation of CO_2 requires electron transfer towards CO_2 and is therefore particularly observed for electron-rich, *i.e.*, anionic, metal centers or on metal cations that are prone to convert into higher (positive) oxidation states. The electron transfer is often observed to be solvent induced, *i.e.*, it sets in only after a certain number of ligand molecules is bound to the metal center.[228a,312] IR spectra of Al–CO_2 and Mg–CO_2 have been obtained with rotational resolution in He droplets, revealing for both systems the presence of two isomers, a linear and a T-shaped one.[313]

Metal cluster reactivities. Reactions of CO_2 with small anionic Ni group metal (Ni, Pd, Pt) clusters had been studied by Hintz and Ervin.[314] Noteworthy, Pd and Pt showed sequential addition of CO_2 units, while for Ni formation of products with composition $Ni_nO(CO_2)_m^-$ is found. O atom transfer from CO_2 (as well as from O_2 and N_2O) towards small Fe_n^+ (n = 2–4) clusters had been reported also by Gehret and Irion[315] and, as further example, the cross sections for the oxygen atom transfer reactions $M_n^+ + CO_2 \rightarrow M_nO^+ + CO$ (M = Fe, Cr; n = 1–18) as function of collision energy have been determined by Griffin and Armentrout,[316] finding a bimodal energy dependence. This behavior can be explained either by a change from a spin-forbidden pathway at low energy, *e.g.*, for the dissociation $CO_2(^1\Sigma_g^-) \rightarrow CO(^1\Sigma^+) + O(^3P)$, to spin-allowed pathways at higher energy, or a precursor mediated activated adsorption.[316a] Recently, the reactivity of anionic coinage clusters with CO_2 has been studied using DFT calculations, pin-pointing the importance of frontier orbital symmetry for forming activated $(M_n–CO_2)^-$ complexes containing partially covalent M–C bonds and a fully delocalized anionic charge.[317] Activation of CO_2 may also be reached by light-induced electron transfer as predicted, *e.g.*, for transition metal doped aluminum clusters.[318]

Molecular and dissociative adsorption. For CO_2 bound to cationic copper clusters, Cu_n^+ (n = 7–13), the experimental IR-MPD spectra of all sizes studied reveal bands at around 650 cm^{-1}, 1274 cm^{-1}, and 1378 cm^{-1},[145] which are close to the values of the bending mode δ and the Fermi dyad for the free CO_2 molecule. Another band detected at nominally 1185 cm^{-1}

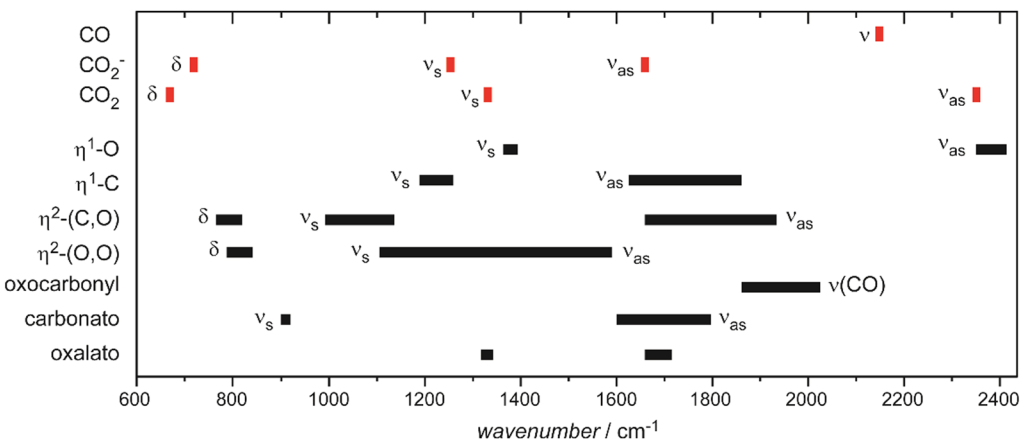

Fig. 37 Characteristic vibrational frequencies of metal–CO_2 complexes and possible products of their intramolecular CO_2 activation. Data in part after ref. 308.

has been assigned to be caused by a small fraction of 2nd harmonic light in the IR beam and thus corresponds to an absorption at 2370 cm^{-1}, close to ν_{as} of free CO_2. These copper complexes, therefore, contain physisorbed, nearly unperturbed CO_2 ligands. Unfortunately, one cannot directly compare to experimental data for anionic (or neutral) Cu clusters, however, CO_2 bound to anionic clusters of the composition CCu_n^- (n = 6–10) and $C_2Cu_n^-$ (n = 3–8) has been studied.[145,286] In short, all these clusters activate CO_2 and a pattern of three peaks around 720 cm^{-1}, 1150 cm^{-1}, and 1630 cm^{-1}, characteristic of a bent CO_2^- unit, and/or an intense band around 2000 cm^{-1}, indicating formation of CO, are seen. The assignment to carbonyl species is supported by separate experiments for CO bound to carbon doped Cu clusters, CCu_n^- (n = 4–10), that locate the carbonyl stretch ν(CO) in the anionic carbonyls at around 2020 cm^{-1}. For some sizes both vibrational patterns, for CO_2^- and CO, are present, suggesting co-existence of corresponding isomers.[286]

Also anionic cobalt clusters with $n \geq 7$ have been found to dissociate CO_2 under formation of adsorbed CO and oxide species.[284] The carbonyl ligands lead to pronounced IR bands for all $Co_nO(CO)^-$ (n = 7–13) complexes at about 1870 cm^{-1}, see Fig. 38. This is very close to ν(CO) of the corresponding pure cobalt carbonyls $Co_n(CO)^-$ that exhibit such a band between 1860 cm^{-1} and 1881 cm^{-1}, depending on their size.[134] These anionic carbonyl and oxocarbonyl species show a slight increase of ν(CO) with cluster size that can be rationalized by the charge dilution model, as described before. DFT calculations for $Co_7[CO]_2^-$ revealed that the dissociation of CO_2 upon adsorption into CO and O is energetically favorable and the experimental IR spectra agree to the predictions for the oxocarbonyl $Co_7O(CO)^-$ isomers.[284]

As a last example, the activation of CO_2 by small anionic platinum clusters Pt_n^- (n = 4–7)[285] is discussed. IR-MPD spectra of $Pt_n[CO_2]^-$ have been obtained in the 400 cm^{-1} to 2100 cm^{-1} range and analyzed by comparison to the results of DFT calculations. The findings for the smallest sized complex, $Pt_4[CO_2]^-$, are summarized in Fig. 39. In the spectral range investigated, three bands are seen at 800 cm^{-1}, 1130 cm^{-1}, and 1600 cm^{-1} that are assigned to bend (δ), symmetric stretch (ν_s), and antisymmetric stretch (ν_{as}) vibrations of chemically bound CO_2^-. In marked contrast, these bands are essentially absent in the spectra of the larger cluster complexes. Instead, for $n > 4$, an intense new band is observed in the 1950–2000 cm^{-1} range.[285] This agrees well with the ν(CO) values of 1940–1950 cm^{-1} determined for CO bound to anionic Pt clusters of similar size.[139] Results of DFT calculations reveal that for all sizes studied the dissociation of CO_2 in CO and O is energetically favorable, only for $Pt_4[CO_2]^-$, the activated molecular complex is stabilized through a comparably high barrier of 1.3 eV for breaking the OC–O bond.[285]

3.2.3 OCS. Carbonylsulfide, OCS, is isostructural as well as isoelectronic to CO_2 and resembles it in many chemical aspects. One obvious difference is the lower symmetry resulting in more structural flexibility as a ligand, allowing for, *e.g.*, S- and O-bound complexes. Further, metal sulfides are often stronger bound compared to the corresponding oxides which facilitates S–CO dissociation. The IR active vibrational fundamentals of isolated $^{16}O^{12}C^{32}S$ are ν(CO) at 2062.22 cm^{-1}, ν(CS) at 858.95 cm^{-1}, and δ(OCS) at 520.41 cm^{-1}.[296]

There exist only comparably little data on the metal coordination chemistry of OCS[319] or its interaction with metal surfaces.[310c] In many cases the reaction proceeds under release of CO and formation of metal sulfides. This is explained by the $d\pi \rightarrow \pi^*$ backdonation in TM-OCS complexes leading to a weakening of the S–CO bond and its subsequent breakage.[319] Sulfide formation is also apparent in the few experimental studies of OCS, interacting with metal clusters.

In case of cationic clusters of platinum and rhodium, Pt_n^+ ($n \leq 15$) and Rh_n^+ ($n \leq 25$) only complexes of the composition M_nS^+ could be observed suggesting rapid dissociative adsorption of OCS even when the complexes are formed at low temperature (−100 °C).[288]

Complexes with neutral silver clusters formed at ~77 K show an enhanced abundance for Ag_nOCS containing an even number of Ag atoms. Photodissociation of these complexes in the UV leads to desorption of OCS in case of the even-sized Ag clusters, while odd-sized clusters show an additional Ag_nS photolysis product.[320] The wavelength dependence of the dissociation resembles that for the bare Ag clusters, such that an initial excitation localized at the Ag cluster is suggested.

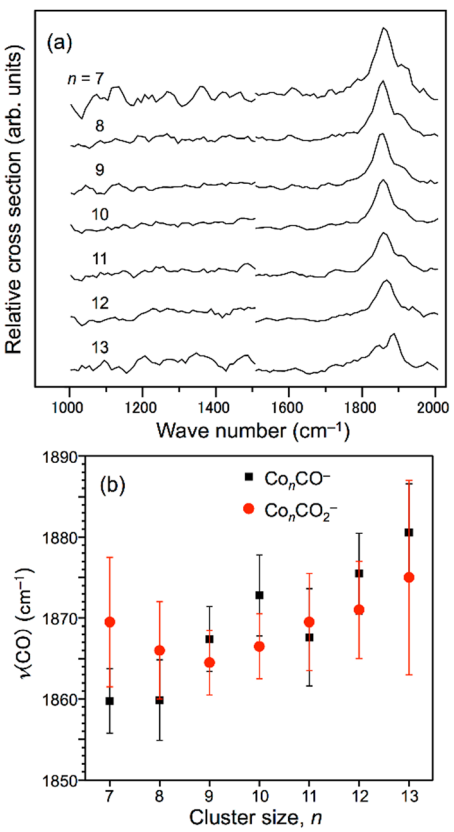

Fig. 38 (a) Infrared multiple photon dissociation spectra of $Co_nCO_2^-$ (n = 7–13). (b) The C–O stretching frequencies of Co_nCO^- (ref. 134) and the peak positions for $Co_nCO_2^-$ as a function of cluster size. Reprinted with permission from ref. 284. Copyright 2016 American Chemical Society.

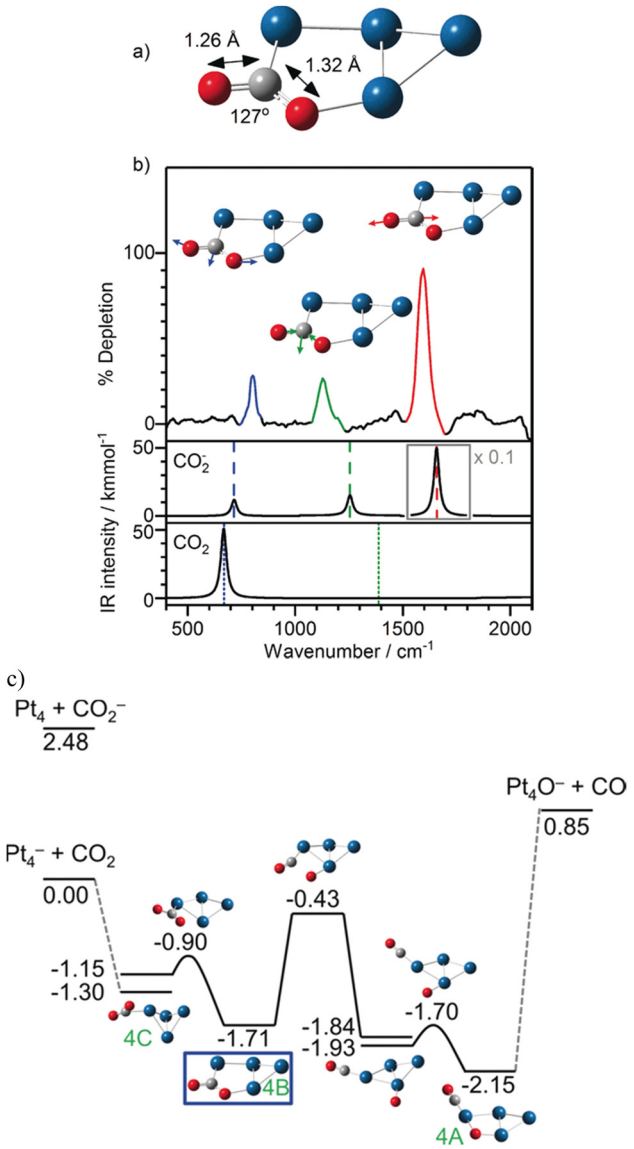

Fig. 39 (a) Calculated structure of the lowest energy isomer 4B of $[Pt_4CO_2]^-$ containing molecularly adsorbed CO_2, (b) IR-MPD spectrum of $[Pt_4CO_2]^-$. The dashed lines indicate the bend (714 cm^{-1}), symmetric stretch (1254 cm^{-1}), and antisymmetric stretch (1658 cm^{-1}) vibrations in free CO_2^-. The dotted lines indicate the positions of the bend (667 cm^{-1}) and infrared inactive symmetric stretch (1388 cm^{-1}) vibrations in free CO_2 (the antisymmetric stretch lies at 2349 cm^{-1}). (c) Energy surface for the adsorption and dissociation of CO_2 on Pt_4^- ($2S + 1 = 4$) calculated at the B3P86/SDD level of theory. Although CO_2 undergoes dissociation in the putative global minimum structure, the experimental spectra are consistent with a strongly activated, but molecularly-adsorbed, structure 4B, lying 1.71 eV below the $CO_2 + Pt_4^-$ asymptote. Reprinted from ref. 285 with permission of John Wiley and Sons.

These observations can be compared to the findings from IR-MPD spectroscopy of the cationic gold cluster complexes, Au_nOCS^+ (n = 3–10).[288] For these species, bands close to the vibrational fundamentals of free OCS are found, at about 2100, 790, and 500 cm^{-1}. The blue-shifted values for ν(CO) as well as red-shifted ν(CS) – compared to isolated OCS – indicate a binding of the intact molecule *via* the S-terminus. Results of DFT calculations (UB3P86/SDD) suggest that OCS binds in most cases in μ_1 coordination to a single Au atom in the cluster. A slightly more red-shifted ν(CS), in case of Au_5OCS^+, points to the presence of a μ_2 complex that appears to be facilitated by the particular flexible planar structure of Au_5^+. While for Au_5OCS^+ a bow-tie μ_1-structure is predicted as ground state, a nearly isoenergetic trapezoidal structure with μ_2-bridging OCS (+0.08 eV) can be reached over a comparably low barrier of 0.12 eV explaining its contribution to the IR-MPD spectrum.

The branching ratios for the photodissociation channels (CO *vs.* OCS loss) are, similar to the case of the neutral Ag clusters, size dependent and show a pronounced odd/even alternation. Clusters with an open electronic shell-structure, *i.e.*, even-sized Au_n^+ and odd-sized Ag_n, show CO loss and sulfide formation, while for odd-sized clusters release of intact OCS is the preferred dissociation channel. This behavior can be understood by a more efficient $d\pi \rightarrow \pi^*$ backdonation in the open-shell systems leading to significantly lowered barriers for S–CO dissociation, such that they are even submerged compared to the energies of the free reactants. DFT calculations for Au_8^+ and Au_9^+ reacting with OCS indicate that mainly the barrier heights are effected, while the overall thermodynamics of OCS complex formation *vs.* dissociation into sulfide and CO are very similar. Further, for the vibrational frequencies of OCS modes in the complexes, no obvious oscillations with cluster size have been detected, showing that there are no significant differences for the bond activation in the odd *vs.* even n molecular complexes.

3.2.4 N_2O. Binding mechanism. Nitrous oxide, N_2O, is a linear molecule isoelectronic to CO_2 and can be described by the following resonance structures which already illustrate the rather different strength of its two internal bonds and the capability to act as single O atom source. A comprehensive overview on the binding and activation of N_2O by metal centers has been given by Tolman.[321]

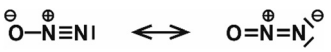

Reacting with metal centers, N_2O can transfer a single O atom, though in gas-phase reactions with metal cations also N-transfer has been observed.[29c,322] O-abstraction under release of N_2 is – for the reactions with many transition metal atoms or ions – formally spin-forbidden, as the metal species and the corresponding oxide do not share the same multiplicity in their ground states. Stable molecular adducts have been found as products of gas-phase reactions with cations of certain late transition metals (3d: Mn, Ni, Cu, Zn; 4d: Mo and later; 4d: Au, Hg, for further examples see below). These different reaction pathways for the TM cations have been explained by a combination of overall exothermicity, the effect of activation barriers, and spin conservation.[29c,322] Similar reactivities are found for N_2O reacting with transition metal surfaces: O-transfer in case of most TM studied (for some metals accompanied with N-transfer) and molecular adsorption for Ru, Ir, Pt, Cu, and Ag.[310c] There are only a few stable, structurally characterized, complexes of N_2O with TM atoms, most containing an N-bound

N_2O ligand.[323] Computational studies targeting the reduction mechanism of N_2O and concomitant O-transfer, however, sometimes imply the (initial) presence of an O-bound complex.[324]

Vibrational modes and frequencies. The IR active vibrational fundamentals of gas-phase $^{14}N_2{}^{16}O$ are ν(NN) at 2223.7 cm^{-1}, ν(NO) at 1284.9 cm^{-1}, and δ(NNO) at 588.7 cm^{-1}.[296] For N_2O adsorbed at the surfaces of late transition metals generally only small shifts from these values are seen. For such systems, the M–(N_2O) stretch has been observed in the 230–330 cm^{-1} range.[310c] Changes of these vibrational frequencies upon binding to single TM atoms or TM clusters are discussed in the following.

Complexes with metal atoms. Some complexes of N_2O with metal atoms have been spectroscopically characterized in the gas phase or in cryogenic matrices. The N_2O complexes of *neutral* Ni, Pd, Pt, Rh, and Ru atoms have been characterized by their IR spectra in Ar matrices[325] and by DFT calculations. The comparison suggests the presence of N-bound complexes and the binding is described by a donation/backdonation mechanism involving the 7σ HOMO and 3π* LUMO of N_2O, respectively, that implies some destabilization of the N–O bond. Accordingly, ν(NO) bands observed 50–150 cm^{-1} red-shifted compared to the free molecule are assigned to N-bound N_2O. The N–N bond is predicted to be weaker affected by the coordination to a metal atom and there are only small (blue)-shifts seen for ν(NN) (44 cm^{-1} for Pt).[325a] It shall be noted, however, that in case of *cationic* metal cluster complexes red-shifts of ν(NO) of the same magnitude as observed for these neutral species in Ar matrices are assigned to O-bound N_2O, while N-bound ligands are characterized by ν(NO) being blue-shifted compared to unbound N_2O, see the discussion below for $Co_n(N_2O)^+$.

In cases of gas-phase complexes of group 9 and 11 metal (Co, Rh, Ir and Cu, Ag, Au) atoms with multiple (m = 2–7) N_2O ligands, $M(N_2O)_m^+$, two well separated features are found in the region of the ν(NN) stretch.[326] Both features are blue-shifted relative to ν(NN) of unbound N_2O, one is only little shifted and not much changing with metal or number of N_2O ligands, the second feature is shifted by about 50–140 cm^{-1} and the value (and shape) depends more on the metal as well as ligand coverage. Supported by DFT calculations (B3P86/def2TZVP) the latter is assigned to be the signature of N-bound N_2O, while the hardly shifted features have been – with the exception of $Ir(N_2O)_m^+$ – related to O-bound ligands. DFT calculations reveal, however, that these O-bound complexes are significantly less stable. The presence of isomers containing O-bound ligands is explained by their stabilization through a significant barrier for rotation towards N-binding of 0.6–0.9 eV, calculated for the binary complexes $M(N_2O)^+$.[326]

In addition to ν(NN) being structure sensitive, in case of Co, Rh, Ir, also the effect of different spin states onto ν(NN) – and the change of the preferred state with N_2O coverage – has been discussed.[326] Interestingly, DFT calculations for $Ir(N_2O)_2^+$ reveal for the quintet state complexes very similar values of ν(NN) for O and N-bound N_2O close to that of free N_2O, while in the energetically favored triplet state the features associated with N-binding would be, again, significantly blue-shifted. Accordingly, the broad features seen in the spectra of $Ir(N_2O)_m^+$ close to ν(NN) of free N_2O are assigned to a convolution of bands related to O as well as N-bound ligands for quintet state complexes. For $Ir(N_2O)_m^+$, these are the only features observed in the spectra. The missing spectroscopic signatures of triplet state complexes are in line with a submerged barrier predicted for O-transfer on the triplet surface and the experimentally observed efficient formation of IrO_m^+ by sequential N_2O reduction.[322,326b]

Metal cluster reactivities. O-Transfer is the dominant reaction channel observed for late transition metal clusters reacting with N_2O in the gas-phase under single-collision conditions.[238c,314,327] For instance, in case of reactions of Rh cluster cations with N_2O studied within an FT-ICR mass spectrometer,[238c] only the oxide products of the reaction – including those of sequential N_2O decompositions by a single metal cluster – but no molecular N_2O adducts are observed. In the size-range studied ($n < 30$), the bimolecular rate coefficients for the reaction are strongly and non-monotonically size-dependent and vary over nearly three orders of magnitude. Overall, for most clusters the cross section reaches only a fraction of 1–50% of the theoretical collision cross section calculated *via* the surface charge capture (SCC) model.[274] Other reactions of Rh_n^+, for instance their oxidation by NO, proceed with rates close to the values predicted by the SCC model. It has been concluded, that the individual structures of the Rh clusters must have a significant influence on the N_2O decomposition rate.[238c]

A strong structure sensitivity may be understood based on the structures of the – in the aforementioned reactivity studies – unobserved entrance channel complexes and the mechanism of N_2O decomposition that presumably involves a bending (or rotation) of the N_2O ligand from an initially N-bound N_2O complex towards a geometry that allows for Rh–O bond formation. Indeed, the reaction profile for N_2O reduction by Rh_6^+ calculated using DFT (Fig. 40) reveals the bending of N_2O induced by backdonation into the 3π* LUMO as a major barrier in its activation.[73b] The mechanism appears very similar to predictions for the decomposition of N_2O on extended surfaces of Rh and other platinum metals.[321]

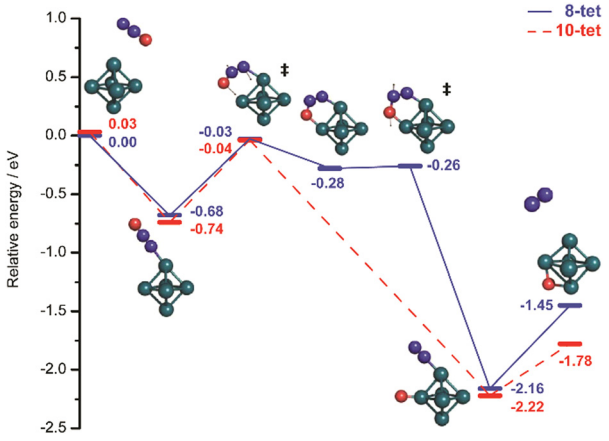

Fig. 40 Reaction profile for activation and decomposition of N_2O by the Rh_6^+ cluster calculated using the eigenvector following method (DFT: TPSSh/def2-TZVP). Reprinted with permission from ref. 73b. Copyright 2011 American Chemical Society.

IR spectroscopy. While unobserved under single-collision conditions, complexes of molecular N_2O with TM clusters can be collisionally stabilized, *e.g.*, within the high-pressure region of laser vaporization cluster sources, in particular at low temperature.[290,292,328]

IR spectra of $Rh_n(N_2O)^+$ complexes (n = 4–8) have been obtained *via* dissociation of Ar-tagged complexes formed at 173 K (Fig. 41).[73b,290,291] As mentioned before, Ar tagging results in a higher spectroscopic sensitivity, in particular at low IR frequencies. It also helps to stabilize the complexes in their entrance-channel geometries to avoid rapid oxidative decomposition of the complexes. Spectra have been recorded in a wide spectral range from 100 cm^{-1} to 2350 cm^{-1} covering the regions where, *e.g.*, ν(NN), ν(NO), and δ(NNO) for molecularly bound N_2O are expected, as well as the low frequency region of metal-metal vibrations. Consistently, all these spectra contain distinct bands close to the vibrational modes of unbound N_2O.[73b,290] For all $Rh_n(N_2O)^+$ complexes (n = 4–8), ν(NN) and ν(NO) are slightly blue-shifted compared to free N_2O, and seen around 2250 cm^{-1} and 1320 cm^{-1}, respectively. The bending mode, δ(NNO), for these complexes is measured around 560 cm^{-1}, ~30 cm^{-1} below the value for free N_2O. These band positions fit very well to the predictions for N-bound N_2O. DFT calculations (TPSSh/def2-TZVP) for $Rh_6(N_2O)^+$ find an O-bound isomer 0.44 eV less stable then the N-bound one and locate, as most striking difference to the N-bound structures, their ν(NO) significantly shifted to lower frequencies, even to below ν(NO) of the free molecule.[73b]

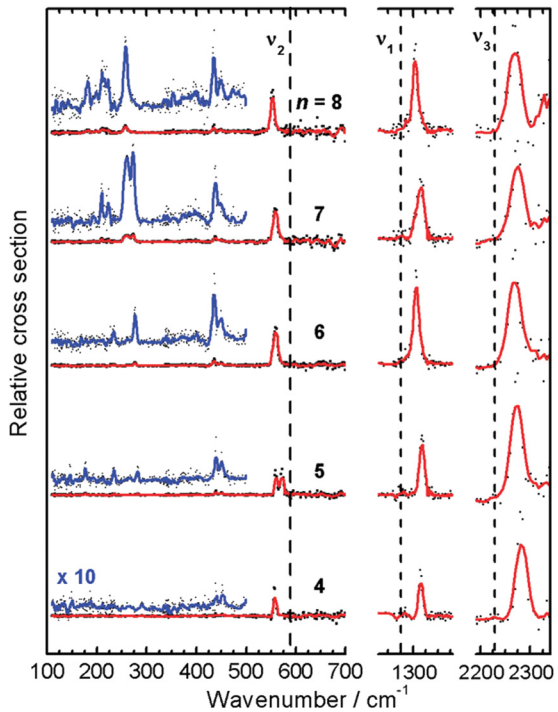

Fig. 41 IR-MPD spectra of argon-tagged $Rh_nN_2O^+$ (n = 4–8) complexes. The strong bands observed close to those of free N_2O (indicated by dashed lines) indicate molecular adsorption *via* the terminal N-atom; ν_1 (N–O stretch), ν_2 (NNO bend), ν_3 (N–N stretch). Bands in the far-IR are due to internal vibrations of the Rh clusters as well as to Rh-(N_2O) modes. The double-peak structures seen at nominal wavenumbers of ~440/450 cm^{-1} are artifacts stemming from minor admixtures of third (3 × 440 cm^{-1} = 1320 cm^{-1}) and fifth harmonics (5 × 450 cm^{-1} = 2250 cm^{-1}) to the FEL radiation, *i.e.*, they relate to the intense absorptions of ν_1 and ν_3. Reprinted with permission from ref. 73*b*. Copyright 2011 American Chemical Society.

The Rh–N_2O stretch in these cluster complexes is predicted around 280–285 cm^{-1}, and although there have been no direct assignments to the experimental bands given, it is tempting to relate a band seen in all the experimental far-IR spectra around 260–280 cm^{-1} to that vibration. Such an assignment would be also consistent with the values of M–N_2O stretch vibrations for N_2O adsorbed at the surface of other platinum group metals.[310c]

In the far-IR range, below 300 cm^{-1}, also M–M vibrations contribute to the spectra of the $Rh_n(N_2O)^+$ complexes. Thus, the available spectral data is sensitive to the coordination geometry of the N_2O ligand and the internal structure of the rhodium cluster in this complex. The far-IR spectra have been compared to the outcome of DFT calculations (TPSSh/def2-TZVP), but no distinct assignments could be made. However, in general, the cluster cores of the calculated low energy isomers[73b] resemble those determined based on the far-IR spectra of Rh_n^+ clusters.[27c,329] Furthermore, for certain sizes, *e.g.*, n = 6 and 7, there are strong similarities in the spectra of bare Rh cluster and N_2O complex supporting the idea, that the structure of the metal cluster core may not significantly change upon N_2O addition. This goes along with a calculated, moderate N_2O binding energy of about 0.7–0.8 eV in the cationic Rh cluster complexes.[73b,291]

The aforementioned data have been measured *via* IR-PD of $Rh_n(N_2O)Ar^+$ complexes, and similar results – but limited to the spectral regions around ν(NN), ν(NO), and δ(NNO) – have been obtained for complexes without any Ar messengers, $Rh_n(N_2O)^+$, formed at 308 K.[73b,291] The spectral signatures for these complexes are very similar to those obtained using the Ar messenger, only the bands have a broader width that can be related to the higher internal energy of the complexes as well as to an increased FEL bandwidth, connected to the higher FEL pulse energies used for IR-MPD. Overall, all these $Rh_n(N_2O)^+$ complexes are found to contain N-bound N_2O. Their IR induced fragmentation behavior has been analyzed in very detail, revealing two competing dissociation channels: either direct loss of a complete N_2O entity or loss of N_2, implying transfer of an O-atom towards the Rh cluster.[73b,291] For the Ar complexes, Ar loss forms a 3rd fragmentation channel.

The observation of an effective O-transfer channel for N_2O complexes that are spectroscopically characterized as containing N_2O bound *via* the terminal N-atom, *i.e.*, having the O-atom initially pointing away from the metal, strengthened the interest in the mechanism of this IR-induced reaction. Based on the experimental observation that the IR-induced chemistry exhibits no particular mode-selectivity,[73b] as indicated by similar fragmentation behaviors for excitation *via* the three ligand modes ν(NN), ν(NO), and δ(NNO), it has been concluded that the process can be described as the ligand forming an IR chromophore from which the absorbed energy is, through IVR, rapidly redistributed towards the metal framework. The energy increase in this cluster complex upon absorption of several IR photons, then can be sufficient to overcome the barriers towards N_2O decomposition or, depending on the relative strength of the M-N_2O bonding, the

complex may simply decompose back into the reactants, Rh_n^+ + N_2O, see Section 5.

The relative energies for these two processes sensitively determine the branching ratio between the two channels. For instance, $Rh_6N_2O^+$ shows, as most of the $Rh_n(N_2O)^+$ complexes studied, a significant fraction of the Rh_6O^+ product upon IR-excitation, consistent with the highest barrier towards O-transfer being submerged compared to the energy of the reactants (Fig. 40).[73b] In contrast, for $Rh_5N_2O^+$ this barrier, involving the bending of N_2O and the formation of an intermediate $\mu_2(\eta^1{:}\eta^1)$-N_2O complex with the terminal O and N-atoms bound to neighbored metal atoms, slightly exceeds the N_2O binding energy. As result, $Rh_5N_2O^+$ does not show much formation of an O-transfer product upon IR-pumping but mostly N_2O loss.[291] Addition of an O-atom to the cluster changes the energy landscape significantly, the barrier of $Rh_5O(N_2O)^+$ to decomposition is now submerged by ~0.3 eV and nearly all of it reacts into $Rh_5O_2^+$.[291] Very similar reactivities are observed upon collisional activation of $Rh_n(N_2O)^+$ supporting the assumption of a thermal excitation mechanism.[328] For $Rh_n(N_2O)_m^+$ (n = 5, 6; m = 1–5) stored collision-free for a prolonged time in an FT-ICR mass spectrometer, even the absorption of background blackbody radiation has been observed to induce both processes, N_2O desorption as well as decomposition. The size-specific branching ratios are somehow different from the IR-MPD studies which is explained by the orders of magnitude lower photon absorption rate that avoids an 'overheating' of the complexes into regimes where entropic effects become more relevant.[330]

For Au_n^+ (n = 3–7) clusters, molecular N_2O complexes have been studied in the ranges of ν(NN) and ν(NO).[289] These complexes exhibit their ν(NO) and ν(NN) bands at around 1340 cm^{-1} and 2270 cm^{-1}, respectively, slightly blue-shifted compared to isolated N_2O, with the shifts decreasing with cluster size. The band-positions agree well with N-bound N_2O, which is, based on the results of DFT calculations (TPSSh/def2-TZVP) for $Au_3N_2O^+$ (n = 3, 4), the energetically preferred orientation.

N_2O complexes of cobalt clusters, $Co_n(N_2O)^+$ (n = 1–5),[289] differ from the aforementioned Au and Rh complexes in that their IR spectra indicate the presence of N- as well as O-bound ligands (Fig. 42), similar to the atomic complexes.[326b] Bands attributed to ν(NN) and ν(NO) are found at values characteristic for N-bound N_2O at 1323–1345 cm^{-1} and 2271–2280 cm^{-1} for $Co_n(N_2O)^+$ (n = 1–5, red-shifting with increasing n), similar as discussed before. However, for the smaller sizes (n = 1–4), additional bands 100–140 cm^{-1} red-shifted compared to ν(NO) of gaseous N_2O, as well as band-shoulders that are – within the experimental resolution – coinciding with ν(NN) of free N_2O are observed and have been assigned to O-bound N_2O. According to DFT calculations (TPSSh/def2-TZVP), the N-bound isomers are again, for all studied Co cluster cations, energetically favored. The observation of O-bound species, therefore, is explained by a significant (but hitherto not quantified) barrier for rotation towards the preferred N-bound structure (see above for calculated barriers for the atomic complexes).[289] The dominating IR-MPD channel for the N_2O complexes of Co and Au clusters is loss of N_2O.

Anionic and cationic Pt clusters get readily oxidized by N_2O[314,327a] and this reactivity becomes also apparent in IR-MPD studies of $Pt_n(N_2O)^+$ (n = 1–8).[292] Overall, the IR spectra of these complexes (formed at −140 °C) are similar to the spectra of N_2O TM-cluster complexes discussed before, mainly indicating N-bound ligands that lead to intense features blue-shifted to ν(NO) and ν(NN) of free N_2O. For certain sizes (n = 1, 2, and possibly 8), there is also evidence for O-bound N_2O based on the appearance of bands red-shifted to ν(NO) of free N_2O, in case of n = 8, also a band red-shifted to ν(NN) is visible. The mass-spectrometric abundances of the Pt_n^+ + N_2O reaction products reveal a strong increase in activity for O-transfer from n = 6 onwards. The smaller clusters mainly form molecular complexes, $Pt_nN_2O^+$, while the dominating product for the larger clusters is the oxide, Pt_nO^+. For n = 6, the abundance of $Pt_nN_2O^+$ is even negligible, such that no IR spectrum could be recorded for that complex size. This tendency is also repeated in the observed IR-MPD channels revealing for the smaller sizes mainly N_2O loss upon IR excitation, while for n = 7 and 8 loss of the intact molecule and oxide formation are nearly equally observed. The calculated (DFT: TPSSh/def2-TZVP-GD3-BJ) reaction mechanisms for oxidative decomposition qualitatively resemble that of $Rh_6N_2O^+$ (Fig. 40) and the strong increase in O-transfer activity with growing cluster size can be related to decreasing barrier heights for the activation and bending of N_2O towards the Pt_n^+ clusters. For the larger clusters, this barrier lies very close to or below the energy for dissociation back into the reactants (Pt_n^+ + N_2O) such that the two reaction channels compete with each other. For completeness, for all considered Pt_n^+ clusters, the O-bound complexes are consistently predicted to be about 0.5 eV less stable than the N-bound structures.[292]

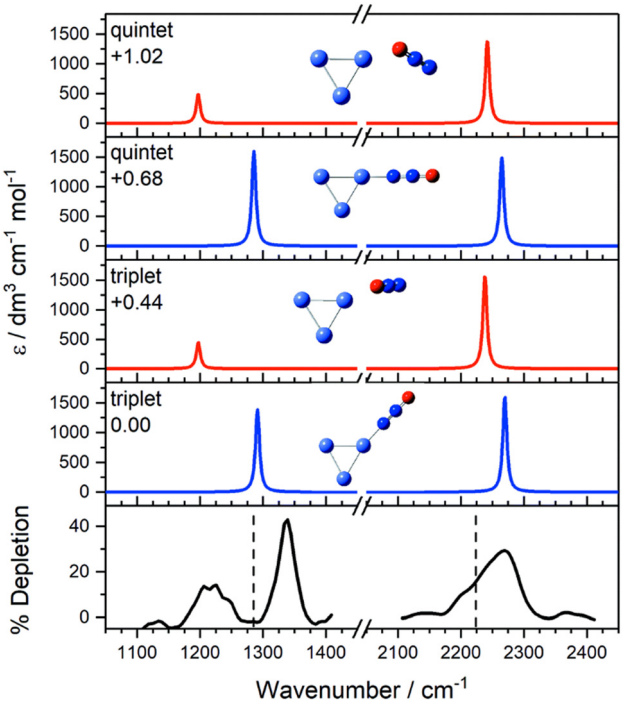

Fig. 42 IR-MPD spectrum of $Co_3(N_2O)^+$ along with spectra of low-lying N-(blue) and O-bound (red) isomers calculated using DFT (TPSSh/def2-TZVP). The vertical dashed lines in the IR-MPD spectrum indicate ν(NN) and ν(NO) in unbound N_2O. Reproduced from ref. 289 with permission from the PCCP Owner Societies.

3.2.5 NO_2. Nitrogen dioxide, NO_2, being isoelectronic with CO_2^-, can bind to metals similarly to CO_2 in a variety of binding motifs, N or O-bound and also as a bidentate ligand. N-Bound NO_2 is usually referred to as nitro, O-bound as nitrito.[32d,310c] The vibrational fundamentals of unbound NO_2 are at 1617.8 cm^{-1} (ν_{as}), 1318 cm^{-1} (ν_s), and 749.65 cm^{-1} (δ).[331] Due to the bent structure of NO_2, all these modes are IR active.

So far, only the IR spectrum of $Au_4(NO_2)^-$ had been characterized in a study of NO reacting with anionic gold clusters.[332] While the complex could, in principle, be formed in a disproportionation reaction upon addition of multiple NO molecules to the cluster, the NO pressure dependence of its abundance let conclude it to be due to contamination of NO by traces of NO_2. The IR-MPD spectrum of $Au_4(NO_2)^-$ was measured in a wide range from 150 to 1800 cm^{-1} and exhibits a broad band at 1415 cm^{-1} with a shoulder at 1325 cm^{-1} and two more bands at 345 cm^{-1} and 825 cm^{-1}. Comparison has been made to spectra from DFT calculations suggesting attachment of an intact NO_2 unit to the *y*-shaped Au_4^- entity. N and O-bound isomers are found to be nearly isoenergetic and suggested both as plausible structures.[332] The experimental frequencies agree fairly well to those of stable TM nitro complexes.[32d]

3.2.6 HCN. For HCN bound to Mg_n (n = 2–6),[293] Cu_n (n = 1–3),[294] Zn_n (n = 1–4)[295] rotationally resolved infrared spectra as well as Stark spectra have been obtained in superfluid He droplets. Bands are found close to the value of the ν(H–C) fundamental for free HCN, 3311.47 cm^{-1} (ref. 296), indicating the presence of relatively weak N-bound complexes. Due to the cryogenic environment, the complexes are frozen out in their entrance channel geometry without protolysis. Depending on metal and cluster nuclearity, the HCN is binding either μ_1 atop (all Cu_n, Mg_4, Zn_4), μ_2 bridging (Mg_2, Zn_2), or μ_3 face-capping (Mg_3, Zn_3).

Table 8 Summary of experimental studies on the vibrational spectroscopy of gas-phase metal cluster complexes with 4-atomic and larger molecules

Molecule	Metal	System	Cluster sizes (n)	Coverage (m)	Method[a]
NH_3	Fe	$Fe_n[NH_3]_m$	7–16	1, 2	IR-MPD, CO_2[333]
	Ag	$Ag_n[NH_3]_m$	2–18	1, 2	IR-MPD, CO_2[100,334]
		$Ag_n[NH_3]_m$	3–5	1, 2	IR-MPD[99]
CH_4	Ta	$Ta_n[CH_4]_m^+$; $Ta_n[CH_2][CH_4]_m^+$	4	Unspecified	IR-MPD[335]
	Fe	$Fe_n[CH_4]_m^+$	2–4	1–4	IR-PD[336]
	Pt	$Pt_n[CH_4]_m^+$	3–5	1	IR-MPD[63a]
	Cu	$Cu_n[CH_4]_m^+$	2–4	1	IR-MPD[337]
	Au	$Au_n[CH_4]_m^+$	2–4	1	IR-MPD[64c]
C_2H_4	Ag	$Ag_n[C_2H_4]_m$	3–7	1–4	IR-MPD, CO_2[338]
	Au	$Au_n[C_2H_4]_m^+$	2–4	1–3	IR-MPD[339]
C_2H_6	Au	$Au_n[C_2H_6]_m^+$	2–4	1–3	IR-MPD[340]
Benzene	Ag	$Ag_n[C_6H_6]_m$	3–7	1–4	IR-MPD, CO_2[341]
C_2H_4O	Ag	$Ag_n[C_2H_4O]_m$	3–8	1–2	IR-MPD, CO_2[338]
Methanol	Fe	$Fe_n[CH_3OH]_m$	5–15	1, 2	IR-MPD, CO_2[81,342]
	Co	$Co_n[CH_3OH]_m^+$	2–6	1–3	IR-PD[343]
		$Co_n[CH_3OH]_m^-$	1–4	1–3	IR-PD[344]
	Ni	$Ni_n[CH_3OH]_m^+$	3,4	1–4	IR-PD[77g]
	Cu	$Cu_n[CD_3OH/D]_m$	3–11	1–2	IR-MPD, CO_2[345]
	Ag	$Ag_n[CD_3OH/D]_m$	3–22	1–2	IR-MPD, CO_2[345]
	Au	$Au_n[CD_3OH/D]_m$	3–13	1–4	IR-MPD, CO_2[345]
	Au	$Au_n[CH_3OH]_m^+$	1–10,15	1–3	IR-MPD, CO_2[346]
		$Au_n[CD_3OH/D]_m^+$	1–7	1–4	IR-MPD[347]
Ethanol	Co	$Co_n[C_2H_5OH]_m^-$	1–4	1–3	IR-PD[344,348]
	Au	$Au_n[C_2H_5OH]_m$	3,9,11	1–4	IR-MPD, CO_2[349]
	Co/Ni	$Co_nNi[C_2H_5OH]_m^-$	3	1	IR-PD[350]
Propanol	Co	$Co_n[C_3H_7OH]_m^-$	1–4	1–3	IR-PD[344]
Formic acid	Mn	$Mn_n[HCOOH]_m^+$	1–3	1	IR-MPD[351]
Formate	Cu	$Cu_n[HCOO]_m^-$	1–3	2, 3, 5, 7	IR-MPD[352]
Acetic acid	Mn	$Mn_n[CH_3COOH]_m^+$	1–3	1	IR-MPD[351]
Propionic acid	Mn	$Mn_n[C_2H_5COOH]_m^+$	1–3	1	IR-MPD[351]
Methyl acetate	Mn	$Mn_n[CH_3COOCH_3]_m^+$	1–3	1	IR-MPD[351]

[a] IR-MPD – infrared multiple photon dissociation using IR-FELs; IR-MPD, CO_2 – IR-MPD using line-tunable CO_2 laser; IR-PD – infrared photo dissociation employing OPO/OPA or DFM/OPA lasers as IR sources; HeIRSS – Infrared laser Stark spectroscopy in superfluid He droplets.

3.3 4-Atomic and larger ligands

3.3.1 NH_3. Ammonia usually binds to metal centers *via* donation through the N-lone pair. The surface chemistry of NH_3 on metals has been intensively studied as it is of particular relevance for understanding its formation from the elements, *i.e.*, *via* the Haber-Bosch and related processes.[353] As a 4-atomic molecule with C_{3v} symmetry, ammonia has 6 vibrational modes, four of them being pairwise degenerate. Vibrational transitions in free NH_3 are affected by inversion tunneling, but this is not of relevance for the following discussion. Refraining from these details, the vibrational fundamentals of NH_3 are at 3444 cm^{-1} (ν_d, *e*), 3337 cm^{-1} (ν_s, a_1), 1627 cm^{-1} (δ_d, *e*), and 950 cm^{-1} (δ_s, a_1).[296]

The corresponding modes for molecularly adsorbed NH_3 at metal surfaces are in the ranges of 3340–3430 cm^{-1} (ν_a), 3200–3360 cm^{-1} (ν_s), 1565–1640 cm^{-1} (δ_a), and 1070–1170 cm^{-1} (δ_a), indicating a slight weakening of the N–H bonds upon metal binding. The M–N stretch is found in the 355–570 cm^{-1} range. These numbers are for the so called α-state of adsorbed NH_3, a weaker bound β-state, additionally appearing at higher NH_3 surface coverage, can be related to hydrogen bonded NH_3 molecules.[354] For the vibrational spectroscopy of ammonia complexes of metal atoms in the range of the N–H stretches, solvation shell effects and hydrogen bonding see, *e.g.*, ref. 355 and references therein. For data, *e.g.*, on early TM atoms reacting with NH_3 in cryogenic matrices and the vibrational signatures of complex formation and successive dehydrogenation towards amido (TM–NH_2) and imido (TM=NH) complexes, see ref. 356.

To identify molecular absorbates and to distinguish them from partly dehydrogenated species, the umbrella mode, *i.e.*, in the complexes the symmetric deformation δ_s, is of particular relevance and this mode has been targeted in all the present IR studies of NH_3–metal cluster complexes.

Complexes of NH_3 with small neutral Ag clusters were studied already in early IR-MPD experiments using CO_2 lasers. Data for the umbrella mode of molecularly adsorbed NH_3 could be obtained for $Ag_2(NH_3)$ (ref. 100*a*) and a range of other sizes, $Ag_n(NH_3)_{1,2}$ (n = 4–18),[100b,334] but were limited by the available scanning range and the spectral gaps occurring when using $^{12}C^{16}O_2$ as lasing medium. For instance, δ_s is found for $Ag_2(NH_3)$ at 1065 ± 5 cm^{-1}, however, the band maximum falls in a gap of no emission lines of $^{12}C^{16}O_2$, see Fig. 43a. The complex is found to have a linear Ag–Ag–N arrangement.[100a] For the other sizes, δ_s falls typically in the 1075–1089 cm^{-1} range for complexes with a single NH_3, while those containing two NH_3 molecules have their δ_s at slightly lower wavenumbers (1065–1081 cm^{-1}). The only exception is seen for n = 12 where this order is reversed. For certain sizes, *e.g.*, n = 10, 14, 17, relatively narrow (fwhm ~7 cm^{-1}) bands are observed, while for other sizes multiple bands, relating to different binding sites or broad unstructured features are seen. The change in band-shape and width between the differently sized complexes has been related to the Ag_n–NH_3 binding thermodynamics, which point – depending on cluster size – to either local binding of NH_3 at a particular cluster site or the presence of a fluxional complex, *i.e.*, the NH_3 being free to move on the clusters' surface between several different binding sites.[334] Ammonia complexes of small neutral silver clusters, $Ag_n(NH_3)_m$ (n = 3–5, m = 1, 2), where the first metal cluster complexes to be studied using an IR-FEL (Fig. 43b).[99] Due to the extended wavelength range – compared to CO_2 lasers – it was also possible to characterize the δ_s modes of (partially) deuterated ammonia complexes, which have been located up to ~250 cm^{-1} (for full deuteration) below that of the non-deuterated ammonia complexes. The observed shifts of δ_s are consistent with the variation of the reduced mass in the complexes of NH_3, ND_2H, and ND_3.

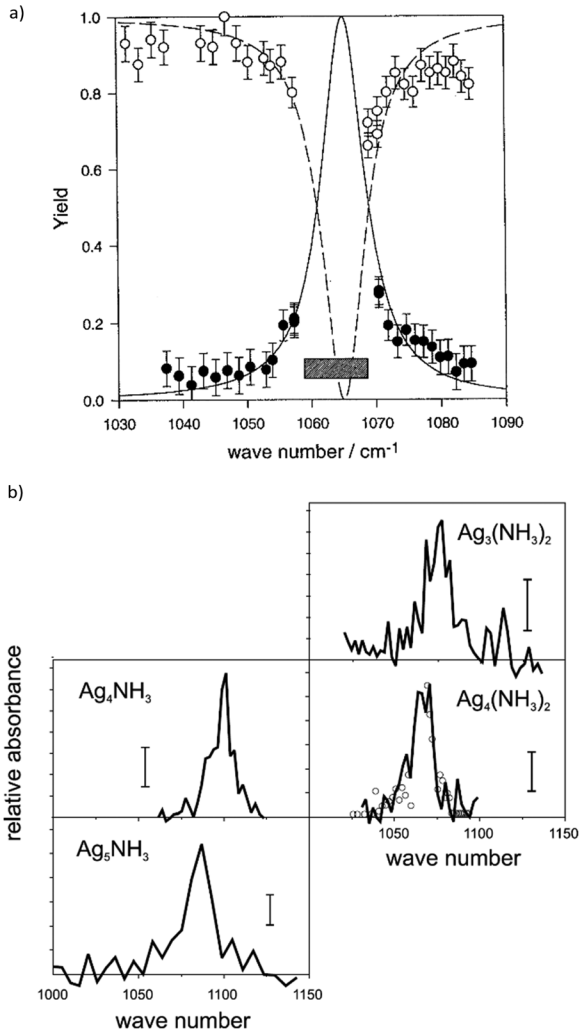

Fig. 43 IR-MPD spectra of neutral $Ag_n(NH_3)_{1,2}$ complexes in the region of the NH_3 symmetric deformation (umbrella) mode, δ_s. (a) Spectrum of $Ag_2(NH_3)$ measured using a line-tunable CO_2 laser with its emission gap being marked by a grey bar. IR-MPD of $Ag_2(NH_3)$ is monitored optically *via* UV photodissociation of the remaining fraction at 308 nm that proceeds under photoemission (○). Likewise, the concomitant formation of Ag_2 is monitored *via* laser induced fluorescence at 431 nm (●). Reprinted with permission from ref. 100*a*. Copyright (1995) by the American Physical Society. (b) IR-MPD spectra obtained using an IR-FEL (FELIX), detecting the depletion mass spectrometrically after ionization of the complexes at 193 nm (6.4 eV). For $Ag_4(NH_3)_2$, the FEL spectrum (—) is superimposed to the data obtained with a CO_2 laser (○). Reprinted from ref. 99. Copyright (2002), with permission from Elsevier.

$Fe_n(NH_3)$ (n = 7–16) is the only other ammonia-metal cluster system studied in the IR range. Using a tunable CO_2 laser, no signals where found in the 880–1090 cm^{-1} range for complexes of NH_3, however, for the ND_3 complexes bands attributable to the δ_s mode appeared between 880 and 888 cm^{-1} with slight variations of the band positions depending on cluster size. The finding is consistent with a significant up-shift of δ_s upon complexation to metal centers as seen for ammonia molecularly adsorbed on metal surfaces and as predicted by model DFT calculations for $Fe_n(NH_3)$ (n = 1, 4, 7, 13) using the PBE functional.[333]

3.3.2 CH_4. This section is kept short as the IR spectroscopy of complexes between metal ions or clusters and methane has been comprehensively reviewed very lately by Roithová and Bakker.[357] Focusing on mass-selected ions in the gas-phase, their review mostly contains information on cationic systems, only little on anions (simply due to lack of data), and it does not cover the earlier miscellaneous spectroscopic studies of (neutral) TM atom complexes in cryogenic matrices, see, *e.g.* ref. 358.

To summarize the results on TM cluster-CH_4 complexes and without attempting to go in-depth here, recent data from IR spectroscopic investigations can be categorized into either identifying weakly bound, intact CH_4 ligands with barely to markedly activated C–H bonds as seen for Fe_n^+ (n = 2–4),[336] Pt_n^+ (n = 3–5),[63a] and Cu_n^+ (n = 2–4),[337] or partly dehydrogenated species like in the case of Au_n^+ (n = 2–4)[64c] and Ta_4^+.[335] The later example shows for ions of composition $Ta_4[CH_2][CH_4]_m^+$ (m = 0, 1, 2…, including other methane isotopologues) the presence of a carbide–dihydride core, $H_2Ta_4C^+$, with CH_4 ligands essentially acting as messenger, while complexes with composition $Ta_4[CH_4]_m^+$ contain only intact CH_4.[335]

For cationic gold cluster-methane complexes, features are seen outside the typical range of the C–H deformation modes of 1200–1600 cm^{-1}. By comparison to predictions from Born-Oppenheimer spin density functional theory molecular dynamics these features have been interpreted as due to contributions from a hydrido-methyl isomer $H–Au_n–CH_3^+$.[64c] Howsoever, specifically the ability of ground-state Au_2^+ to activate CH_4 – and catalyze it's coupling to ethane – at low temperature has been lately questioned based on experimental thermodynamical data.[41c,359] Nevertheless, hyperthermal collisions[64c] or Au_2^+ in an (long-living) excited state could be involved in an CH_4 activation process. Then again the spectral data evidencing $H–Au_n–CH_3^+$ formation is presented also for Ar complexes[64c] that can be expected to specifically sample the coldest part of the cluster distribution.

In case of the – towards methane highly reactive – platinum clusters,[360] ligand exchange of initially bound Ar with CH_4 at 180 K has been pursued for a controlled formation of a molecular complex and to avoid dehydrogenation.[63a] IR excitation can induce dehydrogenation in these complexes, see Section 5.

The iron cluster-methane complexes have been characterized in the 2700–3100 cm^{-1} range, where the C–H stretches are located, while all other IR spectra of TM cluster-CH_4 complexes are reporting the range of the C–H deformation modes of 1200–1600 cm^{-1} or a somewhat extended range.

3.3.3 Other hydrocarbons, C_2H_4O. Apart from CH_4, only few IR studies of complexes between TM clusters and hydrocarbons exist. Using CO_2 laser excitation, complexes of neutral silver clusters, Ag_n^+ (n = 3–7), with ethylene, ethylene oxide and benzene (as well as with their deuterated analogs) have been characterized.[338,341] The limited spectral details that were observable around 10 μm for the silver cluster complexes imply molecular, largely unperturbed adsorption of these molecules to the Ag clusters.

More recently, IR spectra in the 200–1800 cm^{-1} range have been obtained of small cationic gold clusters, Au_n^+ (n = 2–4) complexed with ethane or ethylene.[339,340] The spectra of the complexes of Au_2^+ with ethane indicate co-existence of isomers either containing intact C_2H_6 ligands or having a C–H bond broken to form an ethyl group and a bridge bound H atom. For the complexes of gold trimer and tetramer, the spectra suggest the presence of the encounter complex in a dominating fraction, but a (minor) contribution of some singly dehydrogenated ethane, *i.e.*, formation of hydrido-ethyl, has not been excluded.[340] For gold-ethylene complexes, $Au_n(C_2H_4)_m^+$ (n = 2–4, m = 1–3), the IR-MPD spectra in the 500–1700 cm^{-1} range appear overall similar and are assigned to C_2H_4 π-bound to the cationic gold cluster by partial electron donation leading to an activation of C–C bonds, while there is no sign of activated C–H bonds.[339] Complexes of the cationic gold dimer with co-adsorbed C_2H_4 and O_2 (ref. 169) are discussed in Section 4.

3.3.4 Alcohols. Simple alcohols usually bind to metal centers forming a σ O-donor complex. However, on the surfaces of reactive metals (most TM excluding the coinage metals) also dissociative adsorption – deprotonation of the hydroxyl group under formation of alkoxides and metal hydrides – is frequently observed already at low temperature.[361] To distinguish between these binding forms and to investigate further reactions like dehydration or oxidation, studies of the corresponding TM cluster complexes have been pursued already from the mid-1980s on and there is a comparably large amount of spectroscopic data for metal cluster complexes of differently sized alcohols.

Even the earliest studies from the Exxon group demonstrating size-selective IR-MPD of a metal cluster adsorbate were for the complex of an alcohol, neutral $Fe_8(CH_3OH)$.[81,342c] Using a CO_2 laser, for this and other sizes (n = 1–12), depletion bands at 985 cm^{-1} and 1075 cm^{-1} had been identified and assigned to the C–O stretch of a methoxy group and the Fe–H stretch of bridge bound hydrogen, respectively. However, in reactivity studies, different isotopologues of methanol showed comparable reactivity towards iron clusters, *i.e.*, there was no identifiable H/D kinetic isotope effect which would have been expected if complex formation involves dissociation of the alcohol group.[342d] Later, these studies had been extended by Knickelbein, again using CO_2 laser IR-MPD, to slightly larger iron cluster sizes and IR spectral data was obtained for complexes of the different methanol isotopologues CH_3OH, CH_3OD, CD_3OH, and CD_3OD.[342a,b] Taking the isotope effects onto the spectra into account, these measurements resulted in overall similar data compared to the initial ones, however, find small but significant shifts for the bands assigned to the C–O stretch depending on the isotopologues. Magnitude and direction of these shifts agree with the changes of the gas-phase values for the C–O stretch, *e.g.*, between CD_3OD and CD_3OH.

Therefore, the initial assignment of dissociative chemisorption had been challenged and, instead, the formation of an O-donor complex with intact methanol ligands was suggested. Consistently, the feature at higher frequency (1075 cm^{-1} for $Fe_8(CH_3OH)$) was re-assigned to a rocking-mode of the methyl group.[342a,b]

Similar conclusions, *i.e.*, nondissociative adsorption *via* the O donor atoms, were obtained for deuterium substituted methanol (CD_3OH and CD_3OD) bound to small neutral Cu, Ag, and Au clusters.[345] The complexes were formed in a flow-tube reactor maintained at 60–70 K, ionized by 6.4 eV photons prior mass spectrometric detection, and studied by CO_2 laser IR-MPD in the 9–11 μm range. For the complexes with a single methanol ligand, the C–O stretches are found in the 955–970 cm^{-1} range, rather independent of the metal and cluster size. At larger coverage, the bands assigned to the C–O stretches shift slightly to higher frequency – by 5–10 cm^{-1} per methanol molecule – which has been related to the interactions among the methanol ligands.[345]

The analogue complexes of neutral Au clusters with ethanol, $Au_n(CH_3CH_2OH)_m$ (n = 3, 9, 11; m = 1–4), have been studied using the same experimental technique as for the aforementioned methanol complexes.[349] Using UV photons of 6.4 eV, cluster complexes with n = 3, 9, 11 have been effectively ionized. The complexes exhibit bands at or slightly to the red of 1030 cm^{-1} (more precise frequency measurements were hindered by a gap in the CO_2 laser emission curve).[349] This band slightly broadens and shifts to the blue with increasing number of ligands on an Au cluster, in addition a weaker band around 1080–1090 cm^{-1} appears. An assignment of these bands is less straightforward as in case of the methanol complexes, due to several (mixed) ligand modes in the 1000–1100 cm^{-1} region and the potential presence of different ethanol conformers (anti/gauge). Accompanying DFT calculations suggest an assignment of the ~1030 cm^{-1} band to the ν(CCO) + δ(OH) and/or $\rho(CH_2)$ + $\rho(CH_3)$ modes of the gauche conformer in the $Au_n(CH_3CH_2OH)$ complexes.[349]

Also complexes of cationic gold clusters with methanol, $Au_n(CH_3OH)_m^+$ (n = 1–10, 15; m = 1–3), have been studied by CO_2 laser IR-MPD around 10 μm.[346] The studies combine experimental characterization of charged cluster complexes in a Penning trap mass spectrometer with Car-Parinello molecular dynamics simulations. Central findings are a cluster size-specific shift of the band assigned to ν(CO) and, again, it was concluded that the methanol molecules adsorb intact *via* the O-atom. Compared to free methanol, ν(CO) is red-shifted to values similar as seen in the corresponding cationic complexes, see above. The red-shift generally decreases with cluster size but becomes nearly constant for n = 5–7 with ν(CO) at 966.3 cm^{-1} (for m = 1). After n = 7 a step-like decrease of the shift is found. This step has been explained by ν(CO) being sensitive to a reduction of coordination number of the Au atom the methanol ligand is bound to, thereby detecting the 2D to 3D transition occurring in these small cationic Au clusters.[346b–d] The 2D to 3D transition – with Au_8^+ being indeed the first cationic gold cluster size forming a 3D structure – was confirmed by a more structure sensitive technique shortly thereafter, *via* the measurement of ion mobilities.[110] In addition, the study reports the observation of a low-frequency onset of bands between 1080 and 1086 cm^{-1} that are assigned to a CH_3 rocking mode.[346d]

IR-MPD spectra for an extended frequency range (615–1760 cm^{-1}) became accessible in a later study of cationic gold cluster-methanol complexes, $Au_n[CD_3OH/D]_m^+$ (n = 1–7; m = 1–4), using FELIX.[347] These spectra now resolve, in addition to ν(CO) at around 925 cm^{-1}, the higher frequency band around 1085 cm^{-1} that is assigned to a coupled CD_3 deformation/C–O stretching mode. In the spectral range studied, only these two bands are found to be sensitive to the interaction with the Au cluster showing, similar to the studies discussed here before, a size-dependent red-shift compared to unbound methanol that is decreasing with cluster size, see Fig. 44. This has been explained by an increasing charge delocalization with growing cluster size leading to a decrease of the fractional charge at the Au binding site. This is very similar to the electrostatic polarization effect discussed for CO complexes (see Section 3.1.2) and leads to a decrease of charge donation from methanol to the cationic Au cluster with increasing cluster size. Hence, also the amount of methanol activation decreases with size.[346c,d,347] A similar effect is observed for increasing methanol coverage. In that case, the total charge donated to the cationic Au cluster is split over multiple methanol molecules leading to a reduction of the C–O activation with coverage. This is reflected in a decreasing red-shift

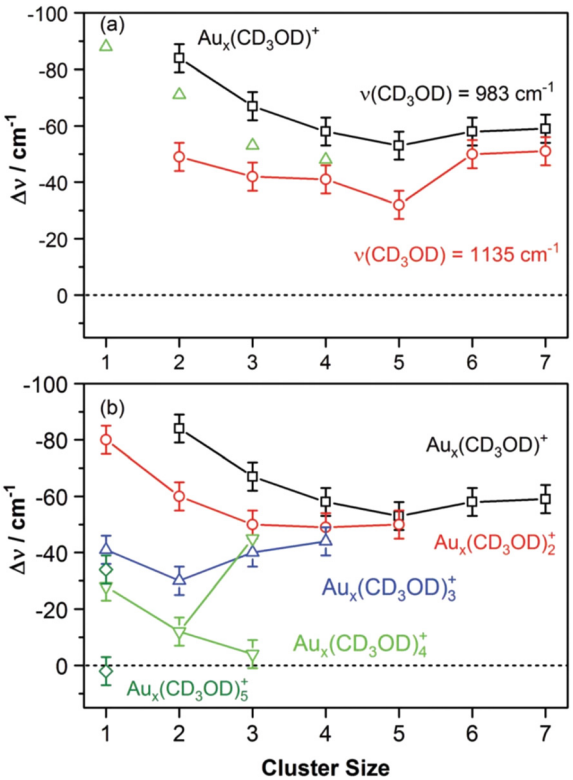

Fig. 44 (a) Shift of ν(CO) (black squares) and of the coupled CD_3 deformation/C–O stretching mode (red circles) in $Au_n(CD_3OD)_m^+$ complexes relative to unbound CD_3OD from IR-MPD spectra obtained with FELIX. Calculated values of ν(CO) are shown as green triangles. (b) ν(CO) for different ligand coverages. Reprinted from ref. 347. Copyright (2019), with permission from De Gruyter.

of ν(CO) with increasing number of adsorbed methanol molecules, see Fig. 44b.

All other studies of TM cluster alcohol complexes have focused on the regions of the O–H and C–H stretch vibrations which are accessible through IR generation in OPO/OPA or DFM/OPA systems (see Section 2.6).

Complexes of nickel cluster cations with methanol $Ni_n(CH_3OH)_m^+$ (n = 3, 4; m = 1–4) have been studied in the region of ν(O–H) and all exhibit a single intense band between 3634 and 3645 cm^{-1}, which is only slightly (~40 cm^{-1}) red-shifted compared to ν(O–H) of free methanol at 3681 cm^{-1}.[77g] For complexes with multiple CH_3OH, no bands have been observed below 3600 cm^{-1} that would signify hydrogen bonding between the ligands. DFT calculations (BPW91/6-311+G(d,p)) for $Ni_n(CH_3OH)^+$ (n = 3, 4) indicate, that dissociative complex formation into hydroxy-methyl $Ni_n(CH_3)(OH)^+$ species is energetically feasible, whereas hydrido-methoxy $Ni_n(CH_3O)(H)^+$ complexes are less stable compared to molecular chemisorption of intact CH_3OH. As the calculated ν(O–H) for $Ni_4(CH_3)(OH)^+$ and $Ni_4(CH_3OH)^+$ are similar, 3641 cm^{-1} and 3666 cm^{-1}, respectively, and these are close to the experimental value of 3645 cm^{-1}, their coexistence has been suggested. For $Ni_3(CH_3)(OH)^+$, however, ν(O–H) is calculated to be at 3596 cm^{-1} and the measured value is 3634 cm^{-1}. Therefore, it is concluded that – for this cluster size – the presence of this species is unlikely, although the DFT calculations predict it to be 0.4 eV more stable compared to non-dissociated $Ni_3(CH_3OH)^+$.[77g] The $Ni_n(CH_3)(OH)^+$ species is proposed as intermediate in the de-methanation of methanol that is observed to occur – under single collision conditions – efficiently for several nickel cluster cations including Ni_4^+, but not for Ni_3^+.[362]

Similar conclusions have been drawn – based on their IR-spectra and related DFT calculations – for the corresponding cobalt cluster complexes, $Co_n(CH_3OH)_m^+$ (n = 1–6; m = 1–3).[343] IR spectra of these complexes have been determined in a wider spectral range (2800–6800 cm^{-1}), including the typical regions of ν(C–H), ν(O–H), and part of the near-IR. Studies of the Co_n^+ + CH_3OH reaction indicate – in addition to simple (and successive) methanol attachment – also formation of dehydrogenated species, $Co_n(CH_2O)^+$. Furthermore, a complex of mass 246 u was found in low intensity, whose mass agreed with that of $Co_2(CH_3OH)_4^+$, however, its formation does not follow the kinetics expected for successive CH_3OH addition.[343a] It can be thus speculated about the nature of this ion and a possible role in the CH_3OH dehydrogenation process. Accompanying DFT calculations predict dissociative methanol binding into $Co_n(CH_3)(OH)^+$ being energetically preferred over molecular chemisorption and accessible *via* $Co_n(CH_3OH)^+$ over a submerged barrier, at least in the case of n = 4, while formation of $Co_n(CH_3O)(H)^+$ is slightly less favorable. However, evidence for the $Co_n(CH_3)(OH)^+$ species mostly comes from the theoretical predictions, as the spectroscopic fingerprints, *i.e.*, the predicted ν(O–H) and ν(C–H) frequencies for $Co_n(CH_3OH)_m^+$ and $Co_n(CH_3)(OH)(CH_3OH)_{m-1}^+$ species are nearly indistinguishable, such that an unambiguous identification – based on the part of the vibrational spectrum studied – would be very difficult. In the IR-PD process only loss of intact CH_3OH is observed, as it was the case for the corresponding Ni complexes, but no IR induced H_2 or CH_2O loss that could further support the presence of an intermediate for methanol dehydrogenation.[343a]

In a subsequent study by the same authors also near-IR spectra of $Co_n(CH_3OH)_3^+$ (n = 1–3) are reported, which show close to 4000 cm^{-1} the low-frequency onset of a broad band for n = 2, 3. By comparison to near-IR optical spectra from TD-DFT calculations this band is suggested as signature of $Co_n(CH_3)(OH)^+$ with the methanol fragments bound at bridge-sites between the Co atoms.[343b]

The results discussed before for the Co and Ni cluster methanol complexes can be compared to later results that base on better resolved spectra of ethanol complexes, $Co_3(C_2H_5OH)^+$, $Co_3Ni(C_2H_5OH)^+$, as well as of the mixed complex $Co_3(C_2H_5OH)(H_2O)^+$.[348,350] For $Co_3(C_2H_5OH)^+$, the O–H stretch is found at 3667 cm^{-1} which is only 10 cm^{-1} redshifted relative to the calculated value for the O-donor bound molecular complex with triangular Co_3^+. Compared to the aforementioned $Co_3(CH_3OH)^+$, this mode is blue-shifted by 18 cm^{-1} which has been explained by a stronger positive inductive effect and therefore a stronger O–H bond in the larger alcohol.[348] In case of $Co_3Ni(C_2H_5OH)^+$, two bands are experimentally found in the region characteristic for ν(O–H), at 3638 cm^{-1} and 3663 cm^{-1}, with the latter being significantly more intense. By comparison to predictions from DFT and CCSD(T) calculations, the higher frequency band is assigned to a structure with a pyramidal Co_3Ni core. Furthermore, complexes containing an intact C_2H_5OH ligand fit the observation best. The lower frequency ν(O–H) band of $Co_3Ni(C_2H_5OH)^+$ at 3638 cm^{-1}, on the other hand, is found to be indicative of adsorption at a planar-rhombic Co_3Ni core structure and best agreement for ν(O–H) is seen in case of a dissociated hydroxy-ethyl complex $Co_3Ni(C_2H_5)(OH)^+$.[350] However, in both cases ν(O–H) appears not to be sensitive to at which TM, either Co or Ni, the ethanol is actually adsorbed to. For the mixed complex, $Co_3(C_2H_5OH)(H_2O)^+$, four bands are found in the region of ν(O–H), indicating that an isomeric mixture must be present. Using DFT calculations (BPW91/6311+G(d,p)) two isomers are identified contributing to the experimental spectrum, one having the ligands, C_2H_5OH and H_2O, bound to different atoms of triangular Co_3^+ (type I) and another (type II) where only ethanol is directly bound to Co *via* the O-donor, and its hydroxyl-H forms a hydrogen bridge to the water molecule.[348] The characteristic spectroscopic signature of such a hydrogen bond would be expected, unfortunately, clearly below the 3600–3800 cm^{-1} range studied.

Finally, for cobalt clusters comparison can be made also to complexes in the anionic charge state. IR spectra of $Co_n(alc)_m^-$ (n = 1–4, alc = methanol, ethanol, *n*-propanol, m = 1–3) have been reported in the ~3100–3300 cm^{-1} range, showing essentially for these complexes one band per ligand which is interpreted as the pattern of O–H stretching mode(s) of a single isomer per system.[344] The large red-shifts found for ν(O–H) indicate a distinctly different binding situation in these anions compared to all the cationic TM-alcohol complexes discussed before. DFT and CASPT2 calculations identify that the TM–ligand interaction is through Co–H–OR hydrogen bonding (of intact alcohol moieties), see Fig. 45, in contrast to O-donor interaction in the cations. Furthermore, all

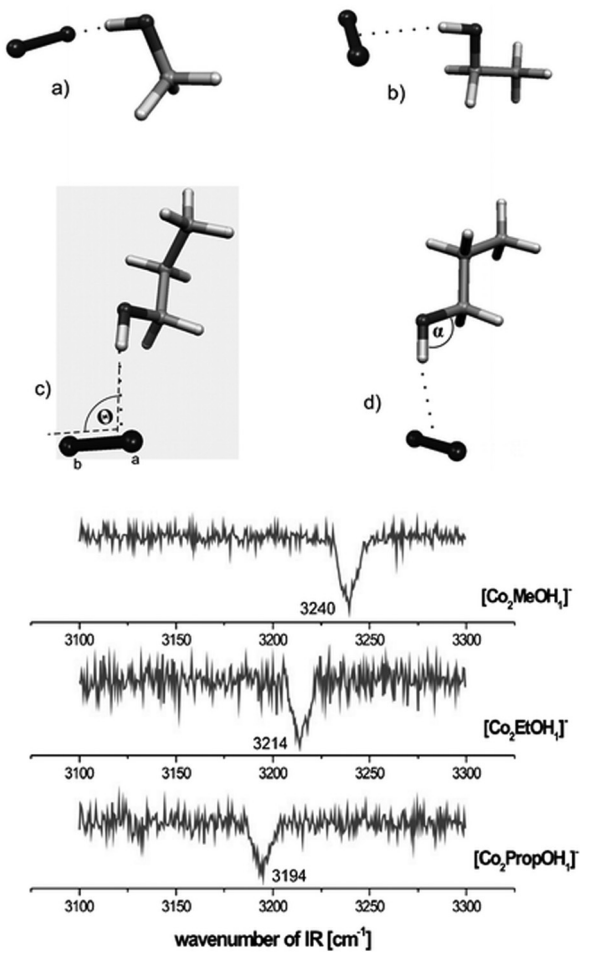

Fig. 45 Top (a–d) Calculated structures for $Co_2(alc)^-$ complexes with alc = methanol, ethanol, and *n*-propanol. In case of *n*-propanol two isomers are shown, with the gauche-isomer (c) being ~600 cm^{-1} more stable compared to the anti-isomer (d). (Bottom) IR depletion spectra of $Co_2(alc)^-$ complexes. The spectrum of the propanol complex is assigned to the gauge-isomer (c) as ν(O–H) of the other isomer is predicted considerably above the experimental value. Reproduced from ref. 344*a* with permission from the PCCP Owner Societies.

alcohol ligands are predicted to bind directly to the metal, hydrogen bonding between multiple alcohol ligands appears energetically less favored. The OH-group of the alcohol is not bound to a single Co atom but is pointing towards the center of a Co–Co bond in the cluster. With increasing size of the alcohol, ν(O–H) shifts to lower frequencies (Fig. 45). On the other hand, with increasing Co cluster size, ν(O–H) increases slightly. Overall, the experimentally observed spectral patterns are very similar for the different alcohols indicating comparable structures in their complexes.

3.3.5 Carboxylates. For gas-phase metal cluster carboxylates, *i.e.*, metal compounds of deprotonated carboxyl acids, so far two IR studies have been reported.[351,352] Anionic copper formate clusters, $Cu_n(HCO_2)_m^-$, containing up to three copper atoms (and their deuterated analogues) produced by electrospray ionization out of a solution have been investigated over the 800–4000 cm^{-1} range, giving access mostly to C–O and C–H stretch vibrations. Depending on the composition, the complexes either contain Cu(I) or Cu(II) which is found to have a significant effect on the position of the C–H stretch fundamentals, while the C–O stretches are less effected.[352] Formate ligands bind in bidentate and monodentate geometries, which are distinguishable, *e.g.*, by their different positions of the symmetric and antisymmetric ν(C–O) stretches of the carboxyl group. For instance, $Cu(HCO)_2^-$ only contains monodentate formate units and shows these modes around 1300 cm^{-1} and 1644 cm^{-1}, respectively, while in $Cu_2(HCO)_3^-$ the bidentate formate bridging the two Cu atoms has its ν_{sym}(C–O) significantly blue-shifted to 1358 cm^{-1}, whereas for ν_{asym}(C–O) two red-shifted bands are found at 1610 and 1629 cm^{-1}. For a given composition, many different conformers are identified that differ by rotation of monodentate formate groups.[352] Their contribution to the experimental spectrum may explain the observed broad width of the IR bands and a number of additional lower intensity signals.

Finally, in an extensive IR study of carboxylic (formic, acetic and propionic) acids and methyl acetate bound to small manganese clusters, Mn_n^+ (n = 1–3), the structure of these complexes in terms of the acids' conformational structures has been investigated.[351] The IR spectra obtained in the 600–1800 cm^{-1} range are found to mostly depend on the acid ligand and they change not significantly for different cluster sizes, indicating a similar binding motif for a given ligand in the $Mn_n(acid)^+$ complexes. The experimental spectra are rather complex and have been interpreted by comparison to spectra predicted by DFT calculations. In these complexes, the acid molecules are not deprotonated, *i.e.*, all contain an intact carboxyl (–COOH) group interacting with the metal *via* a carbonyl group. The appearance of strong bands in the 1500–1800 cm^{-1} range, significantly red-shifted from the value for the carboxyl group in the isolated acids, has been assigned to stretches of the carbonyl groups binding to the metal. Overall, the spectra are interpreted in terms of a mixture of complexes having their carboxylic acid group in either *trans* (O–H pointing towards O–Mn) or *cis* (O–H pointing away from O–Mn) arrangement. While for gas-phase carboxylic acid molecules the *cis* conformer is energetically non-favored, in the Mn complexes it is stabilized and the *trans* and *cis* forms are predicted to be nearly isoenergetic.[351]

3.3.6 Other. Cyanoacetylene (HCCCN) complexes with small neutral magnesium clusters, Mg_n (m = 1–4), have been grown and characterized in superfluid He droplets in the region of ν(C–H).[363] Rotationally resolved infrared spectra as well as Stark spectra have been obtained and show that complexes binding to Mg_n *via* the H and the N-terminus coexist in the He droplets. The H-bonded complexes showing ν(C–H) red-shifted compared to the gas-phase value of HCCCN (3327.4 cm^{-1}) by 22–64 cm^{-1}, while the N-bonded complexes have their ν(C–H) significantly less red-shifted by ~1–9 cm^{-1}. For both classes of isomers, the red-shift increases with the size of the Mg clusters.[363]

4 Co-Adsorption

The binding characteristics of ligands in metal cluster complexes may be determined not only by the intrinsic properties of

the pristine TM cluster as discussed before, but can depend also on the binding of additional, often different, ligands on the same cluster. Such co-adsorbed ligands generally alter the electronic and/or structural properties of the metal cluster and the availability of adsorption sites. Thereby they can significantly change the adsorption environment and also provide additional reaction partners.

Co-Adsorption can be competitive, *e.g.*, if the different reacting species compete for specific adsorption sites on the metal clusters, or cooperative, in case the binding of one species promotes that of the other.[29e,k,260a,364] Examples for the simplest case, the adsorption of multiple but identical ligands on a single cluster, have been given already before. Also the formation of different co-adsorbed species that are, however, originating from the same type of ligand, *e.g.*, through simultaneous dissociative and intact adsorption of a molecular ligand on a cluster has been discussed already in the preceding sections.

Vibrational spectroscopy provides not only information on the structure of a complex but can give a handle to quantify the effect of co-adsorbed species on the electronic properties of a cluster complex. For instance, the change of electron density at the metal by added electron accepting or donating ligands effects the degree of C–O activation in co-adsorbed carbonyl ligands *via* the π backdonation mechanism. The use of ν(C–O) for probing the metal clusters' electron density has been extensively discussed before in Section 3.1.2.

Charged metal clusters undergo – through interaction with ligands – a solvational stabilization *via* charge–(induced)dipole interactions which can have a determining effect, in particular on reactions involving electron transfer. For instance, the binding of O_2 to gold clusters is well-known to be affected by co-adsorbates.[182b,260,365] IR-MPD studies showed that for $Au_2O_2(C_2H_4)_m^+$ (m = 0–2) ν(O–O) gradually decreases with increasing number of co-adsorbed ethylene ligands from 1503 cm^{-1} over 1458 cm^{-1} to 1441 cm^{-1}. This gradual decrease reflects a small, with number of ethylene ligands increasing, partial energy transfer into the dioxygen's π* orbitals that leads to a, however, still only very weakly activated O_2 (see Section 3.1.4).[169] Similarly, the activation of O_2 in $Au_4(O_2)_m^+$ is found to depend on the total number of O_2 ligands and resembles with ν(O–O) ≈ 1260 cm^{-1} for m = 3 that in $Au_4O_2Ar_3^+$.[43c] For Au_{12}^+ and Au_{21}^+ covered by multiple O_2 ligands, solvation even facilitates formation of superoxo (O_2^-) species that are identified by a ν(O–O) band at ≈1065 cm^{-1}, *i.e.*, in these complexes formally a full electron from the already singly positively charged gold cluster is transferred towards a single O_2 ligand.[43c] Driving forces for the latter reaction is the formation of closed electronic shells with 10 and 20 electrons, respectively, together with a higher solvational stabilization of the formally two-fold positively charged metal core of the superoxo complex compared to the initially singly charged cluster.

When multiple different ligands bind to a metal cluster, the order of adsorption can be critical for forming a specific reaction product. For instance, investigating CO adsorption on cationic hydrogen pre-covered vanadium clusters reveals for most sizes intact CO binding, as indicated by the detection of a ν(C–O) band in the 2120–2070 cm^{-1} range for $V_xH_m(CO)^+$ species.[117] On bare V_n^+, however, CO spontaneously dissociates and forms carbide and oxide species such that no ν(C–O) is detectable for $V_n(CO)^+$ complexes, see Section 3.1.2. The difference in CO reactivity is explained by H species occupying bridge and facet sites of the vanadium cluster (Section 3.1.1) and thus blocking potential binding sites for the CO dissociation products. As dissociation thereby becomes unfavorable, CO remains bound molecularly in μ_1 (atop) configuration. CO dissociation is only observed for certain sizes, *e.g.*, $V_5H_6CO^+$ and $V_9H_{12}CO^+$, with incomplete H coverage or where the H layer can undergo rearrangement to effectively make room for CO dissociation.[117] $V_7H_{10}CO^+$ appears to be an interesting intermediate case, where a band attributed to $\nu(\mu_1$-CO) is detected at 2163 cm^{-1} and a second one at 1650 cm^{-1} – well above the typical range for H in bridging or face-capping configuration. Based on DFT calculations (BP86/TZVP), the latter is assigned to activated CO η^2-bound in a strongly tilted configuration between two V atoms.

The order of adsorption has been found to be relevant also for the structure of $Ru_8[H_2][N_2]_4^+$. This complex appears interesting in the context of N_2 activation and hydrogenation. It was formed at cryogenic temperatures by reacting Ru_8^+ with either H_2 or N_2 first in a hexapole reaction cell and then adding the second reactant after transfer of the initially formed complex to the FT-ICR cell.[118] The IR spectra of the thus formed $Ru_8[H_2][N_2]_4^+$ reveal differences depending on in which order H_2 and N_2 are admitted. The main differences are found in the region of ν(Ru–H), around 1800 cm^{-1}, while the pattern of ν(N–N), around 2000 cm^{-1} is not much changed. N_2 pre-adsorption precludes migration of hydride species, such that if N_2 is adsorbed first, the H species formed after H_2 dissociates are localized at adjacent Ru atoms (proximal positions), while if H_2 is allowed to react first, the H-atoms can migrate to slightly more stable distal positions before the path is blocked by the N_2 ligands.[118]

5 IR induced reactions

This section summarizes examples for reactions in TM cluster complexes during IR-MPD that release molecular fragments which differ from the initially absorbed ligand species as characterized by their IR-MPD spectra. Thus, in such cases the adsorbed species has undergone a chemical transformation induced by IR excitation.

The simplest example are TM-hydride complexes, see Section 3.1.1. The reaction of H_2 with TM clusters usually leads to a dissociation of the H_2 molecule on the cluster surface and formation of a complex containing two separate atomic H ligands, while upon IR-MPD this complex loses hydrogen again as H_2 entity. Apparently, the recombination of atomic H ligands represents an *IR induced reaction*, which is – although H–H recombination can be related with substantial reaction barriers – more feasible then ejection of single H atoms due to the significant bond energy gained in H_2 formation.

Generally, as IR multiple photon excitation does rely on fast internal vibrational energy redistribution (IVR) throughout the

entire cluster complex, in case the internal energy of a metal cluster complex becomes sufficiently high, its fragmentation proceeds under kinetic control. Reactions in cluster complexes induced by such ergodic excitation mechanism do not show mode-selectivity, *i.e.*, their pathway does not depend on which specific vibrational mode is excited, but rather on the total increase of internal energy and its rate.[366] The independence of the IR-MPD fragmentation pathway on the excited mode has been discussed, *e.g.*, in Section 3.2.4 using the example of $Rh_n(N_2O)^+$ complexes. The behavior can be different in systems where IVR is inefficient, *e.g.*, typically in very small complexes[367] with their inherently low density of vibrational states – thereby also states that can act as doorway for IVR get scarce – or in other complexes with hindered IVR,[368] *i.e.*, through a strong frequency mismatch between initially excited and background modes. Furthermore, direct electronic excitation may lead to fragmentation patterns different from vibrational excitation. This can be observed even for low energy electronic excitation in the (near)IR.[40d]

In case the fragmentation of a cluster complex does not involve particular steric or electronic demands leading to additional barriers, the activation barrier for dissociation is largely determined by the overall dissociation energy. If no other reaction pathways are accessible for an M_n–L complex at this energy, the 'simple' loss of the ligand L can be observed as dominating fragmentation channel. However, also more complex and cluster size dependent reaction patterns have been observed, in particular, in cases of energetically competing pathways.

For a complex of a metal cluster with a molecular ligand, principally at least two reactions need to be considered: (i) intact molecular desorption *vs.* (ii) ligand activation and reorganization. An example, where both processes have been observed, are complexes of cationic platinum clusters with methane and Ar, $Pt_nCH_4Ar_2^+$, formed *via* ligand exchange of Ar with CH_4. These complexes are characterized by their IR-MPD spectra to contain only slightly activated, though intact CH_4 entities,[63a] see Section 3.3.2. However, they show different prevailing fragmentation channels depending on the Pt cluster size.

Partial dehydrogenation in competition with CH_4 and Ar desorption is seen for Pt_3^+ and Pt_5^+, while for Pt_4^+ a dehydrogenation channel is not observed. Schematic potential energy curves illustrating both pathways, *i.e.*, desorption of intact CH_4 *vs.* C–H activation followed by partial dehydrogenation and H_2 desorption, are depicted in Fig. 46. Here, the right part of the scheme leading to partial dehydrogenation is strongly simplified and only an effective reaction barrier is plotted for the stepwise dehydrogenation that actually involves a large number of single reaction steps.[369] Already from this simple scheme it should be obvious that the preferred fragmentation channel depends on the relative heights of the barrier for desorption (*i.e.* largely given by the dissociation energy) and the effective barrier for ligand activation. A comparably high barrier along the bond activation and dehydrogenation path results in molecular desorption being prevailing during IR-MPD. On the other hand, submerged barriers on the bond activation path may result in a spontaneous bond activation including further stabilizing reactions occurring already during formation of the complex, *i.e.*, it may not be possible or difficult to isolate a molecular complex. This is the case, *e.g.*, for CO reacting with clusters of the early transition metals (Section 3.1.2). For NO, even both adsorption modes have been observed, for instance for iridium clusters[160] (Section 3.1.5).

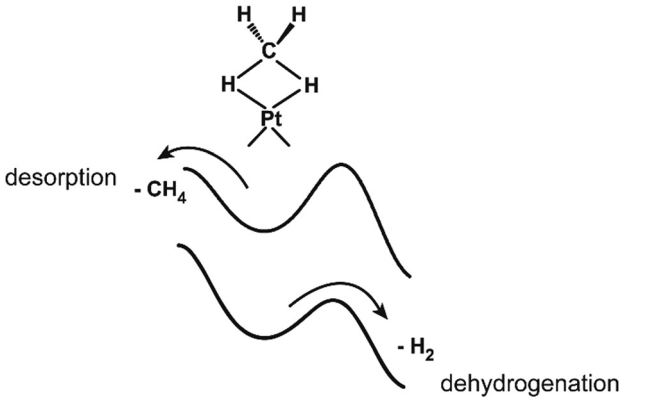

Fig. 46 Schematic potential energy curves for the IR induced desorption *vs.* dehydrogenation processes in $Pt_nCH_4^+$. IR excitation induces dehydrogenation for Pt_3^+ and Pt_5^+ (lower curve), while for Pt_4^+ the main reaction channel is loss of intact CH_4 (upper curve), for details see ref. 63*a*. Reprinted from ref. 29*h* with permission of John Wiley and Sons.

IR absorption through modes of a molecular ligand may also trigger its decomposition towards fragments that are each significantly stronger bound to the metal cluster than the molecular ligand initially. This would be usually the case, *e.g.*, for dissociatively bound CO or NO. Then, observation of any IR-MPD process may become difficult, or the experiment has to be performed at extreme IR fluence to reach the high internal energies needed for fragmentation or even ionization, see the discussion of intra-cavity FEL experiments in Section 2.6. The problem may – at least in part – be circumvented by using weakly bound messengers (He, Ne, Ar complexes) for detecting the IR absorption of the complex, see Section 2.2. However, the presence of the messenger and the low temperature conditions to form messenger complexes may already alter the properties of the complex.

If stable molecular complexes can be formed and the barriers for dissociation *vs.* activation and reaction in these complexes are comparable, it depends on the subtleties of the cluster system which path is actually preferred to occur after IR excitation. Here the detailed cluster properties, like specific geometries or electronic structures come into play. As for many metal clusters, these undergo characteristic size-dependent changes and this naturally also may influence the pathway of IR induced reactions.

For instance, closed/open shell oscillations in the electronic configuration of cationic gold clusters complexed with OCS, Au_nOCS^+,[288] cause the size-dependent variations in the IR induced sulfide formation together with CO loss as has been discussed in Section 3.2.3. Noteworthy, the IR-MPD spectra of the Au_nOCS^+ complexes do not show related oscillations in band positions revealing that there is no variation in the initial activation of the ligand in the stable complex but the difference must be in the rates of the IR-induced reactions leading to its decomposition.

Other systems showing characteristic size dependencies in their IR-MPD pathways are complexes of cationic Rh and Pt clusters with N_2O, as discussed in Section 3.2.4. Also in these cases the variations between O-transfer and N_2O release, *e.g.*, for $Pt_nN_2O^+$ a strong increase in the O-transfer channel from $n = 6$ onwards, can be related to the effective barrier height in the O-transfer channel which is, in case of $n = 6$, calculated to be submerged with respect to the energy of the free reactants.[292] The steric requirements for the bending of the N-bound N_2O to transfer its O to a metal atom in the cluster can explain the high sensitivity of the reaction towards the cluster's structure, see before.

The (sometimes strong) changes of electronic structure and geometry with size, as well as an often high structural flexibility are inherently cluster-specific properties, however, their underlying reactivity follows also more general principles. This has been further detailed for NO complexes of late transition metal clusters (Section 3.1.5), where – following the Bell–Evans–Polanyi principle – the cluster's affinity to atomic oxygen is the key property determining the barrier height for NO dissociation and thereby the overall course of the reaction.[158b]

We will conclude here the discussion of IR induced reactions in TM cluster complexes with classical examples for models of intermediates in CO oxidation processes, namely co-adsorbates of oxygen species and carbon monoxide on TM clusters. These co-adsorbates are usually formed by reactions of the metal clusters with oxidants like O_2 or N_2O (as single O-atom source[371]) as well as CO.

In studies of CO bound to oxidized copper or gold dimers, $Cu_2O_2(CO)_n^+$ (n = 3–7)[146] and $Au_2O_2(CO)_n^-$ (n = 2–6),[44] there have been no indications for CO oxidation reactions, neither within the complexes nor induced by IR excitation, although Au_2^- is well-known to catalyse CO oxidation by O_2 in the gas phase.[42] This discrepancy has been explained by a much longer reaction time in the latter experiment that is performed in an ion trap allowing for the formation of thermodynamically more stable carbonate complexes which have been proposed as intermediates of the CO oxidation.[44] Furthermore, the multiple CO ligands may act as coolant such that IR excitation of the complex leads to desorption of the weakly bound CO ligands rather than activating the CO oxidation pathway.

Noteworthy, O/CO co-adsorbates can also be prepared by reaction of *anionic* clusters of late TM with CO_2 where the CO_2 gets activated and split into co-adsorbed oxide and carbonyl species as observed for certain cobalt, platinum, as well as carbon doped copper clusters, see Section 3.2.2. While this decomposition of CO_2 into O and CO in the TM cluster complexes is confirmed by their vibrational spectra, for cobalt IR-MPD proceeds *via* release of CO, but for the platinum complexes CO_2 is effectively re-formed, *i.e.*, CO is oxidized back to CO_2. This is the same reaction as observed when reacting pre-oxidized platinum clusters with CO: CO_2 is released and the bare Pt clusters form which then can be re-oxidized (by O_2 or N_2O) to close a catalytic cycle, see Fig. 47. A similar reaction is well known for anionic as well as cationic platinum clusters in the gas phase.[370,372] Stable O/CO co-adsorbates as intermediates have not been observed in these reactivity experiments. The formation of the intermediates by dissociating CO_2 (Fig. 47, red arrows) appears as an appealing approach, though it is unfortunately not proven that these complexes are identical to the ones formed by successive addition of O and CO to the platinum clusters.

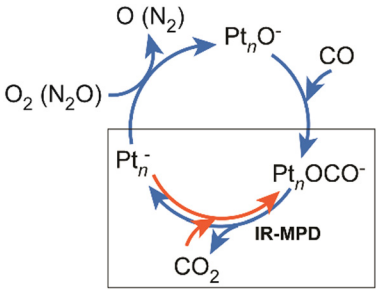

Fig. 47 CO_2 activation by anionic platinum clusters (red arrows) in relation to the catalytic cycle for CO oxidation by O_2 or N_2O after Shi and Ervin (clockwise circle of blue arrows).[370] The O/CO co-adsorbates are short-lived intermediates and have not been observed in the original reactivity studies. Such complexes can be formed, however, by direct reaction of Pt_n^- (n = 5–7) with CO_2. IR-MPD of these complexes occurs under release of CO_2 again.[285] For further details of the CO_2 activation, see Section 3.2.2.

In case of cationic platinum clusters, Pt_n^+ (n = 3–7), however, co-adsorption of O_2 and CO (in part together with Ar as messenger) under stabilizing multiple collision conditions at ambient temperature allowed for formation and spectroscopic characterization of a number of stable product complexes.[63b] For $Pt_4O_2COAr^+$, two different types of complexes are identified to contribute to its IR-MPD spectrum (Fig. 48): one containing oxygen in form of a peroxo group, the other as two separate bridging oxo groups. After IR excitation, the complexes evolve CO_2 (with a branching ratio of about 2/3 for CO_2 *vs.* CO release which may relate to the different binding types of oxygen in the complexes)

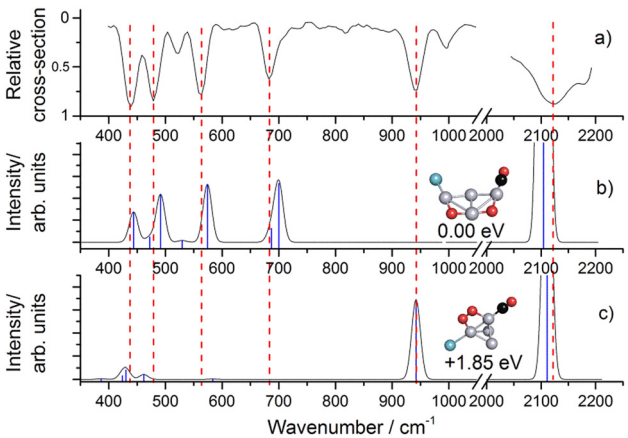

Fig. 48 Experimental IR-MPD spectrum of $Pt_4O_2COAr^+$ (a) compared to the predicted spectrum (DFT: TPSS/def2-TZVP) for the putative global minimum isomer (b) and a second isomer (c) containing a peroxo unit that explains the strong band at 940 cm^{-1}. The intense ν(CO) band at 2125 cm^{-1} is in these experiments highly saturated and therefore appears strongly broadened. Reproduced from ref. 63*b* with permission from the Royal Society of Chemistry.

such that a dominant fraction of these co-adsorbates can be truly understood as reaction intermediates in the oxidation of CO by O_2.

6 Conclusions and outlook

The introduction of IR-FELs in the field of molecular spectroscopy facilitates unique experiments that allow for unprecedented insights into the reactions of gas-phase transition metal clusters with small molecular ligands. Free electron lasers as accelerator based light sources cover, compared to other laser systems, extremely wide spectral ranges and provide sufficiently high photon fluence to effectively drive infrared multiple photon dissociation (IR-MPD) of such metal cluster complexes. Cluster size and composition specific vibrational spectra are obtained by a combination of IR-MPD (or IR-PD) with mass spectrometric detection of the fragmentation. The spectroscopic data reviewed here provides detailed insights into the coordination geometry of ligands to isolated transition metal clusters, the type of binding, activation of bonds within the ligands and further reactions, happening spontaneously or being induced by the absorption of IR photons, as well as how these depend on the metal cluster's size and, in certain cases, their charge states.

The possibilities to effectively produce clusters of various transition metals in different sizes and charge states *via* laser ablation, the interrogation of their gas-phase chemistry using mass spectrometry, the development of various structure sensitive experiments and of powerful theoretical approaches like novel DFT and *ab initio* methods, as well as the tool box of action spectroscopies, and in particular their applications to IR spectroscopy have indeed provided *valuable insights to chemisorption and catalysis on surfaces*, just as envisioned by Earl Muetterties in the earlier years of metal cluster science. This review highlights many of the similarities between the chemistry of molecules adsorbed on extended metal surfaces and bound to metal clusters as observed by using infrared spectroscopy.

Nevertheless, it should became very clear that clusters differ from metals in their extended form in important aspects, not only in the number of surface *vs.* bulk atoms that naturally leads to a much higher fraction of surface sites in a nano-dispersed system, but that there are also more fundamental differences related to cluster-specific properties, like the discrete molecular-like electronic structure, size-dependent geometrical arrangements, lower over-all atomic coordination and finally, a high structural flexibility that goes much beyond that of surfaces of well-ordered crystalline materials.

Small clusters rather resemble exposed metal particles within a '*granule surface*', a picture introduced already nearly 100 years ago by H. S. Taylor in his '*Theory of the Catalytic Surface*'.[373] Low-coordinated atomic sites within such structures are suggested to be responsible for certain catalytic surface reactivities and they are strongly connected with the concept of *active sites* as introduced by Taylor. He already notices that atoms in such granules '*will have a greater freedom of motion*', which may be interpreted as a structural flexibility, an inherent property of many (small) reacting metal clusters. Noteworthy, the picture of metal clusters adhered to a surface is not outdated by today, but still a very successful and widespread conceptual model to obtain an understanding of heterogeneous catalytic reactions and it gets further extended to more complex systems.[34d]

So far, in most cases the IR spectroscopic characterization of these gas-phase TM complexes has focused on the internal ligand modes, as these are generally well localized and do not depend much on the detailed cluster structure. Further, they are usually easier to study experimentally – in particular by using fragmentation techniques like IR-MPD – since they occur at higher energy and often show significant higher IR intensities than, for instance, external M–L modes, as has been discussed exemplary in Section 3.1.2 for carbonyl complexes. Furthermore, this spectral data can be, in many cases, readily compared to those of adsorbates on surfaces or of stable, structurally well characterized complexes, which facilitates the assignments often even without comparison to detailed quantum-chemical calculation.

In fact, despite this has been pursued from the beginning of cluster reactivity studies in the gas phase on, there exist only very few examples yet where such IR spectra allowed for a full structural characterization of a gas-phase metal cluster complex (aside from stable cluster compounds and very small systems like complexes of metal dimers), detailing how the structure of a reacting cluster changes from its initial structure. This requires spectroscopic information for the metal cluster complex over a wide spectral range, including the far-IR region where the metal cluster modes are located, equivalent data for the unreacted cluster, and reliable predictions of structures and their related IR spectra by quantum chemical methods. Despite all the recent progress in the field of quantum-chemical calculations, this usually still constitutes the bottleneck in such studies of transition metal cluster complexes. Certainly, for a better understanding of the role of structural flexibility in the cluster's reactivities further insights into how the metal framework is affected upon complex formation would be highly desired.

Such structural changes may be sensed, of course, also by other experimental techniques and the combination of IR-MPD (and similar action spectroscopies) with structure sensitive separation methods, in particular ion mobility mass spectrometry, is a strongly emerging field.[374] Notably, the first detection of structural flexibility and isomerism in a transition metal cluster by ion mobility mass spectrometry dates back just over 20 years,[38a] but to our knowledge, such studies have not been extended yet to reacted transition metal clusters.

The review has been limited to complexes of transition metal clusters, however, this is just a small subset of inorganic cluster systems of relevance for modeling surface chemistry relevant for heterogeneous catalytic reactions. By today, a wide selection of clusters with more complex composition that are often also more stable are scrutinized for their ability, *e.g.*, to activate and functionalize small molecules like N_2 or CH_4.[233,244b,375] These clusters typically contain transition metal atoms in higher oxidation states (in a bare neutral cluster it is formally zero) in the form of oxides, carbides, nitrides *etc.* Thereby they can

provide more divers and rather different types of active metal sites compared to a bare metal cluster. In this regard, also mixed-metal systems are of high interest which contain isolated active metal atoms that can be seen as model for single-atom catalysts, a relative new and promising class of heterogeneous catalysts.[376]

The concepts described here that make action spectroscopies exceptionally sensitive methods, allowing to obtain IR spectra of extremely dilute media like isolated cluster complexes, have been lately also applied to surfaces to effectively discriminate between IR absorption of surface and bulk sites. In such experiments, the rapid desorption of surface bound noble gas atoms upon resonant IR absorption at specific surface sites competes with dissipation towards the bulk and allows, therefore, the measurement of surface specific IR spectra by determining the efficacy of noble gas atom desorption as function of IR excitation frequency.[377]

Overall, it has been demonstrated that the characterization of metal cluster complexes by gas-phase vibrational spectroscopy can give detailed structural information, but aside from the ability to trigger reactions in these complexes *via* IR-MPD, dynamical aspects have not played a significant role in these investigations. Studies of dynamical processes in isolated metal cluster complexes, like the mechanism of energy dissipation upon vibrational excitation of a specific (ligand) mode, its mechanisms and time-scales as well as in-depth insight into the single steps of IR induced reactions are largely unexplored by experiment. For such experiments, the wide spectral tunability of IR-FELs as well as the time structure of the light that is emitted in trains of micropulses of a (adjustable) duration between several 100 fs and few ps, together with their transform-limited bandwidth, make them superior light sources for IR pump-probe experiments. Specifically for such experiments, an upgrade of the FHI-FEL is close to completion that will allow lasing at two largely independently tunable wavelengths from two separate undulators that are fed, however, by essentially the same electron macropulse. This is expected to keep the light pulses from the two undulators well synchronized on a ps timescale.[86] Then, the delay between micropulses out of the two trains can be controlled without affecting the time-structure within the two separate macropulses.

The wide success of IR-FEL based experiments and, in particular, of those utilizing action spectroscopy in the gas phase has in the last years significantly increased the demands for beam time at such facilities. Therefore, the world-wide number of IR-FELs particularly designed also for those experiments is constantly increasing, with, *e.g.*, FeliChEM in Hefei (China) being today one of the youngest facilities. New IR-FELs are getting proposed, for instance, entirely new ones like in Canada[378] or as extensions of existing electron accelerator systems. Together with the already existing facilities, such new installations will literally light the future of infrared spectroscopy.

List of abbreviations

APES	Anion photoelectron spectroscopy
BO	Bond order
DFM	Difference frequency mixing
DFT	Density functional theory
FEL	Free electron laser
FELICE	Free Electron Laser for Intra Cavity Experiments
FELIX	Free Electron Laser for Infrared eXperiments (located at RU Nijmegen, until 2012 at FOM Institute Rijnhuizen, Nieuwegein, The Netherlands)
FT-ICR	Fourier transform ion cyclotron resonance (mass spectrometer)
fwhm	Full width at half maximum
HeIRSS	Infrared laser Stark spectroscopy in superfluid He droplets
IR-PD	Infrared photo dissociation
IR-MPD	Infrared multiple photon dissociation
IVR	Intramolecular vibrational (energy) redistribution
L	Ligand
M	Metal (atom)
m	Number of ligands, coverage
MS	Mass spectrometer (or spectrometry)
n	Number of atoms, cluster size
Ng	Noble gas (atom)
OPO	Optical parametric oscillator
OPA	Optical parametric amplifier
TD-DFT	Time-dependent density functional theory
TM	Transition metal (atom)
ToF	Time-of-flight (mass spectrometer)
VUV	Vacuum ultraviolet

Conflicts of interest

There are no conflicts to declare.

Acknowledgements

I gratefully acknowledge the contributions from all authors of the original papers. I thank in particular Gerard Meijer and Gert von Helden for their continued support and helpful comments on the manuscript. This work has been supported by the Max Planck Society and the Deutsche Forschungsgemeinschaft through a Heisenberg grant (FI 893/5). Open Access funding provided by the Max Planck Society.

References

1 E. L. Muetterties, *Science*, 1977, **196**, 839–848.
2 E. L. Muetterties, *J. Organomet. Chem.*, 1980, **200**, 177–190.
3 (*a*) G. Blyholder, *Surf. Sci.*, 1974, **42**, 249–260; (*b*) J. E. Hülse and M. Moskovits, *Surf. Sci.*, 1976, **57**, 125–142; (*c*) H. Conrad, G. Ertl, H. Knözinger, J. Küppers and E. E. Latta, *Chem. Phys. Lett.*, 1976, **42**, 115–118; (*d*) H.-J. Freund and G. Hohlneicher, *Ber. Bunsenges. Phys. Chem.*, 1979, **83**, 100–108.
4 (*a*) J. R. Lombardi and B. Davis, *Chem. Rev.*, 2002, **102**, 2431–2460; (*b*) O. Hübner and H. J. Himmel, *Chem. – Eur. J.*, 2018, **24**, 8941–8961.

5 X. Lin, N. Nilius, H. J. Freund, M. Walter, P. Frondelius, K. Honkala and H. Häkkinen, *Phys. Rev. Lett.*, 2009, **102**, 206801.
6 Z. Li, H.-Y. T. Chen, K. Schouteden, T. Picot, T.-W. Liao, A. Seliverstov, C. Van Haesendonck, G. Pacchioni, E. Janssens and P. Lievens, *Sci. Adv.*, 2020, **6**, eaay4289.
7 (*a*) J. Li, X. Li, H.-J. Zhai and L.-S. Wang, *Science*, 2003, **299**, 864–867; (*b*) P. Gruene, D. M. Rayner, B. Redlich, A. F. G. van der Meer, J. T. Lyon, G. Meijer and A. Fielicke, *Science*, 2008, **321**, 674–676.
8 (*a*) in *Clusters of Atoms and Molecules I: Theory, Experiment, and Clusters of Atoms*, ed. H. Haberland, Springer-Verlag, Berlin, 1994; (*b*) *Clusters of Atoms and Molecules II: Solvation and Chemistry of Free Clusters, and Embedded, Supported and Compressed Clusters*, ed. H. Haberland, Springer-Verlag, Berlin, 1994; (*c*) H. Pauly, *Atom, Molecule and Cluster Beams I: Basic Theory, Production and Detection of Thermal Energy Beams*, Springer, 2000; (*d*) H. Pauly, *Atom, Molecule and Cluster Beams II: Cluster Beams, Fast and Slow Beams, Accessory Equipment and Applications*, Springer, 2000.
9 (*a*) T. G. Dietz, M. A. Duncan, D. E. Powers and R. E. Smalley, *J. Chem. Phys.*, 1981, **74**, 6511–6512; (*b*) V. E. Bondybey and J. H. English, *J. Chem. Phys.*, 1981, **74**, 6978–6979; (*c*) M. A. Duncan, *Rev. Sci. Instr.*, 2012, **83**, 041101.
10 (*a*) H. Haberland, M. Karrais and M. Mall, *Z. Phys. D*, 1991, **20**, 413–415; (*b*) H. R. Siekmann, C. Lüder, J. Faermann, H. O. Lutz and K. H. Meiwes-Broer, *Z. Phys. D*, 1991, **20**, 417–420.
11 (*a*) D. C. Parent and S. L. Anderson, *Chem. Rev.*, 1992, **92**, 1541–1565; (*b*) M. B. Knickelbein, *Ann. Rev. Phys. Chem.*, 1999, **50**, 79–115; (*c*) R. A. J. O'Hair and G. N. Khairallah, *J. Cluster Sci.*, 2004, **15**, 331–363; (*d*) Z. Luo, A. W. Castleman and S. N. Khanna, *Chem. Rev.*, 2016, **116**, 14456–14492.
12 (*a*) W. D. Knight, K. Clemenger, W. A. de Heer, W. A. Saunders, M. Y. Chou and M. L. Cohen, *Phys. Rev. Lett.*, 1984, **52**, 2141–2143; (*b*) T. P. Martin, *Phys. Rep.*, 1996, **273**, 199–241; (*c*) S. Neukermans, E. Janssens, R. E. Silverans and P. Lievens, in *The Chemical Physics of Solid Surfaces*, ed. D. P. Woodruff, Elsevier, 2007, vol. 12, pp. 271–297.
13 P. Weis, *Int. J. Mass Spectrom.*, 2005, **245**, 1–13.
14 D. Schooss, M. N. Blom, J. H. Parks, B. V. Issendorff, H. Haberland and M. M. Kappes, *Nano Lett.*, 2005, **5**, 1972–1977.
15 (*a*) W. A. de Heer and P. Milani, *Rev. Sci. Instr.*, 1991, **62**, 670–677; (*b*) M. B. Knickelbein, *J. Chem. Phys.*, 2002, **116**, 9703–9711.
16 (*a*) M. M. Kappes, M. Schär, P. Radi and E. Schumacher, *J. Chem. Phys.*, 1986, **84**, 1863–1875; (*b*) D. G. Leopold, J. Ho and W. C. Lineberger, *J. Chem. Phys.*, 1987, **86**, 1715–1726; (*c*) O. Cheshnovsky, K. J. Taylor, J. Conceicao and R. E. Smalley, *Phys. Rev. Lett.*, 1990, **64**, 1785–1788; (*d*) B. A. Collings, K. Athanassenas, D. Lacombe, D. M. Rayner and P. A. Hackett, *J. Chem. Phys.*, 1994, **101**, 3506–3513; (*e*) S. Minemoto, A. Terasaki and T. Kondow, *J. Chem. Phys.*, 1996, **104**, 5770–5775; (*f*) M. B. Knickelbein, *Philos. Mag. B*, 1999, **79**, 1379–1400.
17 (*a*) M. Förstel, W. Schewe and O. Dopfer, *Angew. Chem., Int. Ed.*, 2019, **58**, 3356–3360; (*b*) M. Förstel, K. M. Pollow, K. Saroukh, E. A. Najib, R. Mitric and O. Dopfer, *Angew. Chem., Int. Ed.*, 2020, **59**, 21403–21408; (*c*) M. Förstel, K. Pollow, T. Studemund and O. Dopfer, *Chem. – Eur. J.*, 2021, **27**, 15075–15080.
18 (*a*) W. A. de Heer, W. D. Knight, M. Y. Chou and M. L. Cohen, *Solid State Phys.*, 1987, **40**, 93–181; (*b*) G. Wrigge, M. A. Hoffmann and B. V. Issendorff, *Phys. Rev. A: At., Mol., Opt. Phys.*, 2002, **65**, 063201.
19 (*a*) G. Ganteför, in *Quantum Phenomena in Clusters and Nanostructures*, ed. S. N. Khanna and A. W. Castleman Jr, Springer, 2003, pp. 29–54; (*b*) Y. D. Kim and G. Ganteför, *J. Mol. Struct.*, 2004, **692**, 139–144; (*c*) D. M. Neumark, *J. Phys. Chem. A*, 2008, **112**, 13287–13301; (*d*) H. J. Zhai and L. S. Wang, *Chem. Phys. Lett.*, 2010, **500**, 185–195; (*e*) J. L. Mason, C. N. Folluo and C. C. Jarrold, *J. Chem. Phys.*, 2021, **154**, 200901.
20 (*a*) D. Stolcic, M. Fischer, G. Ganteför, Y. D. Kim, Q. Sun and P. Jena, *J. Am. Chem. Soc.*, 2003, **125**, 2848–2849; (*b*) W. Huang, H.-J. Zhai and L.-S. Wang, *J. Am. Chem. Soc.*, 2010, **132**, 4344–4351.
21 (*a*) K. Hirsch, J. T. Lau, P. Klar, A. Langenberg, J. Probst, J. Rittmann, M. Vogel, V. Zamudio-Bayer, T. Möller and B. von Issendorff, *J. Phys. B: At., Mol. Opt. Phys.*, 2009, **42**, 154029; (*b*) J. Bahn, P. Oelßner, M. Köther, C. Braun, V. Senz, S. Palutke, M. Martins, E. Rühl, G. Ganteför, T. Möller, B. von Issendorff, D. Bauer, J. Tiggesbäumker and K. H. Meiwes-Broer, *New J. Phys.*, 2012, **14**, 075008.
22 K. Siegbahn, *Rev. Mod. Phys.*, 1982, **54**, 709–728.
23 (*a*) S. Peredkov, M. Neeb, W. Eberhardt, J. Meyer, M. Tombers, H. Kampschulte and G. Niedner-Schatteburg, *Phys. Rev. Lett.*, 2011, **107**, 233401; (*b*) M. Niemeyer, K. Hirsch, V. Zamudio-Bayer, A. Langenberg, M. Vogel, M. Kossick, C. Ebrecht, K. Egashira, A. Terasaki, T. Möller, B. V. Issendorff and J. T. Lau, *Phys. Rev. Lett.*, 2012, **108**, 057201.
24 (*a*) R. L. Whetten, D. M. Cox, D. J. Trevor and A. Kaldor, *Phys. Rev. Lett.*, 1985, **54**, 1494–1497; (*b*) R. L. Whetten, M. R. Zakin, D. M. Cox, D. J. Trevor and A. Kaldor, *J. Chem. Phys.*, 1986, **85**, 1697–1698; (*c*) J. Conceicao, R. T. Laaksonen, L. S. Wang, T. Guo, P. Nordlander and R. E. Smalley, *Phys. Rev. B: Condens. Matter Mater. Phys.*, 1995, **51**, 4668–4671; (*d*) A. Bérces, P. A. Hackett, L. Lian, S. A. Mitchell and D. M. Rayner, *J. Chem. Phys.*, 1998, **108**, 5476–5490; (*e*) B. E. Salisbury, W. T. Wallace and R. L. Whetten, *Chem. Phys.*, 2000, **262**, 131–141.
25 S. J. Riley, *J. Non-Cryst. Solids*, 1996, **205–207**, 781–787.
26 (*a*) D. J. Wales, *Energy Landscapes: Applications to Clusters, Biomolecules and Glasses*, Cambridge University Press, 2004; (*b*) B. Assadollahzadeh and P. Schwerdtfeger, *J. Chem. Phys.*, 2009, **131**, 064306–064311; (*c*) C. V. Ciobanu, C.-Z. Wang and K.-M. Ho, *Atomic Structure Prediction of Nanostructures, Clusters and Surfaces*, Wiley-VCH, 2013; (*d*) M. P. Johansson, I. Warnke, A. Le and F. Furche, *J. Phys. Chem. C*, 2014, **118**,

29370–29377; (*e*) M. Jäger, R. Schäfer and R. L. Johnston, *Adv. Phys. X*, 2018, **3**, 1516514; (*f*) J. Zhang and V. A. Glezakou, *Int. J. Quantum Chem.*, 2021, **121**, e26553; (*g*) S. M. Woodley and S. T. Bromley, in *Frontiers of Nanoscience*, ed. S. T. Bromley and S. M. Woodley, Elsevier, 2018, vol. 12, pp. 1–54.

27 (*a*) N. Shao, W. Huang, Y. Gao, L.-M. Wang, X. Li, L.-S. Wang and X. C. Zeng, *J. Am. Chem. Soc.*, 2010, **132**, 6596–6605; (*b*) M. Sierka, *Prog. Surf. Sci.*, 2010, **85**, 398–434; (*c*) D. J. Harding, P. Gruene, M. Haertelt, G. Meijer, A. Fielicke, S. M. Hamilton, W. S. Hopkins, S. R. Mackenzie, S. Neville and T. R. Walsh, *J. Chem. Phys.*, 2010, **133**, 214304; (*d*) J. Du, X. Sun and G. Jiang, *J. Chem. Phys.*, 2012, **136**, 094311; (*e*) T. Rapps, R. Ahlrichs, E. Waldt, M. M. Kappes and D. Schooss, *Angew. Chem., Int. Ed.*, 2013, **52**, 6102–6105; (*f*) J. van der Tol, D. Jia, Y. Li, V. Chernyy, J. M. Bakker, M. T. Nguyen, P. Lievens and E. Janssens, *Phys. Chem. Chem. Phys.*, 2017, **19**, 19360–19368; (*g*) M. Kraft, J. R. Flores, W. Klopper, M. M. Kappes and D. Schooss, *J. Phys. Chem. A*, 2021, **125**, 3135–3145.

28 (*a*) M. B. Knickelbein and S. Yang, *J. Chem. Phys.*, 1990, **93**, 1476–1477; (*b*) F. A. Akin and C. C. Jarrold, *J. Chem. Phys.*, 2003, **118**, 1773–1778; (*c*) A. Fielicke, C. Ratsch, G. von Helden and G. Meijer, *J. Chem. Phys.*, 2005, **122**, 091105; (*d*) W. Huang, R. Pal, L.-M. Wang, X. C. Zeng and L.-S. Wang, *J. Chem. Phys.*, 2010, **132**, 054305.

29 (*a*) K. M. Ervin, *Chem. Rev.*, 2001, **101**, 391–444; (*b*) P. B. Armentrout, *Int. J. Mass Spectrom.*, 2003, **227**, 289–302; (*c*) D. K. Böhme and H. Schwarz, *Angew. Chem., Int. Ed.*, 2005, **44**, 2336–2354; (*d*) T. M. Bernhardt, *Int. J. Mass Spectrom.*, 2005, **243**, 1–29; (*e*) S. M. Lang, D. M. Popolan and T. M. Bernhardt, in *The Chemical Physics of Solid Surfaces*, ed. D. P. Woodruff, Elsevier, 2007, vol. 12, pp. 53–90; (*f*) S. M. Lang and T. M. Bernhardt, *Phys. Chem. Chem. Phys.*, 2012, **14**, 9255–9269; (*g*) H. Schwarz, *Isr. J. Chem.*, 2014, **54**, 1413–1431; (*h*) D. J. Harding and A. Fielicke, *Chem. – Eur. J.*, 2014, **20**, 3258–3267; (*i*) Y.-X. Zhao, Q.-Y. Liu, M.-Q. Zhang and S.-G. He, *Dalton Trans.*, 2016, **45**, 11471–11495; (*j*) S. M. Lang and T. M. Bernhardt, in *Clusters: Structure, Bonding and Reactivity*, ed. M. T. Nguyen and B. Kiran, Springer International Publishing, Cham, 2017, pp. 325–359; (*k*) G. Niedner-Schatteburg, in *Clusters – Contemporary Insight in Structure and Bonding*, ed. S. Dehnen, Springer International Publishing, Cham, 2017, pp. 1–40; (*l*) Y.-X. Zhao, X.-G. Zhao, Y. Yang, M. Ruan and S.-G. He, *J. Chem. Phys.*, 2021, **154**, 180901.

30 (*a*) R. L. Johnston, *Atomic and Molecular Clusters*, Taylor & Francis, London, 2002; (*b*) *Nanocatalysis*, ed. U. Heiz and U. Landman, Springer Verlag, Berlin, Heidelberg, 2007; (*c*) *Gold Clusters*, *Colloids and Nanoparticles I*, ed. D. M. P. Mingos, Springer, 2014; (*d*) *Gold Clusters, Colloids and Nanoparticles II*, ed. D. M. P. Mingos, Springer, 2014; (*e*) Z. Luo and S. N. Khanna, *Metal Clusters and Their Reactivity*, Springer Singapore, Singapore, 2020; (*f*) *Atomically Precise Metal Nanoclusters*, ed. T. Pradeep, Elsevier, 2023.

31 (*a*) in *Top. Catal. (Size-Selected Clusters as Model Systems for Catalysis)*, ed. K. R. Asmis and A. Fielicke, 2018, vol. 61, iss. 1–2; (*b*) *Z. Phys. Chem. (Gas Phase Model Systems for Catalysis)*, ed. S. M. Lang, 2019, vol. 233, iss. 6; (*c*) *J. Phys.: Condens. Matter (Virtual Special Issue: Spectroscopy of Gas-Phase and Supported Clusters)*, ed. J. Bakker and E. Janssens, 2019, vol. 30, iss. 31; (*d*) *J. Phys. Chem. C (Virtual Special Issue on Metal Clusters, Nanoparticles, and the Physical Chemistry of Catalysis)*, ed. T. Tsukuda and H. Häkkinen, 2021, vol. 125, iss. 9; (*e*) *J. Phys. Chem. A (Virtual Issue on Experiment–Theory Synergies in the Study of Metal and Metal-Containing Clusters)*, ed. C. M. Aikens and C. C. Jarrold, 2023, vol. 127, iss. 1.

32 (*a*) N. Sheppard, in *Vibrational Spectroscopy of Adsorbates*, ed. R. F. Willis, Springer, Berlin, 1980, pp. 165–176; (*b*) *Handbook of Vibrational Spectroscopy, Applications in Industry, Materials and the Physical Sciences*, ed. J. M. Chalmers and P. R. Griffiths, John Wiley & Sons Ltd, Chichester, UK, 2002, vol. 4; (*c*) K. Nakamoto, *Infrared and Raman Spectra of Inorganic and Coordination Compounds*, Part A, John Wiley & Sons, Inc., New York, 6 edn, 2008; (*d*) K. Nakamoto, *Infrared and Raman Spectra of Inorganic and Coordination Compounds*, Part B, John Wiley & Sons, Inc., New York, 6 edn, 2009.

33 (*a*) J. Jortner, *Z. Phys. D*, 1992, **24**, 247–275; (*b*) W. A. de Heer, *Rev. Mod. Phys.*, 1993, **65**, 611–676; (*c*) E. Roduner, *Chem. Soc. Rev.*, 2006, **35**, 583–592; (*d*) M. Arenz, S. Gilb and U. Heiz, in *The Chemical Physics of Solid Surfaces*, ed. D. P. Woodruff, Elsevier, 2007, vol. 12, pp. 1–51; (*e*) P. Jena and Q. Sun, *Chem. Rev.*, 2018, **118**, 5755–5870; (*f*) G. Pacchioni, *Inorg. Chim. Acta*, 2022, **530**, 120680.

34 (*a*) F. Baletto and R. Ferrando, *Rev. Mod. Phys.*, 2005, **77**, 371–423; (*b*) R. Ferrando, J. Jellinek and R. L. Johnston, *Chem. Rev.*, 2008, **108**, 845–910; (*c*) M. Schlangen and H. Schwarz, *Catal. Lett.*, 2012, **142**, 1265–1278; (*d*) J. Sauer and H.-J. Freund, *Catal. Lett.*, 2015, **145**, 109–125.

35 (*a*) M. Haruta, T. Kobayashi, H. Sano and N. Yamada, *Chem. Lett.*, 1987, 405–408; (*b*) M. Haruta and M. Daté, *Appl. Catal., A*, 2001, **222**, 427–437; (*c*) T. Ishida, T. Murayama, A. Taketoshi and M. Haruta, *Chem. Rev.*, 2020, **120**, 464–525.

36 (*a*) *Atomic Clusters: From Gas Phase to Deposited*, ed. D. P. Woodruff, Elsevier, Amsterdam, 2007; (*b*) S. Yamazoe, K. Koyasu and T. Tsukuda, *Acc. Chem. Res.*, 2014, **47**, 816–824; (*c*) Y. Du, H. Sheng, D. Astruc and M. Zhu, *Chem. Rev.*, 2020, **120**, 526–622.

37 (*a*) D. Schooss, P. Weis, O. Hampe and M. M. Kappes, *Philos. Trans. R. Soc., A*, 2010, **368**, 1211–1243; (*b*) L.-M. Wang and L.-S. Wang, *Nanoscale*, 2012, **4**, 4038–4053.

38 (*a*) P. Weis, T. Bierweiler, E. Vollmer and M. M. Kappes, *J. Chem. Phys.*, 2002, **117**, 9293–9297; (*b*) L. M. Ghiringhelli, P. Gruene, J. T. Lyon, D. M. Rayner, G. Meijer, A. Fielicke and M. Scheffler, *New J. Phys.*, 2013, **15**, 083003.

39 (*a*) V. A. Spasov, Y. Shi and K. M. Ervin, *Chem. Phys.*, 2000, **262**, 75–91; (*b*) K. Hansen, A. Herlert, L. Schweikhard and M. Vogel, *Phys. Rev. A*, 2006, **73**, 063202.

40 (*a*) S. Gilb, K. Jacobsen, D. Schooss, F. Furche, R. Ahlrichs and M. M. Kappes, *J. Chem. Phys.*, 2004, **121**, 4619–4627;

(*b*) A. Shayeghi, R. L. Johnston and R. Schäfer, *Phys. Chem. Chem. Phys.*, 2013, **15**, 19715–19723; (*c*) K. Hansen, P. Ferrari, E. Janssens and P. Lievens, *Phys. Rev. A*, 2017, **96**, 022511; (*d*) A. E. Green, A. S. Gentleman, W. Schöllkopf, A. Fielicke and S. R. Mackenzie, *Phys. Rev. Lett.*, 2021, **127**, 033002.

41 (*a*) M. Neumaier, F. Weigend, O. Hampe and M. M. Kappes, *J. Chem. Phys.*, 2005, **122**, 104702; (*b*) M. Yamaguchi, K. Miyajima and F. Mafuné, *J. Phys. Chem. C*, 2016, **120**, 23069–23073; (*c*) N. S. Shuman, S. G. Ard, B. C. Sweeny, A. A. Viggiano, C. J. Owen and P. B. Armentrout, *J. Phys. Chem. A*, 2020, **124**, 3335–3346.

42 L. D. Socaciu, J. Hagen, T. M. Bernhardt, L. Wöste, U. Heiz, H. Häkkinen and U. Landman, *J. Am. Chem. Soc.*, 2003, **125**, 10437–10445.

43 (*a*) A. P. Woodham, G. Meijer and A. Fielicke, *Angew. Chem., Int. Ed.*, 2012, **51**, 4444–4447; (*b*) A. P. Woodham, G. Meijer and A. Fielicke, *J. Am. Chem. Soc.*, 2013, **135**, 1727–1730; (*c*) A. P. Woodham and A. Fielicke, *Angew. Chem., Int. Ed.*, 2014, **53**, 6554–6557.

44 H. Liu, X. Xing, X. Wang, H. Qu, G.-J. Wang and M.-F. Zhou, *Chem. – Eur. J.*, 2016, **22**, 2085–2091.

45 (*a*) P. Gruene, B. Butschke, J. T. Lyon, D. M. Rayner and A. Fielicke, *Z. Phys. Chem.*, 2014, **228**, 337–350; (*b*) B. R. Goldsmith, J. Florian, J.-X. Liu, P. Gruene, J. T. Lyon, D. M. Rayner, A. Fielicke, M. Scheffler and L. M. Ghiringhelli, *Phys. Rev. Mater.*, 2019, **3**, 016002; (*c*) P. Ferrari, G.-L. Hou, O. V. Lushchikova, F. Calvo, J. M. Bakker and E. Janssens, *Phys. Chem. Chem. Phys.*, 2020, **22**, 11572–11577.

46 X.-M. Luo, Y.-K. Li, X.-Y. Dong and S.-Q. Zang, *Chem. Soc. Rev.*, 2023, **52**, 383–444.

47 *Activation of Small Molecules*, ed. W. B. Tolman, Wiley-VCH, Weinheim, 2006.

48 (*a*) M. A. Duncan, *Int. J. Mass Spectrom.*, 2000, **200**, 545–569; (*b*) E. J. Bieske and O. Dopfer, *Chem. Rev.*, 2000, **100**, 3963–3998; (*c*) K. R. Asmis, A. Fielicke, G. von Helden and G. Meijer, in *Atomic Clusters: From Gas Phase to Deposited*, ed. D. P. Woodruff, Elsevier, Amsterdam, 2007, pp. 327–375; (*d*) P. Gruene, J. T. Lyon and A. Fielicke, in *Handbook of Nanophysics*, ed. K. Sattler, Taylor & Francis, 2010, ch. 9, vol. 2; (*e*) K. R. Asmis, *Phys. Chem. Chem. Phys.*, 2012, **14**, 9270–9281; (*f*) J. Roithová, *Chem. Soc. Rev.*, 2012, **41**, 547–559; (*g*) H. J. Zeng, N. Yang and M. A. Johnson, *Faraday Discuss.*, 2019, **217**, 8–33.

49 Y. Hashimoto, H. Hasegawa, K. Yoshinari and I. Waki, *Anal. Chem.*, 2003, **75**, 420–425.

50 O. Asvany, P. Kumar P, B. Redlich, I. Hegemann, S. Schlemmer and D. Marx, *Science*, 2005, **309**, 1219–1222.

51 E. R. Bernstein, *Int. J. Mass Spectrom.*, 2015, **377**, 248–262.

52 (*a*) A. Fielicke, J. T. Lyon, M. Haertelt, G. Meijer, P. Claes, J. de Haeck and P. Lievens, *J. Chem. Phys.*, 2009, **131**, 171105; (*b*) G. Li, C. Wang, H.-J. Zheng, T.-T. Wang, H. Xie, X.-M. Yang and L. Jiang, *Chin. J. Chem. Phys.*, 2021, **34**, 51–60.

53 (*a*) R. J. Meier, *Vib. Spectrosc.*, 2007, **43**, 26–37; (*b*) M.-P. Gaigeot, *Spectrochim. Acta, Part A*, 2021, **260**, 119864; (*c*) R. Han, R. Ketkaew and S. Luber, *J. Phys. Chem. A*, 2022, **126**, 801–812.

54 (*a*) G. von Helden, D. van Heijnsbergen and G. Meijer, *J. Phys. Chem. A*, 2003, **107**, 1671–1688; (*b*) V. J. F. Lapoutre, M. Haertelt, G. Meijer, A. Fielicke and J. M. Bakker, *J. Chem. Phys.*, 2013, **139**, 121101.

55 M. Haertelt, V. J. F. Lapoutre, J. M. Bakker, B. Redlich, D. J. Harding, A. Fielicke and G. Meijer, *J. Phys. Chem. Lett.*, 2011, **2**, 1720–1724.

56 C. P. McNary and P. B. Armentrout, *Phys. Chem. Chem. Phys.*, 2014, **16**, 26467–26477.

57 (*a*) J. L. Lyman, H. W. Galbraith and J. R. Ackerhalt, *Los Alamos Sci.*, 1982, **3**, 66–85; (*b*) V. S. Letokhov, *Nonlinear Laser Chemistry*, Springer-Verlag, Berlin, 1983; (*c*) V. S. Letokhov, *Laser Control of Atoms and Molecules*, Oxford University Press, 2007.

58 D. J. Auerbach, J. C. Tully and A. M. Wodtke, *Nat. Sci.*, 2021, **1**, e10005.

59 A. H. Zewail, *J. Phys. Chem. A*, 2000, **104**, 5660–5694.

60 J. Oomens, B. G. Sartakov, G. Meijer and G. von Helden, *Int. J. Mass Spectrom.*, 2006, **254**, 1–19.

61 (*a*) M. Hippler, M. Quack, R. Schwarz, G. Seyfang, S. Matt and T. Märk, *Chem. Phys. Lett.*, 1997, **278**, 111–120; (*b*) N. C. Polfer, *Chem. Soc. Rev.*, 2011, **40**, 2211–2221.

62 (*a*) M. Okumura, L. I. Yeh and Y. T. Lee, *J. Chem. Phys.*, 1985, **83**, 3705–3706; (*b*) M. B. Knickelbein and W. J. C. Menezes, *Phys. Rev. Lett.*, 1992, **69**, 1046–1049.

63 (*a*) D. J. Harding, C. Kerpal, G. Meijer and A. Fielicke, *Angew. Chem., Int. Ed.*, 2012, **51**, 817–819; (*b*) A. C. Hermes, S. M. Hamilton, G. A. Cooper, C. Kerpal, D. J. Harding, G. Meijer, A. Fielicke and S. R. Mackenzie, *Faraday Discuss.*, 2012, **157**, 213–225.

64 (*a*) N. R. Walker, R. S. Walters, E. D. Pillai and M. A. Duncan, *J. Chem. Phys.*, 2003, **119**, 10471–10474; (*b*) M. Brümmer, C. Kaposta, G. Santambrogio and K. R. Asmis, *J. Chem. Phys.*, 2003, **119**, 12700–12703; (*c*) S. M. Lang, T. M. Bernhardt, V. Chernyy, J. M. Bakker, R. N. Barnett and U. Landman, *Angew. Chem., Int. Ed.*, 2017, **56**, 13406–13410.

65 F. Müller, J. Sauer, X. Song and K. R. Asmis, *J. Phys. Chem. A*, 2021, **125**, 9571–9577.

66 (*a*) K. R. Asmis, T. Wende, M. Brummer, O. Gause, G. Santambrogio, E. C. Stanca-Kaposta, J. Dobler, A. Niedziela and J. Sauer, *Phys. Chem. Chem. Phys.*, 2012, **14**, 9377–9388; (*b*) M. Savoca, J. Langer, D. J. Harding, D. Palagin, K. Reuter, O. Dopfer and A. Fielicke, *J. Chem. Phys.*, 2014, **141**, 104313.

67 J. H. Marks, E. Miliordos and M. A. Duncan, *J. Chem. Phys.*, 2021, **154**, 064306.

68 D. Bellert and W. H. Breckenridge, *Chem. Rev.*, 2002, **102**, 1595–1622.

69 P. Zeppenfeld, in *Springer Materials (Landolt-Börnstein - New Series Group III Condensed Matter)*, ed. A. P. Bonzel, Springer-Verlag, Berlin Heidelberg, 2001, vol. 42A1, ch. Noble gases on metals and semiconductors.

70 P. Ferrari, L. Delgado-Callico, O. V. Lushchikova, M. Bejide, F. J. Wensink, J. M. Bakker, F. Baletto and E. Janssens, *J. Phys. Chem. Lett.*, 2022, **13**, 4309–4314.

71 (*a*) E. D. Pillai, T. D. Jaeger and M. A. Duncan, *J. Am. Chem. Soc.*, 2007, **129**, 2297–2307; (*b*) A. Straßner, C. Wiehn,

M. P. Klein, D. V. Fries, S. Dillinger, J. Mohrbach, M. H. Prosenc, P. B. Armentrout and G. Niedner-Schatteburg, *J. Chem. Phys.*, 2021, **155**, 244305.

72 (*a*) J. P. Toennies and A. F. Vilesov, *Angew. Chem., Int. Ed.*, 2004, **43**, 2622–2648; (*b*) M. Y. Choi, G. E. Douberly, T. M. Falconer, W. K. Lewis, C. M. Lindsay, J. M. Merritt, P. L. Stiles and R. E. Miller, *Int. Rev. Phys. Chem.*, 2006, **25**, 15–75; (*c*) A. Mauracher, O. Echt, A. M. Ellis, S. Yang, D. K. Bohme, J. Postler, A. Kaiser, S. Denifl and P. Scheier, *Phys. Rep.*, 2018, **751**, 1–90; (*d*) D. Verma, R. M. P. Tanyag, S. M. O. O'Connell and A. F. Vilesov, *Adv. Phys. X*, 2019, **4**, 1553569; (*e*) T. González-Lezana, O. Echt, M. Gatchell, M. Bartolomei, J. Campos-Martínez and P. Scheier, *Int. Rev. Phys. Chem.*, 2020, **39**, 465–516.

73 (*a*) A. Fielicke, G. von Helden, G. Meijer, D. B. Pedersen, B. Simard and D. M. Rayner, *J. Phys. Chem. B*, 2004, **108**, 14591–14598; (*b*) S. M. Hamilton, W. S. Hopkins, D. J. Harding, T. R. Walsh, M. Haertelt, C. Kerpal, P. Gruene, G. Meijer, A. Fielicke and S. R. Mackenzie, *J. Phys. Chem. A*, 2011, **115**, 2489–2497.

74 (*a*) M. F. Vernon, J. M. Lisy, H. S. Kwok, D. J. Krajnovich, A. Tramer, Y. R. Shen and Y. T. Lee, *J. Phys. Chem.*, 1981, **85**, 3327–3333; (*b*) D. W. Michael and J. M. Lisy, *J. Chem. Phys.*, 1986, **85**, 2528–2537; (*c*) W. A. de Heer, K. Selby, V. Kresin, J. Masui, M. Vollmer, A. Chatelain and W. D. Knight, *Phys. Rev. Lett.*, 1987, **59**, 1805–1808.

75 (*a*) S. C. Richtsmeier, E. K. Parks, K. Liu, L. G. Pobo and S. J. Riley, *J. Chem. Phys.*, 1985, **82**, 3659–3665; (*b*) J. Woenckhaus and J. A. Becker, *Rev. Sci. Instr.*, 1994, **65**, 2019–2022; (*c*) A. Fielicke and K. Rademann, *J. Phys. Chem. A*, 2000, **104**, 6979–6982.

76 N. Heine and K. R. Asmis, *Int. Rev. Phys. Chem.*, 2015, **34**, 1–34.

77 (*a*) D. S. Cornett, M. Peschke, K. LaiHing, P. Y. Cheng, K. F. Willey and M. A. Duncan, *Rev. Sci. Instr.*, 1992, **63**, 2177–2186; (*b*) S. Becker, K. Dasgupta, G. Dietrich, H. J. Kluge, S. Kuznetsov, M. Lindinger, K. Lützenkirchen, L. Schweikhard and J. Ziegler, *Rev. Sci. Instr.*, 1995, **66**, 4902–4910; (*c*) J. Husband, F. Aguirre, P. Ferguson and R. B. Metz, *J. Chem. Phys.*, 1999, **111**, 1433–1437; (*d*) P. Maitre, S. Le Caer, A. Simon, W. Jones, J. Lemaire, H. Mestdagh, M. Heninger, G. Mauclaire, P. Boissel, R. Prazeres, F. Glotin and J.-M. Ortega, *Nucl. Instrum. Methods Phys. Res., Sect. A*, 2003, **507**, 541–546; (*e*) A. Schweizer, J. M. Weber, S. Gilb, H. Schneider, D. Schooss and M. M. Kappes, *J. Chem. Phys.*, 2003, **119**, 3699–3710; (*f*) J. J. Valle, J. R. Eyler, J. Oomens, D. T. Moore, A. F. G. van der Meer, G. von Helden, G. Meijer, C. L. Hendrickson, A. G. Marshall and G. T. Blakney, *Rev. Sci. Instr.*, 2005, **76**, 023103; (*g*) S. Hirabayashi, R. Okawa, M. Ichihashi, T. Kondow and Y. Kawazoe, *J. Phys. Chem. A*, 2007, **111**, 7664–7669; (*h*) J. M. Bakker, T. Besson, J. Lemaire, D. Scuderi and P. Maître, *J. Phys. Chem. A*, 2007, **111**, 13415–13424; (*i*) S. Dillinger, J. Mohrbach, J. Hewer, M. Gaffga and G. Niedner-Schatteburg, *Phys. Chem. Chem. Phys.*, 2015, **17**, 10358–10362; (*j*) J. Martens, G. Berden, C. R. Gebhardt and J. Oomens, *Rev. Sci. Instr.*, 2016, **87**, 103108; (*k*) M. Förstel, B. K. Jaeger, W. Schewe, P. H. Sporkhorst and O. Dopfer, *Rev. Sci. Instr.*, 2017, **88**, 123110; (*l*) E. M. Cunningham, T. Taxer, J. Heller, M. Ončák, C. van der Linde and M. K. Beyer, *Phys. Chem. Chem. Phys.*, 2021, **23**, 3627–3636.

78 (*a*) K. R. Asmis, M. Brümmer, C. Kaposta, G. Santambrogio, G. von Helden, G. Meijer, K. Rademann and L. Wöste, *Phys. Chem. Chem. Phys.*, 2002, **4**, 1101–1104; (*b*) A. Svendsen, U. J. Lorenz, O. V. Boyarkin and T. R. Rizzo, *Rev. Sci. Instr.*, 2010, **81**, 073107; (*c*) A. B. Wolk, C. M. Leavitt, E. Garand and M. A. Johnson, *Acc. Chem. Res.*, 2014, **47**, 202–210; (*d*) O. Asvany, S. Brünken, L. Kluge and S. Schlemmer, *Appl. Phys. B*, 2014, **114**, 203–211; (*e*) A. Günther, P. Nieto, D. Müller, A. Sheldrick, D. Gerlich and O. Dopfer, *J. Mol. Spectrosc.*, 2017, **332**, 8–15.

79 J. R. Eyler, *Mass Spectrom. Rev.*, 2009, **28**, 448–467.

80 F. Bierau, P. Kupser, G. Meijer and G. von Helden, *Phys. Rev. Lett.*, 2010, **105**, 133402.

81 M. R. Zakin, R. O. Brickman, D. M. Cox, K. C. Reichmann, D. J. Trevor and A. Kaldor, *J. Chem. Phys.*, 1986, **85**, 1198–1199.

82 M. B. Knickelbein, G. M. Koretsky, K. A. Jackson, M. R. Pederson and Z. Hajnal, *J. Chem. Phys.*, 1998, **109**, 10692–10700.

83 I. Swart, F. M. F. de Groot, B. M. Weckhuysen, P. Gruene, G. Meijer and A. Fielicke, *J. Phys. Chem. A*, 2008, **112**, 1139–1149.

84 J. M. J. Madey, *J. Appl. Phys.*, 1971, **42**, 1906–1913.

85 (*a*) T. G. Marshall, *Free-Electron Lasers*, Macmillian Publishing Company, New York, 1985; (*b*) C. A. Brau, *Free-Electron Lasers*, Academic Press, Inc., 1990; (*c*) K.-J. Kim, Z. Huang and R. Lindberg, *Synchrotron Radiation and Free-Electron Lasers*, Cambridge University Press, 2017.

86 W. Schöllkopf, W. B. Colson, M. De Pas, D. Dowell, S. Gewinner, S. C. Gottschalk, H. Junkes, G. Meijer, J. Rathke, T. Schultheiss, A. M. M. Todd, L. M. Young and G. von Helden, *39th Free Electron Laser Conference (FEL2019)*, JACoW Publishing, Geneva, Switzerland, 2019, pp. 52–55.

87 D. A. G. Deacon, L. R. Elias, J. M. J. Madey, G. J. Ramian, H. A. Schwettman and T. I. Smith, *Phys. Rev. Lett.*, 1977, **38**, 892–894.

88 J. F. Schultz, M. J. Lavan, E. W. Pogue and T. W. Meyer, *Nucl. Instrum. Methods Phys. Res., Sect. A*, 1992, **318**, 9–15.

89 (*a*) S. V. Benson, F. Wu Shain, B. A. Hooper, J. M. J. Madey, E. B. Szarmes, B. Richman and L. Vintro, *Nucl. Instrum. Methods Phys. Res., Sect. A*, 1990, **296**, 110–114; (*b*) W. B. Colson, E. D. Johnson, M. J. Kelley and H. A. Schwettman, *Phys. Today*, 2002, **55**, 35–41.

90 (*a*) P. F. González-Díaz, M. Santos, C. L. Sigüenza and J. A. Torresano, *Laser Chem.*, 1992, **12**, 143642; (*b*) B. E. Newnam, J. W. Early and J. L. Lyman, *Nucl. Instrum. Methods Phys. Res., Sect. A*, 1994, **341**, 142–145; (*c*) J. L. Lyman, B. E. Newnam, J. W. Early and A. F. G. van der Meer, *J. Phys. Chem. A*, 1997, **101**, 49–54; (*d*) A. K. Petrov, E. N. Chesnokov, S. R. Gorelik, K. D. Straub, E. B. Szarmes and J. M. J. Madey, *J. Phys. Chem. A*, 1997, **101**, 7200–7207.

91 R. Cramer, R. F. Haglund and F. Hillenkamp, *Int. J. Mass Spectrom. Ion Processes*, 1997, **169–170**, 51–67.
92 M. Putter, G. von Helden and G. Meijer, *Chem. Phys. Lett.*, 1996, **258**, 118–122.
93 G. von Helden, I. Holleman, G. M. H. Knippels, A. F. G. van der Meer and G. Meijer, *Phys. Rev. Lett.*, 1997, **79**, 5234–5237.
94 P. J. Neyman, W. B. Colson, S. C. Gottschalk, A. M. M. Todd, J. Blau and K. R. Cohn, *38th International Free Electron Laser Conference (FEL2017)*, JACoW Publishing, 2018, pp. 204–209.
95 D. van Heijnsbergen, G. von Helden, M. A. Duncan, A. J. A. van Roij and G. Meijer, *Phys. Rev. Lett.*, 1999, **83**, 4983–4986.
96 J. Oomens, A. J. A. van Roij, G. Meijer and G. von Helden, *Astrophys. J.*, 2000, **542**, 404–410.
97 J. Oomens, A. G. G. M. Tielens, B. Sartakov, G. von Helden and G. Meijer, *Astrophys. J.*, 2003, **591**, 968–985.
98 (*a*) J. Lemaire, P. Boissel, M. Heninger, G. Mauclaire, G. Bellec, H. Mestdagh, A. Simon, S. L. Caer, J. M. Ortega, F. Glotin and P. Maitre, *Phys. Rev. Lett.*, 2002, **89**, 273002; (*b*) K. Fukui and K. Takahashi, *Anal. Chem.*, 2012, **84**, 2188–2194.
99 B. Simard, S. Dénommée, D. M. Rayner, D. van Heijnsbergen, G. Meijer and G. von Helden, *Chem. Phys. Lett.*, 2002, **357**, 195–203.
100 (*a*) D. M. Rayner, L. Lian, R. Fournier, S. A. Mitchell and P. A. Hackett, *Phys. Rev. Lett.*, 1995, **74**, 2070–2073; (*b*) D. M. Rayner, L. Lian, K. Athanassenas, B. A. Collings, R. Fournier, S. A. Mitchell and P. A. Hackett, *Surf. Rev. Lett.*, 1996, **3**, 649–654.
101 C. Bostedt, T. Gorkhover, D. Rupp and T. Möller, in *Synchrotron Light Sources and Free-Electron Lasers: Accelerator Physics, Instrumentation and Science Applications*, ed. E. Jaeschke, S. Khan, J. R. Schneider and J. B. Hastings, Springer International Publishing, Cham, 2019, pp. 1–49.
102 J. M. Ortega, *Jpn. J. Appl. Phys.*, 2002, **41**(Suppl. 41–1), 20–38.
103 (*a*) D. Oepts, A. F. G. van der Meer and P. W. van Amersfoort, *Infrared Phys. Technol.*, 1995, **36**, 297–308; (*b*) P. W. van Amersfoort, R. J. Bakker, J. B. Bekkers, R. W. B. Best, R. van Buuren, P. F. M. Delmee, B. Faatz, C. A. J. van der Geer, D. A. Jaroszynski, P. Manintveld, W. J. Mastop, B. J. H. Meddens, A. F. G. van der Meer, J. P. Nijman, D. Oepts, J. Pluygers, M. J. van der Wiel, W. A. Gillespie, P. F. Martin, M. F. Kimmitt, C. R. Pidgeon, M. W. Poole and G. Saxon, *Nucl. Instrum. Methods Phys. Res., Sect. A*, 1992, **318**, 42–46.
104 (*a*) B. L. Militsyn, G. von Helden, G. J. M. Meijer and A. F. G. van der Meer, *Nucl. Instrum. Methods Phys. Res., Sect. A*, 2003, **507**, 494–497; (*b*) J. M. Bakker, V. J. F. Lapoutre, B. Redlich, J. Oomens, B. G. Sartakov, A. Fielicke, G. von Helden, G. Meijer and A. F. G. van der Meer, *J. Chem. Phys.*, 2010, **132**, 074305.
105 V. Zhaunerchyk, D. Oepts, R. T. Jongma and W. J. van der Zande, *Phys. Rev. Spec. Top.--Accel. Beams*, 2012, **15**, 050701.
106 M. Yokoyama, F. Oda, K. Nomaru, H. Koike, M. Sobajima, M. Kawai, H. Kuroda and K. Nakai, *Nucl. Instrum. Methods Phys. Res., Sect. A*, 2003, **507**, 261–264.
107 W. Schöllkopf, S. Gewinner, H. Junkes, A. Paarmann, G. von Helden, H. Bluem and A. M. Todd, *Proc. SPIE 9512, Advances in X-ray Free-Electron Lasers Instrumentation III*, SPIE, 2015, p. 95121L.
108 H. Li, Z. He, F. Wu, L. Tang, Z. Zhao, T. Zhang, T. He, K. Xuan, H. Zhang, W. Wei, P. Lu, Z. Zhou, L. Shang, G. Liu, H. Xu, X. He, S. Jiang, X. Pei, C. Gao, Q. Jia, J. Bao, S. Zhang and L. Wang, *Chin. J. Lasers - Zhongguo Jiguang*, 2021, **48**, 1700001.
109 *Gas-Phase IR Spectroscopy and Structure of Biological Molecules*, ed. A. M. Rijs and J. Oomens, Springer International Publishing, Cham, 2015.
110 S. Gilb, P. Weis, F. Furche, R. Ahlrichs and M. M. Kappes, *J. Chem. Phys.*, 2002, **116**, 4094–4101.
111 P. Ferrari, E. Janssens, P. Lievens and K. Hansen, *Int. Rev. Phys. Chem.*, 2019, **38**, 405–440.
112 (*a*) W. R. Bosenberg and D. R. Guyer, *J. Opt. Soc. Am. B*, 1993, **10**, 1716–1722; (*b*) R. E. van Outersterp, J. Martens, A. Peremans, L. Lamard, F. Cuyckens, J. Oomens and G. Berden, *Analyst*, 2021, **146**, 7218–7229.
113 D. V. Fries, M. P. Klein, A. Steiner, M. H. Prosenc and G. Niedner-Schatteburg, *Phys. Chem. Chem. Phys.*, 2021, **23**, 11345–11354.
114 M. Gerhards, *Opt. Commun.*, 2004, **241**, 493–497.
115 P. F. Bernath, in *An Introduction to Laser Spectrocopy*, ed. D. L. Andrews and A. A. Demikov, Kluwer Academic, New York, 2nd edn, 2002, pp. 211–232.
116 T. Liang, S. D. Flynn, A. M. Morrison and G. E. Douberly, *J. Phys. Chem. A*, 2011, **115**, 7437–7447.
117 I. Swart, A. Fielicke, B. Redlich, G. Meijer, B. M. Weckhuysen and F. M. F. de Groot, *J. Am. Chem. Soc.*, 2007, **129**, 2516–2520.
118 S. Dillinger, M. P. Klein, A. Steiner, D. C. McDonald, M. A. Duncan, M. M. Kappes and G. Niedner-Schatteburg, *J. Phys. Chem. Lett.*, 2018, **9**, 914–918.
119 I. Swart, A. Fielicke, D. M. Rayner, G. Meijer, B. M. Weckhuysen and F. M. F. de Groot, *Angew. Chem., Int. Ed.*, 2007, **46**, 5317–5320.
120 I. Swart, P. Gruene, A. Fielicke, G. Meijer, B. M. Weckhuysen and F. M. F. de Groot, *Phys. Chem. Chem. Phys.*, 2008, **10**, 5743–5745.
121 C. Kerpal, D. J. Harding, D. M. Rayner and A. Fielicke, *J. Phys. Chem. A*, 2013, **117**, 8230–8237.
122 O. V. Lushchikova, H. Tahmasbi, S. Reijmer, R. Platte, J. Meyer and J. M. Bakker, *J. Phys. Chem. A*, 2021, **125**, 2836–2848.
123 J. Vanbuel, E. M. Fernández, P. Ferrari, S. Gewinner, W. Schöllkopf, L. C. Balbás, A. Fielicke and E. Janssens, *Chem. – Eur. J.*, 2017, **23**, 15638–15643.
124 J. Vanbuel, E. M. Fernández, M. Jia, P. Ferrari, W. Schöllkopf, L. C. Balbás, M. T. Nguyen, A. Fielicke and E. Janssens, *Z. Phys. Chem.*, 2019, **233**, 799–812.
125 P. Ferrari, H. T. Pham, J. Vanbuel, M. T. Nguyen, A. Fielicke and E. Janssens, *Chem. Commun.*, 2021, **57**, 9518–9521.
126 M. Jia, J. Vanbuel, P. Ferrari, E. M. Fernández, S. Gewinner, W. Schöllkopf, M. T. Nguyen, A. Fielicke and E. Janssens, *J. Phys. Chem. C*, 2018, **122**, 18247–18255.
127 (*a*) J. Vanbuel, M. Jia, P. Ferrari, S. Gewinner, W. Schöllkopf, M. T. Nguyen, A. Fielicke and E. Janssens, *Top. Catal.*, 2018, **61**, 62–70; (*b*) M. Jia, J. Vanbuel,

P. Ferrari, W. Schöllkopf, A. Fielicke, M. T. Nguyen and E. Janssens, *J. Phys. Chem. C*, 2020, **124**, 7624–7633.
128 X. Zhou, J. Cui, Z. H. Li, G. Wang, Z. Liu and M. Zhou, *J. Phys. Chem. A*, 2013, **117**, 1514–1521.
129 X. Zhou, J. Cui, Z. H. Li, G. Wang and M. Zhou, *J. Phys. Chem. A*, 2012, **116**, 12349–12356.
130 J. T. Lyon, P. Gruene, A. Fielicke, G. Meijer and D. M. Rayner, *J. Chem. Phys.*, 2009, **131**, 184706.
131 G. Wang, J. Cui, C. Chi, X. Zhou, Z. H. Li, X. Xing and M. Zhou, *Chem. Sci.*, 2012, **3**, 3272–3279.
132 C. Chi, J. Cui, Z. H. Li, X. Xing, G. Wang and M. Zhou, *Chem. Sci.*, 2012, **3**, 1698–1706.
133 D. T. Moore, J. Oomens, J. R. Eyler, G. Meijer, G. von Helden and D. P. Ridge, *J. Am. Chem. Soc.*, 2004, **126**, 14726–14727.
134 A. Fielicke, G. von Helden, G. Meijer, D. B. Pedersen, B. Simard and D. M. Rayner, *J. Chem. Phys.*, 2006, **124**, 194305.
135 J. Cui, X. Zhou, G. Wang, C. Chi, Z. H. Li and M. Zhou, *J. Phys. Chem. A*, 2014, **118**, 2719–2727.
136 A. Fielicke, G. von Helden, G. Meijer, B. Simard, S. Dénommée and D. M. Rayner, *J. Am. Chem. Soc.*, 2003, **125**, 11184–11185.
137 I. Swart, F. M. F. de Groot, B. M. Weckhuysen, D. M. Rayner, G. Meijer and A. Fielicke, *J. Am. Chem. Soc.*, 2008, **130**, 2126–2127.
138 C. Kerpal, D. Harding, G. Meijer and A. Fielicke, *Eur. Phys. J. D*, 2011, **63**, 231–234.
139 P. Gruene, A. Fielicke, G. Meijer and D. M. Rayner, *Phys. Chem. Chem. Phys.*, 2008, **10**, 6144–6149.
140 J. Cui, G. Wang, X. Zhou, C. Chi, Z. Hua Li, Z. Liu and M. Zhou, *Phys. Chem. Chem. Phys.*, 2013, **15**, 10224–10232.
141 (*a*) G. Ganteför, G. Schulze Icking-Konert, H. Handschuh and W. Eberhardt, *Int. J. Mass Spectrom. Ion Processes*, 1996, **159**, 81–109; (*b*) G. Schulze Icking-Konert, H. Handschuh, G. Ganteför and W. Eberhardt, *Phys. Rev. Lett.*, 1996, **76**, 1047–1050.
142 J. Cui, X. Xing, C. Chi, G. Wang, Z. Liu and M. Zhou, *Chin. J. Chem.*, 2012, **30**, 2131–2137.
143 P. Ferrari, J. Vanbuel, N. M. Tam, M. T. Nguyen, S. Gewinner, W. Schöllkopf, A. Fielicke and E. Janssens, *Chem. – Eur. J.*, 2017, **23**, 4120–4127.
144 J. Cui, X. Zhou, G. Wang, C. Chi, Z. Liu and M. Zhou, *J. Phys. Chem. A*, 2013, **117**, 7810–7817.
145 O. V. Lushchikova, PhD thesis, Radboud University, Nijmegen, 2021.
146 K. Xin, Y. Chen, L. Zhang, X. Wang and G. Wang, *J. Phys. Chem. A*, 2020, **124**, 3859–3864.
147 Y.-L. Wang, H.-J. Zhai, L. Xu, J. Li and L.-S. Wang, *J. Phys. Chem. A*, 2010, **114**, 1247–1254.
148 A. Fielicke, G. von Helden, G. Meijer, B. Simard and D. M. Rayner, *J. Phys. Chem. B*, 2005, **109**, 23935–23940.
149 A. Fielicke, G. von Helden, G. Meijer, B. Simard and D. M. Rayner, *Phys. Chem. Chem. Phys.*, 2005, **7**, 3906–3909.
150 H. A. Abdulhussein, P. Ferrari, J. Vanbuel, C. Heard, A. Fielicke, P. Lievens, E. Janssens and R. L. Johnston, *Nanoscale*, 2019, **11**, 16130–16141.
151 A. Fielicke, G. von Helden, G. Meijer, D. B. Pedersen, B. Simard and D. M. Rayner, *J. Am. Chem. Soc.*, 2005, **127**, 8416–8423.
152 Y. D. Kim and G. Ganteför, *Chem. Phys. Lett.*, 2003, **382**, 644–649.
153 Y. D. Kim, D. Stolcic, M. Fischer and G. Ganteför, *J. Chem. Phys.*, 2003, **119**, 10307–10312.
154 C. Kerpal, D. J. Harding, J. T. Lyon, G. Meijer and A. Fielicke, *J. Phys. Chem. C*, 2013, **117**, 12153–12158.
155 S. Dillinger, J. Mohrbach and G. Niedner-Schatteburg, *J. Chem. Phys.*, 2017, **147**, 184305.
156 J. Mohrbach, S. Dillinger and G. Niedner-Schatteburg, *J. Phys. Chem. C*, 2017, **121**, 10907–10918.
157 M. P. Klein, A. A. Ehrhard, J. Mohrbach, S. Dillinger and G. Niedner-Schatteburg, *Top. Catal.*, 2018, **61**, 106–118.
158 (*a*) T. Nagata, K. Koyama, S. Kudoh, K. Miyajima, J. M. Bakker and F. Mafuné, *J. Phys. Chem. C*, 2017, **121**, 27417–27426; (*b*) M. Yamaguchi, Y. Zhang, S. Kudoh, K. Koyama, O. V. Lushchikova, J. M. Bakker and F. Mafuné, *J. Phys. Chem. Lett.*, 2020, **11**, 4408–4412; (*c*) F. Mafuné, J. M. Bakker and S. Kudoh, *Chem. Phys. Lett.*, 2021, **780**, 138937.
159 T. Nagata, S. Kudoh, K. Miyajima, J. M. Bakker and F. Mafuné, *J. Phys. Chem. C*, 2018, **122**, 22884–22891.
160 M. Yamaguchi, Y. Zhang, O. V. Lushchikova, J. M. Bakker and F. Mafuné, *J. Phys. Chem. A*, 2022, **126**, 6668–6677.
161 A. Fielicke and D. M. Rayner, unpublished results.
162 M. Yamaguchi, Y. Zhang, O. V. Lushchikova, J. M. Bakker and F. Mafuné, *J. Phys. Chem. A*, 2021, **125**, 9040–9047.
163 M. Yamaguchi, S. Kudoh, K. Miyajima, O. V. Lushchikova, J. M. Bakker and F. Mafuné, *J. Phys. Chem. C*, 2019, **123**, 3476–3481.
164 Y. Zhang, M. Yamaguchi, K. Kawada, S. Kudoh, O. V. Lushchikova, J. M. Bakker and F. Mafuné, *J. Phys. Chem. A*, 2022, **126**, 36–43.
165 F. von Gynz-Rekowski, N. Bertram, G. Ganteför and Y. D. Kim, *J. Phys. Chem. B*, 2004, **108**, 18916–18918.
166 (*a*) Y. D. Kim and G. Ganteför, *Chem. Phys. Lett.*, 2003, **383**, 80–83; (*b*) Y. D. Kim, G. Ganteför, Q. Sun and P. Jena, *Chem. Phys. Lett.*, 2004, **396**, 69–74.
167 A. P. Woodham, PhD thesis, Technische Universität Berlin, 2014.
168 (*a*) Y. D. Kim, M. Fischer and G. Ganteför, *Chem. Phys. Lett.*, 2003, **377**, 170–176; (*b*) Q. Sun, P. Jena, Y. D. Kim, M. Fischer and G. Ganteför, *J. Chem. Phys.*, 2004, **120**, 6510–6515.
169 S. M. Lang, T. M. Bernhardt, J. M. Bakker, B. Yoon and U. Landman, *J. Am. Soc. Mass Spectrom.*, 2019, **30**, 1895–1905.
170 (*a*) G. J. Kubas, *J. Organomet. Chem.*, 2001, **635**, 37; (*b*) J. W. Tye, M. Y. Darensbourg and M. B. Hall, in *Activation of Small Molecules*, ed. W. B. Tolman, Wiley-VCH, Weinheim, 2006, pp. 121–158; (*c*) G. J. Kubas, *J. Organomet. Chem.*, 2014, **751**, 33–49.
171 K. Christmann, in *Springer Materials (Landolt-Börnstein - New Series Group III Condensed Matter)*, ed. A. P. Bonzel, Springer-Verlag, Berlin Heidelberg, 2006, vol. 42A5, ch. 3.4.1 Adsorbate properties of hydrogen on solid surfaces.
172 (*a*) R. H. Crabtree, *Angew. Chem., Int. Ed. Engl.*, 1993, **32**, 789–805; (*b*) G. J. Kubas, *Proc. Natl. Acad. Sci. U. S. A.*, 2007, **104**, 6901–6907.

173 R. H. Crabtree, *Chem. Rev.*, 2016, **116**, 8750–8769.
174 K. P. Huber and G. H. Herzberg, *Molecular Spectra and Molecular Structure IV. Constants of Diatomic Molecules*, Van Nostrand Reinhold Co., 1979.
175 L. Andrews, *Chem. Soc. Rev.*, 2004, **33**, 123–132.
176 L. Andrews, X. Wang, M. E. Alikhani and L. Manceron, *J. Phys. Chem. A*, 2001, **105**, 3052–3063.
177 (*a*) V. Dryza, B. L. J. Poad and E. J. Bieske, *Phys. Chem. Chem. Phys.*, 2012, **14**, 14954–14965; (*b*) V. Dryza and E. J. Bieske, *Int. Rev. Phys. Chem.*, 2013, **32**, 559–587.
178 G. D. Dickenson, M. L. Niu, E. J. Salumbides, J. Komasa, K. S. E. Eikema, K. Pachucki and W. Ubachs, *Phys. Rev. Lett.*, 2013, **110**, 193601.
179 B. R. Bender, G. J. Kubas, L. H. Jones, B. I. Swanson, J. Eckert, K. B. Capps and C. D. Hoff, *J. Am. Chem. Soc.*, 1997, **119**, 9179–9190.
180 (*a*) A. S. Mårtensson, C. Nyberg and S. Andersson, *Phys. Rev. Lett.*, 1986, **57**, 2045–2048; (*b*) A. S. Mårtensson, C. Nyberg and S. Andersson, *Surf. Sci.*, 1988, **205**, 12–24.
181 I. Swart, PhD Thesis, Utrecht University, 2008.
182 (*a*) L. Zhu, J. Ho, E. K. Parks and S. J. Riley, *J. Chem. Phys.*, 1993, **98**, 2798–2804; (*b*) S. M. Lang, T. M. Bernhardt, R. N. Barnett, B. Yoon and U. Landman, *J. Am. Chem. Soc.*, 2009, **131**, 8939–8951.
183 D. M. Heinekey, A. Lledós and J. M. Lluch, *Chem. Soc. Rev.*, 2004, **33**, 175–182.
184 (*a*) A. Fielicke, A. Kirilyuk, C. Ratsch, J. Behler, M. Scheffler, G. von Helden and G. Meijer, *Phys. Rev. Lett.*, 2004, **93**, 023401; (*b*) C. Ratsch, A. Fielicke, A. Kirilyuk, J. Behler, G. von Helden, G. Meijer and M. Scheffler, *J. Chem. Phys.*, 2005, **122**, 124302.
185 (*a*) S. Nonose, Y. Sone, K. Onodera, S. Sudo and K. Kaya, *Chem. Phys. Lett.*, 1989, **164**, 427–432; (*b*) W. J. C. Menezes and M. B. Knickelbein, *Chem. Phys. Lett.*, 1991, **183**, 357–362; (*c*) A. Pramann, A. Nakajima and K. Kaya, *J. Chem. Phys.*, 2001, **115**, 5404–5410.
186 D. M. Cox, D. J. Trevor, R. L. Whetten and A. Kaldor, *J. Phys. Chem.*, 1988, **92**, 421–429.
187 M. F. Jarrold and J. E. Bower, *J. Am. Chem. Soc.*, 1988, **110**, 70–78.
188 L.-F. Cui, X. Li and L.-S. Wang, *J. Chem. Phys.*, 2006, **124**, 054308.
189 (*a*) L. Andrews and X. Wang, *Science*, 2003, **299**, 2049–2052; (*b*) X. Wang, L. Andrews, S. Tam, M. E. DeRose and M. E. Fajardo, *J. Am. Chem. Soc.*, 2003, **125**, 9218–9228; (*c*) L. Andrews and X. Wang, *J. Phys. Chem. A*, 2004, **108**, 4202–4210.
190 P. Ferrari, J. Vanbuel, E. Janssens and P. Lievens, *Acc. Chem. Res.*, 2018, **51**, 3174–3182.
191 (*a*) H.-J. Zhai, B. Kiran and L.-S. Wang, *J. Chem. Phys.*, 2004, **121**, 8231–8236; (*b*) X. Wu, Z. Qin, H. Xie, R. Cong, X. Wu, Z. Tang and H. Fan, *J. Chem. Phys.*, 2010, **133**, 044303.
192 O. Hübner and H.-J. Himmel, *Angew. Chem., Int. Ed.*, 2020, **59**, 12206–12212.
193 (*a*) R. Hoffmann, *Rev. Mod. Phys.*, 1988, **60**, 601; (*b*) G. Frenking and N. Fröhlich, *Chem. Rev.*, 2000, **100**, 717–774; (*c*) M. Zhou, L. Andrews and C. W. Bauschlicher, Jr., *Chem. Rev.*, 2001, **101**, 1931–1961; (*d*) G. Frenking, I. Fernández, N. Holzmann, S. Pan, I. Krossing and M. Zhou, *JACS Au*, 2021, **1**, 623–645.
194 (*a*) G. Frenking, C. Loschen, A. Krapp, S. Fau and S. H. Strauss, *J. Comput. Chem.*, 2007, **28**, 117–126; (*b*) H. Kim, V. D. Doan, W. J. Cho, R. Valero, Z. Aliakbar Tehrani, J. M. L. Madridejos and K. S. Kim, *Sci. Rep.*, 2015, **5**, 16307; (*c*) P. Chaquin, Y. Canac, C. Lepetit, D. Zargarian and R. Chauvin, *Int. J. Quantum Chem.*, 2016, **116**, 1285–1295; (*d*) C. Poggel and G. Frenking, *Chem. – Eur. J.*, 2018, **24**, 11675–11682.
195 G. Blyholder, *J. Phys. Chem.*, 1964, **68**, 2772–2778.
196 A. Föhlisch and H. P. Bonzel, in *Springer Materials (Landolt-Börnstein - New Series Group III Condensed Matter)*, ed. H. P. Bonzel, Springer-Verlag, Berlin Heidelberg, 2005, vol. 42A4, ch. 3.7.1 CO and N2 Adsorption on Metal Surfaces.
197 (*a*) B. J. Morris-Sherwood, C. B. Powell and M. B. Hall, *J. Am. Chem. Soc.*, 1984, **106**, 5079–5083; (*b*) S. Ding and M. B. Hall, in *The Chemical Bond I: 100 Years Old and Getting Stronger*, ed. D. M. P. Mingos, Springer International Publishing, Cham, 2016, pp. 199–248.
198 (*a*) A. M. Ricks, Z. E. Reed and M. A. Duncan, *J. Mol. Spectrosc.*, 2011, **266**, 63–74; (*b*) M. K. Assefa, J. L. Devera, A. D. Brathwaite, J. D. Mosley and M. A. Duncan, *Chem. Phys. Lett.*, 2015, **640**, 175–179.
199 (*a*) X. Wu, L. Zhao, J. Jin, S. Pan, W. Li, X. Jin, G. Wang, M. Zhou and G. Frenking, *Science*, 2018, **361**, 912–916; (*b*) J. Jin, T. Yang, K. Xin, G. Wang, X. Jin, M. Zhou and G. Frenking, *Angew. Chem., Int. Ed.*, 2018, **57**, 6236–6241; (*c*) C. Chi, S. Pan, J. Jin, L. Meng, M. Luo, L. Zhao, M. Zhou and G. Frenking, *Chem. – Eur. J.*, 2019, **25**, 11772–11784; (*d*) J. Jin, S. Pan, X. Jin, S. Lei, L. Zhao, G. Frenking and M. Zhou, *Chem. – Eur. J.*, 2019, **25**, 3229–3234.
200 A. Fielicke, P. Gruene, G. Meijer and D. M. Rayner, *Surf. Sci.*, 2009, **603**, 1427–1433.
201 (*a*) D. M. Cox, K. C. Reichmann, D. J. Trevor and A. Kaldor, *J. Chem. Phys.*, 1988, **88**, 111–119; (*b*) L. Holmgren, M. Andersson and A. Rosen, *Surf. Sci.*, 1995, **331–333**, 231; (*c*) M. Andersson, L. Holmgren and A. Rosén, *Surf. Rev. Lett.*, 1996, **3**, 683–686; (*d*) L. Holmgren and A. Rosén, *J. Chem. Phys.*, 1999, **110**, 2629–2636.
202 I. Balteanu, U. Achatz, O. P. Balaj, B. S. Fox, M. K. Beyer and V. E. Bondybey, *Int. J. Mass Spectrom.*, 2003, **229**, 61–65.
203 (*a*) M. A. Nygren, P. E. M. Siegbahn, C. M. Jin, T. Guo and R. E. Smalley, *J. Chem. Phys.*, 1991, **95**, 6181–6184; (*b*) L. Holmgren, H. Grönbeck, M. Andersson and A. Rosén, *Phys. Rev. B: Condens. Matter Mater. Phys.*, 1996, **53**, 16644–16651; (*c*) N. Veldeman, P. Lievens and M. Andersson, *J. Phys. Chem. A*, 2005, **109**, 11793–11801.
204 (*a*) J. De Haeck, N. Veldeman, P. Claes, E. Janssens, M. Andersson and P. Lievens, *J. Phys. Chem. A*, 2011, **115**, 2103–2109; (*b*) P. Ferrari, L. M. Molina, V. E. Kaydashev, J. A. Alonso, P. Lievens and E. Janssens, *Angew. Chem., Int.*

Ed., 2016, **55**, 11059–11063; (*c*) P. Ferrari, G. Libeert, N. M. Tam and E. Janssens, *CrystEngComm*, 2020, **22**, 4807–4815.
205 N. Sheppard and T. T. Nguyen, in *Advances in Infrared and Raman Spectroscopy*, ed. R. E. Hester and R. J. H. Clark, Heyden, London, 1978, vol. 5, pp. 67–148.
206 (*a*) M. Zhou and L. Andrews, *J. Chem. Phys.*, 1999, **111**, 4548–4557; (*b*) B. Liang and L. Andrews, *J. Phys. Chem. A*, 2000, **104**, 9156–9164.
207 (*a*) C. O. Quicksall and T. G. Spiro, *Chem. Commun.*, 1967, 839–840; (*b*) C. O. Quicksall and T. G. Spiro, *Inorg. Chem.*, 1968, **7**, 2365–2369; (*c*) S. F. A. Kettle and P. L. Stanghellini, *Inorg. Chem.*, 1979, **18**, 2749–2754; (*d*) D. M. Adams and I. D. Taylor, *J. Chem. Soc., Faraday Trans. 2*, 1982, **78**, 1561–1571.
208 (*a*) B. Tremblay, G. Gutsev, L. Manceron and L. Andrews, *J. Phys. Chem. A*, 2002, **106**, 10525–10531; (*b*) B. Tremblay, L. Manceron, G. L. Gutsev and L. Andrews, *J. Chem. Phys.*, 2002, **107**, 8479–8485.
209 M. E. Alikhani, S. M. O. Souvi, M. Ibrahim and B. Tremblay, *J. Mol. Spectrosc.*, 2019, **361**, 8–15.
210 T. Bennett, R. H. Adnan, J. F. Alvino, V. Golovko, G. G. Andersson and G. F. Metha, *Inorg. Chem.*, 2014, **53**, 4340–4349.
211 T. Risse, A. Carlsson, M. Bäumer, T. Klüner and H.-J. Freund, *Surf. Sci.*, 2003, **546**, L829–L835.
212 G. Brodén, T. N. Rhodin, C. Brucker, R. Benbow and Z. Hurych, *Surf. Sci.*, 1976, **59**, 593–611.
213 D. B. Pedersen, D. M. Rayner, B. Simard, M. A. Addicoat, M. A. Buntine, G. F. Metha and A. Fielicke, *J. Phys. Chem. A*, 2004, **108**, 964–970.
214 V. J. F. Lapoutre, PhD thesis, University of Amsterdam, 2013.
215 (*a*) B. Hammer and J. K. Norskov, *Adv. Catal.*, 2000, **45**, 71–129; (*b*) M. Gajdos, A. Eichler and J. Hafner, *J. Phys.: Condens. Matter*, 2004, **16**, 1141–1164; (*c*) A. Nilsson, L. G. M. Pettersson, B. Hammer, T. Bligaard, C. H. Christensen and J. K. Nørskov, *Catal. Lett.*, 2005, **100**, 111–114.
216 F. Abild-Pedersen and M. P. Andersson, *Surf. Sci.*, 2007, **601**, 1747.
217 L. Jiang and Q. Xu, *J. Phys. Chem. A*, 2005, **109**, 1026–1032.
218 M. Lepage, T. Visser, F. Soulimani, A. M. Beale, A. Iglesias-Juez, A. M. J. van der Eerden and B. M. Weckhuysen, *J. Phys. Chem. C*, 2008, **112**, 9394–9404.
219 G. Pacchioni, S.-C. Chung, S. Krüger and N. Rösch, *Surf. Sci.*, 1997, **392**, 173–184.
220 M. Zhou and L. Andrews, *J. Am. Chem. Soc.*, 1999, **121**, 9171–9175.
221 E. Waldt, A.-S. Hehn, R. Ahlrichs, M. M. Kappes and D. Schooss, *J. Chem. Phys.*, 2015, **142**, 024319.
222 M. Frank, M. Bäumer, R. Kühnemuth and H.-J. Freund, *J. Phys. Chem. B*, 2001, **105**, 8569–8576.
223 (*a*) C. Lemire, R. Meyer, S. K. Shaikhutdinov and H.-J. Freund, *Surf. Sci.*, 2004, **552**, 27–34; (*b*) A. Beniya, N. Isomura, H. Hirata and Y. Watanabe, *Phys. Chem. Chem. Phys.*, 2014, **16**, 26485–26492.
224 B. Qiao, A. Wang, X. Yang, L. F. Allard, Z. Jiang, Y. Cui, J. Liu, J. Li and T. Zhang, *Nat. Chem.*, 2011, **3**, 634–641.
225 J. B. A. Davis, A. Shayeghi, S. L. Horswell and R. L. Johnston, *Nanoscale*, 2015, **7**, 14032–14038.
226 (*a*) P. Fayet, M. J. McGlinchey and L. H. Wöste, *J. Am. Chem. Soc.*, 1987, **109**, 1733–1738; (*b*) D. M. P. Mingos and D. J. Wales, *J. Am. Chem. Soc.*, 1990, **112**, 930–932.
227 (*a*) J. W. Lauher, *J. Am. Chem. Soc.*, 1978, **100**, 5305–5314; (*b*) D. M. P. Mingos, T. Slee and L. Zhenyang, *Chem. Rev.*, 1990, **90**, 383–402; (*c*) D. M. P. Mingos and D. J. Wales, *Introduction to Cluster Chemistry*, Prentice-Hall, London, 1990; (*d*) P. B. Armentrout, *Science*, 2018, **361**, 849–850.
228 (*a*) A. M. Ricks, A. D. Brathwaite and M. A. Duncan, *J. Phys. Chem. A*, 2013, **117**, 11490–11498; (*b*) A. D. Brathwaite, J. A. Maner and M. A. Duncan, *Inorg. Chem.*, 2014, **53**, 1166–1169; (*c*) A. D. Brathwaite, H. L. Abbott-Lyon and M. A. Duncan, *J. Phys. Chem. A*, 2016, **120**, 7659–7670.
229 G.-J. Wang and M.-F. Zhou, *Chin. J. Chem. Phys.*, 2018, **31**, 1–11.
230 (*a*) N. Zhang, M. Luo, C. Chi, G. Wang, J. Cui and M. Zhou, *J. Phys. Chem. A*, 2015, **119**, 4142–4150; (*b*) H. Qu, F. Kong, G. Wang and M. Zhou, *J. Phys. Chem. A*, 2016, **120**, 7287–7293; (*c*) C. Chi, J.-Q. Wang, H. Qu, W.-L. Li, L. Meng, M. Luo, J. Li and M. Zhou, *Angew. Chem., Int. Ed.*, 2017, **56**, 6932–6936; (*d*) H. Qu, F. Kong, G. Wang and M. Zhou, *J. Phys. Chem. A*, 2017, **121**, 1627–1632; (*e*) J.-Q. Wang, C. Chi, H.-S. Hu, X. Li, M. Luo, J. Li and M. Zhou, *Angew. Chem., Int. Ed.*, 2020, **59**, 2344–2348.
231 H.-J. Himmel and M. Reiher, *Angew. Chem., Int. Ed.*, 2006, **45**, 6264–6288.
232 T. Stüker, H. Beckers and S. Riedel, *Chem. – Eur. J.*, 2020, **26**, 7384–7394.
233 L.-H. Mou, Z.-Y. Li and S.-G. He, *J. Phys. Chem. Lett.*, 2022, **13**, 4159–4169.
234 L. Geng, C. Cui, Y. Jia, B. Yin, H. Zhang, Z.-D. Sun and Z. Luo, *J. Phys. Chem. A*, 2021, **125**, 2130–2138.
235 P. L. Holland, *Dalton Trans.*, 2010, **39**, 5415–5425.
236 V. E. Bondybey and J. W. Nibler, *J. Chem. Phys.*, 1973, **58**, 2125–2134.
237 I. Gulaczyk, M. Kręglewski and A. Valentin, *J. Mol. Spectrosc.*, 2003, **220**, 132–136.
238 (*a*) M. S. Ford, M. L. Anderson, M. P. Barrow, D. P. Woodruff, T. Drewello, P. J. Derrick and S. R. Mackenzie, *Phys. Chem. Chem. Phys.*, 2005, **7**, 975–980; (*b*) D. Harding, S. R. Mackenzie and T. R. Walsh, *J. Phys. Chem. B*, 2006, **110**, 18272–18277; (*c*) D. Harding, M. S. Ford, T. R. Walsh and S. R. Mackenzie, *Phys. Chem. Chem. Phys.*, 2007, **9**, 2130–2136.
239 (*a*) J. Mohrbach, S. Dillinger and G. Niedner-Schatteburg, *J. Chem. Phys.*, 2017, **147**, 184304; (*b*) A. Straßner, M. P. Klein, D. V. Fries, C. Wiehn, M. E. Huber, J. Mohrbach, S. Dillinger, D. Spelsberg, P. B. Armentrout and G. Niedner-Schatteburg, *J. Chem. Phys.*, 2021, **155**, 244306.
240 J. Jin, G. Wang and M. Zhou, *J. Phys. Chem. A*, 2021, **125**, 6246–6253.
241 *NIST Chemistry WebBook*, ed. P. J. Linstrom and W. G. Mallard, National Institute of Standards and Technology, Gaithersburg MD, NIST Standard Reference Database Number 69, 2020, 20899.

242 C. J. Cramer, W. B. Tolman, K. H. Theopold and A. L. Rheingold, *Proc. Natl. Acad. Sci. U. S. A.*, 2003, **100**, 3635–3640.
243 Y. Gong, M. Zhou and L. Andrews, *Chem. Rev.*, 2009, **109**, 6765–6808.
244 (*a*) K. R. Asmis and J. Sauer, *Mass Spectrom. Rev.*, 2007, **26**, 542–562; (*b*) H. Schwarz and K. R. Asmis, *Chem. – Eur. J.*, 2019, **25**, 2112–2126.
245 (*a*) P. H. Krupenie, *J. Phys. Chem. Ref. Data*, 1972, **1**, 423–534; (*b*) K. P. Huber and G. H. Herzberg, in *"Constants of Diatomic Molecules" (data prepared by Jean W. Gallagher and Russell D. Johnson, III)*, ed. P. J. Linstrom and W. G. Mallard, NIST Chemistry WebBook, Gaithersburg MD, NIST Standard Reference Database Number 69, 20899, https://doi.org/10.18434/T4D303, (retrieved Jan 06, 2023).
246 R. J. Celotta, R. A. Bennett, J. L. Hall, M. W. Siegel and J. Levine, *Phys. Rev. A: At., Mol., Opt. Phys.*, 1972, **6**, 631–642.
247 H. H. Eysel and S. Thym, *Z. Anorg. Allg. Chem.*, 1975, **411**, 97–102.
248 H. Föppl, *Z. Anorg. Allg. Chem.*, 1957, **291**, 12–50.
249 (*a*) R. Burgert, H. Schnöckel, A. Grubisic, X. Li, S. T. Stokes, K. H. Bowen, G. F. Ganteför, B. Kiran and P. Jena, *Science*, 2008, **319**, 438–442; (*b*) B. C. Sweeny, S. G. Ard, A. A. Viggiano, J. C. Sawyer, D. C. McDonald II and N. S. Shuman, *J. Phys. Chem. A*, 2019, **123**, 6123–6129.
250 B. C. Sweeny, D. C. McDonald, II, J. C. Poutsma, S. G. Ard, A. A. Viggiano and N. S. Shuman, *J. Phys. Chem. Lett.*, 2020, **11**, 217–220.
251 B. C. Sweeny, D. C. McDonald, II, N. S. Shuman, A. A. Viggiano, J. Troe and S. G. Ard, *J. Phys. Chem. A*, 2021, **125**, 2069–2076.
252 (*a*) A. P. Woodham and A. Fielicke, in *Gold Clusters, Colloids and Nano-Particles I*, ed. D. M. P. Mingos, 2014, pp. 243–278; (*b*) A. Zavras, G. N. Khairallah and R. A. J. O'Hair, in *Gold Clusters, Colloids and Nanoparticles II*, ed. D. M. P. Mingos, Springer International Publishing, Cham, 2014, pp. 139–230.
253 M. Walter and H. Hakkinen, *Phys. Chem. Chem. Phys.*, 2006, **8**, 5407–5411.
254 (*a*) D. M. Cox, R. Brickman, K. Creegan and A. Kaldor, *Z. Phys. D*, 1991, **19**, 353–355; (*b*) B. J. Winter, E. K. Parks and S. J. Riley, *J. Chem. Phys.*, 1991, **94**, 8618–8621; (*c*) T. H. Lee and K. M. Ervin, *J. Phys. Chem.*, 1994, **98**, 10023–10031.
255 S. Hirabayashi, M. Ichihashi, Y. Kawazoe and T. Kondow, *J. Phys. Chem. A*, 2012, **116**, 8799–8806.
256 M. Schmidt, A. Masson and C. Bréchignac, *Phys. Rev. Lett.*, 2003, **91**, 243401.
257 M. Andersson, J. L. Persson and A. Rosen, *Nanostruct. Mater.*, 1993, **3**, 337–344.
258 R. Pal, L.-M. Wang, Y. Pei, L.-S. Wang and X. C. Zeng, *J. Am. Chem. Soc.*, 2012, **134**, 9438–9445.
259 M. Akita and Y. Moro-oka, *Catal. Today*, 1998, **44**, 183–188.
260 (*a*) S. M. Lang and T. M. Bernhardt, *J. Chem. Phys.*, 2009, **131**, 024310; (*b*) S. M. Lang, T. M. Bernhardt, R. N. Barnett and U. Landman, *J. Phys. Chem. C*, 2011, **115**, 6788–6795.
261 C. Jackschath, I. Rabin and W. Schulze, *Ber. Bunsenges. Phys. Chem.*, 1992, **96**, 1200–1204.
262 M. Gao, D. Horita, Y. Ono, A. Lyalin, S. Maeda and T. Taketsugu, *J. Phys. Chem. C*, 2017, **121**, 2661–2668.
263 C.-Y. Mang, C.-P. Liu and K.-C. Wu, *Mol. Phys.*, 2021, **19**, e1812744.
264 F. Mafuné, K. Koyama, T. Nagata, S. Kudoh, T. Yasuike, K. Miyajima, D. M. M. Huitema, V. Chernyy and J. M. Bakker, *J. Phys. Chem. C*, 2019, **123**, 5964–5971.
265 C. Kerpal, D. J. Harding, A. C. Hermes, G. Meijer, S. R. Mackenzie and A. Fielicke, *J. Phys. Chem. A*, 2013, **117**, 1233–1239.
266 R. Yang, Y. Gong and M. Zhou, *Chem. Phys.*, 2007, **340**, 134–140.
267 D.-H. Lee, B. Mondal and K. D. Karlin, in *Activation of Small Molecules*, ed. W. B. Tolman, Wiley-VCH, Weinheim, 2006, pp. 43–79.
268 (*a*) L. Wang, G. Wang, H. Qu, Z. H. Li and M. Zhou, *Phys. Chem. Chem. Phys.*, 2014, **16**, 10788–10798; (*b*) L. Wang, G. Wang, H. Qu, C. Wang and M. Zhou, *J. Phys. Chem. A*, 2014, **118**, 1841–1849; (*c*) Y. Li, L. Wang, H. Qu, G. Wang and M. Zhou, *J. Phys. Chem. A*, 2015, **119**, 3577–3586.
269 W. A. Brown, in *Springer Materials (Landolt-Börnstein - New Series Group III Condensed Matter)*, ed. A. P. Bonzel, Springer-Verlag, Berlin Heidelberg, 2003, vol. 42A3, ch. 3.7.2 NO, CN and O_2 on Metal Surfaces.
270 W. A. Brown and D. A. King, *J. Phys. Chem. B*, 2000, **104**, 2578–2595.
271 L. Andrews and A. Citra, *Chem. Rev.*, 2002, **102**, 885–912.
272 G. Meizyte, P. A. J. Pearcy, P. D. Watson, E. I. Brewer, A. E. Green, M. Doll, O. A. Duda and S. R. Mackenzie, *J. Phys. Chem. A*, 2022, **126**, 9414–9422.
273 J. M. Bakker and F. Mafuné, *Phys. Chem. Chem. Phys.*, 2022, **24**, 7595–7610.
274 G. Kummerlöwe and M. K. Beyer, *Int. J. Mass Spectrom.*, 2005, **244**, 84–90.
275 M. L. Anderson, M. S. Ford, P. J. Derrick, T. Drewello, D. P. Woodruff and S. R. Mackenzie, *J. Phys. Chem. A*, 2006, **110**, 10992–11000.
276 Y. Tawaraya, S. Kudoh, K. Miyajima and F. Mafuné, *J. Phys. Chem. A*, 2015, **119**, 8461–8468.
277 M. Arakawa, M. Horioka, K. Minamikawa, T. Kawano and A. Terasaki, *J. Phys. Chem. C*, 2020, **124**, 26881–26888.
278 B. Yin, Q. Du, L. Geng, H. Zhang, Z. Luo, S. Zhou and J. Zhao, *J. Phys. Chem. Lett.*, 2020, **11**, 5807–5814.
279 A. Citra, X. Wang and L. Andrews, *J. Phys. Chem. A*, 2002, **106**, 3287–3293.
280 T. D. Jaeger, A. Fielicke, G. von Helden, G. Meijer and M. A. Duncan, *Chem. Phys. Lett.*, 2004, **392**, 409–414.
281 D. M. Kiawi, V. Chernyy, J. Oomens, W. J. Buma, Z. Jamshidi, L. Visscher, L. B. F. M. Waters and J. M. Bakker, *J. Phys. Chem. Lett.*, 2016, **7**, 2381–2387.
282 D. M. Kiawi, J. M. Bakker, J. Oomens, W. J. Buma, Z. Jamshidi, L. Visscher and L. B. F. M. Waters, *J. Phys. Chem. A*, 2015, **119**, 10828–10837.
283 F. Mafuné, A. Manam and S. Kudoh, *Z. Phys. Chem.*, 2019, **233**, 881–894.
284 A. Yanagimachi, K. Koyasu, D. Yubero Valdivielso, S. Gewinner, W. Schöllkopf, A. Fielicke and T. Tsukuda, *J. Phys. Chem. C*, 2016, **120**, 14209–14215.

285 A. E. Green, J. Justen, W. Schöllkopf, A. S. Gentleman, A. Fielicke and S. R. Mackenzie, *Angew. Chem., Int. Ed.*, 2018, **57**, 14822–14826.
286 O. V. Lushchikova, M. Szalay, T. Höltzl and J. M. Bakker, *Faraday Discuss.*, 2023, **242**, 252–268.
287 O. V. Lushchikova, M. Szalay, H. Tahmasbi, L. B. F. Juurlink, J. Meyer, T. Höltzl and J. M. Bakker, *Phys. Chem. Chem. Phys.*, 2021, **23**, 26661–26673.
288 A. E. Green, S. Schaller, G. Meizyte, B. J. Rhodes, S. P. Kealy, A. S. Gentleman, W. Schöllkopf, A. Fielicke and S. R. Mackenzie, *J. Phys. Chem. A*, 2020, **124**, 5389–5401.
289 E. M. Cunningham, A. E. Green, G. Meizyte, A. S. Gentleman, P. W. Beardsmore, S. Schaller, K. M. Pollow, K. Saroukh, M. Förstel, O. Dopfer, W. Schöllkopf, A. Fielicke and S. R. Mackenzie, *Phys. Chem. Chem. Phys.*, 2021, **23**, 329–338.
290 S. M. Hamilton, W. S. Hopkins, D. J. Harding, T. R. Walsh, P. Gruene, M. Haertelt, A. Fielicke, G. Meijer and S. R. Mackenzie, *J. Am. Chem. Soc.*, 2010, **132**, 1448–1449.
291 A. C. Hermes, S. M. Hamilton, W. S. Hopkins, D. J. Harding, C. Kerpal, G. Meijer, A. Fielicke and S. R. Mackenzie, *J. Phys. Chem. Lett.*, 2011, **2**, 3053–3057.
292 G. Meizyte, A. E. Green, A. S. Gentleman, S. Schaller, W. Schöllkopf, A. Fielicke and S. R. Mackenzie, *Phys. Chem. Chem. Phys.*, 2020, **22**, 18606–18613.
293 (*a*) K. Nauta, D. T. Moore, P. L. Stiles and R. E. Miller, *Science*, 2001, **292**, 481–484; (*b*) P. L. Stiles, D. T. Moore and R. E. Miller, *J. Chem. Phys.*, 2004, **121**, 3130–3142.
294 P. L. Stiles and R. E. Miller, *J. Phys. Chem. A*, 2006, **110**, 10225–10235.
295 P. L. Stiles and R. E. Miller, *J. Phys. Chem. A*, 2006, **110**, 5620–5628.
296 T. Shimanouchi, *Tables of Molecular Vibrational Frequencies Consolidated*, National Bureau of Standards, 1972.
297 M. A. Henderson, *Surf. Sci. Rep.*, 2002, **46**, 1–308.
298 M. K. Beyer, *Mass Spectrom. Rev.*, 2007, **26**, 517–541.
299 N. R. Walker, R. S. Walters and M. A. Duncan, *New J. Chem.*, 2005, **29**, 1495–1503.
300 T. E. Cooper, J. T. O'Brien, E. R. Williams and P. B. Armentrout, *J. Phys. Chem. A*, 2010, **114**, 12646–12655.
301 B. Bandyopadhyay, K. N. Reishus and M. A. Duncan, *J. Phys. Chem. A*, 2013, **117**, 7794–7803.
302 Y. Li, G. Wang, C. Wang and M. Zhou, *J. Phys. Chem. A*, 2012, **116**, 10793–10801.
303 J. T. O'Brien and E. R. Williams, *J. Phys. Chem. A*, 2008, **112**, 5893–5901.
304 (*a*) E. K. Parks, B. H. Weiller, P. S. Bechthold, W. F. Hoffman, G. C. Nieman, L. G. Pobo and S. J. Riley, *J. Chem. Phys.*, 1988, **88**, 1622–1632; (*b*) P. S. Bechthold, E. K. Parks, B. H. Weiller, L. G. Pobo and S. J. Riley, *Z. Phys. Chem. Neue Folge*, 1990, **169**, 101–122; (*c*) E. K. Parks, T. D. Klots, B. J. Winter and S. J. Riley, *J. Chem. Phys.*, 1993, **99**, 5831–5839.
305 H. Zhang, H. Wu, Y. Jia, B. Yin, L. Geng, Z. Luo and K. Hansen, *Commun. Chem.*, 2020, **3**, 148.
306 H. Zhang, M. Zhang, Y. Jia, L. Geng, B. Yin, S. Li, Z. Luo and F. Pan, *J. Phys. Chem. Lett.*, 2021, **12**, 1593–1600.
307 M. Trachtman, G. D. Markham, J. P. Glusker, P. George and C. W. Bock, *Inorg. Chem.*, 1998, **37**, 4421–4431.
308 L. G. Dodson, M. C. Thompson and J. M. Weber, *Ann. Rev. Phys. Chem.*, 2018, **69**, 231–252.
309 J. M. Weber, *Int. Rev. Phys. Chem.*, 2014, **33**, 489–519.
310 (*a*) H. J. Freund and M. W. Roberts, *Surf. Sci. Rep.*, 1996, **25**, 225–273; (*b*) D. H. Gibson, *Coord. Chem. Rev.*, 1999, **185–186**, 335–355; (*c*) B. E. Koel, C. Panja, J. Kim and E. Samano, in *Springer Materials (Landolt-Börnstein - New Series Group III Condensed Matter)*, ed. H. P. Bonzel, Springer-Verlag, Berlin Heidelberg, 2005, vol. 42A5, ch. 3.8.4 CO_2, NO_2, SO_2, OCS, N_2O, O_3 on Metal Surfaces; (*d*) M. Aresta, in *Activation of Small Molecules*, ed. W. B. Tolman, Wiley-VCH, Weinheim, 2006, ch. 1, pp. 1–41.
311 W. E. Thompson and M. E. Jacox, *J. Chem. Phys.*, 1999, **111**, 4487–4496.
312 (*a*) B. J. Knurr and J. M. Weber, *J. Am. Chem. Soc.*, 2012, **134**, 18804–18808; (*b*) B. J. Knurr and J. M. Weber, *J. Phys. Chem. A*, 2013, **117**, 10764–10771; (*c*) E. Barwa, T. F. Pascher, M. Ončák, C. van der Linde and M. K. Beyer, *Angew. Chem., Int. Ed.*, 2020, **59**, 7467–7471; (*d*) H. Zheng, X. Kong, C. Wang, T. Wang, D. Yang, G. Li, H. Xie, Z. Zhao, R. Shi, H. Han, H. Fan, X. Yang and L. Jiang, *J. Phys. Chem. Lett.*, 2021, **12**, 472–477.
313 B. J. Thomas, B. A. Harruff-Miller, C. E. Bunker and W. K. Lewis, *J. Chem. Phys.*, 2015, **142**, 174310.
314 P. A. Hintz and K. M. Ervin, *J. Chem. Phys.*, 1995, **103**, 7897–7906.
315 O. Gehret and M. P. Irion, *Chem. – Eur. J.*, 1996, **2**, 598–603.
316 (*a*) J. B. Griffin and P. B. Armentrout, *J. Chem. Phys.*, 1997, **107**, 5345–5355; (*b*) J. B. Griffin and P. B. Armentrout, *J. Chem. Phys.*, 1998, **108**, 8075–8083.
317 E. Lim, J. Heo, X. Zhang, K. H. Bowen, S. H. Lee and S. K. Kim, *J. Phys. Chem. A*, 2021, **125**, 2243–2248.
318 A. Göbel, A. Rubio and J. Lischner, *J. Phys. Chem. A*, 2021, **125**, 5878–5885.
319 K. K. Pandey, *Coord. Chem. Rev.*, 1995, **140**, 37–114.
320 L. A. Brown and D. M. Rayner, *J. Chem. Phys.*, 1998, **109**, 2474–2479.
321 W. B. Tolman, *Angew. Chem., Int. Ed.*, 2010, **49**, 1018–1024.
322 V. V. Lavrov, V. Blagojevic, G. K. Koyanagi, G. Orlova and D. K. Bohme, *J. Phys. Chem. A*, 2004, **108**, 5610–5624.
323 K. Fields, B. M. Barngrover and J. B. Gary, *Inorg. Chem.*, 2020, **59**, 18314–18318.
324 (*a*) A. Delabie, C. Vinckier, M. Flock and K. Pierloot, *J. Phys. Chem. A*, 2001, **105**, 5479–5485; (*b*) X.-Y. Yang, Y.-C. Wang, Z.-Y. Geng and Z.-Y. Liu, *Chem. Phys. Lett.*, 2006, **430**, 265–270.
325 (*a*) X. Jin, G. Wang and M. Zhou, *J. Phys. Chem. A*, 2006, **110**, 8017–8022; (*b*) L. Jiang and Q. Xu, *J. Phys. Chem. A*, 2009, **113**, 5620–5624.
326 (*a*) E. M. Cunningham, A. S. Gentleman, P. W. Beardsmore, A. Iskra and S. R. Mackenzie, *J. Phys. Chem. A*, 2017, **121**, 7565–7571; (*b*) E. M. Cunningham, A. S. Gentleman, P. W. Beardsmore and S. R. Mackenzie, *Phys. Chem. Chem. Phys.*, 2019, **21**, 13959–13967.

327 (*a*) I. Balteanu, O. P. Balaj, M. K. Beyer and V. E. Bondybey, *Phys. Chem. Chem. Phys.*, 2004, **6**, 2910–2913; (*b*) M. L. Anderson, A. Lacz, T. Drewello, P. J. Derrick, D. P. Woodruff and S. R. Mackenzie, *J. Chem. Phys.*, 2009, **130**, 064305.

328 I. S. Parry, A. Kartouzian, S. M. Hamilton, O. P. Balaj, M. K. Beyer and S. R. Mackenzie, *J. Phys. Chem. A*, 2013, **117**, 8855–8863.

329 D. J. Harding, T. R. Walsh, S. M. Hamilton, W. S. Hopkins, S. R. Mackenzie, P. Gruene, M. Haertelt, G. Meijer and A. Fielicke, *J. Chem. Phys.*, 2010, **132**, 011101.

330 I. S. Parry, A. Kartouzian, S. M. Hamilton, O. P. Balaj, M. K. Beyer and S. R. Mackenzie, *Angew. Chem., Int. Ed.*, 2015, **54**, 1357–1360.

331 T. Shimanouchi, *J. Phys. Chem. Ref. Data*, 1972, **6**, 993–1102.

332 M. Yamaguchi and F. Mafuné, *J. Phys. Chem. C*, 2019, **123**, 15575–15581.

333 K. A. Jackson, M. Knickelbein, G. Koretsky and S. Srinivas, *Chem. Phys.*, 2000, **262**, 41–51.

334 D. M. Rayner, K. Athanassenas, B. A. Collings, S. A. Mitchell and P. A. Hackett, in *Theory of Atomic and Molecular Clusters: With a Glimpse at Experiments*, ed. J. Jellinek, Springer-Verlag, Berlin Heidelberg, 1999, pp. 371–395.

335 J. Lengyel, N. Levin, F. J. Wensink, O. V. Lushchikova, R. N. Barnett, U. Landman, U. Heiz, J. M. Bakker and M. Tschurl, *Angew. Chem., Int. Ed.*, 2020, **59**, 23631–23635.

336 (*a*) M. A. Ashraf, C. W. Copeland, A. Kocak, A. R. McEnroe and R. B. Metz, *Phys. Chem. Chem. Phys.*, 2015, **17**, 25700–25704; (*b*) C. W. Copeland, M. A. Ashraf, E. M. Boyle and R. B. Metz, *J. Phys. Chem. A*, 2017, **121**, 2132–2137.

337 O. V. Lushchikova, S. Reijmer, P. B. Armentrout and J. M. Bakker, *J. Am. Soc. Mass Spectrom.*, 2022, **33**, 1393–1400.

338 G. M. Koretsky and M. B. Knickelbein, *J. Chem. Phys.*, 1997, **107**, 10555–10566.

339 S. M. Lang, T. M. Bernhardt, J. M. Bakker, B. Yoon and U. Landman, *J. Phys.: Condens. Matter*, 2018, **30**, 504001.

340 S. M. Lang, T. M. Bernhardt, J. M. Bakker, B. Yoon and U. Landman, *Int. J. Mass Spectrom.*, 2019, **435**, 241–250.

341 G. M. Koretsky and M. B. Knickelbein, *Chem. Phys. Lett.*, 1997, **267**, 485–490.

342 (*a*) M. B. Knickelbein, *Chem. Phys. Lett.*, 1995, **239**, 11–17; (*b*) M. B. Knickelbein, *J. Chem. Phys.*, 1996, **104**, 3517–3525; (*c*) D. M. Cox, A. Kaldor and M. R. Zakin, *Proc. SPIE-Int. Soc. Opt. Eng.*, 1987, **742**, 118–121(Laser Applications to Chemical Dynamics); (*d*) A. Kaldor, D. M. Cox and M. R. Zakin, *Adv. Chem. Phys.*, 1988, **70**, 211–261.

343 (*a*) S. Hirabayashi, R. Okawa, M. Ichihashi, Y. Kawazoe and T. Kondow, *J. Chem. Phys.*, 2009, **130**, 164304; (*b*) S. Hirabayashi, M. Ichihashi, Y. Kawazoe and T. Kondow, *Chem. Phys. Lett.*, 2010, **490**, 19–23.

344 (*a*) P. M. Bialach, M. Braun, A. Lüchow and M. Gerhards, *Phys. Chem. Chem. Phys.*, 2009, **11**, 10403–10408; (*b*) P. M. Bialach, A. Funk, M. Weiler and M. Gerhards, *J. Chem. Phys.*, 2010, **133**, 194304.

345 M. B. Knickelbein and G. M. Koretsky, *J. Phys. Chem. A*, 1998, **102**, 580–586.

346 (*a*) G. Dietrich, K. Dasgupta, S. Krückeberg, K. Lützenkirchen, L. Schweikhard, C. Walther and J. Ziegler, *Chem. Phys. Lett.*, 1996, **259**, 397–402; (*b*) R. Rousseau, G. Dietrich, S. Krückeberg, K. Lützenkirchen, D. Marx, L. Schweikhard and C. Walther, *Chem. Phys. Lett.*, 1998, **295**, 41–46; (*c*) R. Rousseau and D. Marx, *J. Chem. Phys.*, 2000, **112**, 761–769; (*d*) G. Dietrich, S. Krückeberg, K. Lützenkirchen, L. Schweikhard and C. Walther, *J. Chem. Phys.*, 2000, **112**, 752–759.

347 S. M. Lang, T. M. Bernhardt, J. M. Bakker, B. Yoon and U. Landman, *Z. Phys. Chem.*, 2019, **233**, 865–880.

348 W. Jin, M. Becherer, D. Bellaire, G. Lefkidis, M. Gerhards and W. Hübner, *Phys. Rev. B: Condens. Matter Mater. Phys.*, 2014, **89**, 144409.

349 G. M. Koretsky, M. B. Knickelbein, R. Rousseau and D. Marx, *J. Phys. Chem. A*, 2001, **105**, 11197–11203.

350 D. Dutta, M. Becherer, D. Bellaire, F. Dietrich, M. Gerhards, G. Lefkidis and W. Hübner, *Phys. Rev. B*, 2018, **97**, 224404.

351 S. M. Lang, T. M. Bernhardt, J. M. Bakker, R. N. Barnett and U. Landman, *J. Phys. Chem. A*, 2020, **124**, 4990–4997.

352 T. F. Pascher, M. Ončák, C. van der Linde and M. K. Beyer, *J. Chem. Phys.*, 2020, **153**, 184301.

353 G. Ertl, *Catal. Rev.: Sci. Eng.*, 1980, **21**, 201–223.

354 E. Hasselbrink, in *Springer Materials (Landolt-Börnstein - New Series Group III Condensed Matter)*, ed. H. P. Bonzel, Springer-Verlag, Berlin Heidelberg, 2003, vol. 42A3, ch. 3.8.3 Adsorbate Properties of NH3 and PF3 on Metals and Semiconductors.

355 (*a*) T. E. Salter, V. A. Mikhailov, C. J. Evans and A. M. Ellis, *J. Chem. Phys.*, 2006, **125**, 034302; (*b*) N. Koga, K. Ohashi, K. Furukawa, T. Imamura, K. Judai, N. Nishi and H. Sekiya, *Chem. Phys. Lett.*, 2012, **539–540**, 1–6; (*c*) J. Kozubal, T. R. Heck and R. B. Metz, *J. Phys. Chem. A*, 2019, **123**, 4929–4936.

356 (*a*) M. Chen, H. Lu, J. Dong, L. Miao and M. Zhou, *J. Phys. Chem. A*, 2002, **106**, 11456–11464; (*b*) M. Zhou, M. Chen, L. Zhang and H. Lu, *J. Phys. Chem. A*, 2002, **106**, 9017–9023; (*c*) X. Liu, X. Wang, B. Xu and L. Andrews, *Chem. Phys. Lett.*, 2012, **523**, 6–10.

357 J. Roithova and J. M. Bakker, *Mass Spectrom. Rev.*, 2022, **41**, 513–528.

358 (*a*) G. Wang, M. Chen and M. Zhou, *Chem. Phys. Lett.*, 2005, **412**, 46–49; (*b*) H.-G. Cho and L. Andrews, *J. Phys. Chem. A*, 2008, **112**, 12293–12295; (*c*) H.-G. Cho and L. Andrews, *Organometallics*, 2009, **28**, 1358–1368; (*d*) H.-G. Cho and L. Andrews, *Dalton Trans.*, 2011, **40**, 11115–11124.

359 N. S. Shuman, S. G. Ard, B. C. Sweeny, H. Pan, A. A. Viggiano, N. R. Keyes, H. Guo, C. J. Owen and P. B. Armentrout, *Catal. Sci. Technol.*, 2019, **9**, 2767–2780.

360 (*a*) D. J. Trevor, D. M. Cox and A. Kaldor, *J. Am. Chem. Soc.*, 1990, **112**, 3742–3749; (*b*) U. Achatz, C. Berg, S. Joos, B. S. Fox, M. K. Beyer, G. Niedner-Schatteburg and V. E. Bondybey, *Chem. Phys. Lett.*, 2000, **320**, 53–58; (*c*) C. Adlhart and E. Uggerud, *Chem. Commun.*, 2006, 2581–2582; (*d*) G. Kummerlöwe, I. Balteanu, Z. Sun, O. P. Balaj, V. E. Bondybey and M. K. Beyer, *Int. J. Mass Spectrom.*, 2006, **254**, 183–188.

361 J. Vohs, in *Springer Materials (Landolt-Börnstein - New Series Group III Condensed Matter)*, ed. H. P. Bonzel, Springer-Verlag, Berlin Heidelberg, 2003, vol. 42A3, ch. 3.8.8 Oxygenated Hydrocarbons.
362 M. Ichihashi, T. Hanmura, R. T. Yadav and T. Kondow, *J. Phys. Chem. A*, 2000, **104**, 11885–11890.
363 F. Dong and R. E. Miller, *J. Phys. Chem. A*, 2004, **108**, 2181–2191.
364 W. T. Wallace and R. L. Whetten, *J. Am. Chem. Soc.*, 2002, **124**, 7499–7505.
365 A. Lyalin and T. Taketsugu, *J. Phys. Chem. Lett.*, 2010, **1**, 1752–1757.
366 (*a*) T. Baer and W. L. Hase, *Unimolecular Reaction Dynamics*, Oxford University Press, Oxford, 1996; (*b*) K. Hansen, *Statistical Physics of Nanoparticles in the Gas Phase*, Springer, 2013.
367 M. Citir and R. B. Metz, *J. Chem. Phys.*, 2008, **128**, 024307.
368 P. J. J. Carr, M. J. Lecours, M. J. Burt, R. A. Marta, V. Steinmetz, E. Fillion and W. S. Hopkins, *J. Phys. Chem. Lett.*, 2018, **9**, 157–162.
369 L. Lv, Y. Wang, Q. Wang and H. Liu, *J. Phys. Chem. C*, 2010, **114**, 17610–17620.
370 Y. Shi and K. M. Ervin, *J. Chem. Phys.*, 1998, **108**, 1757–1760.
371 M. M. Kappes and R. H. Staley, *J. Am. Chem. Soc.*, 1981, **103**, 1286–1287.
372 O. P. Balaj, I. Balteanu, T. T. J. Roßteuscher, M. K. Beyer and V. E. Bondybey, *Angew. Chem., Int. Ed.*, 2004, **43**, 6519–6522.
373 H. S. Taylor, *Philos. Trans. R. Soc., A*, 1925, **108**, 105–111.
374 (*a*) M. Vonderach, O. T. Ehrler, P. Weis and M. M. Kappes, *Anal. Chem.*, 2011, **83**, 1108–1115; (*b*) K. Koyasu, T. Ohtaki, N. Hori and F. Misaizu, *Chem. Phys. Lett.*, 2012, **523**, 54–59; (*c*) J. Seo, W. Hoffmann, S. Warnke, X. Huang, S. Gewinner, W. Schöllkopf, M. T. Bowers, G. von Helden and K. Pagel, *Nat. Chem.*, 2017, **9**, 39–44; (*d*) M. Z. Kamrath and T. R. Rizzo, *Acc. Chem. Res.*, 2018, **51**, 1487–1495; (*e*) M. Marianski, J. Seo, E. Mucha, D. A. Thomas, S. Jung, R. Schlögl, G. Meijer, A. Trunschke and G. von Helden, *J. Phys. Chem. C*, 2019, **123**, 7845–7853; (*f*) J. T. Buntine, E. Carrascosa, J. N. Bull, U. Jacovella, M. I. Cotter, P. Watkins, C. Liu, M. S. Scholz, B. D. Adamson, S. J. P. Marlton and E. J. Bieske, *Rev. Sci. Instr.*, 2022, **93**, 043201.
375 Y. Yang, Y. X. Zhao and S. G. He, *Chem. – Eur. J.*, 2022, **28**, e202200062.
376 *Chem. Rev. (Heterogeneous Single-Atom Catalysis)*, ed. J. Li, M. F. Stephanopoulos and Y. Xia, 2020, vol. 120, iss. 21.
377 Y. Liu, Z. Wu, H. Kuhlenbeck and H. J. Freund, *Chem. Rec.*, 2021, **21**, 1270–1283.
378 W. S. Hopkins, V. Verzilov, G. Sciaini, I. Burgess and M. Boland, *Can. J. Phys.*, 2019, **97**, vii–x.
379 M. Czerny, *Z. Phys.*, 1929, **53**, 1–12.
380 J. F. W. Herschel, *Philos. Trans. R. Soc. London*, 1840, **130**, 1–59.